

**Functionalized Ti-V Surfaces for Improved Osseointegration and
Tribocorrosion of Biomedical Implants**

by

Arman Butt

B.S. (University of Illinois at Chicago) 2010

B.S. (Loyola University Chicago) 2010

THESIS

Submitted as partial fulfillment of the requirements
for the degree of Doctor of Philosophy in Bioengineering
in the Graduate College of the
University of Illinois at Chicago, 2015

Chicago, Illinois

Defense Committee:

Christos G. Takoudis, Chair and Advisor

David Endington

Gregory Jursich

Cortino Sukotjo, Department of Restorative Dentistry

Tolou Shokuhfar, Department of Mechanical Engineering, Michigan Technological University

Mathew T. Mathew, Department of Orthopedic Surgery, Rush University Medical Center

Bin Yang, Department of Restorative Dentistry

To my mother, Jamila

To my wife, Nairyna

and to my son, Tzeb-Sultaan

whose support and love have motivated me throughout my ups and downs.

ACKNOWLEDGMENTS

First and foremost, I sincerely acknowledge my advisor and dissertation chair, Dr. Christos G. Takoudis for his invaluable guidance throughout my studies. From the very beginning, Dr. Takoudis has made me think beyond my studies and has helped forge my educational experience into a life-changing experience. With great appreciation and debt, I will forever be grateful to him.

I would also like to thank defense committee members Dr. Jursich, Dr. Sukotjo, Dr. Mathew, Dr. Shokuhfar and Dr. Yang for their thoughtful assistance in my studies. Many thanks also go out to AMReL and IBTN members who played a role in the shaping of my educational experience, notably Runshen, Sathees, and Dmitry.

I would like to give thanks to my mom, Jamila, for raising me and shaping me into the man that I am today, for bringing me to the greatest country on Earth, for giving me the encouragement, love, and opportunities to reach this stage of my life. As a saint once said, “If you had a thousand years to live, you can never repay even the one night she spent taking care of you as an infant,” let alone a lifetime of caring. I would like to thank my wife, Nairyna, for being by my side and giving me the encouragement during the low times. Lastly, I am grateful to my son, Tzeb-Sultaan, who has motivated me beyond words to finish my studies. May I be the inspiration for him to accomplish more than I can ever dream of.

Thanks to materials support from American Air Liquide (metal precursor TDEAT) and financial support from the Department of Bioengineering (UIC) and the following National Science Foun-

ACKNOWLEDGMENTS (Continued)

dation grants: CBET # 1067424, CMS # 0609377, CBET # 1067424 and EEC # 1062943.

I would also like to gratefully acknowledge Dr. Wimmer (Director, wear testing lab, Rush University Medical Center) for providing his laboratory facility.

CONTRIBUTION OF AUTHORS

Chapter 1 is an introduction and overview of research techniques used in this dissertation. Chapter 2 is partially adapted from published manuscripts for which I am the primary author (1; 2) or the co-primary author (3). Sweetu Patel assisted in data collection and manuscript writing for chapter 2.1 Dr. Newton Lucchiari Jr. conducted experiments for parts of section 2.3 and 2.4. Dr. Mathew conducted scanning electron microscopy for section 2.3. Dmitry Royhman conducted white light interferometry for section 2.3 and 2.4. Dr. Azhang Hamlekhan assisted in field emission scanning electron microscopy for section 2.2. Maria Runa helped to collect data in **Figure 31**. Caio Peixito helped to collect data in **Figure 8**, **Figure 9**, **Figure 10** and **Table VI**. My advisor, Dr. Christos G. Takoudis, helped with project planning and manuscript corrections. CO-advisors and committee members Dr. Mathew T. Mathew, Dr. Cortino Sukotjo, Dr. Tolou Shokuhfar, and Dr. Gregory Jursich were also instrumental in project planning and contributed to helpful discussions.

As a primary author, I performed all other experiments and wrote the manuscripts. Dr. Takoudis helped with project planning and correcting of manuscripts. Committee members Dr. Cortino Sukotjo and Dr. Mathew were also instrumental in correcting manuscripts.

TABLE OF CONTENTS

<u>CHAPTER</u>		<u>PAGE</u>
1	INTRODUCTION	1
1.1	Background	1
1.2	Tribocorrosion	2
1.3	Wettability and Storage	3
1.4	Surface Modification Techniques	4
1.5	Thesis Overview	5
2	RESULTS AND DISCUSSION	7
2.1	Titanium Surface Functionalization Using Atomic Layer De- position	7
2.1.1	Introduction	7
2.1.2	Methods and Materials	10
2.1.3	Results	14
2.1.4	Discussion	17
2.1.5	Conclusion	24
2.2	Investigation of Long-term Wettability and Storage Titanium Surfaces	26
2.2.1	Introduction	26
2.2.2	Methods and Materials	27
2.2.3	Water Contact Angle (WCA) Measurements	27
2.2.4	Fourier Transform Infrared (FTIR) Spectroscopy	29
2.2.5	Statistical Analysis	29
2.2.6	Results and Discussion	29
2.2.7	Conclusion	44
2.3	Anodization of Thermally Oxidized Ti6Al4V Surfaces	46
2.3.1	Introduction	46
2.3.2	Methods and Materials	47
2.3.3	Results and Discussion	54
2.3.4	Conclusion	79
2.4	Custom-built Tribocorrosion Apparatus and a Pilot Study	81
2.4.1	Introduction	81
2.4.2	Tribocorrosion Apparatus	82
2.4.3	Results and Discussion	93
2.4.4	Conclusion	106
2.5	Tribocorrosion Testing of Thermally-Oxidized Ti-V Surfaces	107
2.5.1	Introduction	107
2.5.2	Materials and Methods	110

TABLE OF CONTENTS (Continued)

<u>CHAPTER</u>		<u>PAGE</u>
2.5.3	Results	115
2.5.4	Discussion	132
2.5.5	Conclusion	134
CITED LITERATURE		135
APPENDICES		163
	Appendix A	164
	Appendix B	169
VITA		199

LIST OF TABLES

<u>TABLE</u>		<u>PAGE</u>
I	Experimental steps at which WCA measurements were performed. .	13
II	Elemental composition, in at. %, of 6 nm-thick TiO ₂ determined by XPS before and after 5 min argon sputtering. The XPS error limit for elemental quantification is 0.5 at. %.	16
III	Summary of surface wettability results, in water contact angle (WCA), after various treatments reported in the literature. BW = before wash, AW = after wash, AS = after sonication, AT = after treatment, and WAT = wash after treatment. X = no WCA reported for that particular step. “*” Indicates the comment included on the same row and under the column Comments’.	21
IV	FTIR table.	32
V	Water Contact Angle measurements as a function of cleaning and storage steps of ALD treated and untreated Ti-II samples.	37
VI	Water Contact Angle measurements for heat-treated Ti-V samples.	43
VII	Breakdown of treatments and respective group labels.	51
VIII	Literature investigated for construction of tribocorrosion system. . .	84
IX	Elemental composition of Ti-V alloy (McMaster-Carr)	90
X	Elemental composition of TiV alloy (McMaster-Carr)	91
XI	Elemental composition of Ti-V alloy (McMaster-Carr)	110
XII	Elemental composition of TiV alloy (McMaster-Carr)	111
XIII	Total weight loss data as derived from white light interferometry. Total mass loss was calculated based on a ellipsoid volume assumption and it was observed that samples treated at 700 °C in both pH 3.0 and 6.5 environments have the least mass loss.	130

LIST OF FIGURES

<u>FIGURE</u>		<u>PAGE</u>
1	Schematic of the ALD system used to deposit TiO ₂ . Black arrows show the direction of the gas movement. Entry Port is the opening through which the sample is loaded. The TDEAT precursor is kept in canister B. The reactor is insulated to maintain pre-specified working temperature.	11
2	WCA measurements (mean \pm SD) were recorded over several stages for (a) Ti-II and (b) Ti-V. Legend: BW = Before DI water wash, AW = After DI water wash, AS = After sonication in 99.8 % methanol, IAA = Immediately after ALD treatment, WAA = DI water wash after ALD treatment. Standard deviation (SD) was calculated from the entire population of WCA measurements (3 WCA measurements per sample, n = 2 samples/group).	15
3	GIXRD diffractograms of 20 nm-thick TiO ₂ films annealed in nitrogen for 5 min at (a) 600 and (b) 800 °C; the inset includes diffractogram of as-deposited TiO ₂ at 200 °C. The grazing incidence angle is 0.7 °.	18
4	XPS core spectra of O 1s (a) and C 1s (b) from 6 nm-thick TiO ₂ before and after 5 min argon sputtering.	19
5	FTIR spectra of 10 nm ALD TiO ₂ on Ti-V surface.	30
6	Surface wettability of Ti-II samples in ambient air storage monitored over the course of 40 days in 5 day intervals.	33
7	Surface wettability of Ti-V samples in ambient air storage monitored over the course of 40 days in 5 day intervals.	34
8	Surface wettability of heat-treated and untreated Ti-V samples in ambient air storage, followed by storage in room temperature DI-water, followed by storage in 37 °C-DI-water.	39
9	Surface wettability of heat-treated and untreated Ti-V samples in room-temperature DI-water storage, followed by storage in 37 °C-DI-water.	40
10	Surface wettability of heat-treated and untreated Ti-V samples in cold DI-water storage, followed by storage in room temperature DI-water, followed by storage in 37 °C-DI-water.	41
11	Schematic with labeled parts of A) the Lindberg furnace and temperature controller, B) anodization set-up, and C) experimental protocol.	48

49figure.caption.19

LIST OF FIGURES (Continued)

<u>FIGURE</u>		<u>PAGE</u>
13	Field emission scanning electron microscopy (FESEM) images of surface topography of A) control and thermally treated at B) 200, C) 300, D) 400, E) 500, F) 600, and G) 700 °C Ti-V samples before and after anodization treatments. Reduced and smaller surface pores are observed as a function of pre-anodization TO-treatment temperature. Circled areas represent dissolution of vanadium rich areas. Anodization treatment was conducted using a fluorine containing ethylene glycol electrolyte at 60 V for 15 min.	55
14	White light interferometry data of A) control and TO-treated thermally treated at B) 200, C) 300, D) 400, E) 500, F) 600, and G) 700 °C Ti-V samples. The data shows an increase in roughness for samples treated at temperatures 500 °C. The data corroborates with FESEM images of TO-treated surfaces (Figure 13). Control is denoted as “a” and all other alphabetical markers are for significant difference vs. control with $p \leq 0.05$. Thermal oxidation was conducted in air.	56
15	FESEM images of TiO ₂ nanotubes (TNT) of A) CTNT, B) 200TNT, and C) 300TNT, D) 400TNT, E) 500TNT, F) 600TNT, and G) 700TNT samples. Longer TNTs are observed on 300TNT samples as compared to all others. Anodization treatment was conducted using a fluorine containing ethylene glycol electrolyte at 60 V for 15 min.	58
16	Dimensions of TNTs: anodized sample surfaces were scratched to remove TNTs onto double sided conductive carbon tape mounted on an aluminum stub. ImageJ was used to measure the TNT length, surface inner diameter (SID), and inner/outer diameters under the surface (ID and OD). INSET: Blowup of OD, SID, and ID. Control is denoted as “a” and all other alphabetical markers are for significant difference vs. control with $p \leq 0.05$. Anodization treatment was conducted using a fluorine containing ethylene glycol electrolyte at 60 V for 15 min. . . .	59
17	Schematics of anodization process. i) Oxidation at the electrolyte and Ti-V interface leads to formation of barrier oxide layer (BOL) and accumulation of H ⁺ ions that attract F ⁻ ions, resulting in etching or dissolution of BOL, ii) etching leads to formation of nano-pores which grow into nanotubes, and iii) as oxidation/dissolution steps reach equilibrium at the Ti-V bulk and nanotube interface, nanotubes grow into the Ti-V bulk. TNTs have potential to be hydrophilic and loaded with antibiotics or cell media. Anodization treatment was conducted on control and heat-treated Ti-V surfaces using a fluorine containing ethylene glycol electrolyte at 60 V for 15 min.	61

LIST OF FIGURES (Continued)

<u>FIGURE</u>		<u>PAGE</u>
18	Absorbance Fourier transform infrared (FTIR) spectra of control and TO-treated samples. Significant differences in chemical composition are observed in the metal-oxide regions as a function of treatment temperature. H ₂ O, CO ₂ , and metal-oxide regions are marked. Absorbance FTIR spectroscopy was conducted with a diffuse reflectance accessory, a deuterated triglycine sulfate (DTGS) KBr detector, and purging time of 1 h.	65
19	Dimensions of TNTs: anodized sample surfaces were scratched to remove TNTs onto double sided conductive carbon tape mounted on an aluminum stub. ImageJ was used to measure the TNT length, surface inner diameter (SID), and inner/outer diameters under the surface (ID and OD). INSET: Blowup of OD, SID, and ID. Control is denoted as “a” and all other alphabetical markers are for significant difference vs. control with $p \leq 0.05$. Anodization treatment was conducted using a fluorine containing ethylene glycol electrolyte at 60 V for 15 min. . . .	66
20	A) Grazing incidence x-ray diffraction (GIXRD) spectroscopy of control and TO-treated samples. Significant differences in crystalline structures are observed as a function of treatment temperature. B) PDF spectra of titanium, anatase, rutile, and alumina are provided. GIXRD spectroscopy was conducted using a point parallel plate configuration, 0.1542 nm x-ray emission line of Cu point focus x-ray source, and 2-theta-omega setting. An angle of incidence of 1 ° was used to optimize sensitivity for the thin crystalline TiO ₂ films.	67
21	Absorbance FTIR spectra of TO/anodized samples. Significant differences in chemical composition are observed for samples with pre-anodization temperatures of above 400 °C. Absorbance FTIR spectroscopy was conducted with a diffuse reflectance accessory, a DTGS KBr detector, and purging time of 1 h.	68
22	Water Contact Angle (WCA) measurements taken after TO-treatment. TO-treatment result in significantly hydrophilic surfaces; WCA increases significantly by Day 14 for all groups; and WCA decreases significantly after methanol sonication and DI-water rinse (denoted by “*”) for all groups except for control and TO-200 samples. Control group is denoted as “A” and all other upper-case alphabetical markers are for significant difference for TO-treatment groups vs. control group on the specific day of WCA measurement with $p \leq 0.05$. Within each treatment group, storage on Day 0 is denoted as “a” and all other lower-case alphabetical markers are for significant difference vs. Day 0 with $p \leq 0.05$. AGAS = AG ed - A fter S onication.	73

LIST OF FIGURES (Continued)

<u>FIGURE</u>		<u>PAGE</u>
23	WCA measurements taken after TO/anodization treatment. TO/anodization treatment result in significantly hydrophilic surfaces; WCA increases significantly over time for all groups; and WCA decreases significantly after methanol sonication and DI-water rinse (denoted by “*”) for all groups except for 600TNT and 700TNT samples. Control group is denoted as “A” and all other upper-case alphabetical markers are for significant difference for TO-treatment groups vs. control group on the specific day of WCA measurement with $p \leq 0.05$. Within each treatment group, storage on Day 0 is denoted as “a” and all other lower-case alphabetical markers are for significant difference vs. Day 0 with $p \leq 0.05$. AGAS = AG ed - A fter S onication.	75
24	Energy dispersive x-ray spectroscopy (EDS) of TNT taken from a 600TNT sample. Titanium, aluminum, vanadium, nitrogen, and fluorine are labeled. Ti, Al, and V are from Ti-V components, with the oxygen from TiO ₂ nanotubes, and residual fluorine and nitrogen from electrolyte and/or presence of fluorine on TNTs in the form of TiF ₆ ⁻² . Spectra from all anodized samples showed calculated oxygen to titanium ratio of 2:1 (TiO ₂). Aluminum and vanadium content are calculated to be less than 3 and 2 %, respectively, indicating that majority of the oxygen content is in the form of TiO ₂	78
25	Custom-built tribocorrosion apparatus: a) image of the tribocorrosion apparatus, b) rendering of the tribocorrosion apparatus, c) power supply, d) potentiostat, and e) data acquisition PC using Sketchup8. . . .	86
26	Rendering of the electrochemical cell and tribometer: schematic of a) working electrode connection, b) electrochemical cell with inlet and outlets for 37 °C water bath, reference electrode (RE), counter electrode (CE) = graphite, and working electrode (WE) = TiV, and c) tribometer indicating placement of weights.	87
27	Custom-built tribocorrosion apparatus placed inside an incubator: a) image of the incubator setup and b) rendering of the incubator setup. .	89
28	Electrochemical impedance spectroscopy before and after sliding. Inset: Modified Rande’s circuit is used to model the oxide film. The graph shows no significant change in the oxide composition before and after sliding.	94
29	a) Potentiodynamic (PD) scan of a control Ti-V sample for corrosion experiment in pH = 6.5 solution. b) Comparison of corrosion and tribocorrosion PD scans of a Ti-V sample in pH = 6.5 solution.	96
30	a) An evolution of potential curve of a control Ti-V sample for tribocorrosion experiment in pH = 6.5 solution. b) Initiation of sliding results in a gradual increase in cathodic voltage observed over several seconds and c) cessation of sliding results in a gradual decrease in cathodic voltage observed over 300 s of rest until OCP is reached.	98

LIST OF FIGURES (Continued)

<u>FIGURE</u>		<u>PAGE</u>
31	An evolution of potential scan of a control TiV sample for tribocorrosion experiment in culture media in an incubator. Alpha minimum essential medium (α -MEM) was supplemented with 10 % fetal bovine serum (FBS), and 1 % penicillinstrepsin, at pH of 7.4 and 37 °C in a humidified atmosphere of 5 % CO ₂ /air.	99
32	a) Potentiostatic scan of a control TiV sample for tribocorrosion experiment in pH = 6.5 solution. b) Initiation of sliding results in a gradual increase in current observed over a period of sliding and c) cessation of sliding results in a gradual decrease in current observed over a period of rest until equilibrium is reached.	101
33	WLI intensity map image of the wear scar region of a Ti-V sample with a 20 \times magnification lens and an image zoom of 2 \times after tribocorrosion pH = 6.5 solution. Wear scar dimensions were measured as \sim 2.0 mm in length and \sim 0.20 mm in width using ImageJ software.	103
34	a) Wear scar depth profile obtained using WLI of control Ti-V sample after tribocorrosion in pH = 6.5 solution. Roughness values were measured as R A = 1.04 μ m, R RMS = 2.02 μ m, and PV = 16.6 μ m. b) Using the wear scar PV value, length, and width, an ellipsoid volume approximation is used to calculate the volume of material lost due to tribocorrosion.	104
35	Scanning electron microscopy (SEM) images of wear scars of Ti-V surfaces under a) free potential, b) potentiodynamic, and c) potentiostatic tribocorrosion conditions. Magnifications of the images at \times 60 and \times 300 and direction of reciprocating alumina pin counter-body are shown. . .	105
36	Nyquist plots derived from electrochemical impedance spectroscopy of thermally oxidized (TO) titanium alloy. Real Z vs. imaginary Z graphs suggest that the oxides have higher constant phase element values, which is indicative of a porous heterogeneous oxide, or a thick crystalline oxide. . .	114
37	Fitting of Nyquist plots suggest that samples TO-treated at temperatures \leq 400 °C (\leq 6 h) produce thin oxides which can be modeled after the “Modified Randle’s circuit.” The circuit includes a resistive element for the solution at the surface and an oxide composed of a resistor and constant phase element in parallel, indicating that the whole oxide behaves as a resistor and there are exchanges of charges at the surface.	115

LIST OF FIGURES (Continued)

<u>FIGURE</u>		<u>PAGE</u>
38	Fitting of Nyquist plots suggest that samples TO-treated at temperatures $400\text{ }^{\circ}\text{C} \leq T \leq 700\text{ }^{\circ}\text{C}$ ($\leq 6\text{ h}$) produce thick oxides which can be modeled after a complex version of the “Modified Randle’s circuit.” The circuit includes a resistive element for the solution at the surface and an oxide composed of two layers, a compact oxide and a oxygen/metal diffusion zone. The circuit indicates that the whole oxide film behaves as a resistor and there are exchanges of charges at the surface, however, within this film, the diffusion zone behaves as a separate entity which also has resistive and charge releasing qualities.	116
39	Absorbance Fourier transform infrared (FTIR) spectra of $200\text{ }^{\circ}\text{C}$ TO-treated samples. Peaks are observed for changes in chemical composition in the metal-oxide region ($400\text{--}1200\text{ cm}^{-1}$) as a function of treatment time. Absorbance FTIR spectroscopy was conducted with a diffuse reflectance accessory, a deuterated triglycine sulfate (DTGS) KBr detector, and purging time of 1 h.	118
40	Absorbance Fourier transform infrared (FTIR) spectra of $400\text{ }^{\circ}\text{C}$ TO-treated samples. Peaks are observed for changes in chemical composition in the metal-oxide region ($400\text{--}1200\text{ cm}^{-1}$) as a function of treatment time. Absorbance FTIR spectroscopy was conducted with a diffuse reflectance accessory, a deuterated triglycine sulfate (DTGS) KBr detector, and purging time of 1 h.	119
41	Absorbance Fourier transform infrared (FTIR) spectra of $700\text{ }^{\circ}\text{C}$ TO-treated samples. Peaks are observed for changes in chemical composition in the metal-oxide region ($400\text{--}1200\text{ cm}^{-1}$) as a function of treatment time. Absorbance FTIR spectroscopy was conducted with a diffuse reflectance accessory, a deuterated triglycine sulfate (DTGS) KBr detector, and purging time of 1 h.	120
42	Anatase and rutile TiO_2 plot vs. TO-treatment temperature. Absorbance FTIR spectra have shown that anatase TiO_2 is present on samples surfaces TO-treated between 300 and $600\text{ }^{\circ}\text{C}$, reaching their peak for samples TO-treated at $400\text{ }^{\circ}\text{C}$. Rutile TiO_2 is present on samples TO-treated at temperatures $\geq 400\text{ }^{\circ}\text{C}$	122
43	Potentiodynamic scans of TO-treated titanium alloy samples in pH 3.0 artificial saliva solution. High temperature treated samples have superior corrosion potential, corrosion rate, and passivation current readings. Interestingly, $400\text{ }^{\circ}\text{C}$ 6h thermally oxidized samples are observed to have best tribocorrosion resistive properties.	123
44	Potentiodynamic scans of TO-treated titanium alloy samples in pH 6.5 artificial saliva solution. High temperature treated samples have superior corrosion potential, corrosion rate, and passivation current readings. . .	124

LIST OF FIGURES (Continued)

<u>FIGURE</u>		<u>PAGE</u>
45	Evolution of potential curves of TO-treated titanium alloy samples for tribocorrosion experiment in pH 3.0 artificial saliva solution. Initiation of sliding results in an increase in cathodic voltage and cessation of sliding results in a decrease in cathodic voltage. High temperature treated samples have delayed or reduced potential drops.	125
46	Evolution of potential curves of a TO-treated titanium alloy samples for tribocorrosion experiment in pH 6.5 artificial saliva solution. Initiation of sliding results in an increase in cathodic voltage and cessation of sliding results in a decrease in cathodic voltage. High temperature treated samples have reduced potential drops.	126
47	Potentiostatic scans of TO-treated titanium alloy samples for tribocorrosion experiment in pH 3.0 artificial saliva solution. Initiation of sliding results in an increase in current observed over a period of sliding and cessation of sliding results in a gradual decrease in current observed over a period of rest until equilibrium is reached. High temperature treated samples have reduced or no current changes.. . . .	128
48	Potentiostatic scans of TO-treated titanium alloy samples for tribocorrosion experiment in pH 3.0 artificial saliva solution. Initiation of sliding results in an increase in current observed over a period of sliding and cessation of sliding results in a gradual decrease in current observed over a period of rest until equilibrium is reached. High temperature treated samples have reduced or no current changes.	129
49	Potentiostatic scans of TO-treated titanium alloy samples for tribocorrosion experiment in pH 3.0 artificial saliva solution. Initiation of sliding results in an increase in current observed over a period of sliding and cessation of sliding results in a gradual decrease in current observed over a period of rest until equilibrium is reached. High temperature treated samples have reduced or no current changes.	131
50	Permission for use of the material in Chapter 2.2 previously published in Journal of Oral Implantology (JOI).	166
51	Permission for use of tables and figures in Chapter 2.4 previously published in Journal of Bio- and Tribo-Corrosion.	167
52	Permission for use of the text in Chapter 2.4 previously published in Journal of Bio- and Tribo-Corrosion.	168
53	A) Grazing incidence x-ray diffraction (GIXRD) spectroscopy of control and TO-treated samples. Significant differences in crystalline structures are observed as a function of treatment temperature. B) PDF spectra of titanium, anatase, rutile, and alumina are provided. GIXRD spectroscopy was conducted using a point parallel plate configuration, 0.1542 nm x-ray emission line of Cu point focus x-ray source, and 2-theta-omega setting. An angle of incidence of 1 ° was used to optimize sensitivity for the thin crystalline TiO ₂ films.	170

LIST OF FIGURES (Continued)

<u>FIGURE</u>		<u>PAGE</u>
54	Compiled FTIR spectra of all TO-treated and control samples. Common peaks are labeled.	174
55	Absorbance Fourier transform infrared (FTIR) spectrum of a control sample. The water (3800-3000 and 2000-1400 cm^{-1}) and carbon dioxide (2380-2320 and 667 cm^{-1}) regions are from the FTIR chamber gases. No other significant signatures are observed as both the background and control have similar chemical composition. Absorbance FTIR spectroscopy was conducted with a diffuse reflectance accessory and a deuterated triglycine sulfate (DTGS) KBr detector.	175
56	Absorbance FTIR spectra of a TO-200 sample. The water (3800-3000 and 2000-1400 cm^{-1}) and carbon dioxide (2380-2320 and 667 cm^{-1}) regions are from the ambient gases in the FTIR chamber. Part A contains the entire spectra and parts B-C contain sections of the spectra containing deconvoluted peaks. Characterization conditions are same as in Figure 55	176
57	Absorbance FTIR spectra of a TO-300 sample. The water (3800-3000 and 2000-1400 cm^{-1}) and carbon dioxide (2380-2320 and 667 cm^{-1}) regions are from the ambient gases in the FTIR chamber. Part A contains the entire spectra and parts B-C contain sections of the spectra containing deconvoluted peaks. Characterization conditions are same as in Figure 55	177
58	Absorbance FTIR spectra of a TO-400 sample. The water (3800-3000 and 2000-1400 cm^{-1}) and carbon dioxide (2380-2320 and 667 cm^{-1}) regions are from the ambient gases in the FTIR chamber. Part A contains the entire spectra and parts B-C contain sections of the spectra containing deconvoluted peaks. Characterization conditions are same as in Figure 55	178
59	Absorbance FTIR spectra of a TO-500 sample. The water (3800-3000 and 2000-1400 cm^{-1}) and carbon dioxide (2380-2320 and 667 cm^{-1}) regions are from the ambient gases in the FTIR chamber. Part A contains the entire spectra and parts B-C contain sections of the spectra containing deconvoluted peaks. Characterization conditions are same as in Figure 55	179
60	Absorbance FTIR spectra of a TO-600 sample. The water (3800-3000 and 2000-1400 cm^{-1}) and carbon dioxide (2380-2320 and 667 cm^{-1}) regions are from the ambient gases in the FTIR chamber. Part A contains the entire spectra and parts B-C contain sections of the spectra containing deconvoluted peaks. Characterization conditions are same as in Figure 55	180

LIST OF FIGURES (Continued)

<u>FIGURE</u>		<u>PAGE</u>
61	Absorbance FTIR spectra of a TO-700 sample. The water (3800-3000 and 2000-1400 cm^{-1}) and carbon dioxide (2380-2320 and 667 cm^{-1}) regions are from the ambient gases in the FTIR chamber. Part A contains the entire spectra and parts B-C contain sections of the spectra containing deconvoluted peaks. Characterization conditions are same as in Figure 55	182
62	Absorbance FTIR spectra of a all anodized samples. Common peaks are labeled. Characterization conditions are same as in Figure 55	186
63	Absorbance FTIR spectra of a 700TNT sample. The water (3800-3000 and 2000-1400 cm^{-1}) and carbon dioxide (2380-2320 and 667 cm^{-1}) regions are from the ambient gases in the FTIR chamber. Part A contains the entire spectra and parts B-D contain sections of the spectra containing deconvoluted peaks. Characterization conditions are same as in Figure 55	188
64	Absorbance FTIR spectra of a 500TNT sample. The water (3800-3000 and 2000-1400 cm^{-1}) and carbon dioxide (2380-2320 and 667 cm^{-1}) regions are from the ambient gases in the FTIR chamber. Part A contains the entire spectra and parts B-D contain sections of the spectra containing deconvoluted peaks. Characterization conditions are same as in Figure 55	189
65	Absorbance FTIR spectra of a 600TNT sample. The water (3800-3000 and 2000-1400 cm^{-1}) and carbon dioxide (2380-2320 and 667 cm^{-1}) regions are from the ambient gases in the FTIR chamber. Part A contains the entire spectra and parts B-D contain sections of the spectra containing deconvoluted peaks. Characterization conditions are same as in Figure 55	190
66	Absorbance FTIR spectra of a CTNT sample. The water (3800-3000 and 2000-1400 cm^{-1}) and carbon dioxide (2380-2320 and 667 cm^{-1}) regions are from the ambient gases in the FTIR chamber. Part A contains the entire spectra and parts B-D contain sections of the spectra containing deconvoluted peaks. Characterization conditions are same as in Figure 55	192
67	Absorbance FTIR spectra of a 200TNT sample. The water (3800-3000 and 2000-1400 cm^{-1}) and carbon dioxide (2380-2320 and 667 cm^{-1}) regions are from the ambient gases in the FTIR chamber. Part A contains the entire spectra and parts B-D contain sections of the spectra containing deconvoluted peaks. Characterization conditions are same as in Figure 55	193

LIST OF FIGURES (Continued)

<u>FIGURE</u>		<u>PAGE</u>
68	Absorbance FTIR spectra of a 300TNT sample. The water (3800-3000 and 2000-1400 cm^{-1}) and carbon dioxide (2380-2320 and 667 cm^{-1}) regions are from the ambient gases in the FTIR chamber. Part A contains the entire spectra and parts B-D contain sections of the spectra containing deconvoluted peaks. Characterization conditions are same as in Figure 55	194
69	Absorbance FTIR spectra of a 400TNT sample. The water (3800-3000 and 2000-1400 cm^{-1}) and carbon dioxide (2380-2320 and 667 cm^{-1}) regions are from the ambient gases in the FTIR chamber. Part A contains the entire spectra and parts B-D contain sections of the spectra containing deconvoluted peaks. Characterization conditions are same as in Figure 55	195

SUMMARY

Various surface modification techniques are used widely to modify medical implant surfaces for specific needs. Deposition techniques such as atomic layer deposition and chemical vapor deposition, thermal oxidation, anodization, sandblasting/acid-etching, and polishing are used to improve various properties such as wettability, mechanical strength, and bio-functionality. Since being discovered in 1790, titanium has been used for various purposes including orthopedic and dental implants. Titanium has been widely used for this purpose due to its mechanical strength, chemical inertness, osseointegration properties, and corrosion resistance. However, further improvements can be made to meet the needs of an aging population and patients who are receiving implants at younger ages. This thesis focuses on atomic layer deposition, thermal oxidation, and anodization to improve osseointegration and tribocorrosion properties.

Long-term wettability and storage of atomic layer deposited 10 nm TiO_2 on CP-Ti and Ti6Al4V samples was investigated. X-ray photoelectron spectroscopy of TiO_2 films indicated presence of trace impurities and Fourier transform infrared spectra and grazing incidence X-ray diffraction suggest the TiO_2 film obtained at 250 °C may contain anatase TiO_2 . In this study, it is established that i) wettability of TiO_2 deposited on CP-Ti and Ti6Al4V is improved ($6 \pm 2^\circ$ and $8 \pm 2^\circ$, respectively), ii) after short-term ambient air storage DI-water rinse or methanol sonication are able to recover wettability, however, not to initial wettability (after cleaning, $12 \pm 4^\circ$ and $15 \pm 3^\circ$, respectively), iii) DI-water wash or methanol sonication after long-term ambient air storage is less effective ($22 \pm 5^\circ$ and $24 \pm 8^\circ$, respectively), iv) UV-treatment

SUMMARY (Continued)

completely recovers wettability after long-term storage, and v) samples stored in methanol, DI-water, or multi-purpose solution immediately after TiO_2 deposition can be used to maintain super-hydrophilicity without the need of UV-treatment.

Anodization of thermally treated (200-700 °C) Ti6Al4V alloy surfaces may improve properties of titanium nanotubes (TNTs). Prior to anodization, titanium alloy surfaces were thermally oxidized at various temperatures for 3 h. Energy dispersive x-ray spectra showed that oxygen diffusion depth increased in the form of TiO_2 as a function of higher temperature thermal treatment and that aluminum diffused towards the surface during thermal treatment at 700 °C. It was discovered that, anodization of a thin anatase surface oxide produced the longest nanotubes. A thick anatase and/or rutile surface oxide (thermally treated at 400 °C or higher) was found to retard the anodization mechanism while no nanotubes were observed in the case of 700 °C-treated/anodized samples. Interestingly, no significant differences were observed between the anodized samples for the nanotube inner or outer diameters. Wettability analysis showed that thermal and thermal-anodization treatments produced hydrophilic surfaces which over time became hydrophobic; delayed hydrophobic behavior over time was observed for thermally-treated/anodized samples. Separately, ALD-deposited samples were annealed in N_2 at temperatures of 300, 450, and 600 °C and then finally anodized. It was discovered that the previous observations in regards to enhanced anodization were amplified on these surfaces, namely on 450 °C treated surface. It was observed that longer and thicker-walled nanotubes were produced which may improve nanotube-interface integrity, and therefore improve tribo-corrosion resistance. This work proposes an enhanced anodization mechanism on thermally

SUMMARY (Continued)

treated Ti6Al4V alloy for possible dental and orthopaedic applications.

Lastly, a compact and cost-effective tribocorrosion apparatus was developed for the investigation of fretting and wear of Ti6Al4V disks in artificial saliva of pH 3.0 and 6.5. Titanium and its type-V alloy are excellent corrosion resistant materials due to their passive surface oxide film. However, the combination of a hard surface oxide and soft substrate results in poor wear resistance. In biological environments, orthopaedic and dental implants experience the synergistic effect of wear and corrosion, i.e., tribocorrosion, which can lead to premature implant failure. This work focuses on thermally oxidized titanium alloy for the investigation of wear in artificial saliva of pH 3.0 and 6.5. Electrochemical impedance spectroscopy, potentiodynamic, free-potential, and potentiostatic analyses were used for electrochemical characterization of thermally oxidized titanium alloy. White light interferometry and Fourier transform infrared spectroscopy were used to analyze wear scars and surface oxides, respectively, on the thermally treated samples. Electrochemical and surface characterizations show that titanium alloy samples treated at 700 °C for 1 and 6 h were observed to have best tribocorrosion resistance in both pH environments with total mass loss calculated to have been decreased by up to 95 % as compared to control samples. The improved tribocorrosion resistance is credited to a thick multi-layered oxide film able to withstand both corrosion and wear.

CHAPTER 1

INTRODUCTION

1.1 Background

Discovered in 1790 and produced in commercial quantities since 1936, titanium has been used for a variety of purposes, including aviation and biomedical implants.(4) While commercially pure titanium consists of α -phase (hexagonal closed packed) and can be converted to β -phase (body centered cubic) at higher temperatures, the most commonly used titanium alloy, Ti-6Al-4V alloy (Ti-V), consists of α - β -phase due to its alloying metals aluminum and vanadium.(4) Due to its superior biocompatibility, mechanical resistance, corrosion resistance, and osseointegration, Ti-V is an excellent orthopedic and dental implant material.(5; 6; 7; 8; 9; 10; 11; 12) Titanium and its alloys are well known for their corrosion resistance due to the rapid oxidation of surface Ti(13; 14; 15), as a result, a protective layer of titanium dioxide (TiO_2) forms on its surface (≤ 10 nm thick)(16). In contrast, titanium and its alloys behave poorly against tribocorrosion, defined as the synergistic combination of oxidation reactions and wear(17). The surface native oxide also has been shown to promote osseointegration as a result of the TiO_2 induced dissociation of water in biological environments and the resultant surface bound hydroxyl groups promote up-regulation of markers such as bone morphogenetic protein (BMP) and TGF- β 1.(18; 19; 20; 21; 22; 23; 24; 25; 26; 27; 28; 29; 30) However, due to the increase in

life-expectancy and swelling elderly population, there is an urgent need for an implant surface which can withstand tribocorrosion and rapidly integrates with the host bone.

1.2 Tribocorrosion

Tribocorrosion has become a major concern in recent years(31; 32; 33; 34) for all implant materials. In 2010, 719,000 knee replacements(35), 500,000 total hip replacements(36) and 700,000 dental implants(6) were conducted, the majority of which will be for patients as young as 45 years of age.(37) While knee and hip implants may last up to 12 years on average, the life-expectancy of the U.S. population continues to rise.(38) Consequently, replacement surgeries for dental, hip, and knee implants have seen an increase of about 100 % over the past decade(37; 39), especially for the 45-64 years of age group(37). Recently, several medical implant manufacturers issued recalls of their hip implants with complications due to tribocorrosion.(40; 41) In one case, implant failure was projected to affect 40 % of implant recipients.(12) While such extreme failures may be rare, weight bearing knee and hip implants, for example, have experienced long term revision rates of 12 %(34) and 17 %(35), respectively, mainly caused by aseptic loosening due to the chronic inflammatory response to tribocorrosion debris.(42) Aseptic loosening is thought to be the result of chronic inflammatory response to implant surface debris and metal ions released as a result of tribocorrosion at the implant-bone interface.(42) For titanium implants, removal of the passive layer as a result of wear allows for the release of metallic debris which are converted to metal ions due to simultaneous corrosion of the exposed bulk metal and debris.(43) Depending on the pH of the environment, passivation and corrosion of exposed titanium is affected. In general, smoking, medication, chronic and systemic diseases can

alter the acidity of saliva and bodily fluids which adversely affects tribocorrosion of implants. (13; 14; 44) For Ti-V alloy, the debris is in the form of Ti, V, and Al particles that act as third-body wear particles and increase material loss during wear. (45; 46) In addition, Ti, Al, and V ions are known to negatively affect osseointegration (45; 46; 47; 48), cause bone diseases (10), and be cytotoxic, respectively, if present at excessive levels (45; 46; 47; 48).

1.3 Wettability and Storage

While titanium and its alloys are well known for bone-implant integration, further improvements may help with joint or dental replacement surgeries with elderly patients, who may have compromised or insufficient host bone. The surface native oxide of Ti and its alloys has been shown to promote osseointegration as indicated by up-regulation of markers such as bone morphogenetic protein (BMP) and TGF- β 1. (18; 19; 20; 21; 22; 23; 24; 25; 26) Specifically, the surface oxide (TiO₂) dissociates water in biological environments and the resultant hydroxyl groups increase the surface energy and promote the process of cellular adhesion. (25; 27; 28; 29; 30) Proper cell growth on dental and orthopedic implant metal ensures proper integration. (49; 50) Thermal oxidation (TO), low pressure chemical vapor deposition (LPCVD), oxinitridation, sandblasting and acid-etching (SLA), atomic layer deposition (ALD) and physical vapor deposition (PVD) can be used to improve these surface properties. (9; 51; 52; 53; 54; 55; 56; 57; 58) Specifically, the above mentioned techniques significantly improve surface wettability of treated samples as compared to the native TiO₂ of titanium (Ti) and its alloys. (9; 51; 52; 53; 54; 55; 56; 57; 58) As reported in literature, however, this surface wettability decreases over time when stored in ambient environment conditions. (59; 60; 61) To improve long-term wettability, Fumi-

nori Iwasa *et al.* performed a study where the effect of UV illumination on surface wettability of micro-rough surfaces with and without deposited TiO_2 was investigated over a period of 7 days.(62) From their findings, it was observed that while water contact angle (WCA) dropped to 0° after 48 hours of UV-illumination, the samples needed to be exposed to the UV-light uninterrupted to maintain long-term hydrophilicity. It is, therefore, necessary to study cleaning and storage methods that may maintain long-term wettability of implant surfaces.

1.4 Surface Modification Techniques

Atomic Layer Deposition (ALD), thermal oxidation (TO), and anodization are promising surface modification techniques for the improvement of osseointegration and tribocorrosion. Both ALD and TO-treatment have shown to improve surface wettability due to the higher temperatures involved. For ALD, Tetrakis DiEthyl Amino Titanium (TDEAT) was used as the Ti precursor and DI-water was used as the oxidant for the TiO_2 deposition. The reactor temperature was maintained at 250°C and the operating pressure at 0.17 Torr. A growth rate of $1.1 \text{ \AA}/\text{cycle}$ was calculated such that deposition a 10 nm film would require 100 cycles. While deposition techniques can be used for tribocorrosion purposes, thick films easily delaminate.(63; 64) TO-treatment, specifically is time and temperature dependent and variance in treatment parameters produces oxide of various thickness and crystalline structures.(65; 66) TO-treatment was conducted in a furnace using air only. The effect of crystalline structure and oxide thickness increases roughness and surface energy(67) which promote surface chemical and biological processes that improve adhesion and may accelerates the formation of fibrin mesh

over the implant surface, resulting in proper implant-biological integration.(67) Tribocorrosion resistance due to TO-treatment has not been explored satisfactorily and even discounted due to the scaling of TiO_2 due to high temperature treatment.(65; 68)

Specifically, anodization forms TiO_2 nanotubes (TNTs) which have significantly greater surface area than as is titanium surfaces. The increased surface area enhances human mesenchymal stem cell (hMSC) adhesion.(10; 69; 70) TNTs are created by an anodic oxidation process using an electrochemical cell and an electrolyte.(10; 71; 72; 73; 74; 75; 76; 77) For a fluorine (F) containing electrolyte, the oxidation and dissolution kinetics of TiO_2 (10; 76; 77) consists of i) H^+ ion induced F^- ion migration leading to formation of a fluoride rich layer at the oxide-metal interface, ii) a flow mechanism results in displacement of the fluoride rich layer towards the cell boundaries, iii) dissolution of the fluoride rich cell boundaries, and iv) dehydration leading to formation of separated TNTs.(10; 77) Changing the applied voltage, fluorine wt. % electrolyte composition, or duration of anodization can affect TNT aspect ratio (diameter/length).(10; 78; 79) Finally, thermally treated TNTs have shown to further improve cellular response.(27; 73; 80; 81) While traditional anodization studies investigate TNTs formed on as-is Ti-V consisting of an amorphous native TiO_2 surface, TNT formation on thicker and crystalline TiO_2 affects the formation of TNTs and may improve their properties.

1.5 Thesis Overview

The thesis is divided into two sections. The first section describes the surface modification and storage techniques used for research and the second section describes the use of the techniques to improve tribocorrosion and osseointegration of titanium alloy. Chapter 2.1 discusses

the investigation of ALD and wettability and Chapter 2.2 discusses long-term storage of ALD treated surfaces. In addition the results are compared to wettability obtained from thermal oxidation. Chapter 2.3 discusses the effects of anodization of thermally oxidized titanium alloy and a surface which has a deposited and thermally treated TiO_2 film. Finally, Chapter 2.4 discusses the process and benefits of a custom-in-house built tribocorrosion system and the effects of thermal oxidation on tribocorrosion resistance of titanium and its alloys.

CHAPTER 2

RESULTS AND DISCUSSION

2.1 Titanium Surface Functionalization Using Atomic Layer Deposition

2.1.1 Introduction

Due to their biocompatibility, high chemical inertia, corrosion resistance, mechanical resistance, high strength to density ratio, and atoxicity, Ti-II and Ti-V are commonly used in dental and orthopaedic implants. (82; 6; 83; 84) Titanium is known to readily react with oxygen in ambient environment to form amorphous native TiO_2 up to a few nm-thick. (85; 86) The native oxide is reported to act as a passive layer, protecting the bulk material from corrosion. (85; 86) However, wear on moving parts abrades the passive layer and exposes the bulk material to the synergistic effects of redox reactions and wear. Redox reactions result in the formation of Ti, vanadium (V) and aluminum (Al) ions, while wear generates Ti, V, and Al particles. (6) Ti ions bring about tissue discoloration in the area adjacent to the implant site and are detrimental to osseointegration because they prevent bone-implant interaction. (48; 87) Al ions can cause bone diseases and neurological disorders; V ions can be cytotoxic if present at excessive levels. (48; 87) Therefore, in order to prevent the synergistic effect of redox reactions and wear on Ti-II/Ti-V, the native oxide needs to be supplemented with a TiO_2 film using methods such as atomic layer deposition (ALD), chemical vapor deposition, physical layer deposition, and thermal oxidation. (51; 52; 88; 54; 55; 56; 57; 58; 9) Advantages of the ALD, for example, include

nano-scale accuracy, high thickness uniformity, high conformality, low processing temperature, and formation of defect and impurity-free films.(55; 89; 90; 91; 92; 93; 94)

Growth and structure control of deposited TiO_2 can improve corrosion and wear resistance properties of biomedical implant surfaces, while positive cellular response is maintained.(84; 95; 96; 97; 98; 99) TiO_2 can increase surface energy and wettability, which enhance osseointegration(100; 101), and it improves implant wear resistance that minimizes particulate formation from the surface and bulk.(98; 99; 102; 103; 104)

ALD of TiO_2 has previously been studied for a variety of applications such as semiconductors, insulation layers for electronic devices, self-cleaning optoelectronic devices, chemical sensors, and passive layers in biomedical applications.(105; 106; 107; 108; 109; 110; 111) However, comprehensive studies on Ti-based implants and related systems are scarce. For example, Huang *et al.* investigated low temperature ALD TiO_2 for micro-electro-mechanical systems and reported that ultraviolet (UV) exposure of samples in vacuum had no effect on TiO_2 samples (112); however, in atmospheric air, UV illumination resulted in rapid super-hydrophilicity (112). They concluded that additional compounds, organic or water, even in small amounts are needed for UV-induced hydrophilicity.(112)

Another study, which investigated plasma source ion implantation on Ti-II samples post-treated with annealing and UV-A exposure for 24 h determined that after 4 weeks, there were no statistical differences in the bone implant contact and bone are avalues between the control and experimental groups.(58) A report on osteoblastic cell behavior on different titanium implant surfaces indicated that surface impurities resulting from substrate polishing or titanium ion re-

lease into the culture media may also affect these systems (113); more importantly, all surfaces studied were reported to be hydrophobic (113).

Kawakami *et al.* investigated 50-200 nm-thick ALD TiO₂ films(114); however, no hydrophilicity or hydrophobicity trends could be identified. Elias *et al.* reported on the relationships between surface properties of titanium and dental implant removal torque (18); the droplets used were very large (on the order of milliliters), but contact angles with water and a hydrophobic liquid showed conflicting and difficult to explain trends.(115)

MacDonald *et al.* investigated thermal and chemical modifications of Ti-Al-V implant materials.(9) Organic surface contamination was found on all surfaces, regardless of treatment. Also, heat treatment in atmospheric conditions was found to result in higher Al/Ti atom ratios than that with heating in oxygen.(9)

In sum, there is a need for a systematic study of Ti-based oral and other biomedical implant systems. The effect of each treatment step needs to be investigated. In this study, ALD is used to deposit 10 nm-thick TiO₂ layers on Ti-II and Ti-V substrates. Water contact angle (WCA) measurements are performed on samples after each treatment step, i.e., before cleaning, after de-ionized (DI) waterwash, MeOH sonication, ALD treatment, and post-ALD DI-water wash to obtain an understanding of optimal cleaning and preparation treatments of dental and other implant surfaces for improved hydrophilicity. Barring any cytotoxicity, it has been reported that increased surface hydrophilicity increases the likelihood of cell adhesion to the surface.(100; 101) X-ray photoelectron spectroscopy(XPS) and grazing incidence X-ray diffraction (GIXRD) results are used to probe surface cleanliness and thin film structure, respectively.

2.1.2 Methods and Materials

2.1.2.1 Sample preparation using sandblasting and acid-etching

etching Ti-II (99.99 % purity) and Ti-V discs (15 mm in diameter and 1 mm-thick) were obtained from McMaster-Carr. The Ti-II and Ti-V discs were blasted with 50 μm alumina grit particles (Alumina(Al_2O_3) powder, Trinity Tool Company, Fraser MI) at 517 kPa, and acid-etched in a solution of 1:1 ratio of sulfuric acid to 30 % hydrogen peroxide for 2 h.

2.1.2.2 Cleaning procedure of as-received samples

Micro-rough surface samples were cleaned with sequential sonication for 60 min in DI water of 17.7 $\text{M}\Omega\text{-cm}$ resistivity (BarnsteadNANOPure, Infinity Ultrapure Water System[®]), and for 60 min in 99.8 % methanol (Sigma Aldrich) using an Ultrasonic Wafer Cleaning System (Branson). After cleaning, the samples were dried with N_2 gas (Zero Grade, Airgas) and stored in plastic petri-dishes(Advantec[®], MFS, Inc.) until the ALD treatment.

2.1.2.3 ALD system preparation and film characterization

The schematic of the custom-designed and built hot wall lowpressure thermal ALD system is shown in **Figure 1**.

Prior to TiO_2 deposition on the substrate, the ALD system was calibrated. Silicon wafers were rinsed with DI water, dried with N_2 and then loaded into the ALD reactor for a series of empty cycles with the precursor line closed and the N_2 gas line open. Next, a predetermined number of cycles were run on silicon wafers with the precursor line open, and the TiO_2 film thickness was measured with spectroscopic ellipsometry (J.A. Woollam Co. M-44). Tetrakis DiEthyl Amino Titanium (TDEAT) was used as the Ti precursor and DI water was used as the

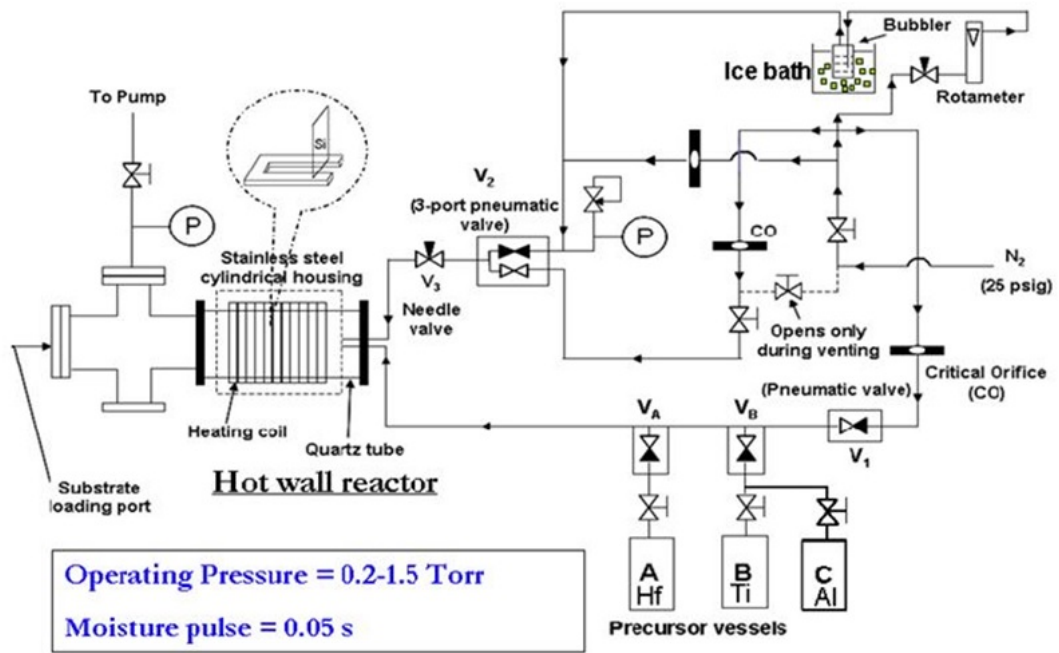


Figure 1: Schematic of the ALD system used to deposit TiO_2 . Black arrows show the direction of the gas movement. Entry Port is the opening through which the sample is loaded. The TDEAT precursor is kept in canister B. The reactor is insulated to maintain pre-specified working temperature.

oxidant for the TiO_2 deposition. The reactor temperature was maintained at 250 °C and the operating pressure at 0.17 Torr [48]. A growth rate of 1.1 Å/cycle was reported earlier (56) and a similar rate was obtained in this study. The deposition was conducted using 100 cycles, which resulted in approximately 10 nm-thick TiO_2 on Ti-II and Ti-V samples.

TiO_2 films 6 nm-thick were probed with an X-ray photoelectron spectrometer (XPS; Kratos AXIS-165) equipped with a monochromatic Al $K\alpha$ (1486.6 eV) x-ray source operating at 15 kV and 10 mA. High-resolution spectra of O 1s and C 1s were collected using a stepsize of 0.1 eV, pass energy of 20 eV and dwell time of 200 ms. Semi-quantitative analysis of peak intensities was performed through spectral peak-fitting, where peaks were subtracted from Shirley-typed backgrounds and deconvoluted using Gaussian-Lorentzian peak shape functions. The binding energy scales of all XPS spectra were calibrated with reference to the adventitious carbon 1s position at 285 eV. A high resolution x-ray diffractometer (PhilipsX'pert) was used to obtain GIXRD spectra of TiO_2 films. The GIXRD spectra were collected at the low angle of incidence of 0.7 ° with an overall diffraction angle resolution of 0.15 °. Grazing incidence X-rays allowed high resolution diffraction patterns with enhanced sensitivity.

2.1.2.4 Water contact angle measurements

WCA measurements were conducted using a Rame'-Hart NRLCA Goniometer (M #100-0, S #2067). A micro-syringe (Hamilton, 802RN) was used to place a 5 µL DI-water droplet onto Ti-II and Ti-V surfaces.

Steps	Labels	Description
1	Before wash (BW)	As received (sandblasted = Al_2O_3 50 μm , 517 kPa, 10 s; acid etched = 1:1 ratio of H_2SO_4 :30 % H_2O_2)
2	After wash (AW)	DI water (17.7 M Ω -cm) wash for 30 s followed by N_2 drying
3	After sonication (AS)	15 min of 99.8 % methanol sonication
4	Immediately after ALD (IAA)	TDEAT precursor, H_2O oxidant, 250 $^\circ\text{C}$, 0.17 Torr, 100 cycles (10 nm-thick TiO_2)
5	After post-ALD wash (WAA)	DI water (17.7 M Ω -cm) wash for 30 s followed by N_2 drying

TABLE I: Experimental steps at which WCA measurements were performed.

2.1.2.5 Before ALD

Prior to loading each sample into the ALD reactor, we probed its hydrophilicity with WCA measurements before any treatment (step 1, **Table VII**), after 30 s of DI-water rinse followed by N_2 gas drying (step 2, **Table VII**), and after 15 min of sonication in 99.8 % methanol (step 3, **Table VII**). This sequential cleaning was performed to remove organic and inorganic particulates from the sample surface.

2.1.2.6 After ALD

The surface wettability characteristics of each sample were monitored with WCA measurements immediately after ALD (step 4, **Table VII**), and post-ALD DI water wash for 30 s followed by drying with N_2 gas (step 5, **Table VII**). After the respective water contact angle measurements, the samples were stored in petri dishes under fluorescent tube light ambient in

the laboratory. Additional experiments on the surface wettability of samples under this light or in the dark resulted in identical WCA, within the experimental uncertainty of the data.

2.1.2.7 Statistical Analysis

ANOVA test with unequal variance was used to determine the significance of surface wettability between groups.

2.1.3 Results

Figure 2 shows the WCA results of Ti-II and Ti-V substrates. The first data (step 1, **Table VII**) were obtained with as-received samples and the WCA for Ti-II and Ti-V substrates were measured to be $31 \pm 8^\circ$ and $54 \pm 2^\circ$, respectively. After cleaning the samples with DI water (step 2, **Table VII**), the WCA for Ti-II and Ti-V decreased to $24 \pm 7^\circ$ and $37 \pm 3^\circ$, respectively. After sonication in 99.8 % methanol (step 3, **Table VII**), the WCA for Ti-II and Ti-V were found to further decrease to $16 \pm 3^\circ$ and $26 \pm 8^\circ$, respectively. Immediately after the ALD of 10 nm-thick TiO_2 (step 4, **Table VII**), the WCA of Ti-II and Ti-V were $12 \pm 2^\circ$ and $13 \pm 3^\circ$, respectively. Finally, after post-ALD cleaning of the samples with DI water (step 5, **Table 1**), the WCA of both Ti-II and Ti-V were $7 \pm 1^\circ$. Therefore, the WCA decreased from 31° to 7° for Ti-II and from 54° to 7° for Ti-V after the aforementioned five-step processing sequence; that is, hydrophilic surfaces were obtained on both materials, regardless of the initial hydrophobicity characteristics of the sample surfaces. ANOVA tests corroborated these results, indicating significance between groups ($p < 0.05$, null hypothesis is rejected).

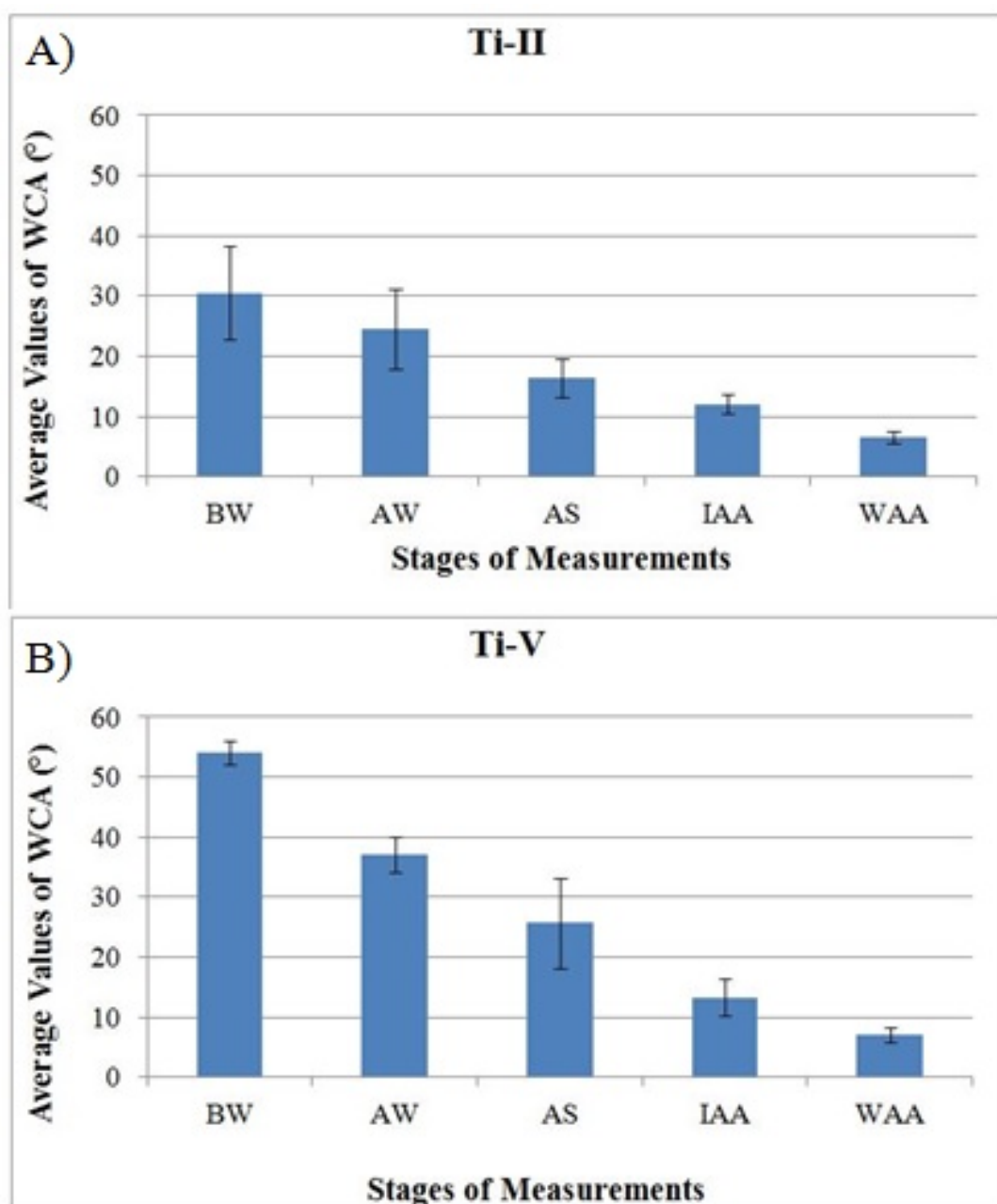


Figure 2: WCA measurements (mean \pm SD) were recorded over several stages for (a) Ti-II and (b) Ti-V. Legend: BW = Before DI water wash, AW = After DI water wash, AS = After sonication in 99.8 % methanol, IAA = Immediately after ALD treatment, WAA = DI water wash after ALD treatment. Standard deviation (SD) was calculated from the entire population of WCA measurements (3 WCA measurements per sample, $n = 2$ samples/group).

Elements	TiO ₂ (at. % before sputtering)	TiO ₂ (at. % after 5 min sputtering)
Ti	22 ± 1	30 ± 1
O	52 ± 1	50 ± 1
C	20 ± 1	4 ± 1
Si	6 ± 1	16 ± 1

TABLE II: Elemental composition, in at. %, of 6 nm-thick TiO₂ determined by XPS before and after 5 min argon sputtering. The XPS error limit for elemental quantification is 0.5 at. %.

GIXRD data of ALD TiO₂ (**Figure 3**) indicated that there were no diffraction peaks for two-theta between 20 ° and 40 °, which suggested amorphous nature of the as-deposited TiO₂ films at 200 °C (116). Diffraction peaks, characteristic of anatase, became apparent upon post-deposition annealing of TiO₂ in nitrogen for 5 min (**Figure 3**). Since the substrate temperature in our systems was 250 °C for the duration of the ALD, anatase TiO₂ could be present.

X-ray photoelectron spectroscopy of as-deposited TiO₂ surfaces showed the 530.5 eV feature of OH in the O 1s spectrum [48], with a considerable amount of surface carbon contamination, which was mostly removed after sputtering (**Table II** and **Figure 4**). **Table II** shows the elemental composition of Ti, O, C, and Si from 6-nm-thick TiO₂ on Si substrates probed with XPS before and after sputtering in argon for 5 min at 4 kV/15 mA (voltage/emission). The atomic ratio of O to Ti was found to be greater than 2 for the unsputtered TiO₂ film and to decrease after sputtering, suggesting the formation of titanium suboxides. The atomic concentration of carbon in the unsputtered films was about 20 %, while it was reduced to ~ 4 % after surface sputtering, indicating that carbon is mostly adventitious and contamination

from air. A higher atomic concentration of silicon was observed after sputtering, due to the resulting attenuated oxide film.

Figure 4 shows XPS core scans for O and C of TiO_2 sample before and after sputtering. **Figure 4(a)** shows that the 530 eV Ti-O-Ti feature before sputtering resulted into three peaks after sputtering; these were assigned to oxygen in titanium dioxide and suboxides next to the Si-O peak at 531.8 eV, which was found to shift to higher binding energy (by 0.3 eV) than that of the unsputtered film. The O-H species from the unsputtered TiO_2 (530.5 eV) was no longer observed after sputtering. The amount of carbon was largely reduced to less than 4 % after sputtering with the removal of C-O and O=C-OH species. Two shoulders at a lower binding energy than that of the adventitious carbon peak could be assigned to possible titanium-carbon (TiC_x) species (117) due to sputtering artifacts (**Figure 4(b)**); these species might result from the re-deposition of sputtered Ti and carbon atoms.

2.1.4 Discussion

WCA of TiO_2 surfaces have been reported in earlier studies (Table 3). Elias *et al.* for example, reported WCA between 47° and 96° after different implant treatments and anodization. (18) Hirakawa *et al.* reported a decrease in WCA from 64° to 1.0° after plasma source ion implanted (PSII) TiO_2 (58), although eventually the bone implant area and bone area between control and PSII implants was not found to be statistically significant. Guehenneuc *et al.* reported a WCA of 134° after sandblasting and acid etching (113) with surface impurities on the substrates after Ti polishing. MacDonald *et al.* reported a decrease in WCA from 43° to 3.8° and 4° after heat treatment at 600°C for 1 h in oxygen and air, respectively (9); how-

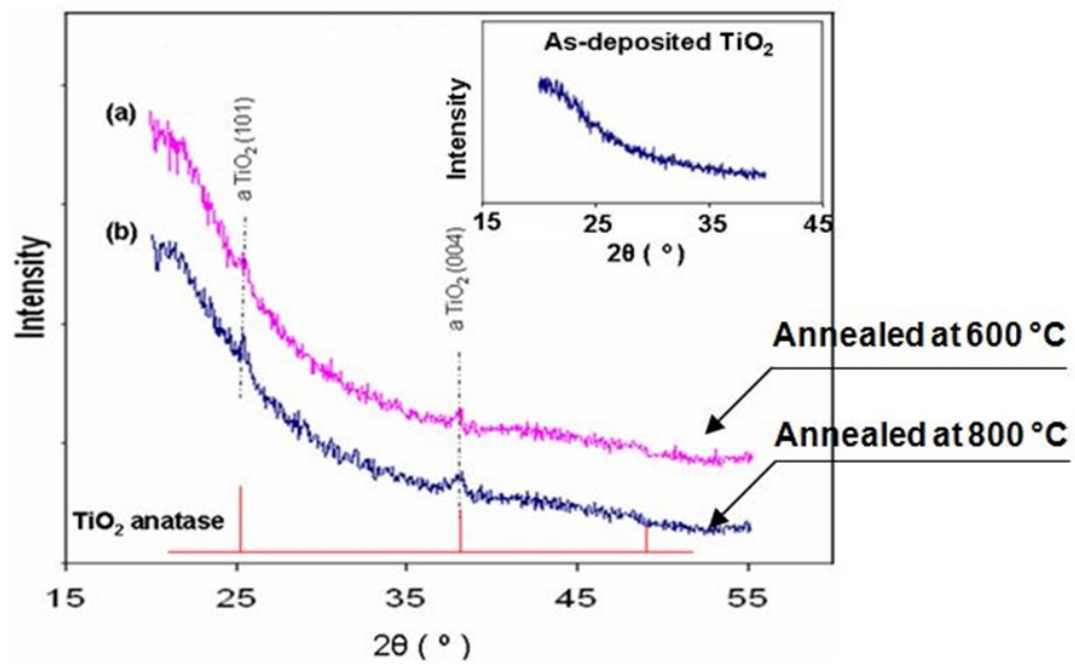


Figure 3: GIXRD diffractograms of 20 nm-thick TiO₂ films annealed in nitrogen for 5 min at (a) 600 and (b) 800 °C; the inset includes diffractogram of as-deposited TiO₂ at 200 °C. The grazing incidence angle is 0.7 °.

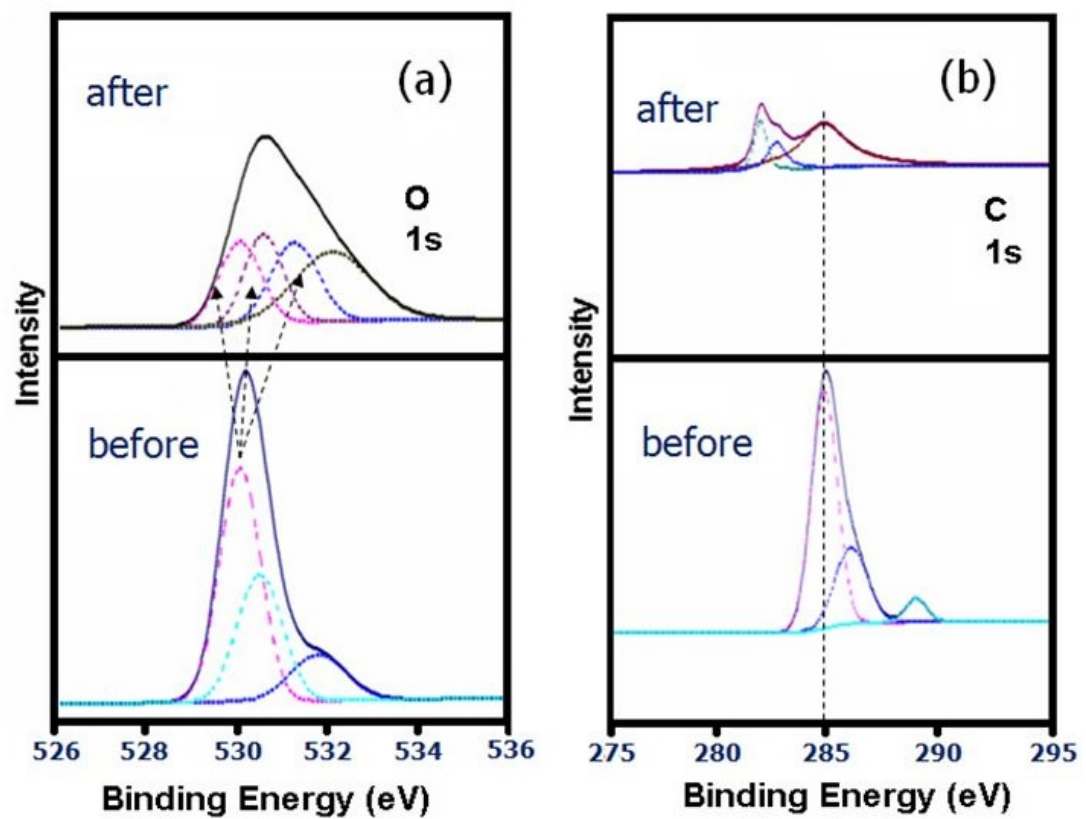


Figure 4: XPS core spectra of O 1s (a) and C 1s (b) from 6 nm-thick TiO_2 before and after 5 min argon sputtering.

ever, organic surface contamination was present on all samples regardless of treatment, while surface roughness was found to increase by about two orders of magnitude. Kawakami *et al.* reported a decrease of WCA from about 100° to 10° after several hours of UV illumination of ALD TiO_2 -covered substrates, without consistent trends; TiO_2 (5, 10, 50, 100, 150 and 200 nm-thick) was deposited using TiCl_4 precursor and H_2O oxidant.(114) Huang *et al.* reported an increase in the WCA from less than 10° to greater than 70° when ALD TiO_2 samples (from TiCl_4 and H_2O) were stored in the dark; furthermore, UV illumination was used to increase the hydrophilicity of TiO_2 substrate surfaces, although the presence of organic and/or inorganic impurities, even in small amounts, was reported to be necessary for UV-induced increased hydrophilicity.(112) Fujishima *et al.* and Nataka and Fujishima reported two possible phenomena for the hydrophilic and oleophilic behavior of TiO_2 surfaces: (a) organic decomposition by superoxide radical anion (O_2^-) and hydroxyl group radical (OH) formation through photo-induced TiO_2 , and (b) creation of electron holes through the photocatalytic activity of TiO_2 .(118; 119)

Such studies suggest a few important issues: (i) it is not clear which pretreatment(s) can effectively lead to desired wettability characteristics of Ti-based substrate surfaces that are of paramount importance in dental implants for example; and (ii) the effectiveness of each treatment step on the wettability of Ti-II and Ti-V surfaces needs to be understood so that pretreatment steps, surface material properties and implant performance relationships could be established.

Since enhanced hydrophilicity results in effective osseointegration, the wettability characteristics of Ti-II and Ti-V surfaces after TiO_2 ALD and cleaning treatments could be of significant

Authors	Coating/ Substrate/ Technique	Before Treatment (WCA (°))		After Treatment (WCA (°))		Comments
		BW	AW/AS	AT	WAT	
Elias <i>et al.</i> (18)	Anodized TiO ₂ on machined Grade-4 unalloyed Ti	85 ± 4	X	47 ± 3	X	WCA on sandblasted & acid etched was 80 ± 5°
Hirakawa <i>et al.</i> (58)	Plasma source ion implanted (PSII) TiO ₂ on sandblasted cp-Ti	X	64	1*	X	* After PSII samples were annealed at 654 °C followed by 24 h UV treatment
Guehennecc <i>et al.</i> (113)	Sandblasted + acid etched cp-Ti	X	134	X	X	TiO ₂ was not supplemented
MacDonald <i>et al.</i> (9)	Thermally oxidized in atmosphere Ti6Al4V alloy	X	43 ± 5	4 ± 2	X	WCA with various other treatments: heated O ₂ : 3.8 ± 2°, peroxide: 6.7 ± 2°, peroxide + butanol: 16 ± 5°, heated (atmosphere) + butanol: 11 ± 3°, heated (O ₂) + butanol: 12 ± 5°
Kawakami <i>et al.</i> (114)	ALD TiO ₂ on stainless steel, deoxidized high phosphorous (DHP) copper, and Nordic gold copper alloy	X	X	5	X	WCA was conducted after 5 hours of UV illumination
Huang <i>et al.</i> (112)	ALD TiO ₂ on silicon substrate	X	X	0	X	ALD TiO ₂ was deposited at various temperatures. WCA after ALD at all temperatures is 0° except at 120 °C (600 °C annealed) which is ~10°

TABLE III: Summary of surface wettability results, in water contact angle (WCA), after various treatments reported in the literature. BW = before wash, AW = after wash, AS = after sonication, AT = after treatment, and WAT = wash after treatment. X = no WCA reported for that particular step. “*” Indicates the comment included on the same row and under the column Comments’.

importance in biomedical implants. Our data on the wettability characteristics of the individual treatment steps used (**Table VII** and **Figure 2**) and the effect of Ti-II and Ti-V functionalization with ALD TiO_2 nanofilms subjected to subsequent DI water wash and N_2 drying leads to several findings. High WCA measurements of as-received samples (**Figure 2**) is attributed to organic and/or inorganic impurities on the sample surfaces from the ambient environment, surface roughness, or leftover electrolyte from the acid-etching treatment. Rinsing with DI water assists with the removal of inorganic particulates, while subsequent sonication of the samples in methanol helps eliminate organic (and/or other inorganic) surface contaminants. DI water wash and methanol sonication were found to yield increasingly hydrophilic surfaces. Removal of inorganic and organic surface contaminants followed by ALD of 10 nm-thick TiO_2 and post-ALD DI water wash and nitrogen drying were shown to consistently yield highly hydrophilic Ti-II and Ti-V surfaces (**Figure 2**). Finally, the wettability characteristics of both Ti-II and Ti-V were apparently independent of the initial state of the surfaces as long as the sequence of pretreatment steps shown in **Table VII** was followed.

It has been reported that at room temperature, H_2O molecules dissociate into H^+ and OH^- (hydroxyl ions) due to the interaction with oxygen vacancies on TiO_2 surfaces, resulting in terminal and bridge hydroxyl groups.(25; 120; 121; 28) Such a hydroxylation has also been reported for methanol and propanol-2.(28) Additionally, amorphous TiO_2 is reported to start changing into the anatase crystalline structure above 200 °C.(115; 122; 123; 124) In this study, since the ALD reactor temperature was 250 °C, there may be some anatase-structured TiO_2 formation, which has been reported to enhance the formation of hydroxyl groups.(125; 126; 127)

Results with our experimental system have indicated increasing formation of anatase TiO_2 with increasing temperature, even after 5 min of post-deposition annealing in N_2 at 600-800 °C (**Figure 3**). Thermodynamically stable anatase TiO_2 is composed of (1 0 1) and (0 0 1) surfaces (Fig. 5b) (125; 126; 127; 128); H_2O adsorbs non-dissociatively on the (1 0 1) surface, while H_2O molecules were found to dissociate spontaneously into H^+ and OH^- on (0 0 1) surfaces.(119; 125; 126; 127) The terminal and bridge hydroxyl groups may act as Brönsted acid sites that anchor H_2O molecules to form $\text{OH-H}_2\text{O}$ complexes, which in turn act as nucleation sites for further water adsorption and increased hydrophilicity.(121)

For a super-hydrophilic surface, the solid surface and measuring liquid have similar properties and the WCA decreases to approximately 0 °.(129) Consequently, the surface free energy (SFE) increases for the solid surface and solidliquid interface as determined by Young's Equation (129). The modified Young's Equation is

$$\gamma^S - \gamma^{SL} = \gamma^L \cos(\theta_{WCA}) \quad (2.1)$$

where γ^{SL} , γ^S , and γ^L are SFE of surface-liquid interface, solid surface and liquid, respectively, and θ_{WCA} is the WCA of the sample surface.(130; 131; 132; 133; 134) Further, as θ_{WCA} decreases to 0 °, $\cos(\theta_{WCA})$ goes to unity (Equation 2.8) and the combined value of the left side reaches its maximum value which is equal to γ^L

$$\gamma^S - \gamma^{SL} = \gamma^L \quad (2.2)$$

From Equation 2.8 it is evident that as $\cos(\theta_{WCA})$ goes to unity and since the surface energy of water, γ^L , remains constant (130; 131), γ^S changes more than γ^{SL} . γ^{SL} and γ^S values are lower for hydrophobic samples and higher for hydrophilic surfaces.(130; 131; 132; 133; 134) Furthermore, XPS characterization of ALD TiO₂ nm-thick films showed stoichiometric TiO₂ with negligible impurities in the films.(115) Additional information is required for an in-depth study of the changes of individual free energies as the surface is altered from different cleaning treatments. Studies on surface roughness and cell culture viability on such substrates remain to be carried out, although none of the five steps shown in **Table VII** are anticipated to have an effect on the roughness of dental and other implant substrates.

2.1.5 Conclusion

Micro-rough surfaces provide more surface area for cellular adhesion and higher SFE improves hydrophilicity, both of which are preferable for cellular response. The surface wettability of micro-rough surfaces Ti-II and Ti-V has been studied after each one of the following sequential steps: before cleaning, DI water wash, sonication in 99.8 % MeOH, 10 nm-thick TiO₂ ALD, and post-ALD DI-water wash and N₂ drying. It was found that Ti-II and Ti-V samples become increasingly hydrophilic after each one of these sequential treatments, and the final surface wettability characteristics were independent of the initial ones for all samples used. The water contact angle of Ti-II and Ti-V surfaces after the aforementioned steps was consistently well below 10°, an important factor in cellular attachment. Also, it is important to probe surface

wettability after each sequential treatment of a substrate; otherwise, conflicting hydrophobicity and/or hydrophilicity results may be obtained because of organic and/or inorganic impurities. Our analyses suggested that the sequential steps used in this study improved surface hydrophilicity likely due to the formation of hydroxyl groups, higher H₂O molecule adsorption on the deposited anatase TiO₂ surface, and removal of possible contaminants which may have inadvertently remained on the samples surfaces. XPS analyses of ALD TiO₂ indicated stoichiometric films with negligible impurities, while GIXRD data suggested the formation of anatase TiO₂ even with a 5 min anneal in N₂.

2.2 Investigation of Long-term Wettability and Storage Titanium Surfaces

2.2.1 Introduction

Proper cell growth on dental and orthopedic implant metal ensures proper integration.(49; 50) Cell growth can be improved by manipulating surface properties such as surface energy, wettability, and composition which play important roles in cell adhesion.(49; 135; 136; 137) Thermal oxidation (TO), low pressure chemical vapor deposition (LPCVD), oxinitridation, sandblasting and acid-etching (SA), atomic layer deposition (ALD) and physical vapor deposition (PVD) can be used to improve these surface properties.(51; 52; 53; 54; 55; 56; 57; 58; 9) Specifically, the above mentioned techniques significantly improve surface wettability of treated samples as compared to the native TiO_2 of titanium (Ti) and its alloys.(51; 52; 53; 54; 55; 56; 57; 58; 9) As reported in literature, however, this surface wettability decreases over time when stored in ambient environment conditions.(59; 60; 61) To improve long-term wettability, Fuminori Iwasa *et al.* performed a study where the effect of UV illumination on surface wettability of micro-rough surfaces with and without deposited TiO_2 was investigated over a period of 7 days.(62) From their findings, it was observed that while water contact angle (WCA) dropped to 0° after 48 hours of UV-illumination, the samples needed to be exposed to the UV-light uninterrupted to maintain long-term hydrophilicity. It is, therefore, necessary to study cleaning and storage methods that may maintain long-term wettability of implant surfaces.

Previously, TiO_2 was deposited using a custom-built low pressure thermal ALD system previously described in Patel *et al.* where CP-Ti (Ti-II) and Ti6Al4V (Ti-V) surfaces ALD deposited with TiO_2 turned super-hydrophilic as compared to untreated surfaces.(3) Major advantages of

ALD are its nano-scale accuracy, high thickness uniformity and high conformality when compared to sol-gel, CVD, and PVD.⁽⁸⁹⁾ In this study, the surface wettability of TiO₂ deposited Ti-II and Ti-V samples was investigated with the following main objectives: 1) to correlate surface wettability to surface composition using Fourier transform infrared spectroscopy, 2) to monitor long-term surface wettability of samples, 3) to investigate cleaning methods to improve wettability after storage without UV-illumination, and 4) to investigate long-term storage methods to maintain the surface wettability over the period of storage.

2.2.2 Methods and Materials

Preparation, cleaning, roughening, and deposition procedures have been previously described.¹⁹ Briefly, Ti-II (99.99% purity) and Ti-V discs (1 mm-thick, 15 mm in diameter) were obtained from McMaster-Carr and blasted with 50 μ m alumina grit particles (Alumina [Al₂O₃] powder, Trinity Tool Company, Fraser MI) at 517 kPa, and acid-etched in a solution of 1:1 ratio of sulfuric acid to 30 % hydrogen peroxide for 2 hours. Tetrakis DiEthyl Amino Titanium (TDEAT) was used as the Ti precursor and deionized (DI) water was used as the oxidant for the TiO₂ deposition (10 nm). The ALD reactor temperature was maintained at 250 °C and its operating pressure at 0.17 Torr.

2.2.3 Water Contact Angle (WCA) Measurements

After deposition, samples were rinsed with DI-water and stored in a glass petri-dish containing ambient air for 40 days. Within the storage period, samples were removed every 5 days from the glass petri-dish and WCA measurements were taken in the following order: 1) as-is

(blow-dried with N_2 gas), 2) after DI-water rinse for 30 seconds and blow-dried with N_2 gas, and 3) after methanol (99.8 %) sonication for 15 minutes followed by 30 seconds of DI-water rinse and blow-dried with N_2 gas. WCA images were captured using a Rame'-Hart NRLCA Goniometer (M #100-0, S #2067). A micro-syringe (Hamilton, 802RN) was used to place 5 μ L of DI-water droplet onto sample surfaces according to the sessile drop method. Captured images of WCA were uploaded using ImageJ software and the *Contact Angle* plugin was used to calculate WCA values.

To investigate storage options, samples were stored in a glass petri-dish containing DI-water, methanol (99.8 %), multi-purpose solution (CVS pharmacy, thimerosal and chlorhexidine free) or ambient air. Surface wettability was monitored by taking WCA measurements over 13 days to observe which medium best maintained initial wettability. Prior to storage, samples were sonicated in methanol for 10 hours and rinsed with DI-water for 30 seconds to remove possible contamination. Furthermore, low intensity UV irradiation ($330 \mu\text{W}/\text{cm}^2$, 15 W Philips TUV 15W/G15 T8) was used for 4 h to cleanse ALD-treated samples to remove any contaminants which DI-water rinse and methanol (99.8%) sonication did not remove. Prior to WCA measurements of samples stored in ambient air, samples were removed from the glass petri-dish and blow-dried with N_2 gas. Samples stored in multi-purpose solution and methanol were rinsed with DI-water and blow-dried with N_2 gas prior to WCA measurements. Samples were returned to respective glass petri-dishes after measurements.

2.2.4 Fourier Transform Infrared (FTIR) Spectroscopy

Chemical composition of ALD-treated surfaces was studied using a diffuse reflectance FTIR spectroscopy (Nicolet, Madison, WI, USA) with a deuterated triglycine sulfate (DTGS) KBr detector. A smooth-polished Ti-V sample was used as a background for all scans. Prior to conducting FTIR scans, each sample was kept inside the FTIR chamber for one hour N₂ purging to optimize signal-to-noise ratio. FTIR spectra were obtained with 1 cm⁻¹ resolution and 512 scans over the range of 4000-400 cm⁻¹. FTIR spectra were analyzed with linear background and deconvoluted using Gaussian-Lorentian peak shape function with a spectral peak-fitting software.

2.2.5 Statistical Analysis

Statistical software (SPSS v. 22.0, SPSS Inc., Chicago, IL, USA) was used for descriptive and statistical analysis. One-way ANOVA was used to determine any significant differences between the means of WCA measurements between and within groups. Due to unequal variances, Games-Howell post hoc analysis was used for pair-wise comparisons within these groups. For all analyses, $p \leq 0.05$ was considered to be statistically significant.

2.2.6 Results and Discussion

2.2.6.1 FTIR Spectroscopy Analysis

Figure 5 shows the FTIR spectra of 10 nm ALD deposited TiO₂ on Ti-II sample. **Figure 5a** shows the entire FTIR spectrum of ALD treated sample. Strong features for H₂O in the regions 3600-3800 cm⁻¹ and 1300-1800 cm⁻¹ are observed; additionally, CO₂ vibration stretches are observed in regions 2200-2400 cm⁻¹ and 667 cm⁻¹. Such features for H₂O and

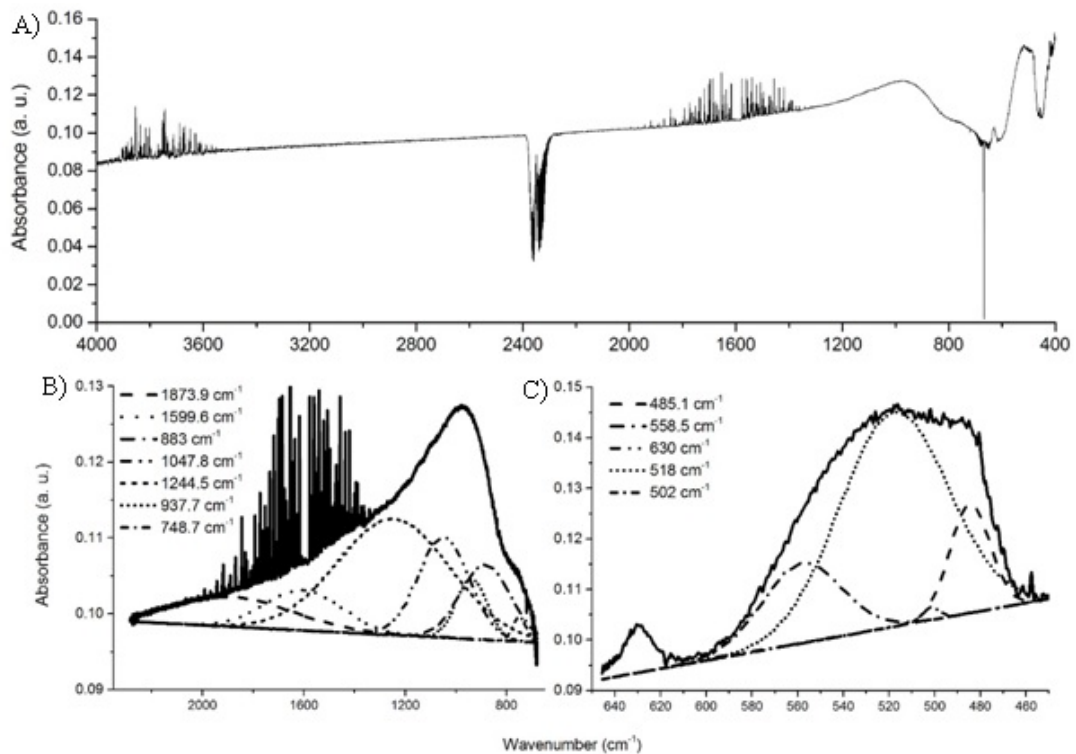


Figure 5: FTIR spectra of 10 nm ALD TiO₂ on Ti-V surface.

CO₂ in the spectrum are always apparent, as they are present in the ambient air in the FTIR sample chamber. **Figure 5b** and **Figure 5c** show the deconvolution of spectral regions 650-2200 cm⁻¹ and 400-650 cm⁻¹, which show the presence of surface H₂O, hydrated TiO₂, CO₂, and by-products of CO₂ and TiO₂. No presence of surface contamination was observed in the FTIR spectra.

Detailed information regarding deconvoluted spectra peak positions and their respective bond vibrations is described in **Table IV**. Briefly, significant amorphous and anatase TiO₂ is observed, which is readily hydrated by the H₂O in the FTIR chamber.

Some of the limitations of FTIR analysis include deviation in peak position from the literature reported values because 1) the IR absorption due to molecules and bonds depends on surrounding chemistry on the sample surface, and 2) the surface roughness may result in a spectra with sloped baseline which may shift peak positions.

2.2.6.2 WCA Analysis

Surface wettability of Ti-II and Ti-V samples in ambient air storage was monitored over the course of 40 days in 5 day intervals (**Figure 6** and **Figure 7**) for insight into the wettability behavior during storage. It has been previously reported by our group that both ALD-treated Ti-II and Ti-V samples are super-hydrophilic when rinsed with DI-water immediately after TiO₂ deposition $6 \pm 2^\circ$ and $8 \pm 2^\circ$, respectively).¹⁹ However, WCA of TiO₂ deposited on Ti-II and Ti-V samples is observed to have increased after 5 days of storage to $50 \pm 10^\circ$ and $63 \pm 6^\circ$, respectively. The behavior was observed for all of the eight-5 day intervals.

There are various reasons reported in literature for the increase in WCA. Surface contamination is one possibility discussed by Yin Haoyong *et al.* The TiO₂ treated samples may attract low-level volatile organic molecules from the air which may lower the surface energy of the metal oxide.(61; 159; 160; 161; 162; 163) It has also been suggested that TiO₂ surfaces have high surface energy when in a dark environment, which allows contaminants to adsorb on the surface.(61; 162; 163) It is also plausible that when samples are stored at room or higher temperature, desorption of H₂O molecule takes place at a greater rate, reducing the surface energy and decreasing wettability over time.(59; 164) It has been previously shown by our group, how-

Wavenumber (cm^{-1})	Peak Area (a.u.)	Chemical Bond Association	Additional Comments
485.1	0.481	436-495 cm^{-1} Ti-O-Ti(138), 450-550 cm^{-1} Ti-O-Ti (139)	This is indicative of an increase in TiO_2 .
502	0.023	450-550 cm^{-1} & Ti-O-Ti (139)	This is also indicative of an increase in TiO_2 .
518.3	2.519	520 cm^{-1} (140) rutile	This is indicative of an increase in TiO_2 , however, the possibility of the presence of rutile is negligible. It is more likely that it is amorphous, and a slightly more chance that it is anatase.
558.5	0.689	550 cm^{-1} anatase TiO_2 (141) , 550 cm^{-1} Ti-O(139)	This is indicative of an increase in TiO_2 that may be of anatase structure.
630	0.207	630 cm^{-1} TiO_2 (142)	This is indicative of an increase in TiO_2 .
668.5	N/A	667 cm^{-1} C-O of CO_2 (143; 144)	Negative (-) quantity, implying that the chamber contained more CO_2 during scan of background sample as compared to the test sample. *See Row 1.*
748.9	0.219	Ti-O-Ti, 763 cm^{-1} (145) , 768-770 cm^{-1} TiO_2 & tita- nium nanotubes TiO_4 amor- phous (146; 141)	This is indicative of an increase in TiO_2 .
883	2.46	893 cm^{-1} O-Os (147) , 870 anat.(146; 141)	The bond belonging to TiO_2 complexes.
937.7	1.237	940 cm^{-1} amorphous TiO_2 (146; 141)	This peak is indicative of an increase in TiO_2 that is amorphous as compared to a control Ti-V sam- ple.
1047.8	3.342	1047 cm^{-1} N-H(148), 1063 cm^{-1} symmetric CO_3^{-2} 43, 1012 cm^{-1} O-O(149), 1048 cm^{-1} anatase/rutile (138), 1137 cm^{-1} Ti-O-H, 1100 cm^{-1} (cation) OH (150; 151)	Various bonds can belong to this peak, but this peak most likely belongs to O-O bond of TiO_2 complexes and O-H bonds of hydrated TiO_2 (*See Row 4*). This is also indicative of an increase in TiO_2 .
1244.5	8.502	Ti-O-O-H (152), 1222 cm^{-1} adsorbed H_2O by H bonds(138)	Bonds belong to O-H bonds of hydrated TiO_2 and H_2O molecules on the TiO_2 surface. (*See Row 4*) This is also indicative of an increase in TiO_2 .
1599.6	2.021	1605 cm^{-1} (153)/ 1610 cm^{-1} (154) liquid H_2O (153; 154; 138), 1600 cm^{-1} , 1627 cm^{-1} adsorbed H-O-H v (155; 156), 1600-1630 cm^{-1} H-O-H ads v (138), 1500- 1700 cm^{-1} OH/N-H(157)	Despite longer purge time, absorbed/ adsorbed H_2O is observed to be higher than on the native TiO_2 of control samples (*See Row 1*).
1873.9	2.466	1870 cm^{-1} of CO(scolova)	Interaction of CO_2 with TiO_2 may result in CO production.
2320 - 2380, 2350	N/A	gaseous CO_2 (158)	Negative (-) quantity, implying that the chamber contained more CO_2 during scan of background sample as compared to the test sample. *Purge of test sample totaled 8 h vs. 1 h for background sample.*

TABLE IV: FTIR table.

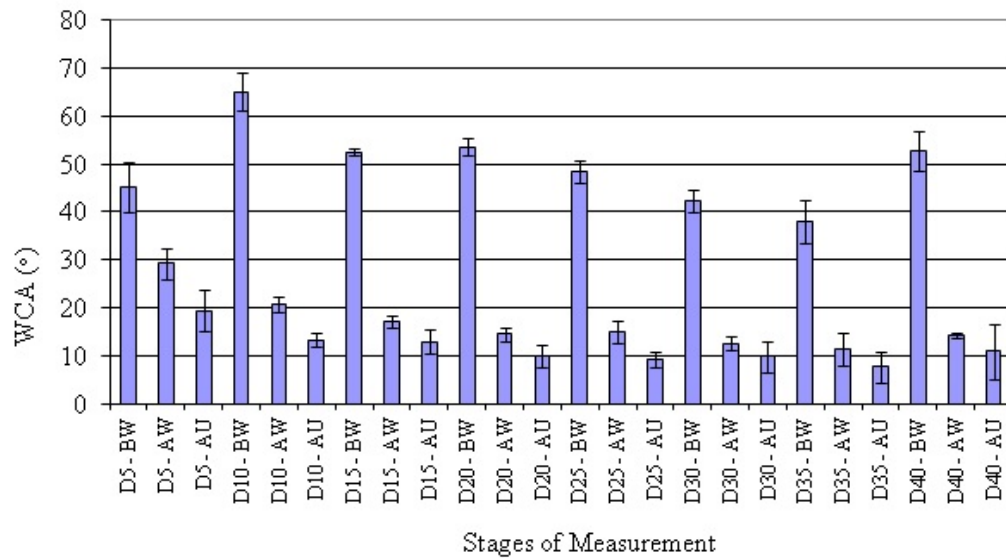


Figure 6: Surface wettability of Ti-II samples in ambient air storage monitored over the course of 40 days in 5 day intervals.

ever, that darkness or light did not have an effect on the WCA measurement on ALD-treated samples(3), therefore, dehydroxylation and surface contaminants are considered as reasons for decreasing wettability.

Hydroxylation of the surface due to dissociation of H_2O molecules has been shown to be enhanced by the crystalline structures of TiO_2 (25; 120; 121) which leads to $OH-H_2O$ complexes when water is introduced to the surface.(121) In this study, the introduction of water was in the form of water droplet from WCA measurements and DI-water rinse. Moreover, methanol was used in sonication as the second method of cleaning. Methanol interacts with TiO_2 in similar manner as H_2O and TiO_2 as previously reported in the literature.(3; 28) The behavior was

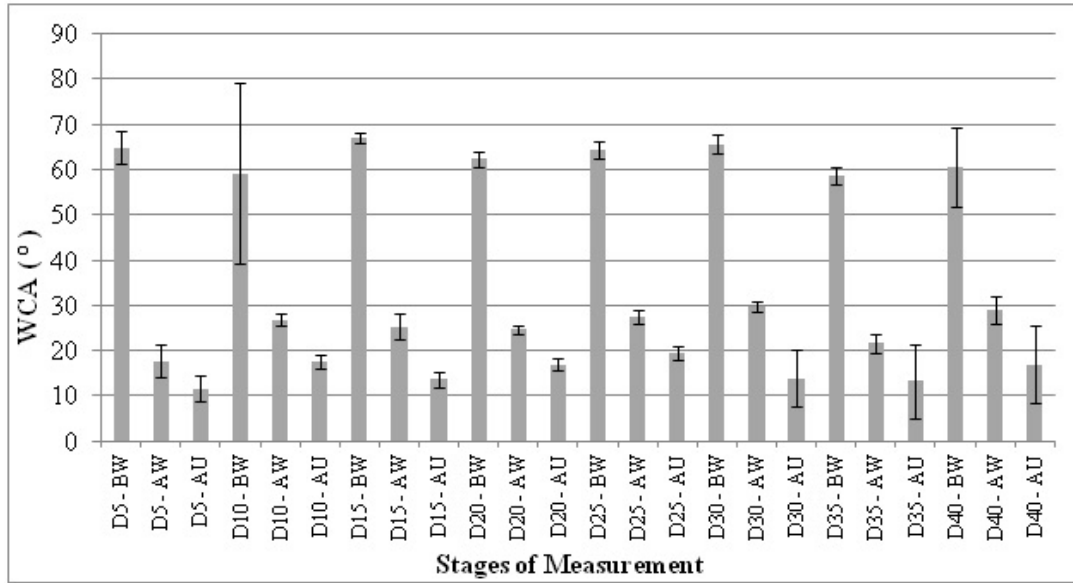


Figure 7: Surface wettability of Ti-V samples in ambient air storage monitored over the course of 40 days in 5 day intervals.

observed for all of the eight-5 day intervals. While introduction of H_2O or methanol improves wettability, gradual dehydroxylation occurs during storage of samples in petri-dish with ambient environment. It has been shown that while samples irradiated with UV were observed to become super-hydrophilic (as low as 0°), their surface wettability reversed upon termination of UV irradiation.(164; 61; 3; 120; 29) As such, the authors were able to show that the ambient heat in dark or visible light resulted in the increase in WCA as the surface is dehydroxylated. In this study, when rinsed with DI-water, the WCA of ALD-treated Ti-II and Ti-V samples decreased to $17 \pm 6^\circ$ and $25 \pm 6^\circ$, respectively, and after methanol (99.8 %) sonication, WCA further decreased to $12 \pm 4^\circ$ and $15 \pm 3^\circ$, respectively (averaged over the eight 5-day inter-

vals). The drop in WCA due to methanol sonication is much smaller after DI-water rinse, than the drop in WCA after DI-water rinse. This may indicate that organic contamination may not have been a major factor in the increase in WCA during the 5-day storage as DI-water rinse would not be as effective in removing organics. The same procedure was followed every 5 days over 40 days of storage and the averaged WCA measurements are given in **Table V**. As a result of the cleaning steps, the samples undergo a significant decrease in WCA from $50 \pm 10^\circ$ to $12 \pm 4^\circ$ for Ti-II samples and $63 \pm 6^\circ$ to $15 \pm 3^\circ$ for Ti-V samples ($p \leq .001$). The results are promising as it is essential to have a protocol for a hydrophilic surface after storage for cellular viability of implant surfaces.(165; 166) No significance difference between ALD-treated Ti-II and Ti-V samples was observed.

When samples were cleaned after storage of over a month in ambient environment, however, the WCA only decreased to $22 \pm 5^\circ$ and $24 \pm 8^\circ$ for CP-Ti and Ti6Al4V samples, respectively. No significance difference between ALD-treated Ti-II and Ti-V samples was observed. While methanol causes disruption of surfactant aggregation and the ultrasonication accelerates this process, it should be noted that methanol may not degrade surface contamination.(167) Therefore, for sufficient surface contamination, methanol may not be able to penetrate the surface contamination layer. After repeated sonication attempts did not yield lower WCA measurements, ALD-treated Ti-II samples were UV-treated for four hours, which resulted in a decrease in WCA to $11 \pm 4^\circ$. In addition, UV-treatment of untreated Ti-II sample resulted in WCA of $23 \pm 3^\circ$, indicating difference in the cleaning ability of anatase TiO_2 of the deposited film and the amorphous TiO_2 of native film. No significance difference between WCA of post-ALD Ti-II

samples and WCA of post-UV ALD-treated Ti-II samples was observed ($p = 0.06$). In addition, as no significant difference was observed between treated Ti-II and Ti-V samples, only treated and untreated Ti-II samples were used for the storage investigation. The decrease in WCA due to UV-treatment may indicate that carbon contamination was removed from the surface. Any contributions from the photocatalytic effect of TiO_2 to the hydrophilicity can be disregarded as they are reversed within tens of μs as the UV-lamp is turned off.(168) As described by A. Mills *et al.* and others, the photocatalytic effect of TiO_2 disintegrates any organics on the surface and results in CO_2 and H_2O and produces a hydrophilic surface.(169; 170; 171) Specifically, the UV-generated electron holes on the surface disintegrate organics directly on the surface, followed by hydroxyl radical surface migration which allows for the oxidation of the organics away from the surface, effectively cleaning the surface from the inside-out, leading to a hydrophilic surface.(169; 170; 171) Mills *et al.* was also able to show that while UV-irradiation itself results in organic decomposition, UV-irradiation alone is not responsible for the inside-out cleaning.(169)

After UV-treatment, TiO_2 deposited Ti-II samples were stored in various storage conditions to investigate long-term storage options. Surface wettability of ALD-treated samples stored in air (control), DI-water, multi-purpose solution (MPS) and methanol (99.8 %) was monitored and the results are shown in **Table V**.

As can be seen, DI-water, MPS, and methanol (99.8 %) equally maintained wettability of stored samples, whereas samples stored in ambient air showed an increase in WCA from $11 \pm$

Cleaning Experiment				
Sample	As-is	After Storage 5 Days in Air	After DI-water Rinse	After Methanol Sonication
ALD-treated Ti-II	$6 \pm 2^\circ$	$50 \pm 10^\circ$	$17 \pm 6^\circ$	$12 \pm 4^\circ$
ALD-treated Ti-V	$8 \pm 2^\circ$	$63 \pm 6^\circ$	$25 \pm 6^\circ$	$15 \pm 3^\circ$
Storage Experiment				
Sample	Post UV-Treatment (4 h)	After Storage (13 Days)		
ALD-treated Ti-II in air (control storage)	$11 \pm 4^\circ$	$25 \pm 5^\circ$ (Significant Difference (SD) from D_0 , $p < 0.001$)		
ALD-treated Ti-II in methanol	$11 \pm 4^\circ$	$16 \pm 4^\circ$ (SD from D_{13} storage in air, $p = 0.003$)		
ALD-treated Ti-II in multi-purpose solution	$11 \pm 4^\circ$	$16 \pm 3^\circ$ (SD from D_{13} storage in air, $p < 0.001$)		
ALD-treated Ti-II in DI-water	$11 \pm 4^\circ$	$16 \pm 4^\circ$ (SD from D_{13} storage in air, $p < 0.001$)		
Un-treated Ti-II in air (control sample, control storage)	$23 \pm 3^\circ$	$33 \pm 2^\circ$ (SD from D_0 , $p = 0.022$) (SD from D_{13} storage in air, $p = 0.01$)		
Un-treated Ti-II in DI-water (control sample)	$23 \pm 3^\circ$	$22 \pm 1^\circ$ (SD from D_{13} storage in air, $p = 0.003$)		

TABLE V: Water Contact Angle measurements as a function of cleaning and storage steps of ALD treated and untreated Ti-II samples.

4 ° to 25 ± 5 ° ($p < 0.001$). Untreated Ti-II samples stored in ambient air showed an increase in WCA from 23 ± 3 ° to 33 ± 2 ° ($p < 0.001$). We note that while wettability was lost during storage of samples that were UV-irradiated, it was not as extensive as the loss of wettability during the initial 5-Day storage post-ALD treatment. The observation may be explained by the possible difference in surface/bulk organic contamination post-ALD vs. post-UV treatment of ALD-treated samples. Sathees *et al.* showed that deposited TiO_2 may contain up to 2 % carbon(172) which may result in altered wettability behavior of the film within the 5-day storage, and UV-degradation of this contamination in the surface/bulk may be responsible for delayed loss of wettability. Specifically, lack of initial surface/bulk contamination may delay accumulation of low-level volatile organics present in ambient air. As a result, storage in ambient air was extended to 21 days where WCA was observed to have increased to 36 ± 6 ° and 36 ± 3 ° of ALD-treated and untreated Ti-II samples, respectively.

A similar storage study was conducted by our group on heat-treated Ti-V samples stored in air vs. cold DI-water (8 ± 2 °C) and room temperature DI-water ($\text{RT} = 25$ °C).(173) Results are given in **Figure 8**, **Figure 9**, and **Figure 10** and summarized in **Table VI**.

It was found that samples stored in DI-water (cold or RT) retained their initial wettability obtained from sandblasting/acid etching (SA) treatments and heat-treatment of SA samples, with 600 °C-3 hours treated sample having the lowest WCA at the end of the storage period. Interestingly, control samples prepared for storage in RT-DI-water were observed to be significantly hydrophobic on Day 0 with as-is measurements of 21 ± 8 °. As Figure 5 shows,

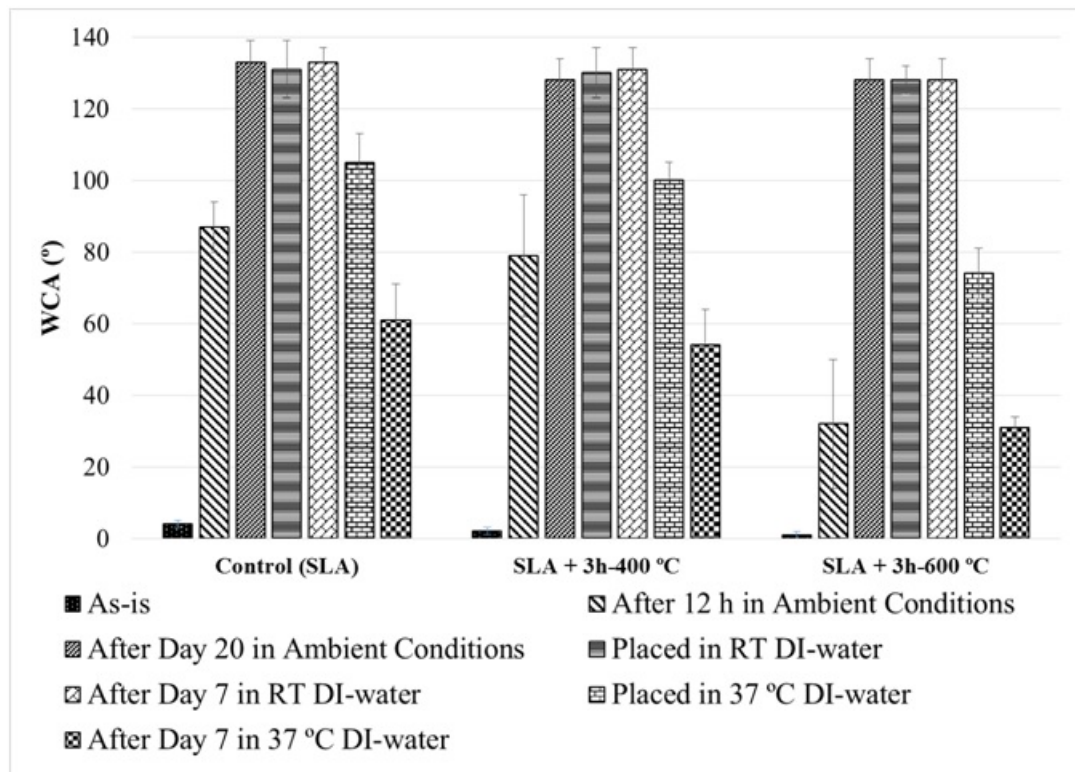


Figure 8: Surface wettability of heat-treated and untreated Ti-V samples in ambient air storage, followed by storage in room temperature DI-water, followed by storage in 37 °C-DI-water.

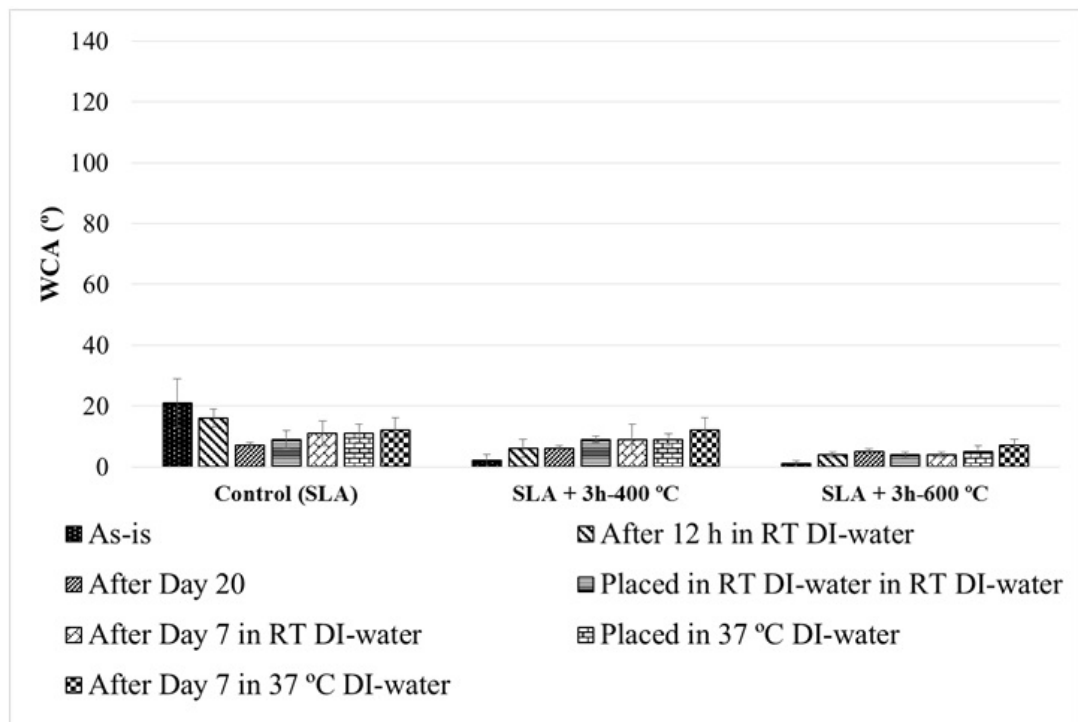


Figure 9: Surface wettability of heat-treated and untreated Ti-V samples in room-temperature DI-water storage, followed by storage in 37 °C-DI-water.

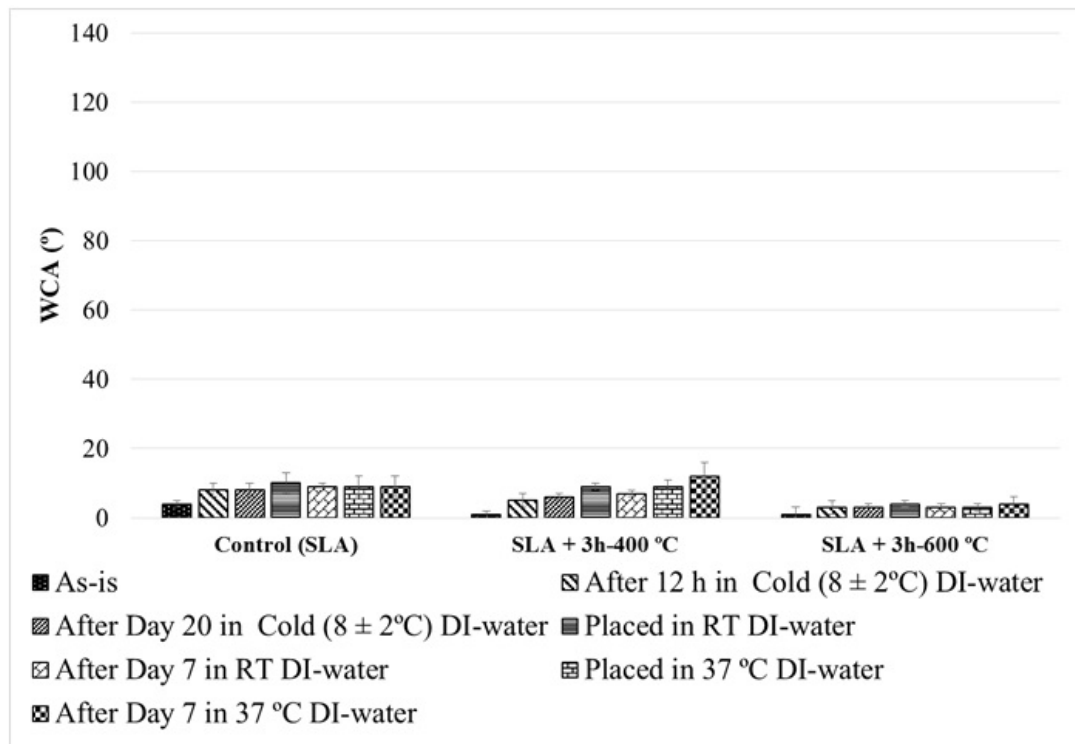


Figure 10: Surface wettability of heat-treated and untreated Ti-V samples in cold DI-water storage, followed by storage in room temperature DI-water, followed by storage in 37°C -DI-water.

however, WCA decreased over time to values similar to those of samples stored in cold DI-water. It may be that chemicals involved in SA treatment were not properly removed from sample surfaces prior to WCA measurement and DI-water storage resulted in a gradual dissolution of these chemicals, as is indicated by the decline in WCA values over the course of DI-water storage. Samples which were stored in ambient air conditions rapidly lost wettability over time and showed that heat-treatment did not have an effect on the extent of the loss of wettability. However, heat-treatment did affect how much the WCA decreased when placed in RT-DI-water and 37 °C-DI-water. Crystalline TiO₂ (anatase and rutile) has been reported in literature to improve dissociation of H₂O on Ti-V surfaces, thereby improving surface wettability.(25; 120; 121) It has also been reported in literature that the solubility of organics in warm water is higher.(174) The study indicates that for best results, storage mediums such as DI-water can be used to hydrate the surface and prevent accumulation of surface contamination.

Comparable to this investigation, a recent study reported by H. Lu *et al.* shows that samples stored in water or isotonic solution (i.e., NaCl or CaCl₂) for extended period of time maintains wettability.(175) F. Rupp *et al.* and G. Zhao *et al.* also studied the wetting behavior of samples with varying degree of roughness stored in air, water or NaCl.(162; 166) Their study concluded that storing samples in either water or NaCl maintains wettability by keeping hydroxyl groups intact on the substrate and by preventing interaction of contaminants from the ambient environment with the sample surface.(162; 166)

Previously it has been shown that ALD-treated samples contain high energy surfaces, which

Storage	Ambient Air			Room Temperature (RT) DI-water			Cold ((8 \pm 2 $^{\circ}$ C)) DI-water		
Sample	Control (SA)	400 $^{\circ}$ C	600 $^{\circ}$ C	Control (SA)	400 $^{\circ}$ C	600 $^{\circ}$ C	Control (SA)	400 $^{\circ}$ C	600 $^{\circ}$ C
As-is	4 \pm 1 $^{\circ}$	2 \pm 1 $^{\circ}$	1 \pm 1 $^{\circ}$	21 \pm 8 $^{\circ}$	2 \pm 2 $^{\circ}$	1 \pm 1 $^{\circ}$	4 \pm 1 $^{\circ}$	1 \pm 1 $^{\circ}$	1 \pm 2 $^{\circ}$
After 12 h	87 \pm 7 $^{\circ}$	79 \pm 17 $^{\circ}$	32 \pm 18 $^{\circ}$	16 \pm 3 $^{\circ}$	6 \pm 3 $^{\circ}$	4 \pm 1 $^{\circ}$	8 \pm 2 $^{\circ}$	5 \pm 2 $^{\circ}$	3 \pm 2 $^{\circ}$
After Day 20	133 \pm 6 $^{\circ}$	128 \pm 6 $^{\circ}$	128 \pm 6 $^{\circ}$	7 \pm 1 $^{\circ}$	6 \pm 1 $^{\circ}$	5 \pm 1 $^{\circ}$	8 \pm 2 $^{\circ}$	6 \pm 1 $^{\circ}$	3 \pm 1 $^{\circ}$
Placed in RT DI-water	131 \pm 8 $^{\circ}$	130 \pm 7 $^{\circ}$	128 \pm 4 $^{\circ}$	9 \pm 3 $^{\circ}$	9 \pm 1 $^{\circ}$	4 \pm 1 $^{\circ}$	10 \pm 3 $^{\circ}$	9 \pm 1 $^{\circ}$	4 \pm 1 $^{\circ}$
After Day 7	133 \pm 4 $^{\circ}$	131 \pm 6 $^{\circ}$	128 \pm 6 $^{\circ}$	11 \pm 4 $^{\circ}$	9 \pm 5 $^{\circ}$	4 \pm 1 $^{\circ}$	9 \pm 1 $^{\circ}$	7 \pm 1 $^{\circ}$	3 \pm 1 $^{\circ}$
Placed in 37 $^{\circ}$ C DI-water	105 \pm 8 $^{\circ}$	100 \pm 5 $^{\circ}$	74 \pm 7 $^{\circ}$	11 \pm 3 $^{\circ}$	9 \pm 2 $^{\circ}$	5 \pm 2 $^{\circ}$	9 \pm 3 $^{\circ}$	9 \pm 2 $^{\circ}$	3 \pm 1 $^{\circ}$
After Day 7	61 \pm 10 $^{\circ}$	54 \pm 10 $^{\circ}$	31 \pm 3 $^{\circ}$	12 \pm 4 $^{\circ}$	12 \pm 4 $^{\circ}$	7 \pm 2 $^{\circ}$	9 \pm 3 $^{\circ}$	12 \pm 4 $^{\circ}$	4 \pm 2 $^{\circ}$

TABLE VI: Water Contact Angle measurements for heat-treated Ti-V samples.

may become contaminated or lose hydroxyl groups when stored in air, whereas, the same high energy surfaces do not experience these symptoms when stored in water.(163) For full effectiveness, storage in a medium such DI-water, methanol, or multi-purpose solution should occur immediately after ALD-treatment so as to maintain the super-hydrophilicity obtained after treatment. The present study also shows that storage in DI-water is sufficient to retain initial surface wettability mostly due ALD treatment.

2.2.7 Conclusion

In this study, long-term wettability and storage of atomic layer deposited 10 nm TiO_2 on CP-Ti and Ti6Al4V samples was investigated. The initial wettability of TiO_2 deposited samples is lost over time, therefore, proper storage conditions are essential to maintaining the hydrophilicity which is important to preserve surface integrity of implants during their shelf life for maximum success. DI-water rinse and methanol sonication have shown to enhance hydrophilicity after a short storage period but with limited effect after long-term storage. It is observed that the long-term wettability of samples can be maintained if stored in a medium such as DI-water so that hydroxyl groups or water molecules may be prevented from evaporating from the surface and/or low volatile organic groups may be prevented from accumulating on the surface from the ambient environment. All samples stored in DI-water (cold or room-temperature) were observed to be hydrophilic with WCA observed to be $\leq 12 \pm 4^\circ$ and as low as $4 \pm 2^\circ$ for heat-treated samples while samples stored in ambient conditions reached as high as $133 \pm 4^\circ$ regardless of heat treatment. In addition, it was determined that for samples stored

at length in ambient conditions, UV-treatment can be employed to recover surface wettability, however, storage in DI-water is recommended after surface treatments for best results.

2.3 Anodization of Thermally Oxidized Ti6Al4V Surfaces

2.3.1 Introduction

By 2010, 719,000 knee replacements(35), 500,000 total hip replacements(37) and 700,000 dental implants(36) will be conducted annually, the majority of which will be for patients as young as 45 years of age.(37) Due to the increasing life expectancy of the U.S. population, longer lasting and rapidly integrated implants are needed. Ti-6Al-4V alloy (Ti-V) is popular for orthopaedic and dental implants due to its biocompatibility, corrosion resistance, atoxicity, and integration to the host bone (osseointegration).(36; 6; 7; 8; 9; 10; 11; 12) Insufficient or poor host bone quality can lead to failures of these implants, resulting in aseptic loosening and lack of osseointegration(176; 42; 177) which may be enhanced by changes in implant surface composition, energy, and topography(36; 8; 9; 49; 135; 178; 24; 28; 25; 29; 30; 179; 180; 181).

The surface native oxide of Ti and its alloys has been shown to promote osseointegration as indicated by up-regulation of markers such as bone morphogenetic protein (BMP) and TGF- β 1./ (24; 25; 18; 19; 20; 21; 22; 23; 26) Specifically, the surface oxide (TiO_2) dissociates water in biological environments and the resultant hydroxyl groups increase the surface energy and promote the process of cellular adhesion.(28; 25; 29; 30; 27) In addition, the passive layer prevents aluminum (Al), vanadium (V), and titanium (Ti) from dissolving into the biological environment (corrosion resistance).(10; 182) Techniques such as atomic layer deposition, chemical vapor deposition, thermal oxidation (TO), sandblasting/acid-etching, and anodization have been used to improve osseointegration as previously discussed.(2) Specifically, as a result of

the increased surface area, TiO₂ nanotubes (TNTs) formed by anodization enhance human mesenchymal stem cell (hMSC) adhesion.(10; 26; 70) TNTs are created by an anodic oxidation process using an electrochemical cell and an electrolyte.(10; 72; 71; 73; 74; 75; 76; 77) For a fluorine (F) containing electrolyte, the oxidation and dissolution kinetics of TiO₂(10; 76; 77) consists of i) H⁺ ion induced F⁻ ion migration leading to formation of a fluoride rich layer at the oxide-metal interface, ii) a flow mechanism results in displacement of the fluoride rich layer towards the cell boundaries, iii) dissolution of the fluoride rich cell boundaries, and iv) dehydration leading to formation of separated TNTs.(10; 77) Changing the applied voltage, fluorine wt. % electrolyte composition, or duration of anodization can affect TNT aspect ratio (diameter/length).(10; 78; 79) Finally, thermally treated TNTs have shown to further improve cellular response.(27; 73; 80; 81)

Previously, prenitridation treated substrates and their effect on the crystallinity of deposited or anodized films has been investigated.(183) While traditional anodization studies investigate TNTs formed on as-is Ti-V consisting of an amorphous native TiO₂ surface, this study aims to investigate TNT formation on thicker and crystalline TiO₂ which may affect the formation of TNTs and their properties.

2.3.2 Methods and Materials

2.3.2.1 Sample Preparation

28 Ti-V disks (diameter=15 mm, height=1 mm) were cut and polished from Ti-V rods (McMaster-Carr). A smooth surface ($R_A = 10 \pm 2$ nm) was achieved by i) wet-grinding using a

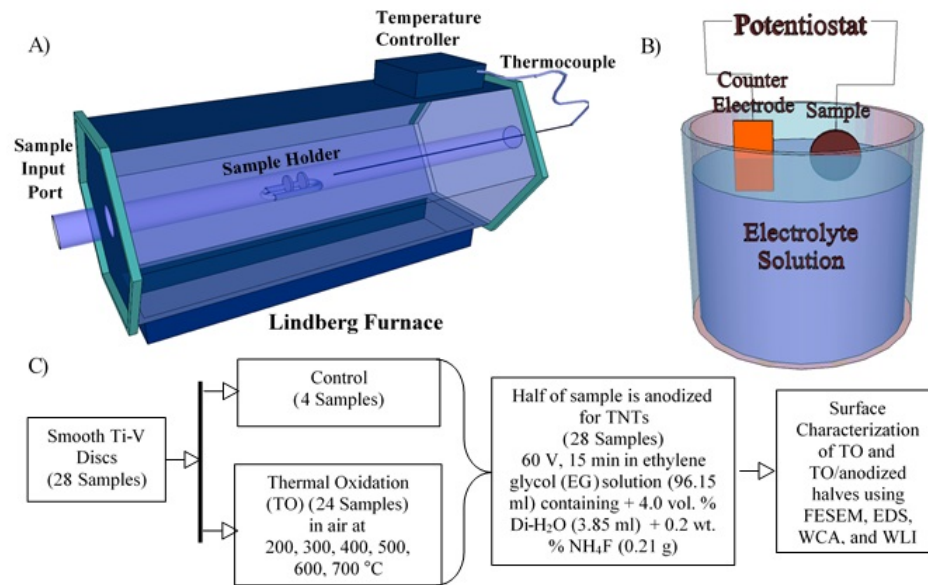


Figure 11: Schematic with labeled parts of A) the Lindberg furnace and temperature controller, B) anodization set-up, and C) experimental protocol.

series of CarbiMet 2 silicon carbide grinding papers (#200, 320, 400, 600, and 800: Buehler), ii) polished using a TexMet Polishing Cloth (Buehler), MetaDi 9 μ diamond paste (Buehler), and MetaDi Fluid lubricant (Beuhler), and iii) fine-polished using a Chemomet I polishing cloth (Buheler) with MasterMed colloidal silica polishing suspension (Buehler). Samples were rinsed with DI-water (17.7 M Ω -cm, Barnstead NANOPure) followed by drying with N₂ gas spray (Grade 4.8, 99.998 %, Progressive Industries, Inc.).

A Lindberg furnace (S# 54032) was used for TO-treatments; a K-type thermocouple was placed at the center of the furnace quartz tube (35 cm from opening) and connected to a temperature controller (JLD-612) to maintain working temperatures (**Figure 11**). A grad-

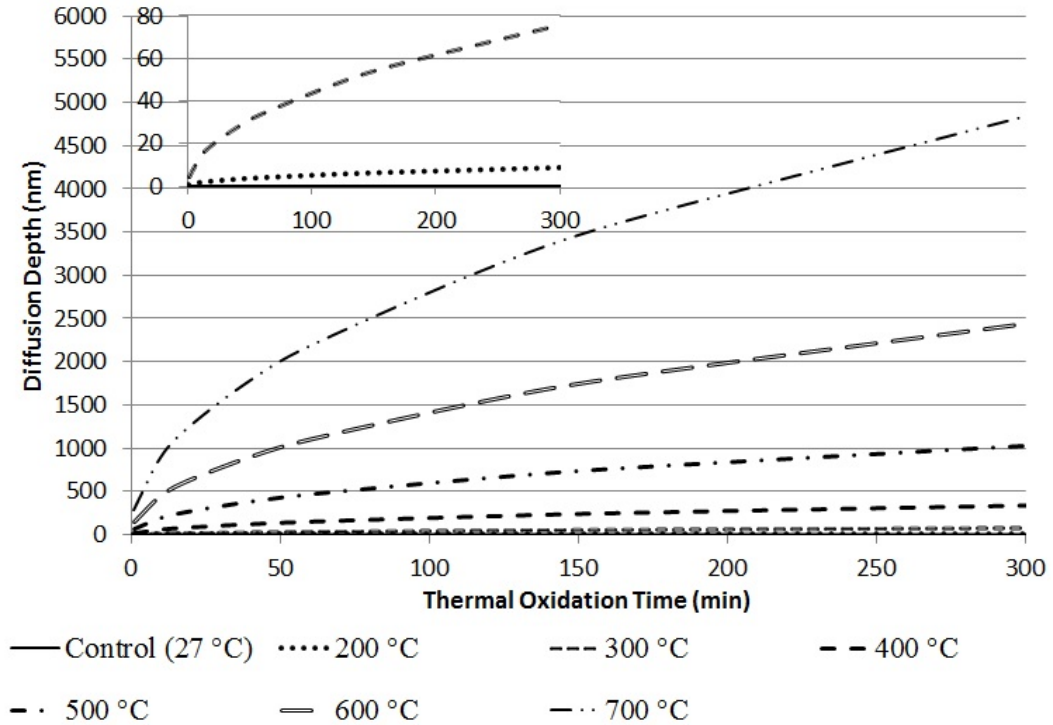


Figure 12: Calculated diffusion depths of oxygen in Ti-V alloy during thermal oxidation (TO) as a function of temperature and time. INSET: Oxygen diffusion depths for control and TO-treatments of 200 and 300 °C. Parameter constants were obtained from the literature.(184; 185)

ual insertion and extraction rate of 5 cm every 5 minutes was used to prevent micro-cracks from thermal shock. Based on diffusion coefficients from literature, **Figure 12** shows oxygen diffusion depth for temperature of treatment up to 700 °C over 5 hours.(184; 185)

However, only the upper most 10-20 % of the calculated diffusion depth is expected to be TiO_2 while the remainder of the diffusion depth may be composed of sub-oxides due to insufficient oxygen diffusion.(186) For example, oxygen is calculated to diffuse 60 nm into Ti-V

from a 3 hour 300 °C TO-treatment, while TiO_2 is reported to be under 12 nm.(186)

For anodization, a voltage source (Keithley 2400 SourceMeter) was connected to Ti-V samples (working electrode) and a copper counter electrode in electrolyte of ethylene glycol (EG, 96.15 ml), 4.0 vol. % DI-water (3.85 ml), and 0.2 wt. % NH_4F (0.21 g) (**Figure 11**). Ti-V samples were anodized at 60 V at room temperature for 15 min. After anodization, samples were rinsed with DI-water, air dried and wrapped in sterile tissue (Kimwipe, Kimtech Science) and stored in a glass petri dish (KIMAX® Petri Dish). The experimental groups are listed in **Figure 11** and **Table VII**.

2.3.2.2 Surface Characterization

Surface characterization was carried out to monitor changes in chemical composition, crystallinity of TNTs, surface morphology, and wettability due to thermal treatment and its effect on anodization.

Surface roughness measurements (average roughness) before and after TO-treatment was carried out using white light interferometry (WLI, NewView 6300, Zygo Corporation). Due to the high aspect-ratio of TNTs, surface roughness measurements were not carried out on anodized samples. A JEOL JSM-6320F field emission scanning electron microscopy (FESEM) system was used for surface characterization of TO-treated and TO/anodized samples (30k magnification). Anodized sample surfaces were scratched to remove TNTs onto double sided conductive carbon tape mounted on an aluminum stub and ImageJ software was used to determine TNT dimensions.

TiO_2 crystallinity of TO-treated samples was studied using Grazing Incidence X-ray Diffrac-

Treatment 1	Short Name	Treatment 2	Short Name
None	Control	Control + Anodized, 60 V, 15 min	CTNT
Thermal Oxida- tion, 200 °C 3 h, in air	TO-200	TO-200 + Anodized, 60 V, 15 min	200TNT
Thermal Oxida- tion, 300 °C 3 h, in air	TO-300	TO-300 + Anodized, 60 V, 15 min	300TNT
Thermal Oxida- tion, 400 °C 3 h, in air	TO-400	TO-400 + Anodized, 60 V, 15 min	400TNT
Thermal Oxida- tion, 500 °C 3 h, in air	TO-500	TO-500 + Anodized, 60 V, 15 min	500TNT
Thermal Oxida- tion, 600 °C 3 h, in air	TO-600	TO-600 + Anodized, 60 V, 15 min	600TNT
Thermal Oxida- tion, 700 °C 3 h, in air	TO-700	TO-700 + Anodized, 60 V, 15 min	700TNT

TABLE VII: Breakdown of treatments and respective group labels.

tion (GIXRD) Spectroscopy, carried out at the Frederick Seitz Materials Research Laboratory Central Facilities, University of Illinois at Urbana-Champaign. A Philips X'pert # 2 MRD system was used with a point parallel plate configuration, 0.1542 nm x-ray emission line of Cu point focus x-ray source, and 2-theta-omega setting. An angle of incidence of 1° was used to optimize sensitivity for the thin crystalline TiO_2 films. Due to the high aspect ratio of TNTs, crystallinity of TO/anodized surfaces apparently could not be studied using GIXRD. For the TO-treated samples, PDF #'s 01-071-1166, 00-021-1276, 00-044-1294, 00-004-0787, 00-022-1058, 00-013-0373 were used for anatase, rutile, titanium, aluminum, vanadium, and alumina (Al_2O_3), respectively.

Chemical composition of TO-treated and TO/anodized surfaces was studied using a diffuse reflectance Fourier transform infrared (FTIR) spectroscopy (Nicolet, Madison, WI, USA) with a deuterated triglycine sulfate (DTGS) KBr detector and an energy dispersive x-ray spectroscopy (EDS) attachment to the JEOL JSM-6320F FESEM. For FTIR spectroscopy, a smooth-polished as-is Ti-V sample was used as a background for all scans, one hour purging time and a 2 cm^{-1} resolution was used over the range of $4000\text{-}400\text{ cm}^{-1}$. FTIR spectra were analyzed with linear background and deconvoluted using Gaussian-Lorentian peak shape function with a spectral peak-fitting software.

Using EDS for TO-treated samples, different locations from the sample surface were analyzed. For TO/anodized samples, surfaces were scratched to remove TNTs onto double sided conductive carbon tape mounted on an aluminum stub; dimensions of randomly selected scratched-off TNTs from anodized surfaces were analyzed. All scans were carried out with 30k magnification.

An acceleration voltage of 10 keV was used for all EDS scans; of the elements expected, two times the emission energy of the element with the highest emission energy is recommended. Emission energies of aluminum (Al), titanium (Ti), and vanadium (V) are 1.486, 4.508 and 4.949 keV, respectively.

Wettability was studied using a goniometer (Rame'-Hart NRL CA). After TO and TO/anodization treatments, samples were wrapped in sterile tissue and stored in a glass petri-dish. Before water contact angle (WCA) measurement, samples were removed from storage and sprayed with N₂ gas for 30 seconds to remove any sterile tissue residue. A micro-syringe (Hamilton, 802RN) was used to place 5 μ L DI-water sessile droplets on TO-treated and TO/anodized Ti-V surfaces. Images of the droplets were taken using the goniometer and ImageJ software with a Contact Angle plugin was used to calculate WCA. WCA measurements were taken at the following stages: 1) immediately after TO-treatment, 2) over a two week storage period following TO-treatment, 3) after methanol sonication and DI-water rinse following storage, 4) immediately after anodization, 5) over a two week storage period following anodization, and 6) after methanol sonication and DI-water rinse following storage. Prior to WCA measurements during the two week storage period, TO and TO/anodized samples (stages 2 and 5, respectively), samples were removed from sterile tissue wrap on Day 1, 2, 7 and 14 and sprayed with N₂ gas for 30 seconds to remove residue. After WCA measurements, samples were returned to sterile tissue wrap for storage.

2.3.2.3 Statistical Analysis

Statistical software (SPSS v. 22.0, SPSS Inc., Chicago, IL, USA) was used for descriptive and statistical analyses. One-way ANOVA was used to determine significance of the differences in surface wettability, average surface roughness, and TNT dimensions. Due to unequal variances, Games-Howell post hoc analysis was used for pair-wise comparisons within these groups. For all analyses, p -values < 0.05 were considered statistically significant.

2.3.3 Results and Discussion

2.3.3.1 Surface Morphology

FESEM images and WLI data of TO-treated samples (**Figure 13** and **Figure 14**, respectively) show a correlation between TO-treatment temperature and resulting surface roughness.(187)

Average roughness (R_A) values for TO-500, TO-600, and TO-700 samples (36 ± 3 , 29 ± 4 , and 180 ± 10 nm respectively) were significantly higher than that of control samples (10 ± 2 nm, $p \leq 0.001$). TiO_2 crystallization (anatase or rutile) due to TO-treatment induces stresses which produce changes in surface morphology, which may in turn increase surface roughness.(188; 189; 190) Surface roughness TO-200, TO-300 and TO-400 groups are similar to that of control samples, indicating that changes due to thermal treatment were insignificant.

For morphological analysis of TNTs, inner diameters (ID), surface pore inner diameters (SID), lengths and outer diameters (OD) were compared (**Figure 13** and **Figure 15**) and results are given in **Figure 16**. Surface pores are visible on CTNT, 200TNT, and 300TNT samples (**Figure 13A - Figure 13C**) with no significant difference. Few surface pores are

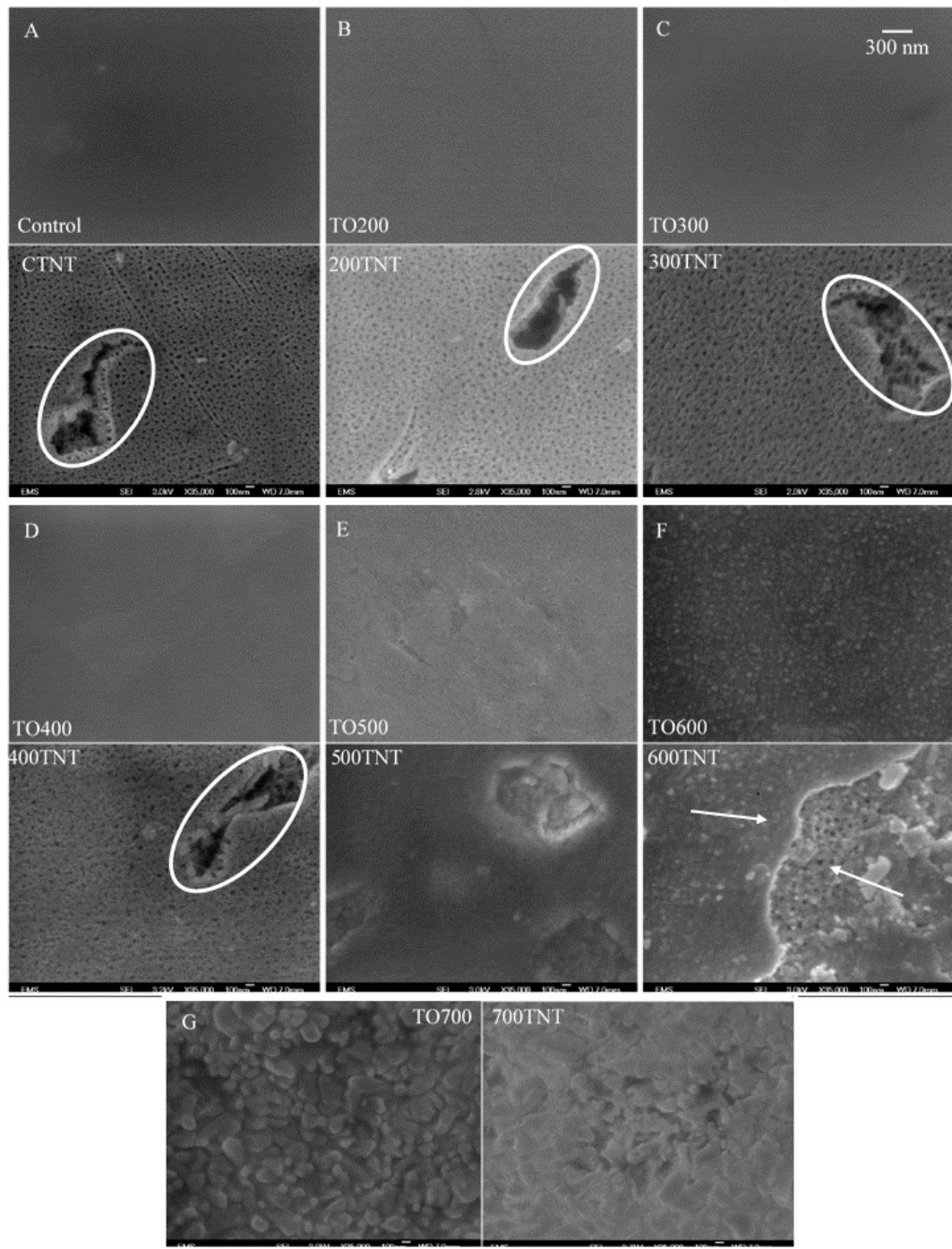


Figure 13: Field emission scanning electron microscopy (FESEM) images of surface topography of A) control and thermally treated at B) 200, C) 300, D) 400, E) 500, F) 600, and G) 700 °C Ti-V samples before and after anodization treatments. Reduced and smaller surface pores are observed as a function of pre-anodization TO-treatment temperature. Circled areas represent dissolution of vanadium rich areas. Anodization treatment was conducted using a fluorine containing ethylene glycol electrolyte at 60 V for 15 min.

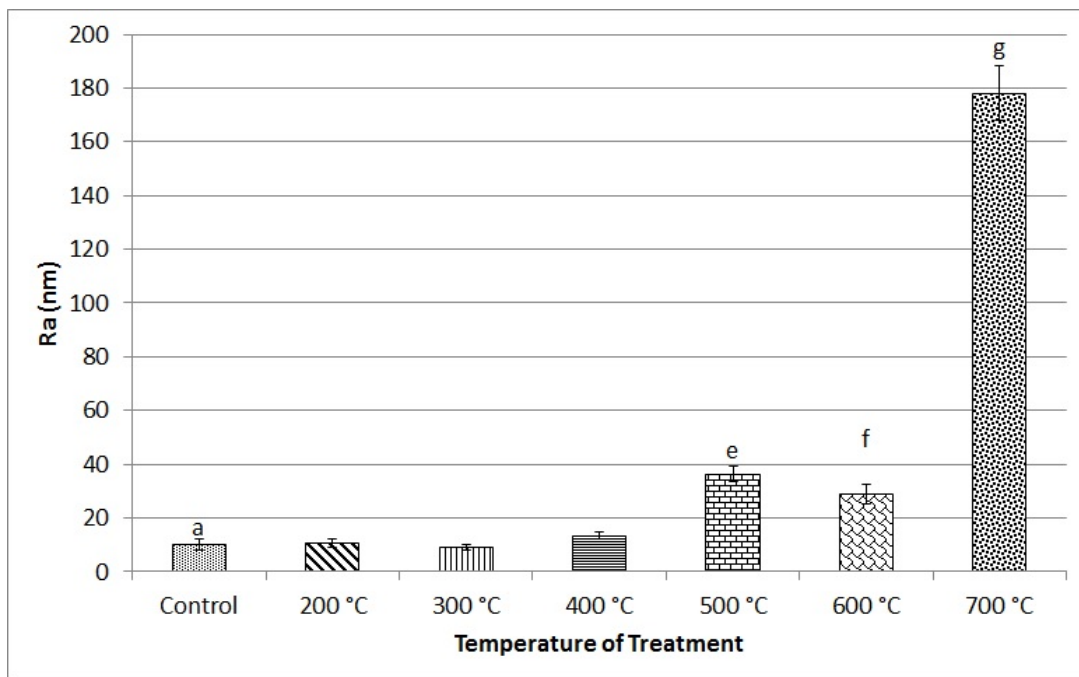


Figure 14: White light interferometry data of A) control and TO-treated thermally treated at B) 200, C) 300, D) 400, E) 500, F) 600, and G) 700 °C Ti-V samples. The data shows an increase in roughness for samples treated at temperatures 500 °C. The data corroborates with FESEM images of TO-treated surfaces (**Figure 13**). Control is denoted as “a” and all other alphabetical markers are for significant difference vs. control with $p \leq 0.05$. Thermal oxidation was conducted in air.

observed for 400TNT sample, and no surface pores are observed for 500TNT, 600TNT, and 700TNT samples (**Figure 13D - Figure 13G**). However, TNTs are observed for all groups except for 700TNT samples (**Figure 13**). 700TNT samples, therefore, are omitted from all morphological analysis. No significant difference was observed in the inner and outer diameters (ID and OD, respectively) of TO/anodized samples. However, significantly longer TNTs were observed for all TO/anodized samples as compared to CTNT samples ($p \leq 0.001$), except for 600TNT ($p = 0.354$) and 700TNT samples (no TNTs). TNTs of 300TNT samples were observed to be the longest among the anodized groups (**Figure 15**).

The morphological differences may be explained by the TO-formed oxide and its effect on the anodization step which forms the barrier-like oxide layer (BOL).(10; 27; 72; 71; 75; 191) During anodization, an equilibrium between oxidation/dissolution of the BOL in the presence of fluoride ions lead to the formation of TNTs.(10; 75) However, an existing oxide (from TO-treatment) may alter the timing of the oxidation/dissolution equilibrium.(2) The final TNT structure composed of a mixture of TiO_2 , TiOH_4 , and $[\text{TiF}_6]^{2-}$; $[\text{TiF}_6]^{2-}$ is the likely by-product of fluorine dissolution of the BOL. Upon removal of the electrolyte, the dehydration of anodized samples leads to TNT separation.(76) As reported in literature, the BOL is formed for a period of time as the initial step of anodization until the oxidation/dissolution equilibrium is reached.(10; 2; 75; 76; 192) Compared to CTNT samples, the 43 % increase in TNT lengths seen on 300TNT samples suggests that the BOL formation step was shortened or subsequent TNT formation was accelerated. A by-product of BOL formation is the production/accumulation of H^+ ions, which attract F^- ions necessary for dissolution of the BOL.(10; 75; 76; 192) Similarly,

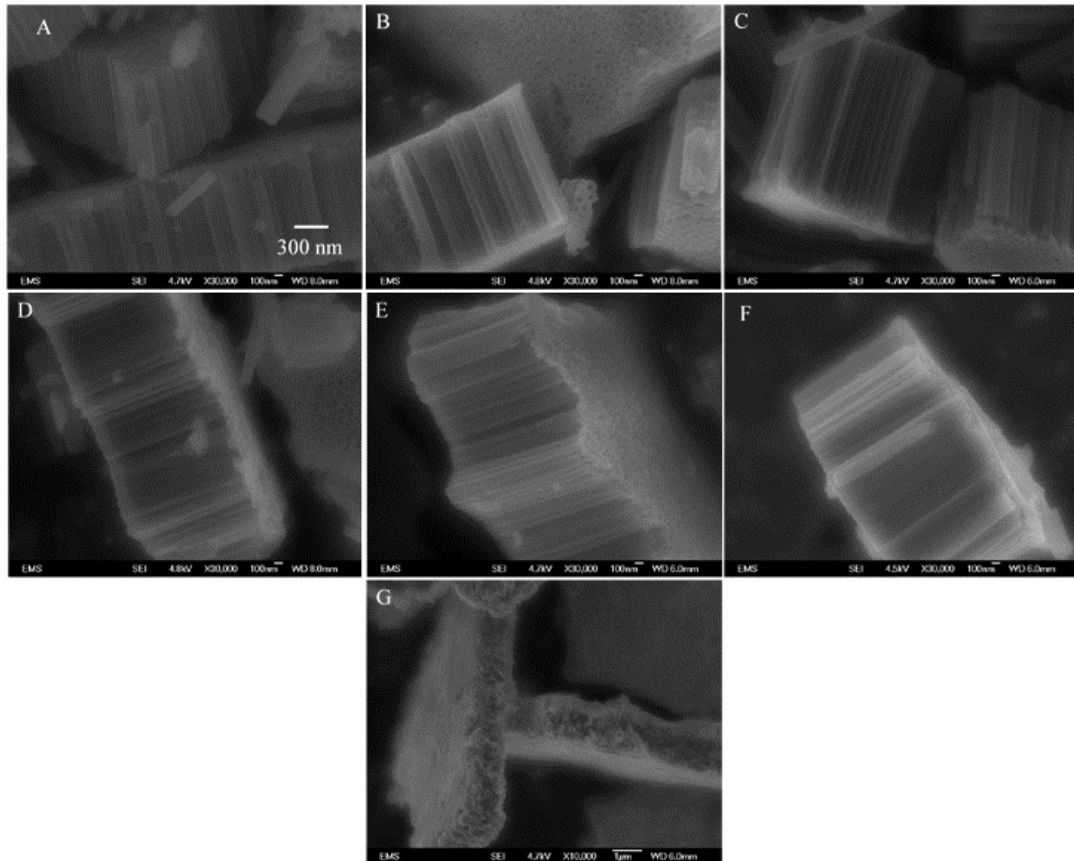


Figure 15: FESEM images of TiO_2 nanotubes (TNT) of A) CTNT, B) 200TNT, and C) 300TNT, D) 400TNT, E) 500TNT, F) 600TNT, and G) 700TNT samples. Longer TNTs are observed on 300TNT samples as compared to all others. Anodization treatment was conducted using a fluorine containing ethylene glycol electrolyte at 60 V for 15 min.

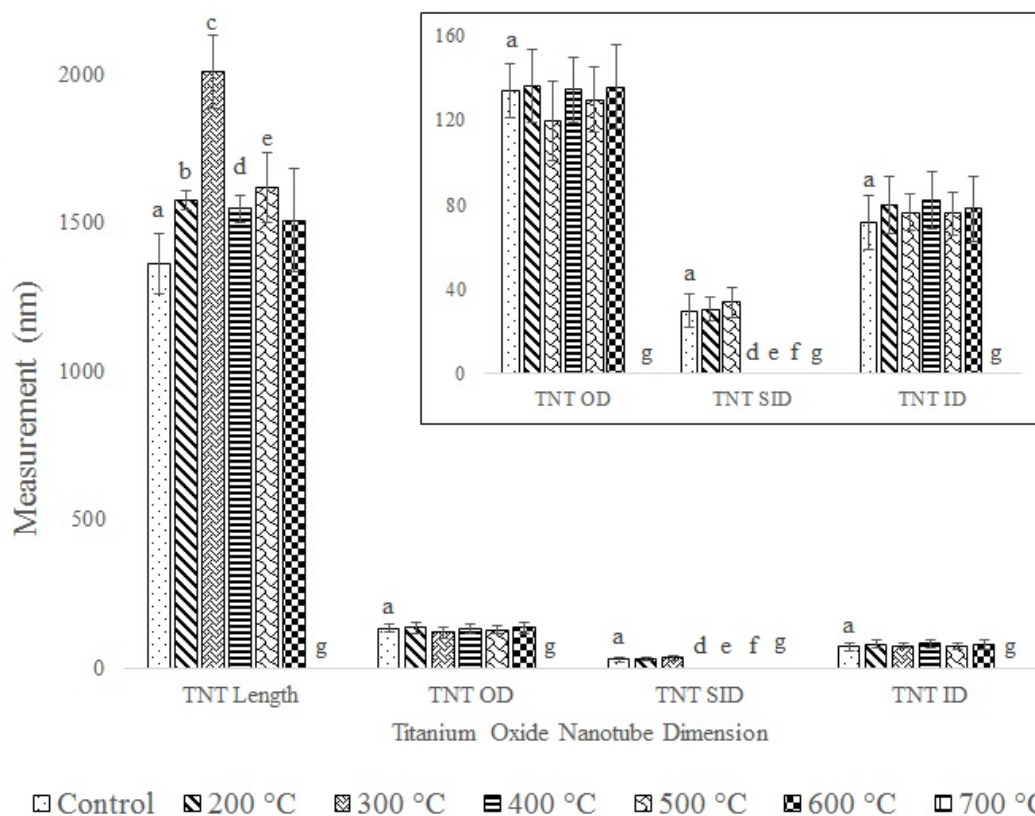


Figure 16: Dimensions of TNTs: anodized sample surfaces were scratched to remove TNTs onto double sided conductive carbon tape mounted on an aluminum stub. ImageJ was used to measure the TNT length, surface inner diameter (SID), and inner/outer diameters under the surface (ID and OD). INSET: Blowup of OD, SID, and ID. Control is denoted as “a” and all other alphabetical markers are for significant difference vs. control with $p \leq 0.05$. Anodization treatment was conducted using a fluorine containing ethylene glycol electrolyte at 60 V for 15 min.

at the bottom of the growing nanotubular structure, new TiO_2 complexes are formed as the underlying bulk Ti-V is exposed to the electrolyte. H^+ ions are produced and accumulate, and F^- ions migrate to the bottom of TNTs and the nanotubular structure grows as the cycle of oxidation/dissolution continues.(10; 75; 76; 192) There are two specific ways the TO-formed TiO_2 may affect this anodization process: 1) by altering H^+ ion production and, therefore, 2) F^- ion transport (**Figure 17**). (2)

Hydrogen Ions: In addition to thicker oxides, thermal treatment can also alter the crystalline structure of the oxide. H_2O dissociation on anatase and rutile surfaces may produce more H^+ ions than on amorphous TiO_2 .(25; 120; 121) Therefore, F^- migration/accumulation at the oxide/electrolyte interface may accelerate, and the dissolution of the BOL and oxidation/dissolution equilibrium and formation of TNTs would be achieved earlier. Although TNTs of all groups (except for 600TNT and 700TNT) acquired significantly longer TNTs ($p \leq 0.001$), the increase in length is 7 - 14 %, while TNTs of 300TNT samples increased by 43 %. The oxidation/dissolution equilibrium may be delayed, however, as a thicker oxide takes longer to dissolve. For example, TO-700 samples are predicted to have an oxide of nearly 800 nm and no TNTs were observed on 700TNT samples.(186) In contrast, TO treatment of 300 °C is expected to result in an oxide of less than 16 nm.(186) It should be noted that TO-600 samples are predicted to have nearly 400 nm of surface oxide (rutile), however, TNTs of 600TNT samples are similar in length to that of CTNT samples ($1.5 \pm 0.2 \mu\text{m}$ vs. $1.4 \pm 0.1 \mu\text{m}$, respectively, $p = 0.354$). While the dissolution of the thicker oxide of TO-600 samples may take more time than control samples, H^+ ion production from dissociation of H_2O by crystalline TiO_2 may attract

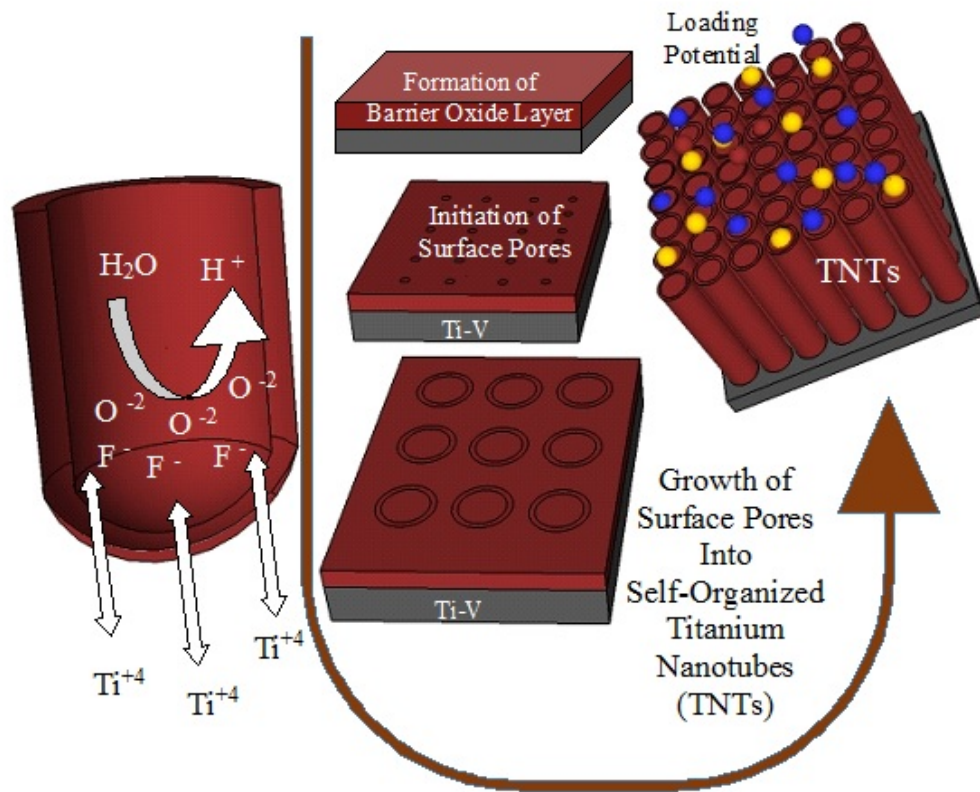


Figure 17: Schematics of anodization process. i) Oxidation at the electrolyte and Ti-V interface leads to formation of barrier oxide layer (BOL) and accumulation of H^+ ions that attract F^- ions, resulting in etching or dissolution of BOL, ii) etching leads to formation of nano-pores which grow into nanotubes, and iii) as oxidation/dissolution steps reach equilibrium at the Ti-V bulk and nanotube interface, nanotubes grow into the Ti-V bulk. TNTs have potential to be hydrophilic and loaded with antibiotics or cell media. Anodization treatment was conducted on control and heat-treated Ti-V surfaces using a fluorine containing ethylene glycol electrolyte at 60 V for 15 min.

more F^- ions to the surface. However, once F^- ions dissolve enough TiO_2 to expose bulk Ti to the electrolyte, the anodization process shifts to formation of TNTs and the amplified presence of F^- ions would accelerate TNT formation. The accelerated TNT formation may be such that TNTs are similar or longer than those of CTNT samples.

Similarly, the oxide of TO-200 samples (amorphous) is predicted to be only a few nms thicker than control samples and 200TNT samples have TNTs of $1.6 \pm 0.03 \mu m$ in length; TO-400 samples are predicted to have 50 nm of oxide (anatase, some rutile) and 400TNT samples have TNTs of $1.5 \pm 0.05 \mu m$ in length; TO-500 samples are predicted to have 160 nm of oxide (anatase-rutile) and 500TNT samples have TNTs of $1.6 \pm 0.1 \mu m$ in length (all longer than CTNT with $p \leq 0.001$). The data suggests that crystalline structures and thickness of TiO_2 play competing roles; the crystalline TiO_2 speeds up the accumulation of H^+ ions and F^- ions during dissolution of TiO_2 and may play a part in accelerating TNT formation while the thicker oxide (50 nm or greater) delays dissolution. Therefore, a thin rutile oxide of about 10 nm, for example, may accelerate anodization.

Fluorine Ions: Crystalline TiO_2 is known to be more reactive than amorphous TiO_2 and diffusivity of TiO_2 increases when doped with non-metals such as fluorine,.(193; 194; 195; 126; 196) In prior work, $\{001\}$ anatase facets were suggested to be the cause for accelerated TNT formation.(2) However, GIXRD data shows that the $\{004\}$ anatase facet, which grows along the $\{001\}$ direction, does not appear for treatment temperatures $< 500^\circ C$. This may explain the

observation that TNTs of 500TNT and are significantly longer and TNTs of 600TNT samples are as long as TNTs of CTNT samples ($p \leq 0.001$ and $p = 0.354$, respectively). In addition, the interstitial spaces within an anatase cell, Wagemaker *et al.* suggests, may promote diffusion of foreign ions and while in small quantities (GIXRD spectra), the anatase structure of TO-300 samples promotes diffusion of F^- ions and therefore anodization steps containing fluorine may accelerate.(76; 194; 197; 198) Although rutile structure has higher diffusion rates for distances of ms when compared to amorphous and anatase TiO_2 , electron transport is slowed for larger distances as ineffective grain stacking (grain boundaries) reduces interparticle connections.(193; 195) Therefore, it may be that the thicker rutile TiO_2 formed during 500, 600 and 700 °C TO-treatment slows transport of F ions within the oxide and therefore the anodization reactions.(193; 195)

The difference in the number and size of surface pores can also be explained by H^+ ion production and F^- ion transport. Water plays two roles in TNT anodization; oxide growth and H^+ ion production. As explained earlier, the accumulation of H^+ ions from TiO_2 production leads to attraction of F^- ions necessary for dissolution kinetics. As TNTs become longer during anodization, the F^- ions accumulate at the bottom of TNTs where new H^+ ions are produced via TiO_2 production; since TiO_2 is no longer formed at the surface, dissolution by F^- ions ceases there.(75; 199; 200; 201) Based on this phenomena, the more TiO_2 exists before anodization, the more TiO_2 will remain on the surface after anodization and reduce the number and size of the surface pores. The remaining TiO_2 , however, may not be more than a few nm's thick. Increasing the water content in the electrolyte solution, however, may accelerate the removal

of extra TiO_2 before the oxidation/dissolution equilibrium is reached.(75; 199; 200; 201)

In summary of this section, two main chemical processes are affected by the surface oxide: H^+ ion production and F^- ion transport. These chemical processes are responsible for the formation of TNTs and therefore affect their morphology. It is observed that a thin crystalline oxide prior to anodization will accelerate TNT formation. In addition, increased H_2O content in the anodization solution would promote surface pore formation.

2.3.3.2 Anodization of TO-treated-ALD-Deposited Ti-V Surfaces

Following these findings, additional experiments were conducted. Ti-V samples were ALD-deposited with 30 nm of TiO_2 , followed by TO-treatment at 300, 450, and 600 °C for 5 mins. The results corroborate previous assumption of crystallinity affecting anodization mechanism. Since 450 °C would convert more of amorphous TiO_2 to anatase TiO_2 , the results are more pronounced than previously. The TNTs are longer, and in addition are thicker walled. This treatment sequence provides an excellent method for thick walled TNTs which may be able to withstand wear conditions better.

2.3.3.3 Surface Composition and TiO_2 Crystallinity

FTIR and GIXRD spectra of TO-treated samples are given in **Figure 18** and **Figure 20**, respectively; FTIR spectra of TO/anodized samples are given in **Figure 21**. All GIXRD peaks are identified by the 2θ location. Due to the small amounts of aluminum and vanadium present in Ti-V, these elements may or may not show up on any given sample.

It is observed that the crystalline structure changes from amorphous to anatase (at as low as 300 °C TO-treatment) and to rutile (at as low as 400 °C TO-treatment). Various facets

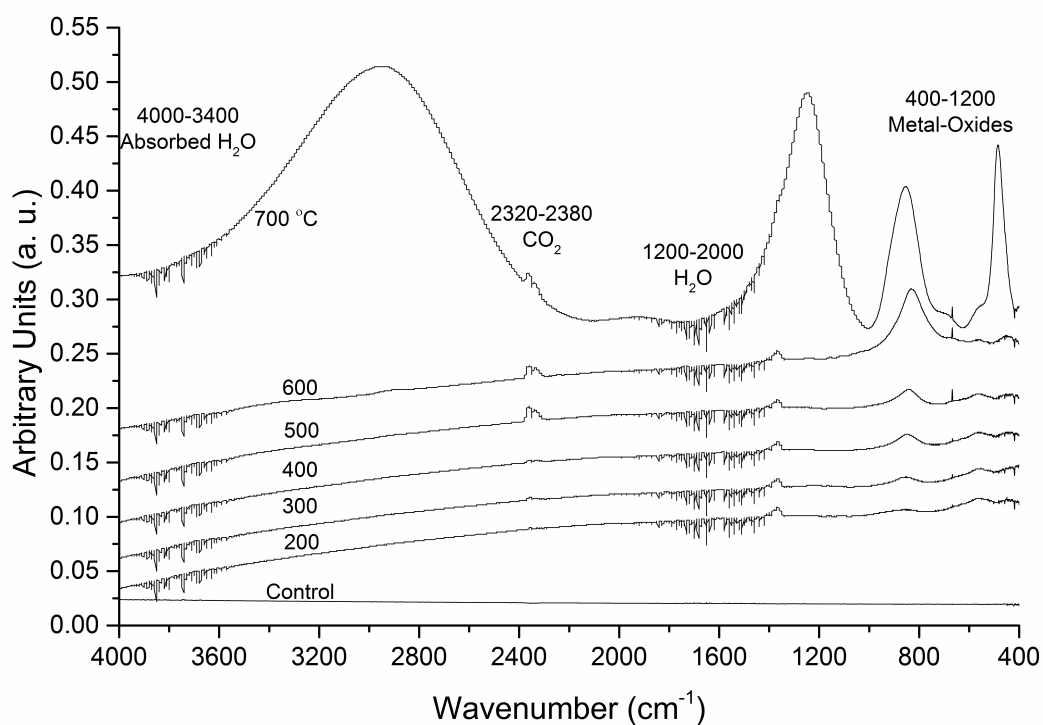


Figure 18: Absorbance Fourier transform infrared (FTIR) spectra of control and TO-treated samples. Significant differences in chemical composition are observed in the metal-oxide regions as a function of treatment temperature. H_2O , CO_2 , and metal-oxide regions are marked. Absorbance FTIR spectroscopy was conducted with a diffuse reflectance accessory, a deuterated triglycine sulfate (DTGS) KBr detector, and purging time of 1 h.

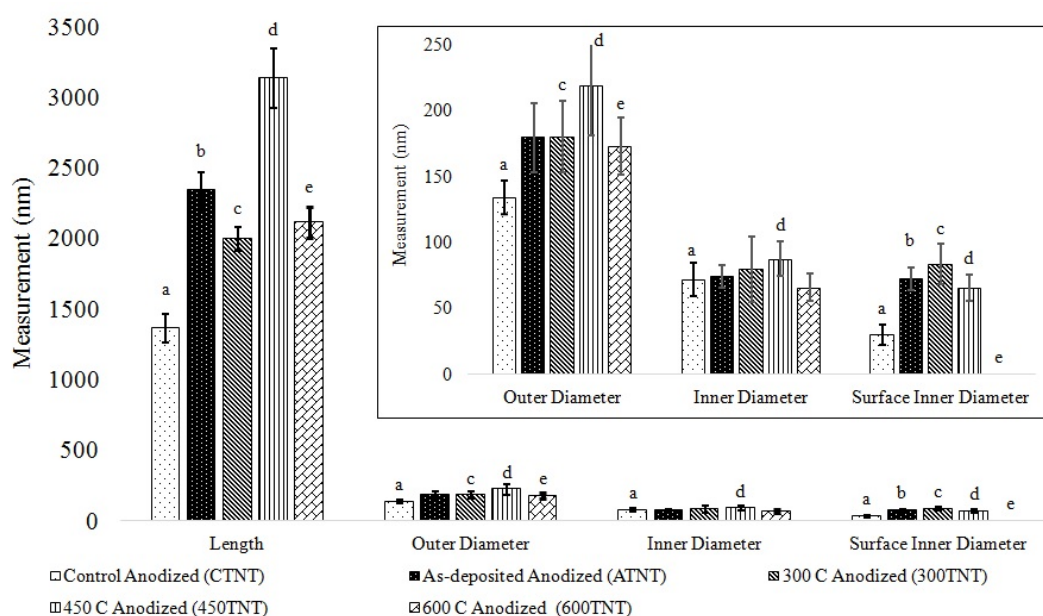


Figure 19: Dimensions of TNTs: anodized sample surfaces were scratched to remove TNTs onto double sided conductive carbon tape mounted on an aluminum stub. ImageJ was used to measure the TNT length, surface inner diameter (SID), and inner/outer diameters under the surface (ID and OD). INSET: Blowup of OD, SID, and ID. Control is denoted as “a” and all other alphabetical markers are for significant difference vs. control with $p \leq 0.05$. Anodization treatment was conducted using a fluorine containing ethylene glycol electrolyte at 60 V for 15 min.

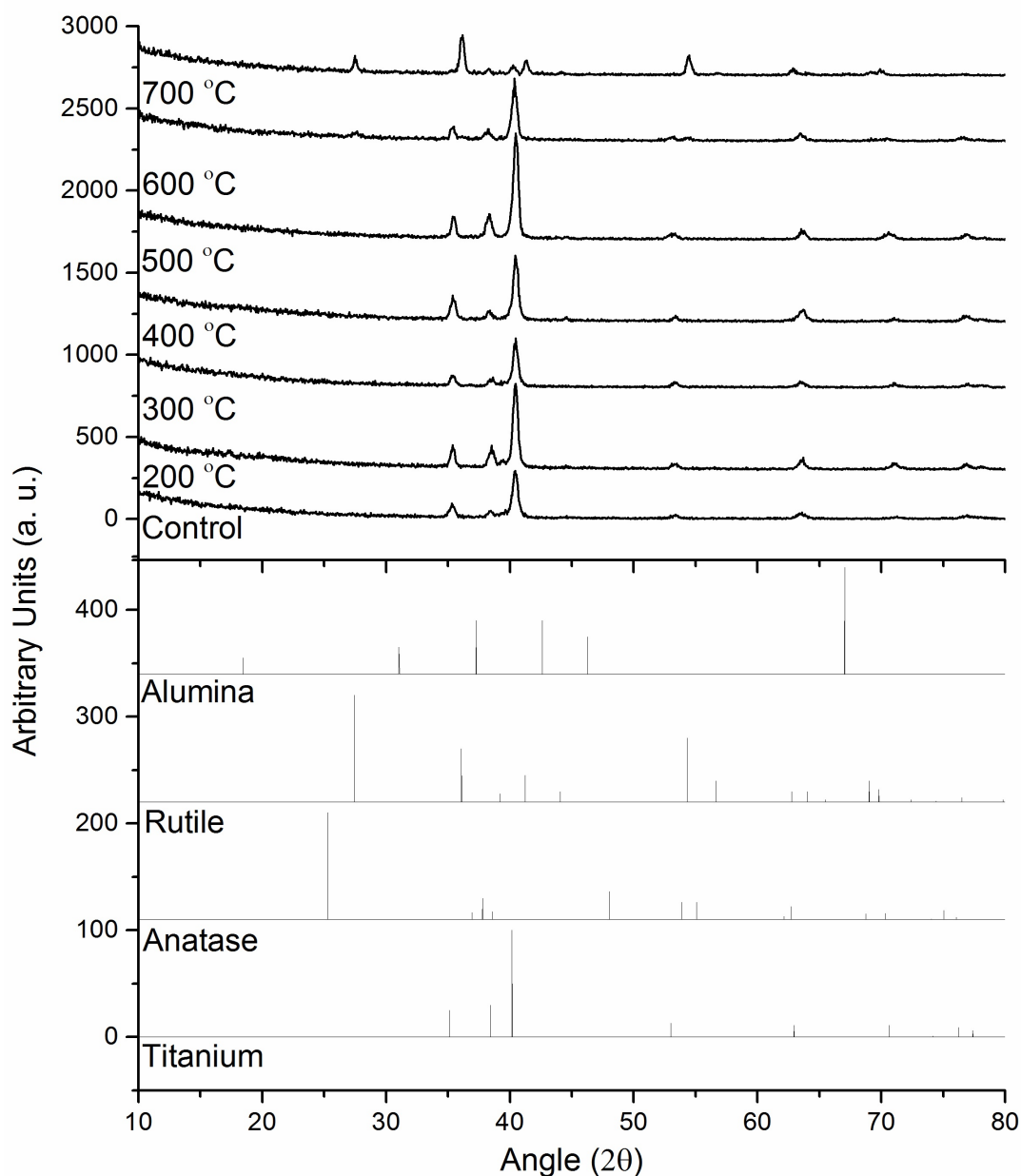


Figure 20: A) Grazing incidence x-ray diffraction (GIXRD) spectroscopy of control and TO-treated samples. Significant differences in crystalline structures are observed as a function of treatment temperature. B) PDF spectra of titanium, anatase, rutile, and alumina are provided. GIXRD spectroscopy was conducted using a point parallel plate configuration, 0.1542 nm x-ray emission line of Cu point focus x-ray source, and 2-theta-omega setting. An angle of incidence of 1° was used to optimize sensitivity for the thin crystalline TiO_2 films.

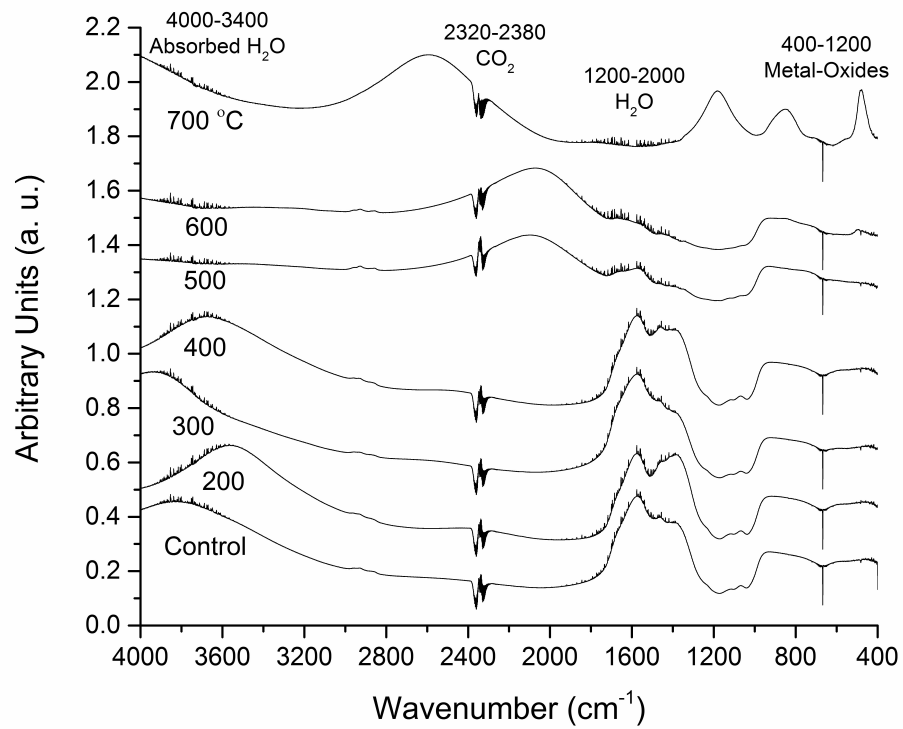


Figure 21: Absorbance FTIR spectra of TO/anodized samples. Significant differences in chemical composition are observed for samples with pre-anodization temperatures of above 400 °C. Absorbance FTIR spectroscopy was conducted with a diffuse reflectance accessory, a DTGS KBr detector, and purging time of 1 h.

of anatase/rutile appear in the spectra at different temperatures, suggesting that some facets of anatase/rutile form at higher temperatures than that of other facets of anatase/rutile. In addition, several titanium peaks are observed decreasing as a function of treatment temperature, suggesting that titanium is oxidized at higher quantities within the volume analyzed by GIXRD. Detailed explanation is given in the supplemental material.

Due to 1) the irregular surface roughness and 2) the various components of the alloy and their effect on surrounding bond stretch/vibrations, peak positions may have blue-shifted (lower cm^{-1}) or red-shifted (higher cm^{-1}) compared to absorption bands reported in literature. The following peaks are observed in all FTIR spectra due to the residual air in the FTIR purging chamber (**Figure 18**). Three minor peaks seen between $2320 - 2380 \text{ cm}^{-1}$ are associated with gas phase CO_2 (158) and the “noise” seen between $3400-4000 \text{ cm}^{-1}$ and between $1200-2000 \text{ cm}^{-1}$ are associated with the O-H bond stretch and vibration intensities of absorbed/adsorbed and dissociated H_2O (153; 202; 150; 150; 149; 155; 156; 203), CO_2 (158), CO_3^{-2} (158; 204), or carboxyl groups (COO^-) from interaction of TiO_2 with CO_2 or any surface carbon contamination(203; 154). While in low quantity, a sharp CO_2 peak is observed at 667 cm^{-1} which increases as a function of TO-treatment temperature, suggesting that crystalline TiO_2 more readily accepts CO_2 absorption.(144; 143) As stated earlier, TO-treatment induces crystallinity and thicker oxides that in general causes a downshift in the metal-oxide peaks. No peaks in the spectra of control samples should be observed since the background sample and control sample are the same.

The FTIR spectra of TO-200 sample, is also nearly flat with some small peaks. Likewise,

increased intensity is observed in the metal-oxide region ($1200\text{-}400\text{ cm}^{-1}$) with increased temperature of treatment, with the greatest change seen in the TO-700 sample. In addition, anatase TiO_2 is observed to increase and decrease as temperature of treatment is raised from 300 to 600 °C and disappear by 700 °C (Supplemental Material). At the same time, rutile TiO_2 is observed to increase at treatment temperatures $\geq 400\text{ °C}$ (Supplemental Material). It is noted that not all peaks for anatase or rutile are observed where these TiO_2 structures are present, which leads to the suggestion that certain temperature of treatments produce different facets of the same TiO_2 structure (corroborated by GIXRD spectra). Finally, a significant increase in alumina and byproducts of reactions between rutile and surface CO_2 , carbon contamination, and H_2O are observed in the spectra of TO-700 samples. Further related explanation is given in the supplemental material.

As seen in **Figure 21**, the intensity of FTIR spectra increased significantly for all TO/anodized samples when compared to TO-treated samples, indicative of the significant increase in TiO_2 due to anodization vs. TO-treatment. While the TO-700 and TO-600 samples may contain up to 800 and 400 nm of oxide, respectively, the remainder of groups contain thinner oxides. By comparison, TNTs between 1.4 and 2.0 μm long are observed on all TO/anodized samples. Therefore, the intensity of the spectra of TO-700 samples is similar to the spectra of TO/anodized samples. As already explained, bulk Ti needs to be exposed to anodization electrolyte before nanotubes can form. The oxide obtained on TO-700 samples may have been too thick to be dissolved within 15 min. As a result, FTIR spectra of 700TNT samples look similar to that of TO-700 samples.

The spectra of TO/anodized samples show, however, that chemical composition of TNTs (seen between 400-1200 cm^{-1}) is nearly similar among the groups (with the exception of 700TNT where no TNTs are observed), indicating that the pre-anodization TO-treatment did not significantly alter the anodization product. Differences in surface CO_2 and H_2O adsorption/adsorption signatures (above 1200 cm^{-1}) are observed on 500TNT and 600TNT samples as compared to the other samples, possibly due to the lack of surface pores which may interfere with absorption/adsorption of CO_2 and H_2O . Based on area-under-the-peak plots of individual peaks, no consistent trends as a function of pre-anodization TO-treatment temperature are apparent. Combinations of amorphous, anatase, and rutile signatures are seen in all samples with significantly larger intensities as compared to TO-treated samples (Supplemental Material).

There are five main regions of interest: 2800-4000 cm^{-1} (water adsorption/absorption), 2800-1800 cm^{-1} (water adsorption/absorption and CO_2 adsorption and reaction by-productions), 1800-1200 cm^{-1} (water adsorption/absorption and anodization electrolyte residue), and 1200-400 cm^{-1} (metal-oxide). Water (H_2O) and carbon dioxide (CO_2) adsorption/absorption occur at higher levels on TO/anodized samples than TO-treated samples; with the exception of 700TNT sample which is similar to the TO-700 sample, indicating that no nanotubes were formed (corroborated by FESEM). For 500TNT and 600TNT samples, few or no surface pores are observed on the surface which is correlated with FTIR spectra with significant differences in the water absorption/adsorption regions (2000-1400 cm^{-1} , 2800-1800 cm^{-1} , and 3800-3000 cm^{-1}). Lack of surface pores would alter the interaction of ambient H_2O and CO_2 with TNTs, and therefore affect the FTIR spectra. Several C-H and N-H bond peaks representing left-over

residue from the anodization solution were also observed in the FTIR spectra of TO/anodized samples. All samples also have signatures for alumina, which may be present in small quantities left-over from the anodization process.

The analysis of FTIR spectra in this study are in agreement with those reported by D. H. Shin *et al.* and S. Patel, *et al.*, however, this study offers in-depth deconvolution analysis not addressed in those studies.(143; 81) It is deduced that the FTIR spectra of TNTs have distinct signatures and that FTIR spectroscopy is rather a simple and effective surface characterization technique which can be used to validate whether TNTs have formed before turning to more elaborate and time consuming technique such as FESEM. GIXRD of TO/anodized samples was not possible due to the high aspect ratio of the nanotubular surface.

2.3.3.4 Variations in Water Contact Angle

WCA measurements for TO-treated and TO/anodized samples are presented in figures 11 and 12, respectively. As seen in **Figure 22**, samples treated at $\geq 500^\circ\text{C}$ obtained the most hydrophilic surfaces ($\leq 5^\circ$) immediately after TO treatment.

For samples treated at $300^\circ\text{C} < T < 700^\circ\text{C}$, WCA was observed to be significantly lower compared to control ($p \leq 0.003$); no significant difference is observed between control and TO-200 samples ($p = 0.77$). Crystalline structure of TiO_2 promotes dissociation of H_2O molecules, leading to hydroxylation of the surface (25; 120; 121) which attracts H_2O molecules that form OH- H_2O complexes and promote water adsorption.(121) Samples treated at temperatures $\geq 300^\circ\text{C}$ have significantly lower WCA after TO-treatment, indicating that formation of anatase and, at higher temperatures, rutile, leads to greater hydroxylation, and therefore lower WCA.

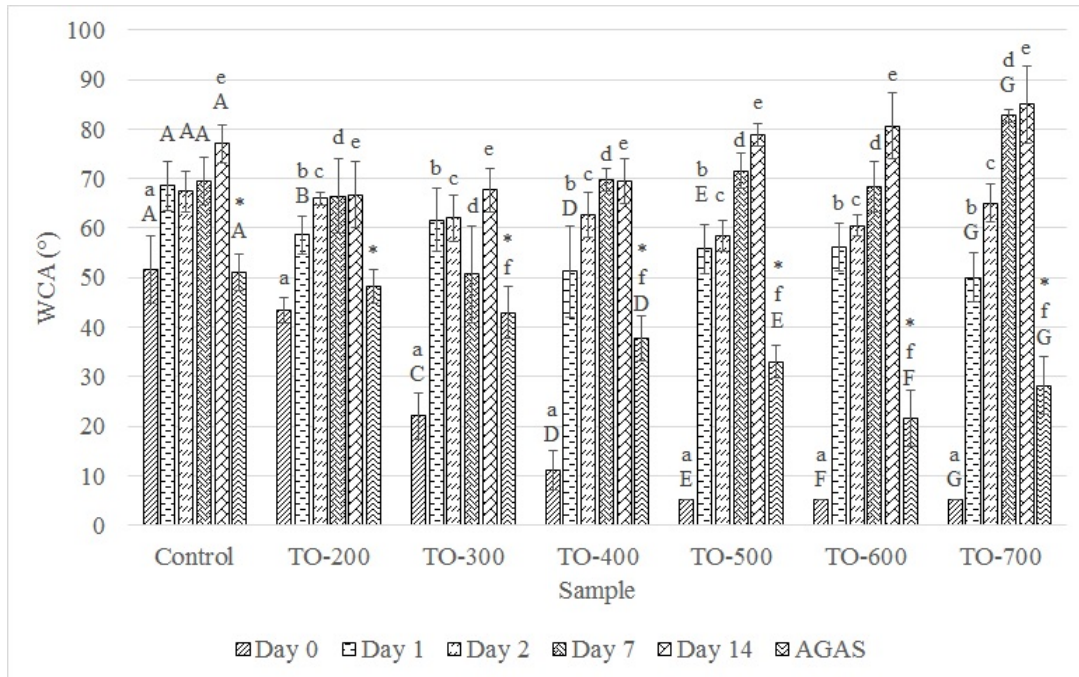


Figure 22: Water Contact Angle (WCA) measurements taken after TO-treatment. TO-treatment result in significantly hydrophilic surfaces; WCA increases significantly by Day 14 for all groups; and WCA decreases significantly after methanol sonication and DI-water rinse (denoted by “*”) for all groups except for control and TO-200 samples. Control group is denoted as “A” and all other upper-case alphabetical markers are for significant difference for TO-treatment groups vs. control group on the specific day of WCA measurement with $p \leq 0.05$. Within each treatment group, storage on Day 0 is denoted as “a” and all other lower-case alphabetical markers are for significant difference vs. Day 0 with $p \leq 0.05$. **AGAS** = **AG**ed - **A**fter **S**onication.

However, samples treated at temperatures $< 400\text{ }^{\circ}\text{C}$ become hydrophobic after just two days, with samples treated at $\geq 400\text{ }^{\circ}\text{C}$ becoming hydrophobic after seven days.

Interestingly, the increase in WCA to $75 \pm 9\text{ }^{\circ}$ for control and TO-treated samples may imply that regardless of treatment, wettability is lost over long periods of storage. Just as hydroxylation leads to hydrophilic surfaces, dehydroxylation during storage is attributed to the hydrophobic behavior. While storage leads to hydrophobic surfaces, a significant decrease in WCA is observed following methanol sonication and DI-water rinse after storage (in **Figure 22**, aged-after sonication = AGAS); decrease in WCA to $36 \pm 10\text{ }^{\circ}$ for all TO-treated samples compared to $51 \pm 4\text{ }^{\circ}$ for control samples, with significant decrease for samples treated at $\geq 400\text{ }^{\circ}\text{C}$ when compared to control samples ($p \leq 0.008$). All samples were stored in similar conditions, therefore the wettability behavior may be explained by TO-formed crystalline structure and its interaction with H_2O . Hydroxylation is a by-product of H_2O dissociation, which produces H^+ ions during anodization; therefore, WCA analysis corroborates the earlier discussion of H^+ ions.

As seen in **Figure 23**, all anodized samples displayed hydrophilic behavior ($\leq 10\text{ }^{\circ}$) regardless of the pre-anodization TO-treatment temperature. FTIR spectra of TO/anodized samples suggest no significant differences between the groups and control/anodized samples, suggesting that no significant changes in the chemical composition or structure occurred due to the TO-treatment. However, the FTIR spectra also show a combination of amorphous, anatase, and rutile TiO_2 for all the TO/anodized samples (Supplemental Material). Therefore, the varying hydrophilic behavior observed may be due to the difference in the aspect ratio of TNTs

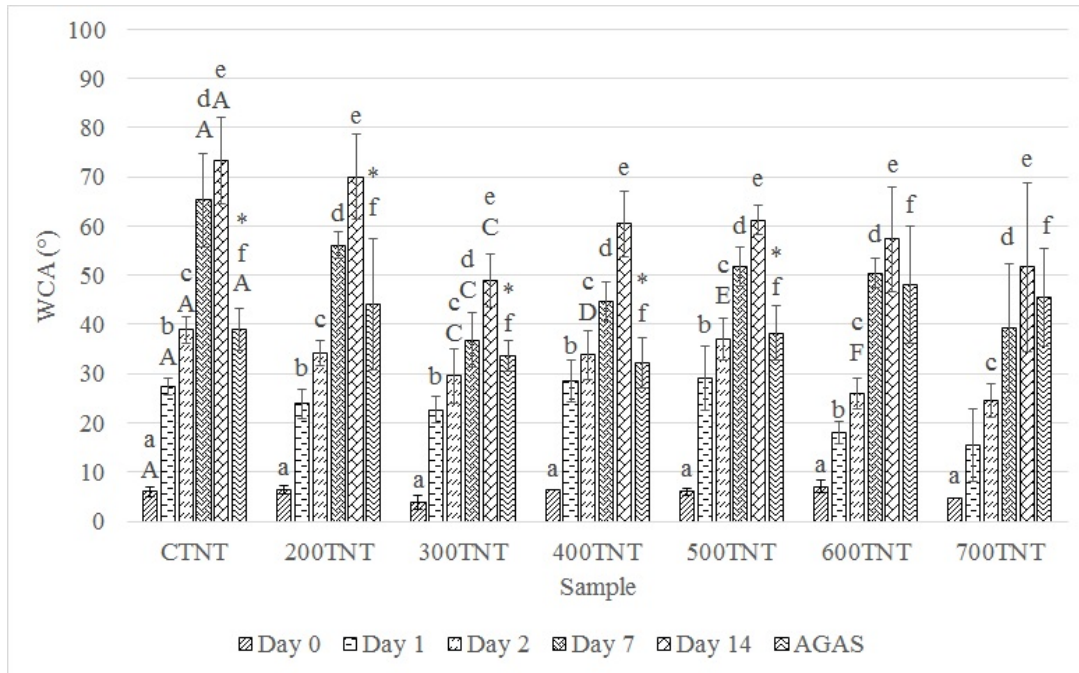


Figure 23: WCA measurements taken after TO/anodization treatment. TO/anodization treatment result in significantly hydrophilic surfaces; WCA increases significantly over time for all groups; and WCA decreases significantly after methanol sonication and DI-water rinse (denoted by “*”) for all groups except for 600TNT and 700TNT samples. Control group is denoted as “A” and all other upper-case alphabetical markers are for significant difference for TO-treatment groups vs. control group on the specific day of WCA measurement with $p < 0.05$. Within each treatment group, storage on Day 0 is denoted as “a” and all other lower-case alphabetical markers are for significant difference vs. Day 0 with $p \leq 0.05$. **AGAS** = **AG**ed - **A**fter **S**onication.

as a function of pre-anodization TO-treatment; surface area available for interaction between TiO_2 and water affects wettability.(10; 27; 70) Previously, average roughness values have been reported for smooth/anodized surfaces to be two orders of magnitude greater than smooth surfaces.(81) Similarly, surface area of anodized surfaces is anticipated to be higher. Storage resulted in increased WCA for anodized groups as well ($61 \pm 12^\circ$ for all anodized samples); wettability of 300TNT samples decreased less than CTNT samples ($68 \pm 4^\circ$ vs. $77 \pm 6^\circ$, $p \leq 0.001$). Hydrophobic behavior on anodized samples was observed to increase at a slower pace as compared to TO-treated samples; WCA increased to $58 \pm 12^\circ$ for all TO/anodized groups compared to $73 \pm 9^\circ$ for control/anodized samples. While wettability of TO-treated samples stabilized within days after thermal treatment, the wettability of anodized groups was not stabilized over the two weeks of storage studied, suggesting a slower dehydroxylation process. The larger surface area of anodized surfaces leads to higher saturation of H_2O during hydroxylation (methanol sonication and water rinse) and dehydroxylation takes longer (during storage). Air entrapment in the nano-structures, however, may lead to even higher WCA in the long run as compared to control and TO-treated samples.(205; 206) It has been reported in the literature that a hydrophobic surface attracts air(205) which, when trapped in the nano-structures of TNTs, would prevent contact between TiO_2 and H_2O (hydrophobic behavior).(205; 206) For anodized samples, methanol sonication and DI-water rinse (in **Figure 23**, aged-after sonication = AGAS) led to a decrease in WCA to $41 \pm 11^\circ$ for all anodized, with significant decreases for CTNT, 200TNT, 300TNT, 400TNT, and 500TNT samples ($p \leq 0.04$). However, no significant difference was observed within the anodized groups. In addition, while a mixture of crystalline

structures are observed in FTIR spectra (Supplemental Material), difference in surface pores suggest some TiO_2 from TO-treatment remain after anodization, which may have affected wettability, especially for TO/anodized samples with surface pores. For those samples, increased surface area of mixed crystalline structure and crystalline oxide left over from TO-treatment on the surface may improve wettability, as seen by WCA measurements taken after methanol sonication and DI-water rinse after storage.

Based on WCA analysis, two outcomes are observed: 1) dehydroxylation of anodized surfaces takes longer to occur due to the larger surface area and 2) once dehydroxylation occurs, hydroxylation from methanol sonication and DI-water rinse may be less effective due to air entrapment. For TO-treated samples, air entrapment is not an issue due to the lack of nano-structures and a greater decrease in WCA is observed when TO-treated samples are rinsed with DI-water.

2.3.3.5 Variations in Elemental Composition

EDS was used to quantify the elemental composition of the TO-treated and TO/anodized surfaces. No difference in elemental composition was found for TO/anodized samples. A sample spectrum is shown in **Figure 24**. TNT O:Ti ratio was calculated to be 2.2 ± 0.5 for all TO/anodized surfaces, indicating presence of TiO_2 in all of the observed TNTs. EDS of TO-treated surfaces had limitations. EDS scans of TO-treated samples were conducted at various angles and locations, however, oxygen was only observed on TO-600 and TO-700 samples as TiO and TiO_2 , respectively. Due to the penetration depth of the EDS ebeam, the Ti-V bulk contributed overwhelmingly to the spectra (90 % Ti, 6 % Al, and 4 % Al).(207; 208)

Based on EDS energy tables, EC for Ti is 4.508 keV and E0 is 10 keV. Using these values,

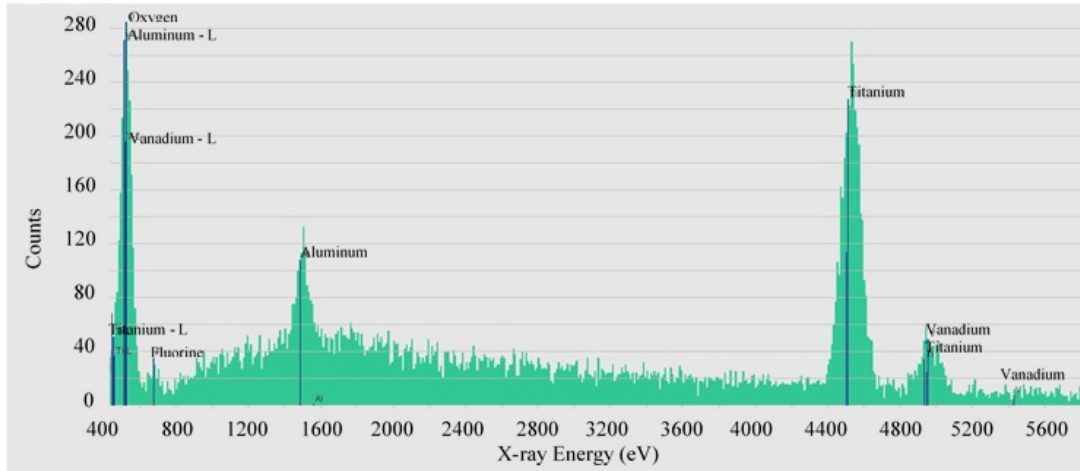


Figure 24: Energy dispersive x-ray spectroscopy (EDS) of TNT taken from a 600TNT sample. Titanium, aluminum, vanadium, nitrogen, and fluorine are labeled. Ti, Al, and V are from Ti-V components, with the oxygen from TiO_2 nanotubes, and residual fluorine and nitrogen from electrolyte and/or presence of fluorine on TNTs in the form of TiF_6^{-2} . Spectra from all anodized samples showed calculated oxygen to titanium ratio of 2:1 (TiO_2). Aluminum and vanadium content are calculated to be less than 3 and 2 %, respectively, indicating that majority of the oxygen content is in the form of TiO_2 .

the EDS e-beam penetration depth into the material is calculated to be roughly 600 nm. In addition, in cases of high acceleration voltages and/or low atomic mass, the excitation volume is in the shape of an elongated tear-drop.(207; 208) Therefore, unless an oxide is several hundred nanometers thick the excitation volume of the ebeam would mostly analyze the bulk Ti-V. Based on diffusion depths, the oxide is negligible for control and 200 °C TO-treated samples and only ~12, 50, and 160 nm thick for 300, 400, and 500 °C TO-treatments, respectively.

2.3.4 Conclusion

The EG/NH₄F/DI-water anodization mechanism on Ti-V samples with TO-formed TiO₂ as a function of treatment temperature was studied. FESEM images and EDS analysis showed that TNTs were formed on all but 700TNT samples and that TNTs were significantly longest on 300TNT samples. Chemical and structural analysis using EDS, FTIR and GIXRD spectroscopy showed that thermal-treatment increases oxide thickness and introduces formation of anatase and rutile crystalline structures of TiO₂. GIXRD spectra showed that changes in crystallinity of TiO₂ can be observed in FTIR spectra (supplementary material). WCA analysis shows that wettability of thermally treated and TO/anodized samples was improved when compared to that of as-is Ti6Al4V and CTNT samples. It is found that anodization of Ti-V alloy with thick crystalline oxide has several likely effects on the anodization process:

1. At the TiO₂ surface/electrolyte interface, crystalline TiO₂ apparently induced production of H⁺ ions from the dissociation of H₂O on the surface leading to increased F⁻ ion migration in comparison with that of an amorphous surface (rutile > anatase > amorphous)
2. Increased presence of F⁻ seems to accelerate reaction with TiO₂ leading to accelerated dissolution of TiO₂, and anatase and rutile seem to accelerate this anodization step when compared to amorphous TiO₂
3. Delay of dissolution/oxidation equilibrium may be a result of the time required to dissolve a thick oxide before bulk Ti is exposed; bulk non-oxidized Ti is likely a necessary component to form TNTs

4. The longer dissolution step for thicker-oxide samples increases the presence of F^- and H^+ ions. Once enough surface TiO_2 has been dissolved to expose any bulk Ti to the electrolyte, TNTs are initiated without complete dissolution of surface TiO_2 . As a result, reduced number and size of surface pores are observed. Therefore, some crystalline TiO_2 likely remains at the surface which can improve long term wettability.

Based on the above, a thin anatase + rutile mixture has been shown to promote alteration in anodization products. Namely, longer and thicker-walled TNTs were produced. In addition, higher anodization voltage and increasing electrolyte water content apparently enhance dissolution of TiO_2 on the TNT surface, such that the surface pores are as wide as the inner-diameter of TNTs. Increased TNT lengths, wider surface pores, and improved wettability can improve cellular response, shelf-life of dental and orthopaedic implants, and create opportunities for drug and cellular media loading applications. In addition, the thicker-walled TNTs and hydrophobic nature of the air-trapping mechanism of nanotubes can be used to improve corrosion resistance of electrodes and other related applications.

2.4 Custom-built Tribocorrosion Apparatus and a Pilot Study

2.4.1 Introduction

Tribocorrosion is defined as the synergistic combination of oxidation/reduction reactions and wear.(17; 209; 210; 211). While implant integration and infection control remain priorities, poor tribocorrosion behavior of biomedical implants has continued to be a major concern.(31; 212; 213; 214) Recently, several medical implant manufacturers issued recalls of their hip implants with complications due to tribocorrosion.(41; 215) In one case, implant failure was projected to affect 40 % of implant recipients.(41; 40) While such an extreme failure may be uncommon, weight-bearing joint replacements, such as knee and hip implants, suffer from long-term revision rates of 12 % (35) and 17 % (38), respectively.(216; 42; 177) The majority of failures are due to aseptic loosening.(216; 42; 177) Aseptic loosening is thought to be the result of chronic inflammatory response to implant surface debris and metal ions released as a result of tribocorrosion at the implantbone interface.(42) While knee and hip implants may last up to 12 years on average, the life-expectancy of the US population continues to rise.(38) Consequently, replacement surgeries for dental, hip, and knee implants have seen an increase of about 100 % over the past decade (37; 39; 217), especially for the 45-64 years age group (37). The increase in life-expectancy coupled with the increase in the elderly population, and increased implantation rate highlights the importance of a longer-lasting implant.

For a comprehensive investigation of biomaterials, such as Ti6Al4V alloy (TiV), tribocorrosion studies are essential. For corrosion and tribology experiments, a potentiostat is used to analyze electrochemical behavior.(209; 218) Investigators and research labs have attempted to modify

existing tribometers or purchase commercial tribocorrosion apparatuses, and even some have attempted construction of a custom-built apparatus. While no standard exists for construction of a tribocorrosion apparatus, existing system designs can be studied to discover features important for a tribocorrosion apparatus. The main objective of this study is to develop an inexpensive, compact, and mobile tribocorrosion apparatus that is simple to use and has good repeatability.

2.4.2 Tribocorrosion Apparatus

In order to develop a tribocorrosion apparatus, an in-depth study of existing literature is required. The findings of the investigation and a validation pilot study are described below.

2.4.2.1 Considerations for Tribocorrosion Apparatus Design

A custom-built tribocorrosion apparatus offers the advantage of flexibility to reflect the needs of the investigation. Priority must be given to important functions of a tribocorrosion apparatus, while some functions may need to be sacrificed. For example, load cells for obtaining normal and friction force values can cost several hundred dollars and may not be necessary initially, but a robust motor which can run continuously for hundreds of cycles is necessary. Once a design is established, the longevity of system components is a primary concern. In particular, the motor used for tribology and the electrochemical cell used for electrochemical measurement are important components. As already mentioned, the motor needs to be able to run continuously for several hundred cycles per sample and test all the samples necessary for successful completion of the study. The electrochemical cell should not leach material into the solution and should be electrically inert. Also, the connecting wiring needs to be isolated

from the solution. It is important to understand that while expensive industrial tribocorrosion apparatuses are meant to function for several years, they may not be necessary for short-term investigations. Finally, an investigator must also consider budget constraints and evolving functional needs.

2.4.2.2 Non-uniformity in Literature

While all tribocorrosion systems are conceptually similar, there are some design differences reported in the literature. For example, a pin or ball of various materials is used as a counter-body, which can have a unidirectional or reciprocal movement against the sample. Other designs feature the sample moving against the stationary counter-body. Furthermore, while linear reciprocating motion is common, a few systems employ a circular track, where the pin or ball moves on the sample in a continuous or intermittent circular path, with or without reciprocation.(218; 219; 220; 221; 222; 223; 224; 225; 226; 227; 228; 229; 230; 231; 232; 233) In some cases, a warm water bath surrounds the electrochemical cell to mimic body temperature.(224; 226; 230) Major differences and similarities between the systems in literature are given in **Table VIII** and briefly described below.

- All of the systems incorporated a counter-body which is resistant to wear and is electrochemically inert; the counter-body was routinely inspected, cleansed, and replaced as needed.(218; 219; 220; 221; 222; 223; 224; 225; 226; 227; 228; 229; 230; 231; 232; 233) The counter-body is required to perform in reproducible manner for every sample and therefore special care needs to be taken. Conductive materials for the counter-body, for example, would alter the electrochemical data.

Citation	Working, Reference, and Counter Electrodes	Pin	Movement	Electrochemical Cell and Electrolyte	Comments
P. Jemmelly, et al., 1999.	AlSi 430 Steel, Mercury Sulfate Electrode (MSE), Coiled Platinum (Pt) Wire	Al ₂ O ₃ Pin w/ Flat Bottom	Pin Reciprocal Linear; 5, 10, and 20 Hz; Triangular Waveform Signal (TWS) of Constant Amplitude; Track Length: 2.3-2.9 mm; Dead-time = 29 ms; 4-45 Mpa	Polyvinyl Chloride (PVC), 60 ml; 0.5 M H ₂ SO ₄ ; 1 M NaOH	Load Cell for Normal Force, Piezoelectric Force Transducer for Frictional Force, a LabView software with 32 kHz acquisition frequency
S. Mischler, et al., 1999.	DIN 34CrNiMo ₆ Carbon Steel, MSE, Pt Wire	Al ₂ O ₃ Pin w/ Flat Bottom	Pin Reciprocal Linear; 5 Hz; Truncated TWS of Constant Amplitude; Track Length: 5.0 mm; 2, 5, 10 N	PVC, Borate Buffer Solution of pH 8.4 (H ₃ BO ₃ /Na ₂ B ₄ O ₇ 0.3 M/0.75 M)	Load Cell for Normal Force, Piezoelectric Force Transducer for Frictional Force, a software with 10 kHz acquisition frequency
J. Takadomou, 1996.	Nickel and Iron of 99.95% Purity, Hg ₂ SO ₄ Electrode (ESS), 2 cm ² Pt Sheet	Al ₂ O ₃ Sphere (D= 5 mm)	Reciprocal Rotation of Ball; 0.2 Hz; Truncated TWS of Constant Amplitude; Track Length: 15.0 mm; 3.5 N	Teflon, Aerated H ₂ SO ₄ Solution; .01 - 1 M	Strain Gauge for Frictional Force, a software with 10 kHz acquisition frequency
Sh. Hassani, et al., 2009.	AlSi 1045 Carbon Steel w/ Electrodeposited Ni-Co Coating, Standard Calomel Electrode (SCE), Coiled Pt Wire	Al ₂ O ₃ Sphere (D= 4.75 mm)	Reciprocal Rotation of Ball; Classic Slider-Crank Mechanism; 1 Hz; Track Length: 5.0 mm; 4.5 N	N/A, 10 w/w % NaOH Solution at pH 13.2	Load Cells for Normal and Frictional Force
A. Berradia, et al., 2006.	Stainless Steel AISI 304L, Hg/Hg ₂ SO ₄ /Saturated K ₂ SO ₄ , Circular Pt Gauze	Corundum Cylinder (D= 7 mm) with Spherical End (D= 200 mm)	Continuous and Intermittent Unidirectional Circular Motion r= 8 mm; 6, 60, and 120 rpm; 5 and 20 N (96 and 207 MPa	N/A, 0.5 M H ₂ SO ₄ ; Ringer's Solution w/ 8.402g/L NaCl, 0.302 g/L KCl and 0.298 g/L CaCl ₂ 6.6	---
S. Mischler, et al., 1993.	Armco Iron Plate, N/A, N/A	Al ₂ O ₃ Pin (D= 4 mm) w/ Truncated Cones (D= .5 mm, 120° Included Angle)	Pin Reciprocal Linear; 5 Hz; TWS of Constant Amplitude; Track Length: 5 mm; Rest-time = 29 ms; 5 N = 25 MPa	PVC, 60 ml; H ₂ SO ₄ ; 2, 6, 8, 10, 14, 18 M; Double-distilled Water	Load Cell for Normal Force, Piezoelectric Force Transducer for Frictional Force, a LabView software
A. Berradia, et al., 2006.	AISI 304L and SS 3M Stainless Steel, Ag/AgCl (3 M KCl), Pt Microelectrode	Corundum Sphere (D= 10 mm)	Reciprocal Sliding of Ball (Fretting); 1, 10 Hz; Truncated TWS of Constant Amplitude; Track Length: 200 um; 1, 2, and 5 N = 493, 621, 842 MPa	N/A, Ringer's Solution: 8.402g/L NaCl, 0.302 g/L KCl and 0.298 g/L CaCl ₂ 6.6 pH	---
D. Sun, et al., 2009.	CoCrMo (ASTM F75), Ag/AgCl, Platinized Titanium and Graphite	ZrO ₂ Sphere (D= 25.4 mm)	Unidirectional Rotation of Ball; 4.0 GPa = 98 N	N/A, 0.9 % NaCl; 25 % Bovine Serum (BS); Slurries for 3-Body Wear: SiC F1200 and Al ₂ O ₃	CMS100 and ESA400 Software
M. S. Jellesen, et al., 2007.	Stainless Steel AISI 316L, SCE, Titanium Net	Al ₂ O ₃ Ring	Reciprocal Rotation of Ball; Sinus-wave Frequency, 15-20 N, 100 rpm	Polypropylene, 0.5 M H ₂ SO ₄	Strain Gauges for Normal and Frictional Force
S. Mischer, et al., 1998.	Stainless Steel 316L; Ti6Al4V; 99.2% Pure Chromium; Low Carbon- Pure Nickel, MSE, Pt Wire	Al ₂ O ₃ Pin (D= 4 mm) w/ Truncated Cones (D= .5 mm, 120° Included Angle)	Pin Reciprocal Linear; 5 Hz; Triangular Waveform Signal of Constant Amplitude; Track Length: 5 mm; Rest-time = 20 ms; 5 N = 25 MPa	PVC, 0.5 M H ₂ SO ₄ ; 0.5 M Na ₂ SO ₄	Load Cell for Normal Force, Piezoelectric Force Transducer for Frictional Force, a LabView software
M. Azzi and J.A. Szpunar, 2007.	ASTM F67 Pure Ti, SCE, Pt Coil	Al ₂ O ₃ Sphere (D= 3/16")	Reciprocal Rotation of Ball; Classic Slider-Crank Mechanism; 1 Hz; Track Length: 5.0 mm; 4.5 N	N/A, Ringer's Solution: 9.0 g/L NaCl, 0.4 g/L KCl and 0.17 g/L CaCl ₂ , 2.1 g/L NaHCO ₃	Load Cells for Normal and Frictional Force
S. Barri, et al., 2001.	TiN Coating on X20Cr13 Steel, Ag/AgCl, Pt Wire	Al ₂ O ₃ Sphere (D= 6 mm)	Reciprocal Linear Motion of Ball; Truncated Triangular Waveform Signal; 2.0 Hz; Dead-time = 69 ms; Track Length: 5.0 mm; 5 N = 767 MPa	PVC, Borate Solution, pH 8.4	Piezoelectric Force Transducer for Normal and Frictional Force, a LabView Software
Y. Yan, et al., 2006.	High and Low Carbon CoCrMo, Stainless Steel 316L, Ag/AgCl, Pt Wire	Silicon Nitride Sphere (D= 12 mm)	Reciprocating Working Electrode; 1 Hz; 80 N	N/A, 50 % Calf Bovine Serum w/ 0.1 % Sodium Azide; Dulbecco's Modified Eagle's Medium (DMEM); 0.36 % NaCl Solution	Load Transducer for Frictional Force,
S. C. Ferreira, et al., 2006.	ZrONy Thin Films on AISI M2 High-Speed Steel, SCE, Pt Wire	Al ₂ O ₃ Pin	Reciprocating Linear Motion; 1 Hz; Track Length = 6 mm; 5 N	Arcylic, 20 ml; Artificial Sweat Solution: 7.5 g/L NaCl, 1.2 g/L KCl, 1 g/L CH ₃ N ₂ O, 1 g/L C ₃ H ₅ O ₃	---
L. Benea, et al., 2009.	20 nm Ni-SiC Coatings on Stainless Steel, Hg/Hg ₂ SO ₄ /Saturated K ₂ SO ₄ , Circular Pt Gauze	Al ₂ O ₃ Pin (D= 7 mm) w/ Spherical End (D= 200 mm)	Intermittent Unidirectional Circular Motion r= 8 mm; 30-120 rpm; 5 - 20 N; Dead-time = .5 -20 s	N/A, 0.5 M K ₂ SO ₄	---
F. Bratu, et al., 2007.	50 um Ni-SiC Coatings on AISI 304L Stainless Steel, Ag/AgCl (3 M KCl), Pt Microelectrode	Corundum Sphere (D= 10 mm)	Reciprocal Rotation of Ball (Fretting); 10 Hz; Truncated Triangular Waveform Signal of Constant Amplitude; Track Length: 200 um; 1, 2, and 5 N = 493, 621, 842 Mpa; Dead-time = 6.6 s	N/A, 0.5 M Na ₂ SO ₄ , pH 6.5	---

TABLE VIII: Literature investigated for construction of tribocorrosion system.

- All electrochemical cells, including the sample holder, were constructed of materials resistant to corrosion, such as polyvinyl chloride (PVC) (218; 219; 220; 224; 228; 229; 234), Teflon (221), acrylic (231), and polypropylene (227), while many others did not mention the choice of material (222; 223; 225; 226; 230; 232; 233). Similar to the considerations for the counter-body, any leached material from the electrochemical cell into the corrosion solution may alter the tribological dynamics (third-body wear) and reaction kinetics.
- Nearly all of the examined apparatuses in the literature measure frequency of pin movement using equipment such as laser diodes, photoelectric sensors, and tachometers.(218; 219; 220; 222; 224; 228; 233) The remainder of the systems mention control of pin movement frequency and amplitude, however, no explanation is given for how pin movement is monitored.(221; 223; 225; 226; 227; 229; 230; 231; 232) In order to replicate biological phenomena, specific frequencies, length, and duration of movement are necessary. This includes, but is not limited to, teeth, knees, and hips. All of these structures experience different loads, movements, and physiological solutions.
- All systems used a combination of load cells and/or piezoelectric transducers for the measurement of normal force and frictional force.(218; 219; 220; 221; 222; 223; 224; 225; 226; 227; 228; 229; 230; 231; 232; 233) Specifically, these components are used to ensure that a constant load is applied to the sample surface and the coefficients of friction are obtained to understand wear dynamics.
- While not mentioned specifically in all of the studies, the placement of counter and reference electrodes (CE and RE, respectively) relative to the working electrode (WE) was

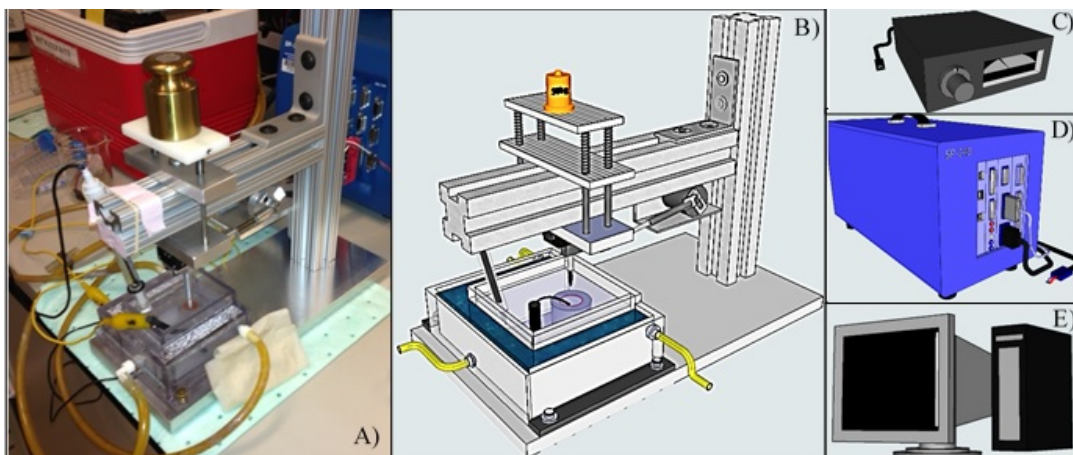


Figure 25: Custom-built tribocorrosion apparatus: **a)** image of the tribocorrosion apparatus, **b)** rendering of the tribocorrosion apparatus, **c)** power supply, **d)** potentiostat, and **e)** data acquisition PC using Sketchup8.

vital to prevent noise and collect accurate data.(218; 219; 220; 221; 222; 223; 224; 225;
226; 227; 228; 229; 230; 231; 232; 233)

2.4.2.3 Non-uniformity in Literature

Based on literature and investigational needs, the final design of the tribocorrosion apparatus and components of the experimental setup are given in **Figure 25**. Sketchup 8.0 (Google Inc., Mountain View, CA, USA) was used to render a 3-dimensional model of the tribocorrosion apparatus to feature the main components (**Figure 25b**).

The tribocorrosion apparatus includes (i) a motor and classic slider-crank mechanism for linear reciprocal counter-body pin movement, (ii) electrochemical cell housing the WE, RE, and CE, and (iii) a water-jacket surrounding the electrochemical cell with input and output ports

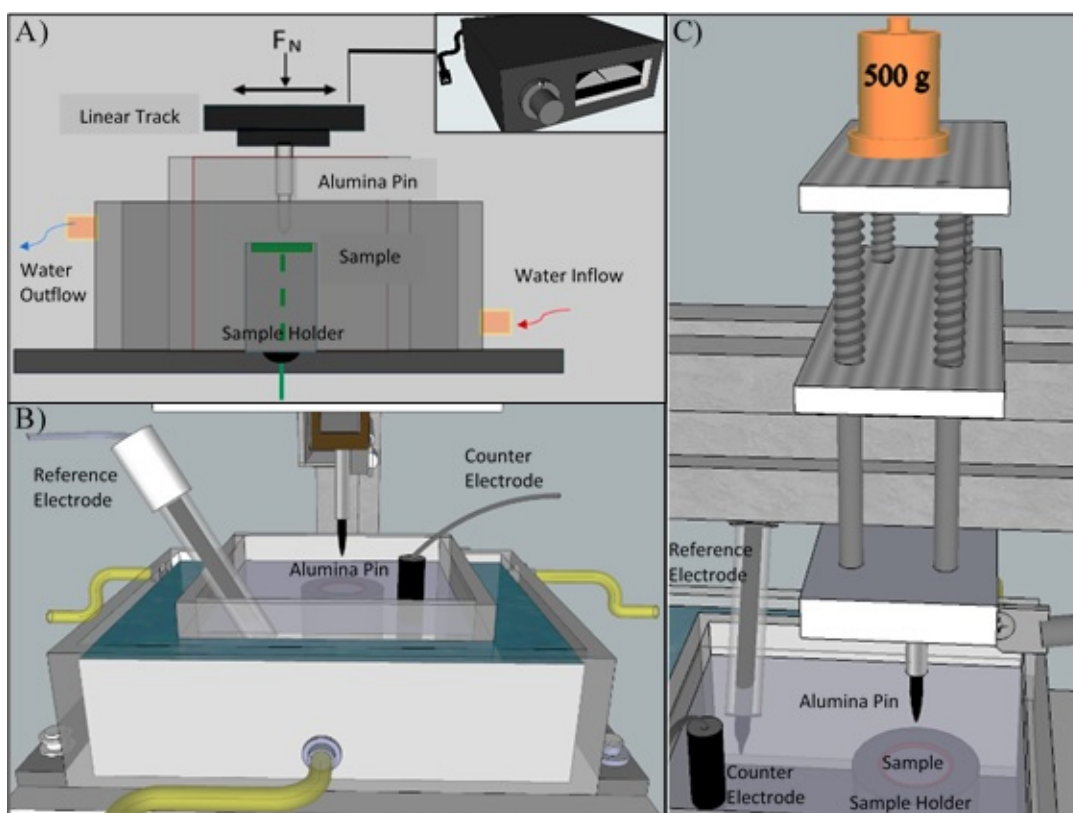


Figure 26: Rendering of the electrochemical cell and tribometer: schematic of **a)** working electrode connection, **b)** electrochemical cell with inlet and outlets for 37 °C water bath, reference electrode (RE), counter electrode (CE) = graphite, and working electrode (WE) = TiV, and **c)** tribometer indicating placement of weights.

for the heated and cooled water, respectively. A variable power supply (Kepco, MPS 620 M, Flushing, NY, USA) is used to power the motor, a potentiostat (G700, Gamry, Warminster, PA, USA) was used for the electrochemical tests, and the data were analyzed using OriginPro 9.0 (OriginLab, Northampton, MA, USA). The electrochemical cell is shown in **Figure 26**.

Isolation of the probe connections to the WE from the corrosion solution required a screw-in method of the sample holder, where the wiring is connected from the bottom of the electrochemical cell (**Figure 26a**). The electrochemical cell is surrounded by a water bath, ensuring the environment is at body temperature (**Figure 26b**). The frequency of reciprocal motion is monitored by a tachometer (Digital Laser Photo Tachometer Non-Contact, Model # DT-2234C+). The counter-body pin is mounted under a frictionless track connected to the motor (**Figure 26c**). The track is mounted to a spring-loaded plate, onto which, weights are added to push the track-mounted pin onto the sample. To determine the load at the point of contact, a load cell was used for calibration. The dimensions of the apparatus are 12.5 in (31.8 cm) in height, 8.0 in (20.3 cm) in width, and 12.5 in (31.8 cm) in length, with a volume displacement of 0.72 ft³ (.02 m³), making it possible to be placed in a compact space, such as an incubator (**Figure 27**). Finally, the custom-designed apparatus was constructed at a low cost, up to two orders of magnitude less than commercial systems.

2.4.2.4 Pilot Study

The custom-built apparatus is validated with an analysis of the tribocorrosion behavior of Ti-V disks in artificial saliva (pH = 6.5, T = 37 °C). For this study, potentiodynamic, free potential, and potentiostatic analyses were used for electrochemical characterization of Ti-V disks. White light interferometry and scanning electron microscopy were used to analyze wear scars on the Ti-V disks. After validation, the apparatus was used to investigate the tribocorrosion behavior of Ti-V disks in culture media inside an incubator (Revco Scientific Inc., M # WJ501TABA, Asheville, NC, USA). The culture media was used as the electrolyte consisting in

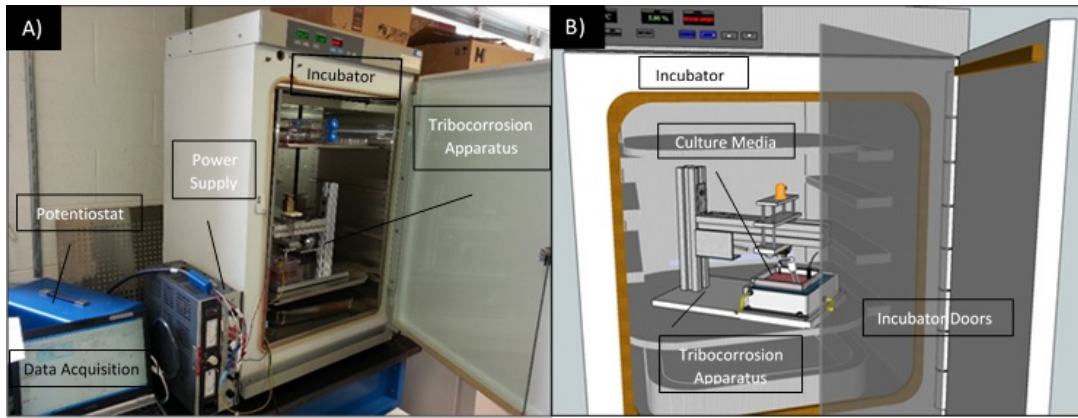


Figure 27: Custom-built tribocorrosion apparatus placed inside an incubator: **a)** image of the incubator setup and **b)** rendering of the incubator setup.

alpha minimum essential medium (α -MEM) supplemented with 10 % fetal bovine serum (FBS), and 1 % penicillinstrepsin, at pH of 7.4 and 37 °C in a humidified atmosphere of 5 % CO₂/air. As **Figure 27** shows, the apparatus is placed inside the incubator with its door closed over the electrode and motor connections. The compactness of the apparatus allows for its use to study implant materials in culture media with live cells to mimic biological conditions to study the effect of osteoblasts and bacteria on tribocorrosion behavior.

In this study, 12 Ti-V disks were cut and polished from Ti-V rods (McMaster-Carr, Elmhurst, IL, USA). The chemical composition of Ti-V alloy is given in **Table XI** (McMaster-Carr). A smooth surface ($R_A = 10 \pm 2$ nm) was achieved by (i) wet-grinding using a series of abrasive pads (#200, 320, 400, 600, and 800; Carbimet 2, Buehler, Lake Bluff, IL, USA), (ii) polishing with a polishing cloth (TexMet, Buehler, Lake Bluff, IL, USA), diamond paste (MetaDi 9-micron, Buehler, Lake Bluff, IL, USA), and lubricant (MetaDi Fluid, Beuhler, Lake Bluff, IL,

Element	Ti	Al	V	Iron	Carbon	Other
wt. %	88.18-90.7	5.50-6.75	3.5-4.5	0.30 max	0.08	0.0-0.268

TABLE IX: Elemental composition of Ti-V alloy (McMaster-Carr)

USA), and (iii) fine-polishing with a separate polishing cloth (Chemomet I, Buheler, Lake Bluff, IL, USA) with colloidal silica polishing suspension (MasterMed, Buehler, Lake Bluff, IL, USA). Polished samples were ultrasonically cleaned for 10 min in 70 % isopropanol (Sigma Aldrich, St. Louis, MO, USA) and 10 min in deionized (DI) water (18.2 M-cm, Barnstead NANOPure, Lake Balboa, CA, USA) and finally dried with N₂ gas (Grade 4.8, 99.998 %, Progressive Industries, Inc., Chicago, IL, USA).

Table XII contains the composition of artificial saliva (AS) as suggested by Liu *et al.* to imitate normal oral conditions.(235) Artificial saliva pH = 6.5 (120 ml) was achieved by adding NaOH (basic) to the AS. To imitate the daily mastication of a person, an alumina ceramic pin was used as the counter-body with a normal force of 1.7 N (Hertzian contact pressure of 24 MPa, contact area of 0.071 mm²) and a 1 Hz reciprocal motion for 1,800 cycles.(236; 237; 238)

As previously mentioned, a Gamry potentiostat (G300, Gamry Inc., Warminster, PA, USA) with a three-electrode configuration (American Society for Testing of Materials (ASTM) guidelines (G61 and G31-72)) was used to conduct standard corrosion tests during sliding such as potentiodynamic (PD), potentiostatic (PS), and free potential (FP) tests (n = 4/group). In addition, electrochemical impedance spectroscopy (EIS) was conducted before and after slid-

Artificial Saliva Component		Concentration
Potassium chloride	KCl	0.4 g/L
Sodium chloride	NaCl	0.4 g/L
Calcium chloride anhydrous	CaCl ₂ ·2H ₂ O	0.9 g/L
Urea	CO(NH ₂) ₂	1.0 g/L
Monosodium phosphate anhydrous (buffer component)	NaH ₂ PO ₄ ·2H ₂ O	0.7 g/L
Sodium sulfide anhydrous (buffer component)	Na ₂ S·9H ₂ O	0.005 g/L
For controlling pH	NaOH	Add as needed

TABLE X: Elemental composition of TiV alloy (McMaster-Carr)

ing. A saturated calomel electrode (SCE) was used as the Reference Electrode (RE), graphite rod as the Counter Electrode (CE), and the exposed surface (1.77 cm²) of the Ti-6Al-4V disks as the Working Electrode (WE). The temperature of the test solution was maintained at 37 ± 1 °C. The standard protocol used for the tests consists of an initial stabilization period, a sliding period, and a final stabilization.(239; 240; 241; 242) First, in order to understand the shift in the corrosion kinetics, potentiodynamic tests were conducted. These were followed by a series of free potential (FP) tests to monitor evolution of potential. Finally, a series of potentiostatic tests (PS) at E_{corr} were conducted to monitor evolution of current. Electrochemical impedance spectroscopy (EIS) was conducted before and after sliding to examine the changes in corrosion kinetics under mechanical stimulation./citeMathew2009,Shukla2005 For the investigation of tribocorrosion behavior of Ti-V disks in culture media, a series of FP tests were conducted to monitor the evolution of potential.

A white light interferometry (WLI) microscope (Zygo New View 6300, Zygo Corporation, Middlefield, CT, USA) and ImageJ software (NIH, Bethesda, MD, USA) were used to analyze the depth, width, and length of the wear scars of the Ti-V surface after tribocorrosion. A simple model as described by Mathew et al. was used to separate the total wear loss due to corrosion and wear. Specifically, **Equation 2.8**, **Equation 2.9**, and **Equation 2.10** were used for the calculations.(209; 218; 219; 241; 243; 244; 245)

$$K_{WC} = (2/3)\pi abcD = K_W + K_C, \quad (2.3)$$

where K_{WC} is the total mass loss due to wear and corrosion (tribocorrosion) and is approximated to be equivalent to half of an ellipsoid with axis a , b , and c , D is the density of the material, K_W is the mass loss due to sliding wear, and K_C is the mass loss due to corrosion. It is assumed that corrosion outside of the wear track is negligible and therefore not considered for calculation of K_{WC} , K_W , and K_C .(210; 211; 222; 243) The weight loss due to corrosion can be estimated using Faradays Law:

$$K_C = Q/ZF \quad (2.4)$$

$$K_C = Mit/ZF, \quad (2.5)$$

where Q is the charge passed, F is the Faradays constant ($96,500 \text{ C mol}^{-1}$), Z is the number of electrons involved in the corrosion process (assumed to be 2), I is the total current, t is the total exposure time, and M is the atomic mass of the material or equivalent weight. Based on

these calculations, relative contributions of corrosion and wear to the wear scar can be estimated by **Equation 2.11**.(245; 246)

$$\text{Synergistic ratio} = K_C/K_W, \quad (2.6)$$

where the ratio determines whether the weight loss is dominated by wear, corrosion, or due to a combination of wear and corrosion: $K_C/K_W \leq 0.1$ for wear dominated, $K_C/K_W > 10.0$ for corrosion dominated, $0.1 \leq K_C/K_W \leq 1.0$ for wear as main component, and $1.0 \leq K_C/K_W \leq 10.0$ for corrosion as main component.(245; 246)

A scanning electron microscope (SEM) (JEOL JSM-6490 LV, Oxford Instruments, Oxford, UK) was used for characterization of surface morphology.

2.4.3 Results and Discussion

2.4.3.1 Electrochemical Analysis

Potentiodynamic (PD), free potential (FP), and potentiostatic (PS) tests were conducted for validation of the tribocorrosion apparatus based on examination of literature. Electrochemical impedance spectroscopy was conducted before and after sliding (**Figure 36**) and the oxide is modeled after a modified Randles circuit which places the polarization resistance (R_P) in parallel with constant phase element (CPE) of the oxide film, in series with the solution resistance (R_S)./citeRuna2013 As reported in the literature, the oxide film did not change significantly before and after sliding.(241; 242) R_S is resistance of the electrolyte between the sample and reference electrode; R_P is the charge transfer resistance at the sample surface and electrolyte interface; CPE is used in place of a capacitance due to the inhomogeneity of the

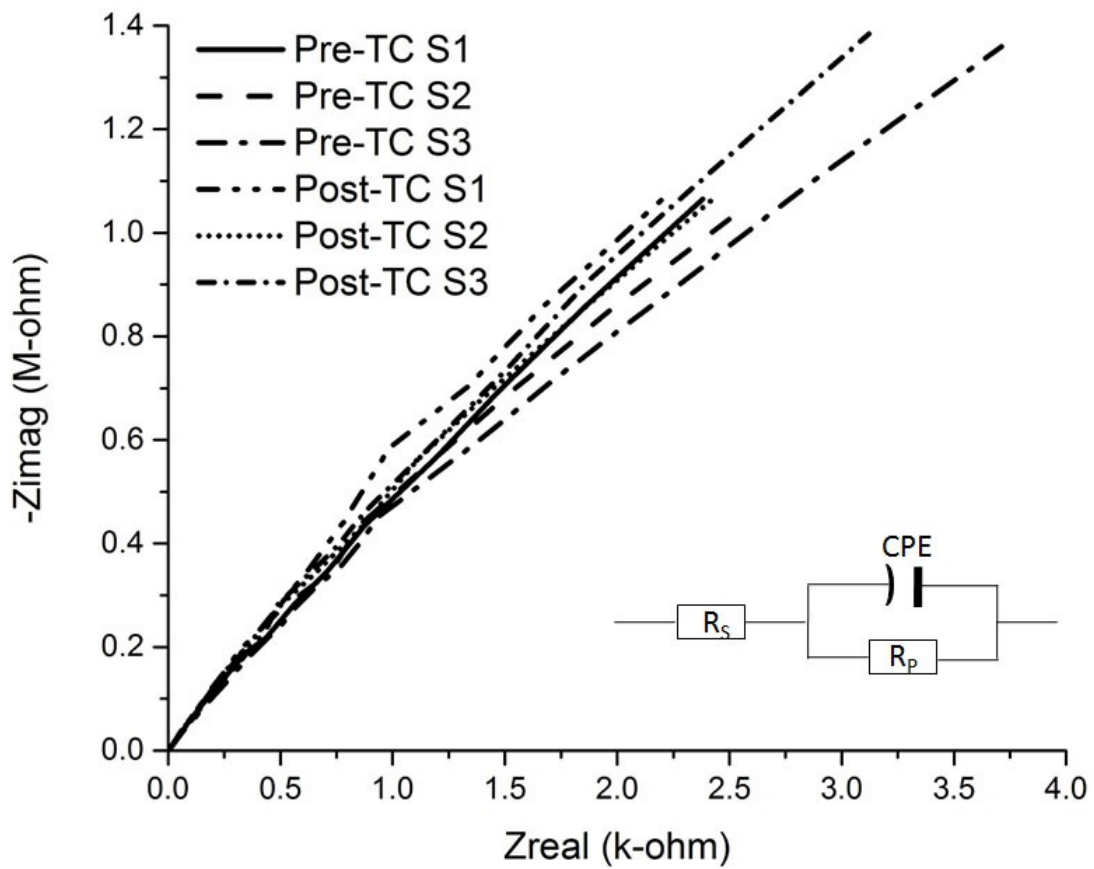


Figure 28: Electrochemical impedance spectroscopy before and after sliding. **Inset:** Modified Randle's circuit is used to model the oxide film. The graph shows no significant change in the oxide composition before and after sliding.

passive layer./citeBarao2012 Before sliding, average R_S , R_P , and CPE are calculated to be $267.9 \pm 11.4 \, \Omega$, $1.1 \pm 0.16 \times 10^7 \, \Omega$, and $2.6 \pm 0.4 \times 10^{-5} \, \text{F} \cdot \text{s}^{(\alpha-1)}$, respectively. After sliding, average R_S , R_P , and CPE are calculated to be 269.1 ± 6.9 , $1.2 \pm 0.11 \times 10^7 \, \Omega$, and $2.6 \pm 0.4 \times 10^{-5} \, \text{F} \cdot \text{s}^{(\alpha-1)}$, respectively. These values are similar to those reported in literature.(241; 242) However, Mathew *et al.* reported R_P values to be much lower.(241)

Potentiodynamic Scan

Figure 29a shows a corrosion-only PD curve of a TiV sample in Artificial Saliva (AS) of pH = 6.5, and **Figure 29b** shows a tribocorrosion PD scan of a TiV sample in AS of pH = 6.5. The observed E_{corr} (corrosion potential), which indicates the readiness of a material to corrode, is similar to values reported for TiV alloy in literature in the range of 0.5 to 1.0 V.(17; 242; 247; 248; 45; 249) Compared to corrosion-only PD scan, the E_{corr} of TiV alloy during tribocorrosion is slightly higher (0.8 vs. 0.6 V. Upon initiation of sliding, the current increased drastically (cathodic shift) and reached a fluctuating range of 1 and 100 A as the passive layer was repeatedly formed and destroyed during sliding. This range of current, also known as passivation current (I_{PASS}), is similar to those reported in the literature [1, 43, 44, 5254].(17; 241; 242; 248; 45; 249) The fluctuating current can be explained as follows. The current increases (cathodic shift) as the passive film is destroyed by the sliding alumina pin.(249) As the pin passes and the worn surface is allowed to interact with the surrounding solution, the surface is repassivated and the current decreases (anodic shift) until the pin slides over the area again to repeat the cycle.(249) As the trend in the graph shows, the depassivation and repassivation process are not in equilibrium; instead, the overall trend is a cathodic shift, where the sliding is causing more depassivation than repassivation. As **Figure 29a** shows, neutral pH corrosion-only PD tests of Ti-V alloy is known to result in a stable I_{PASS} region with no fluctuation or increase in the current.(220; 245; 246; 247) However, under mechanical stimulation (**Figure 29b**), the I_{PASS} region is slightly higher during tribocorrosion and continues to shift to higher current regions during sliding.(249) Comparing corrosion-only and tribocorrosion PD

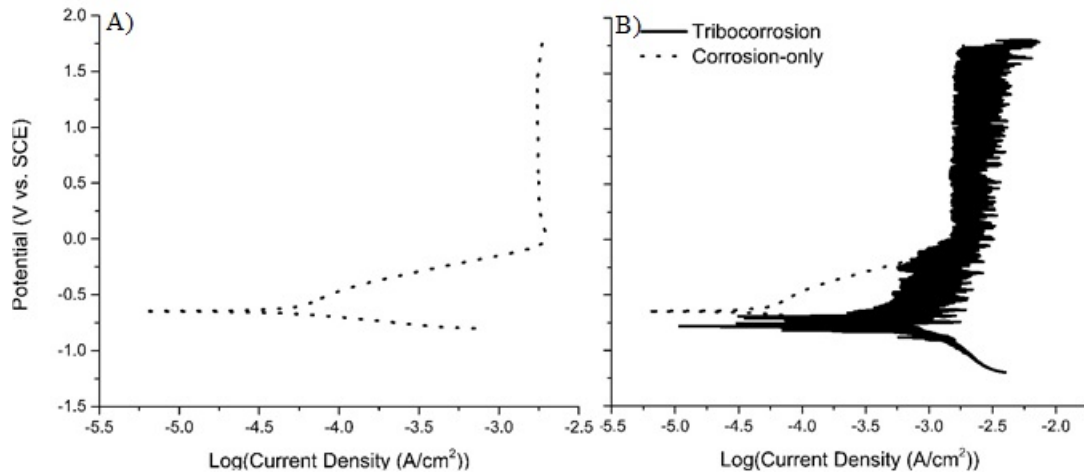


Figure 29: **a)** Potentiodynamic (PD) scan of a control Ti-V sample for corrosion experiment in pH = 6.5 solution. **b)** Comparison of corrosion and tribocorrosion PD scans of a Ti-V sample in pH = 6.5 solution.

scans, it can be seen that the Ti-V alloy has poor tribocorrosion behavior, more specifically, the Ti-V alloy has poor wear resistance.

Evolution of Potential

An evolution of potential curve, obtained from free potential tests (FP), of Ti-V sample in AS of pH = 6.5 is shown in **Figure 30a-c** show the changes in potential during the beginning and end of sliding. It was difficult to compare these results to literature due to the differences in the normal force and contact area used. These parameters affect the contact pressure, which the surface experiences during sliding, and therefore the wear.(210) In the present study, the potential increased during sliding from OCP to the cathodic direction in the range of -0.7 and -0.9 V and stabilized after cessation of sliding. Such a trend is reported in several

studies.(239; 250; 246; 45; 249; 46) This drop and recovery in potential indicates the initiation and cessation of sliding, respectively, of alumina pin on Ti-V alloy samples. Such a drop in potential during sliding indicates the removal of the passive film, which protects the metal from corrosion.(243) Initiation of sliding does not result in an instantaneous decrease in potential. Instead, a gradual decrease in potential is observed over several cycles of sliding until a dynamic equilibrium of depassivation and repassivation is reached (**Figure 30b**). The cessation of sliding does not result in a sudden recovery in voltage either. Instead, a gradual decrease is observed over 300 s of rest until OCP is reached (**Figure 30c**). Comparatively, **Figure 31** shows the evolution of potential of Ti-V disks in culture media placed in an incubator. The evolution of potential follows the same pattern as described before, that is, potential drops rapidly during sliding and gradually increases to OCP once sliding ceases. However, OCP before sliding, the potential drop during sliding, and OCP after sliding are all lower than the potential values observed for the validation portion. The lower potential values indicate that the culture media may have a negative effect on the tribocorrosion behavior of the Ti-V surface. Although cells were not included at this stage, the preliminary results may explain why there are discrepancies between the predicted life-span of implants and the actual in vivo tribocorrosion behavior. While tribocorrosion studies have been studied in water baths to mimic body temperature involving culture media and cells, the compactness of the apparatus (volume displacement of 0.72 ft³ (.02 m³)) makes it possible for the investigation of tribocorrosion behavior of implant materials with cells in an incubator to better mimic in vivo conditions.

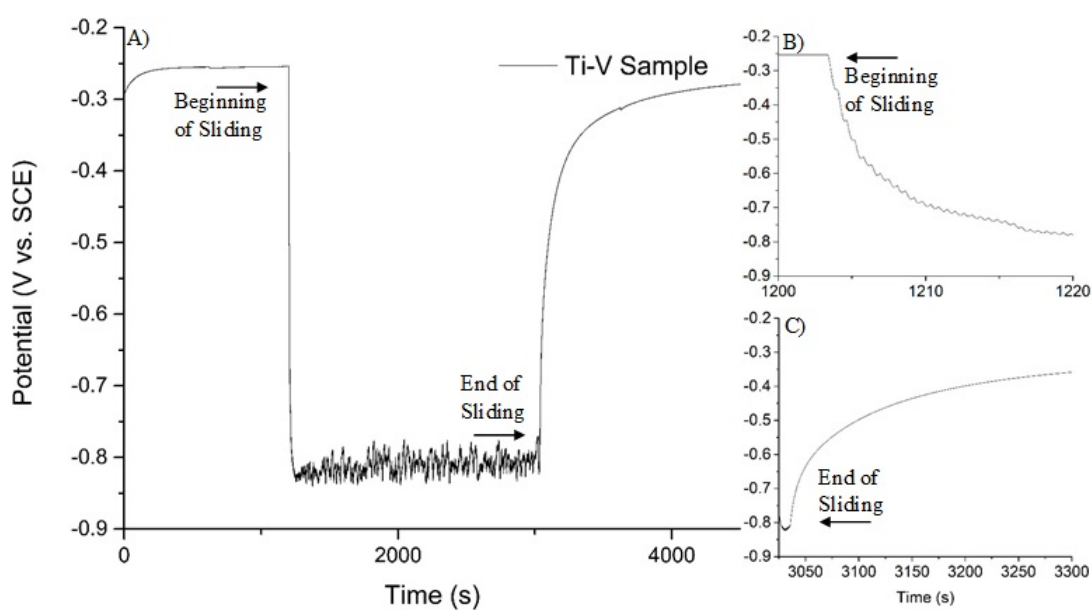


Figure 30: **a)** An evolution of potential curve of a control Ti-V sample for tribocorrosion experiment in pH = 6.5 solution. **b)** Initiation of sliding results in a gradual increase in cathodic voltage observed over several seconds and **c)** cessation of sliding results in a gradual decrease in cathodic voltage observed over 300 s of rest until OCP is reached.

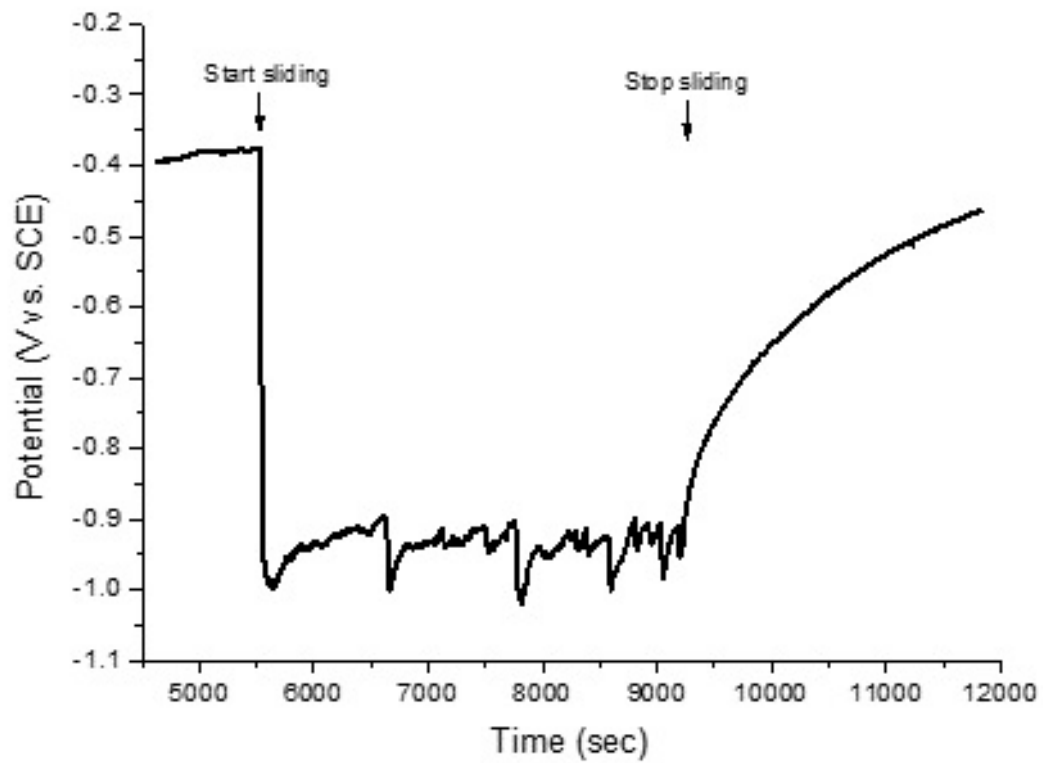


Figure 31: An evolution of potential scan of a control TiV sample for tribocorrosion experiment in culture media in an incubator. Alpha minimum essential medium (α -MEM) was supplemented with 10 % fetal bovine serum (FBS), and 1 % penicillinstrepsin, at pH of 7.4 and 37 °C in a humidified atmosphere of 5 % CO₂/air.

Potentiostatic Scan

A PS curve of Ti-V sample in AS of $\text{pH} = 6.5$ is shown in **Figure 32a-c** which shows the changes in current during the beginning and end of sliding. This test was carried out at E_{corr} which was obtained from the PD scans. While PD scans were easier to compare with literature, PS data depend on the type of counter-body material, contact area, normal force, frequency, and length of sliding. Similar to FP scans, PS scans were difficult to compare with literature due to the various parameters which differ from study to study; however, several comparable observations can be made. In studies involving neutral pH, the current increased (cathodic) dramatically during sliding in tribocorrosion PS tests.(241; 250; 243; 45; 251) The increase and decrease in current indicates the initiation and cessation, respectively, of sliding of alumina pin counter-body on TiV samples. Initiation of sliding does not result in an instantaneous increase in current; however, rather a gradual increase is observed over several cycles of sliding until a dynamic equilibrium of depassivation and repassivation is reached. In the present study, the current fluctuated between 4.0 and 8.0 A during sliding (**Figure 32a**). The current continues to shift to higher current regions during sliding, which is indicative of depassivation.(226; 239; 241; 242) As the sliding of the alumina pin damages the film, repassivation does not occur completely before the pin returns to the same area, therefore the trend is toward depassivation. Additionally, the repassivated oxide layer may not be thick enough and therefore is entirely removed once the pin slides over the area. After sliding is halted, the current decreases (anodic) and is indicative of repassivation of the damaged area.(226; 244) The cessation of sliding does

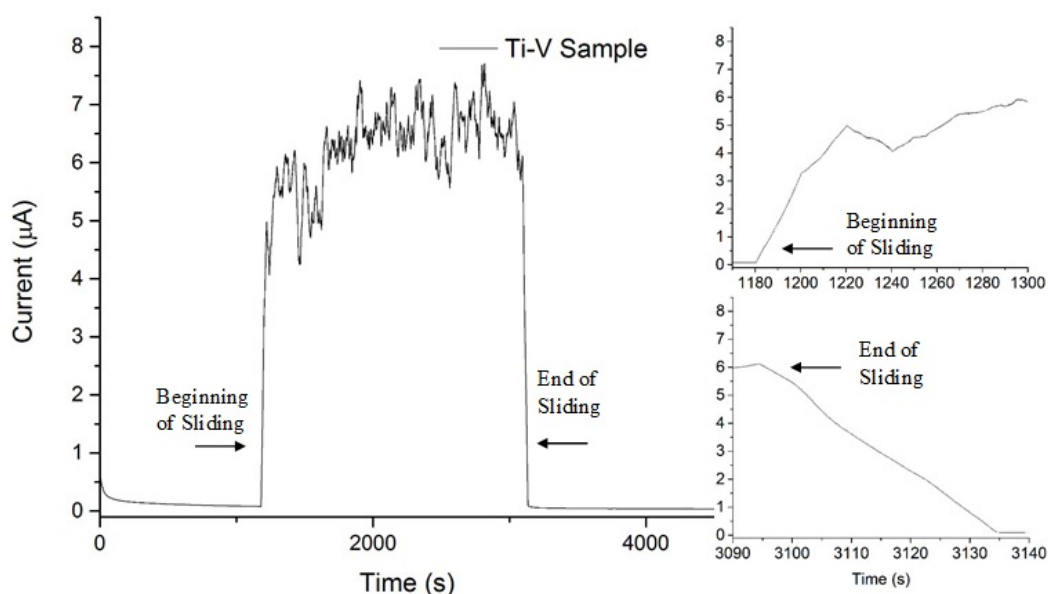


Figure 32: **a)** Potentiostatic scan of a control TiV sample for tribocorrosion experiment in pH = 6.5 solution. **b)** Initiation of sliding results in a gradual increase in current observed over a period of sliding and **c)** cessation of sliding results in a gradual decrease in current observed over a period of rest until equilibrium is reached.

not result in a sudden decrease in current, however, rather a gradual decrease of current is observed over a several seconds until pre-sliding current values are reached.

2.4.3.2 Surface Characterization

Figure 33 shows the WLI intensity map image of the wear scar region of a Ti-V sample with a $20 \times$ magnification lens and an image zoom of $2\times$. The oblique plot of the wear scar region, such as the one shown in **Figure 34**, was used with ImageJ software to measure the depth, width, and length of the wear scars. For potentiostatic scans, the depth, width, and length of the wear scars were measured to be 13.7 ± 2.6 , 202 ± 25 , and 1880 ± 61 μm , respectively. For

free potential scans, the depth, width, and length of the wear scars were measured to be 14.0 ± 2.5 , 212 ± 10 , and $1810 \pm 91 \mu\text{m}$, respectively. No significant difference was observed between potentiostatic and free potential scans. **Figure 35** shows the SEM images of the wear scar of the three Ti-V samples with $\times 60$ and $\times 300$ magnification. As the SEM images show, all three electrochemical tests produced similar wear scars with pitting, grooves, and deformation due to compression and shear. The uniformity of the wear scar length, width, and depth suggest that the mechanical components of the tribocorrosion apparatus behave in a consistent manner.

2.4.3.3 Wear and Corrosion Loss

Using the measured length and width of the wear scar and the assumption that the wear scar resembles an ellipsoid, the total wear loss (K_{WC}) is calculated to be 12.4 ± 1.5 and $12.0 \pm 0.9 \mu\text{g}$ for free potential and potentiostatic scans, respectively, with no significant difference. Using **Equation 2.9** and the current values obtained from potentiostatic scan in **Figure 32a**, K_C is calculated to be $5.25 \pm 0.30 \mu\text{g}$. K_W is calculated to be $6.75 \pm 1.0 \mu\text{g}$, and the estimated synergistic weight loss ratio (K_C/K_W) is calculated to be 0.78 ± 0.1 . For the synergistic weight loss ratio between 0.1 and 1.0, a combination of wear and corrosion occurs where wear may play a larger part. This may be explained with the Archard wear equation

$$Q = KWL/H, \quad (2.7)$$

where Q is the total wear volume produced, W is the total normal load, H is the hardness of the softest contacting surfaces, K is a constant, and L is the sliding distance. As per Archard's equation, the weight loss is inversely proportional to the hardness; Ti-V is observed to be a soft

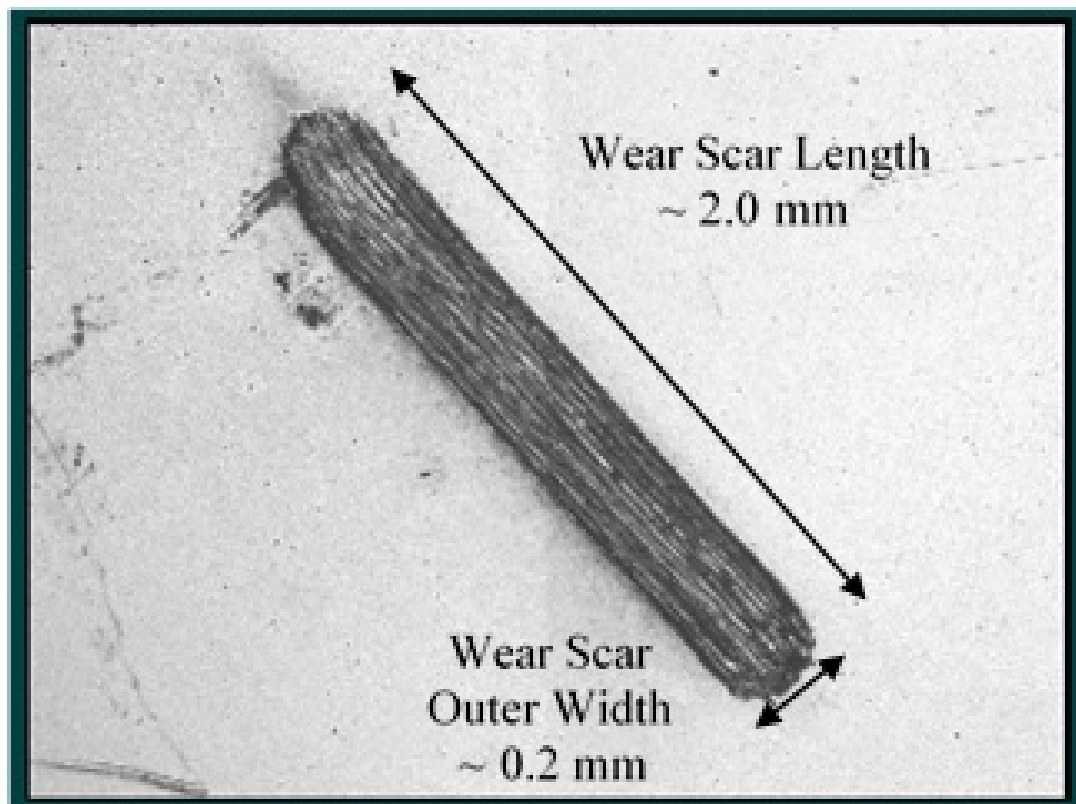


Figure 33: WLI intensity map image of the wear scar region of a Ti-V sample with a 20 \times magnification lens and an image zoom of 2 \times after tribocorrosion pH = 6.5 solution. Wear scar dimensions were measured as ~ 2.0 mm in length and ~ 0.20 mm in width using ImageJ software.

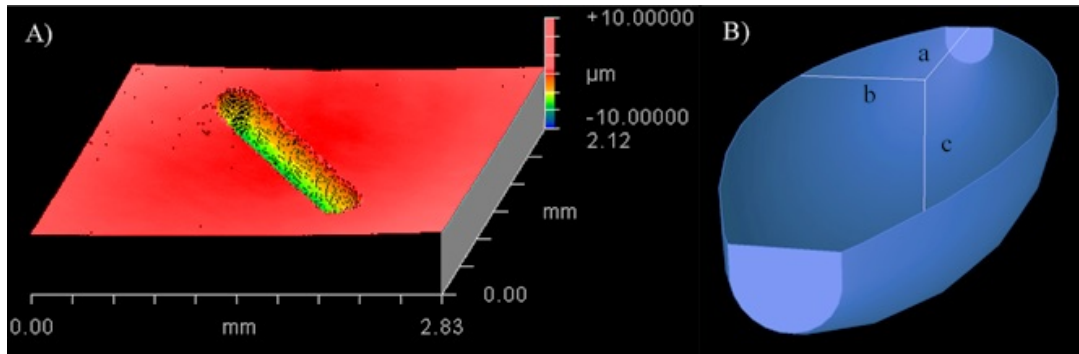


Figure 34: **a)** Wear scar depth profile obtained using WLI of control Ti-V sample after tribocorrosion in pH = 6.5 solution. Roughness values were measured as $R_A = 1.04 \mu\text{m}$, $R_{RMS} = 2.02 \mu\text{m}$, and $PV = 16.6 \mu\text{m}$. **b)** Using the wear scar PV value, length, and width, an ellipsoid volume approximation is used to calculate the volume of material lost due to tribocorrosion.

material and therefore would experience greater weight loss due to tribocorrosion.(252) While exact comparison of weight loss results was not possible with corresponding values reported in the literature, there are some observed similarities. Alves *et al.*, for example, reported wear scar depth of $16.0 \pm 5.66 \mu\text{m}$ for tribocorrosion on CP-Ti (similar density to that of TiV alloy) using a normal force of 2 N, artificial saliva of 37 °C, alumina ball counter-body of 10 mm diameter, 3 mm displacement of 2 Hz and 720 s duration.(253) Licausi *et al.* reported a weight loss of 384 g for tribocorrosion of TiV alloy using alumina ball of diameter 6 mm, a load of 5 N, and artificial saliva of pH 6.0 and 37 °C.(45) However, the path of sliding was circular, longer, and the contact stress was considerably higher, which may explain the greater weight loss.(45) Manhabosco *et al.* reported a wear scar depth of almost 30 μm under tribocorrosive conditions using an alumina ball of diameter 5 mm and normal load, sliding frequency, and sliding distance of 4 N, 1 Hz, and 8 mm, respectively, in a phosphate-buffered saline (PBS) solution (37 °C,

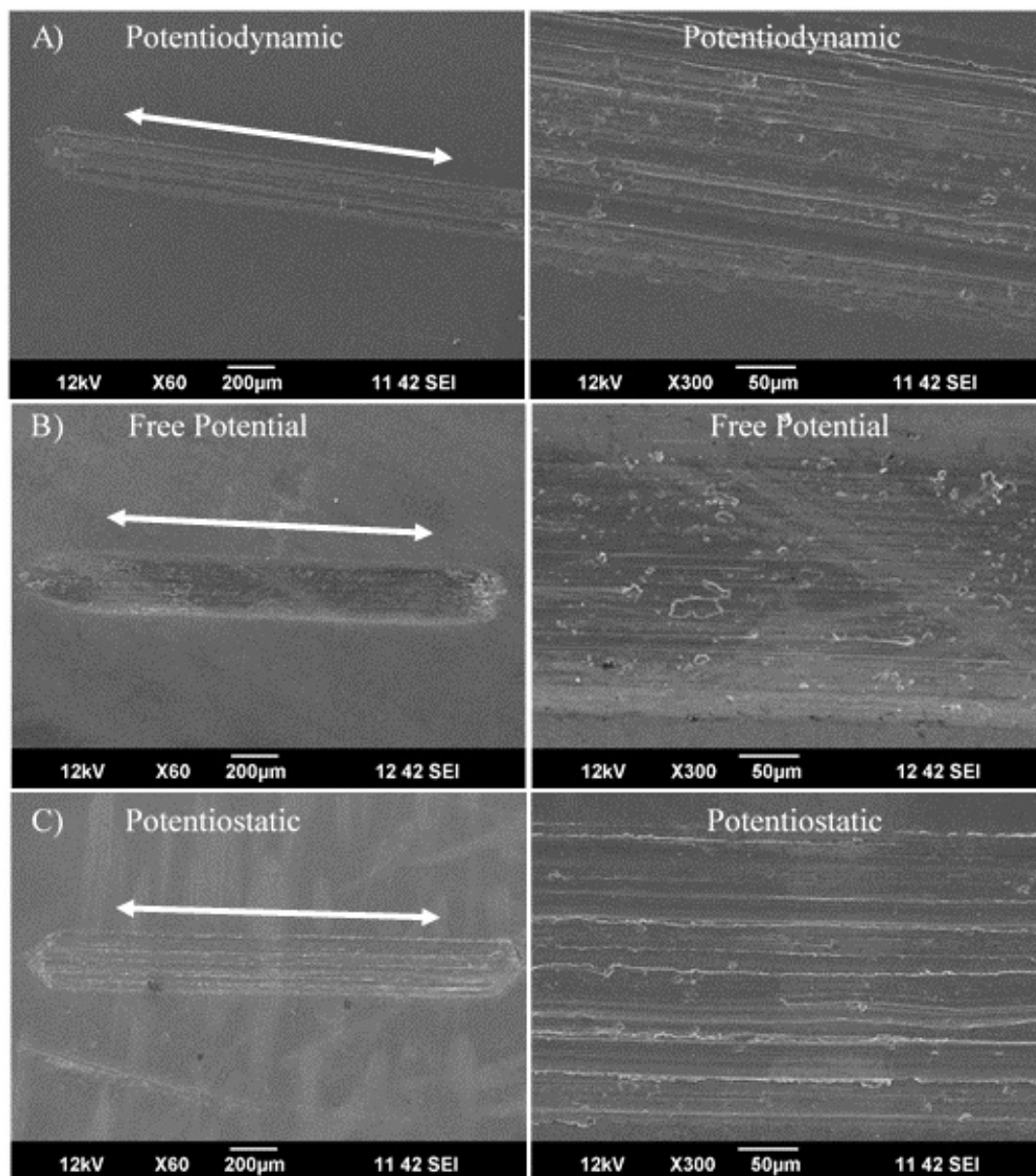


Figure 35: Scanning electron microscopy (SEM) images of wear scars of Ti-V surfaces under a) free potential, b) potentiodynamic, and c) potentiostatic tribocorrosion conditions. Magnifications of the images at $\times 60$ and $\times 300$ and direction of reciprocating alumina pin counter-body are shown.

pH = 7.1).Manhabosco2011 Similar to Licausi *et al.*, the experimental method of Manhabosco *et al.* included greater contact pressure which may explain the deeper scar depth. Runa *et al.* reported a wear loss of $13.6 \pm 3.25 \mu\text{g}$ for tribocorrosion using an alumina ball of diameter 10 mm and normal load of 1 N and sliding distance of 2 mm and 1 Hz in a PBS solution (37 °C, pH = 7.5).(254) Due to similar contact area, wear scar length, and load, Runa *et al.* had similar results to those detailed in this study.(254)

2.4.4 Conclusion

This work demonstrates the feasibility of designing, developing, and building a compact and inexpensive tribocorrosion system. A pilot study was conducted to investigate the tribocorrosion behavior in artificial saliva and a preliminary study involving cell media in an incubator. The construction of a tribocorrosion system requires a detailed examination of existing systems and this study offers an analysis of the needs obtained from literature. The results of the tribocorrosion study of the Ti-V alloy validated the system when compared to the tribocorrosion behavior reported in literature. Using WLI data and Faradays Law, it is observed that the overall trend of the Ti-V alloy is toward depassivation of the surface due to tribocorrosion with wear as the leading component. The use of the system can now be expanded to include fretting and sliding investigations of experimental surface modifications of Ti-V alloy and other metals in dental and orthopedic environments. In addition, the system proves to be suitable for tribocorrosion studies in an incubator to investigate the effects of cells on implant surfaces. Finally, a few additional changes are suggested to improve the design and development of a versatile tribocorrosion apparatus.

2.5 Tribocorrosion Testing of Thermally-Oxidized Ti-V Surfaces

2.5.1 Introduction

Discovered in 1790 and produced in commercial quantities since 1936, titanium has been used for a variety of purposes, including aviation and biomedical implants.(4) While commercially pure titanium consists of α -phase (hexagonal closed packed) and can be converted to β -phase (body centered cubic) at higher temperatures, the most commonly used titanium alloy, Ti-6Al-4V alloy (Ti-V), consists of α - β -phase due to its alloying metals aluminum and vanadium.(4) Due to its superior biocompatibility, mechanical resistance, corrosion resistance, and osseointegration, Ti-V is an excellent orthopedic and dental implant material.(36; 6; 7; 8; 9; 10; 11; 12) Titanium and its alloys are well known for their corrosion resistance due to the rapid oxidation of surface Ti (13; 14; 15), as a result, a protective layer of titanium dioxide (TiO_2) forms on its surface (≤ 10 nm thick) (16). In contrast, titanium and its alloys behave poorly against tribocorrosion, defined as the synergistic combination of oxidation reactions and wear(17). Tribocorrosion has become a major concern in recent years (1; 32; 33; 34) for all implant materials. Notably, the increase in life-expectancy and swelling elderly population highlights the importance of a long-lasting material which rapidly integrates with the host bone, such that the implant recipient requires only one life-time surgery.

For titanium implants, removal of the passive layer as a result of wear allows for the release of metallic debris which are converted to metal ions due to simultaneous corrosion of the exposed bulk metal and debris.(43) Depending on the pH of the environment, passivation and corrosion of exposed titanium is affected. In general, smoking, medication, chronic and systemic diseases

can alter the acidity of saliva and bodily fluids which adversely affects tribocorrosion of implants.(13; 14; 44) While extreme failures may be rare, weight bearing knee and hip implants, for example, have experienced long term revision rates of 12 %(35) and 17 %(38), respectively, mainly caused by aseptic loosening due to the chronic inflammatory response to tribocorrosion debris.(42) For Ti-V alloy, the debris is in the form of Ti, V, and Al particles that act as third-body wear particles and increase material loss during wear.(45; 46) In addition, Ti, Al, and V ions are known to negatively affect osseointegration(45; 46; 47; 48), cause bone diseases(10), and be cytotoxic, respectively, if present at excessive levels (45; 46; 47; 48).

Increasingly, the effect of anodic oxidation, deposition, thermal oxidation (TO) treatments have been studied for the purpose of improving cell response (osseointegration) and tribocorrosion resistance for biological and mechanical purposes.(255; 104; 256) Tribocorrosion resistance due to TO-treatment has not been explored satisfactorily and even discounted due to the scaling of TiO_2 due to high temperature treatment.(68; 65) For example, many reported studies investigated thermal treatment at only one high temperature and a single lengthy time duration and compared to an untreated surface and/or another surface modification treatment.(257; 258) Lower temperatures which can bring a compromise between oxide thickness and integrity have not been satisfactorily studied.(63) Previously it has been shown that higher hardness due to film deposition can improve wear properties(259; 260), however, delamination can occur for thicker films.(63; 64) Thermal oxidation has even been used to improve ceramic particulate-reinforced surface oxides, however, it should be noted that the counter surface was damaged which is equally harmful.(261) In another study, commercially pure titanium (CP-Ti) samples

were subjected to TO-treatment at 650 °C for 14 h and 850 °C for 6 h but the main focus of the study was cooling conditions such as furnace, air, and water cooling.(65) In yet another study, thermal oxidation at 700 °C for 4 hours produced an increase in E_{CORR} (more positive, nobler) and decrease in I_{CORR} and I_{PASS} values, indicating improvement in corrosion potential, corrosion rate, and passivation current, respectively.(260) However, thermal oxidation was conducted with water vapor, not air, and tribocorrosion results show that mass loss decreased by only 47 %. Similar improvements in electrochemical properties have been reported for a surface thermally treated but only after addition of palladium.(68; 260) Many of the reported studies were for commercially pure titanium, and not the more commonly used titanium alloy. The effects of TO-treatment are time and temperature dependent and a study with greater variance in treatment parameters is needed to achieve a better understanding of the produced oxide. TO-treatment increases diffusion of oxygen into the bulk titanium to form and thicken the oxide layer and alter its crystalline structure.(65; 66) In this study, the effect of crystalline structure and oxide thickness on tribocorrosion resistance is investigated in artificial saliva at pH 3.0 (acidic) and pH 6.5 (control) on Ti-V samples TO-treated at temperatures of 200, 400, and 700 °C for 1 and 6 h durations. As a benefit, the increase in roughness and increased surface energy⁴¹ due to the TO-treatment improves surface chemical processes which promotes platelet adhesion and may accelerates the formation of fibrin mesh over the implant surface, resulting in proper implant-biological integration.(67)

Element	Ti	Al	V	Iron	Carbon	Other
wt. %	88.18-90.7	5.50-6.75	3.5-4.5	0.30 max	0.08	0.0-0.268

TABLE XI: Elemental composition of Ti-V alloy (McMaster-Carr)

2.5.2 Materials and Methods

As discussed in the previous section, a custom-built apparatus was validated with an investigation of the tribocorrosion behavior of untreated Ti-V disks in artificial saliva (pH=6.5, $T = 37\text{ }^{\circ}\text{C}$) and compared with literature.(1) For the present study, potentiodynamic (PD), free-potential (FP), and potentiostatic (PS) analyses were used for electrochemical characterization of TO-treated Ti-V disks. In addition, electrochemical impedance spectroscopy (EIS) and Fourier transform infrared (FTIR) spectroscopy was conducted after TO-treatment to get an idea of the oxide structure. White light interferometry was used to analyze wear scars on the Ti-V disks. 63 Ti-V disks were cut and polished from Ti-V rods (McMaster-Carr, Elmhurst, IL, USA). The chemical composition of Ti-V alloy is given in **Table XI** (McMaster-Carr).

A smooth surface ($R_A = 10 \pm 2\text{ nm}$) was achieved by a series of abrasive pads and polishing lubricants. Briefly, polishing was carried out by i) wet-grinding using abrasive pads (# 200, 320, 400, 600, and 800; Carbimet 2, Buehler, Lake Bluff, IL, USA), ii) polishing with a polishing cloth (TexMet, Buehler, Lake Bluff, IL, USA), diamond paste (MetaDi 9-micron, Buehler, Lake Bluff, IL, USA), and lubricant (MetaDi Fluid, Buehler, Lake Bluff, IL, USA), and iii) fine-polishing with a separate polishing cloth (Chemomet I, Buehler, Lake Bluff, IL, USA) with colloidal silica polishing suspension (MasterMed, Buehler, Lake Bluff, IL, USA). Polished

Artificial Saliva Component		Concentration
Potassium chloride	KCl	0.4 g/L
Sodium chloride	NaCl	0.4 g/L
Calcium chloride anhydrous	CaCl ₂ ·2H ₂ O	0.9 g/L
Urea	CO(NH ₂) ₂	1.0 g/L
Monosodium phosphate anhydrous (buffer component)	NaH ₂ PO ₄ ·2H ₂ O	0.7 g/L
Sodium sulfide anhydrous (buffer component)	Na ₂ S·9H ₂ O	0.005 g/L
For controlling pH	NaOH	Add as needed

TABLE XII: Elemental composition of TiV alloy (McMaster-Carr)

samples were ultrasonically cleaned for 10 min in 70 % isopropanol (Sigma Aldrich, St. Louis, MO, USA) and 10 min in deionized (DI) water (18.2 MΩ-cm, Barnstead NANOPure, Lake Balboa, California, USA)) and finally dried with N₂ gas (Grade 4.8, 99.998 %, Progressive Industries, Inc., Chicago, IL, USA). Polished samples were placed inside a Lindberg furnace (S# 54032) for TO-treatments; a κ -type thermocouple was placed at the center of the furnace quartz tube (35 cm from opening) and connected to a temperature controller (JLD-612) to maintain working temperatures. Artificial saliva (120 ml) of pH 3.0 and 6.5 were achieved by adding HCl and NaOH, respectively, as needed. **Table XII** contains the composition of artificial saliva (AS) as suggested by Liu *et al.* to imitate normal oral conditions.(235)

To mimic daily mastication, a normal force of 1.7 N (Hertzian contact pressure of 24 MPa, contact area of 0.071 mm²), and a 1 Hz reciprocal motion for 1800 cycles.(236; 237; 238) An alumina pin was used as the counter-body and a Gamry potentiostat (G300, Gamry Inc.,

Warminster, PA, USA) with a three electrode configuration (American Society for Testing of Materials (ASTM) guidelines (G61 and G31-72)) was used to conduct standard tribocorrosion tests . A saturated calomel electrode (SCE) was used as the Reference Electrode (RE), graphite rod as the Counter Electrode (CE), and the exposed surface (1.77 cm^2) of the Ti-6Al-4V disks as the Working Electrode (WE). The temperature of the test solution was maintained at $37 \pm 1 \text{ }^\circ\text{C}$. The standard protocol used for the tests consists of an initial stabilization period, a sliding period and a final stabilization.(239; 240; 241; 242) A white-light-interferometry (WLI) microscope (Zygo New View 6300, Zygo Corporation, Middlefield, CT, USA) and ImageJ software (NIH, Bethesda, MD, USA) were used to analyze the depth, width, and length of the wear scars of the Ti-V surface after tribocorrosion. As described by Mathew et al. and Butt et al., a simple model was used to separate the total wear loss due to corrosion and wear. Briefly, Equations 1-3 were used for the calculations.(241; 243; 209; 244; 244; 219; 218)

$$K_{WC} = (2/3)\pi abcD = K_W + K_C, \quad (2.8)$$

where K_{WC} is the total mass loss due to wear and corrosion (tribocorrosion) and is approximated to be equivalent to half of an ellipsoid with axis a , b , and c , and D is the density of the material, K_W is the mass loss due to sliding wear, and K_C is the mass loss due to corrosion. It is assumed that corrosion outside of the wear track is negligible and therefore not considered for calculation of K_C .(243; 210; 222; 211) The weight loss due to corrosion can be estimated by using Faradays Law:

$$K_C = Q/ZF \quad (2.9)$$

$$K_C = Mit/ZF, \quad (2.10)$$

where Q is the charge passed, F is the Faradays constant (96,500 C* mol^{-1}), Z is the number of electrons involved in the corrosion process (assumed to be 2), I is the total current, t is the total exposure time, and M is the atomic mass of the material or equivalent weight. Based on these calculations, relative contributions of corrosion and wear to the wear scar can be estimated by Equation 4.(245; 246)

$$\text{Synergistic ratio} = K_C/K_W, \quad (2.11)$$

Where the ratio determines whether the weight loss is dominated by wear, corrosion, or due to a combination of wear and corrosion: $K_C/K_W \leq 0.1$ for wear dominated, $K_C/K_W > 10.0$ for corrosion dominated, $0.1 \leq K_C/K_W \leq 1.0$ for wear as main component, and $1.0 \leq K_C/K_W \leq 10.0$ for corrosion as main component.(245; 246)

Chemical composition and crystallinity of TO-treated sample surfaces was studied using a diffuse reflectance Fourier transform infrared (FTIR) spectroscopy (Nicolet, Madison, WI, USA) with a deuterated triglycine sulfate (DTGS) KBr detector and an energy dispersive x-ray spectroscopy (EDS) attachment to the JEOL JSM-6320F FESEM. For FTIR spectroscopy, a smooth-polished as-is Ti-V sample was used as a background for all scans, one hour purging time and a 2 cm^{-1} resolution was used over the range of $4000\text{-}400 \text{ cm}^{-1}$. FTIR spectra

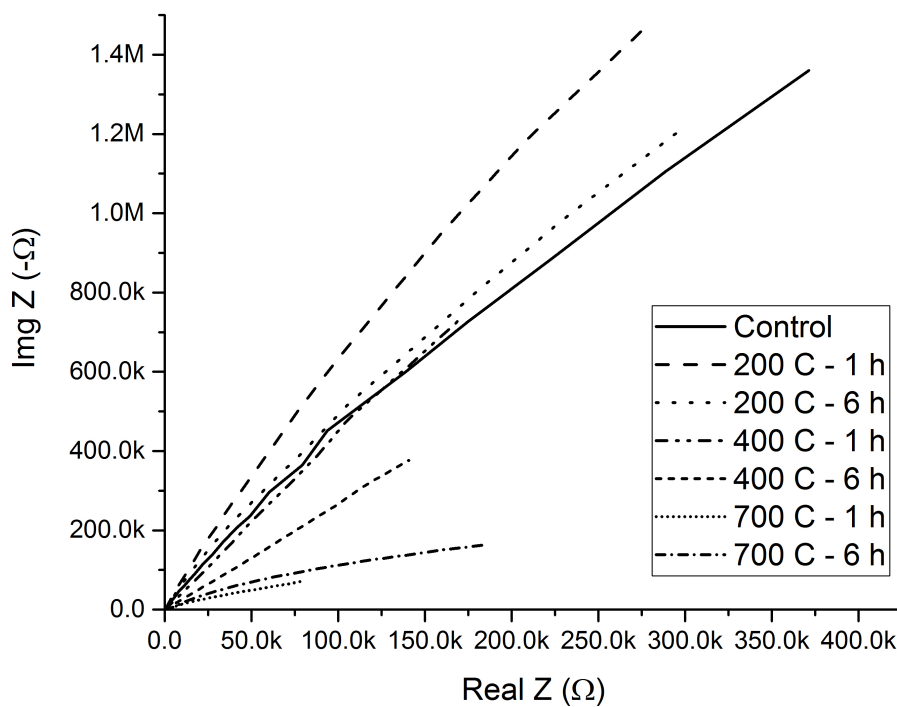


Figure 36: Nyquist plots derived from electrochemical impedance spectroscopy of thermally oxidized (TO) titanium alloy. Real Z vs. imaginary Z graphs suggest that the oxides have higher constant phase element values, which is indicative of a porous heterogeneous oxide, or a thick crystalline oxide.

were analyzed with linear background and deconvoluted using Gaussian-Lorentian peak shape function with a spectral peak-fitting software.

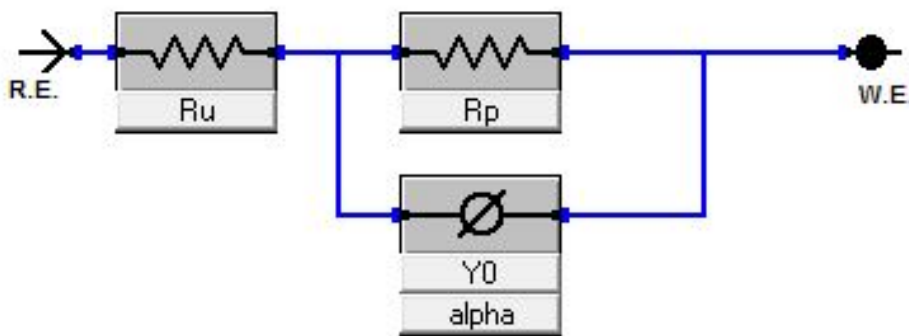


Figure 37: Fitting of Nyquist plots suggest that samples TO-treated at temperatures ≤ 400 °C (≤ 6 h) produce thin oxides which can be modeled after the “Modified Randle’s circuit.” The circuit includes a resistive element for the solution at the surface and an oxide composed of a resistor and constant phase element in parallel, indicating that the whole oxide behaves as a resistor and there are exchanges of charges at the surface.

2.5.3 Results

2.5.3.1 Surface Characterization

In **Figure 36**, EIS Nyquist plots of all samples shows that an increase in surface oxide thickness results in a decrease in imaginary impedance, which correlates to an increase in the value of the constant phase element, indicative of an increase in a porous and heterogeneous surface oxide. In addition, to translate the thicker oxide to an equivalent electrical circuit the modified Randle’s circuit (**Figure 37**) was altered into a more complex circuit as shown in **Figure 38**.

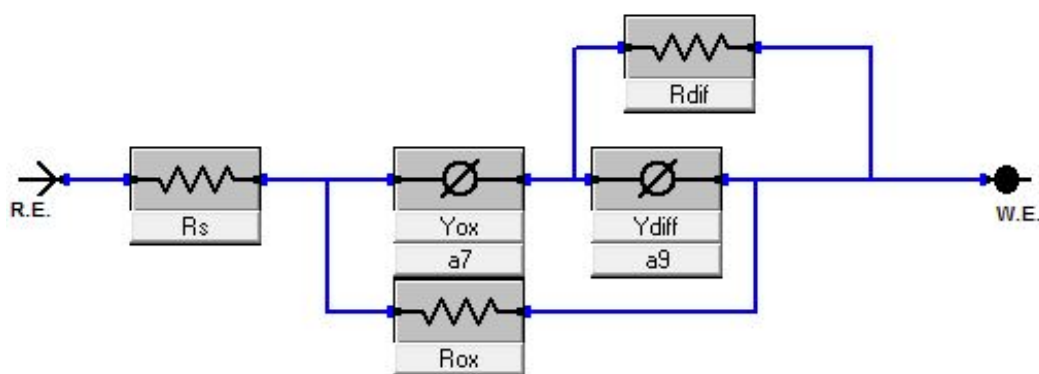


Figure 38: Fitting of Nyquist plots suggest that samples TO-treated at temperatures $400\text{ }^{\circ}\text{C} \leq T \leq 700\text{ }^{\circ}\text{C}$ ($\leq 6\text{ h}$) produce thick oxides which can be modeled after a complex version of the “Modified Randle’s circuit.” The circuit includes a resistive element for the solution at the surface and an oxide composed of two layers, a compact oxide and a oxygen/metal diffusion zone. The circuit indicates that the whole oxide film behaves as a resistor and there are exchanges of charges at the surface, however, within this film, the diffusion zone behaves as a separate entity which also has resistive and charge releasing qualities.

FTIR spectra in **Figure 56**, **Figure 58**, and **Figure 61** and GIXRD spectra (not shown) of TO-treated samples show that 200 °C TO-treated samples have a thin oxide that is of amorphous nature, 400 °C treated surfaces consists of a thicker oxide that is a mixture of anatase and rutile, but mostly anatase TiO_2 , and 700 °C TO-treated surface consists of a thick oxide that is mostly rutile TiO_2 . Various facets of anatase/rutile appear in the spectra at different temperatures, suggesting that some facets of anatase/rutile form at higher temperatures than that of other facets of anatase/rutile. In addition, several titanium peaks are observed decreasing as a function of treatment temperature, suggesting that titanium is oxidized at higher quantities within the volume analyzed by GIXRD (not shown).

For FTIR, due to 1) the irregular surface roughness and 2) the various components of the alloy and their effect on surrounding bond stretch/vibrations, peak positions may have blue-shifted (lower cm^{-1}) or red-shifted (higher cm^{-1}) compared to absorption bands reported in literature. The following peaks are observed in all FTIR spectra due to the residual air in the FTIR purging chamber. Minor peaks between 2320 - 2380 cm^{-1} are associated with gas phase CO_2 (158) and the noise seen between 3400-4000 cm^{-1} and between 1200 - 2000 cm^{-1} are associated with the O-H bond stretch and vibration intensities of absorbed/adsorbed and dissociated H_2O (153; 202; 150; 157; 149; 155; 156; 203), CO_2 (158), CO_3^{-2} (158; 204), or carboxyl groups (COO^-) from interaction of TiO_2 with CO_2 or any surface carbon contamination(158; 204). As seen in **Figure 56**, **Figure 58**, and **Figure 61**, TO-treatment induces crystallinity and thicker oxides that in general causes a downshift in the metal-oxide peaks.

The FTIR spectra of 200 °C TO-treated sample, is nearly flat with some small peaks. Like-

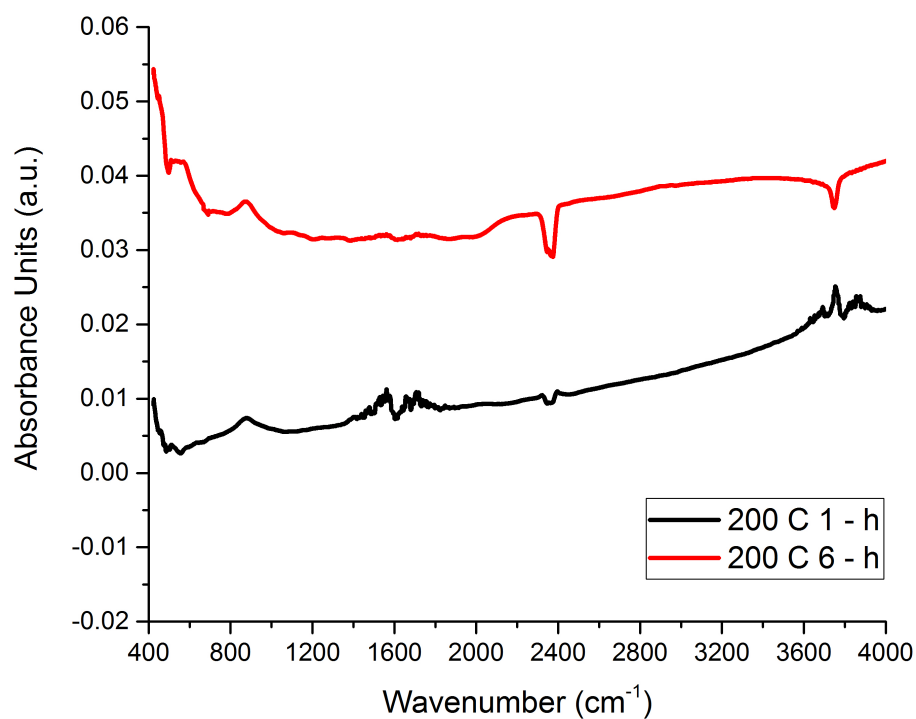


Figure 39: Absorbance Fourier transform infrared (FTIR) spectra of 200 °C TO-treated samples. Peaks are observed for changes in chemical composition in the metal-oxide region (400-1200 cm⁻¹) as a function of treatment time. Absorbance FTIR spectroscopy was conducted with a diffuse reflectance accessory, a deuterated triglycine sulfate (DTGS) KBr detector, and purging time of 1 h.

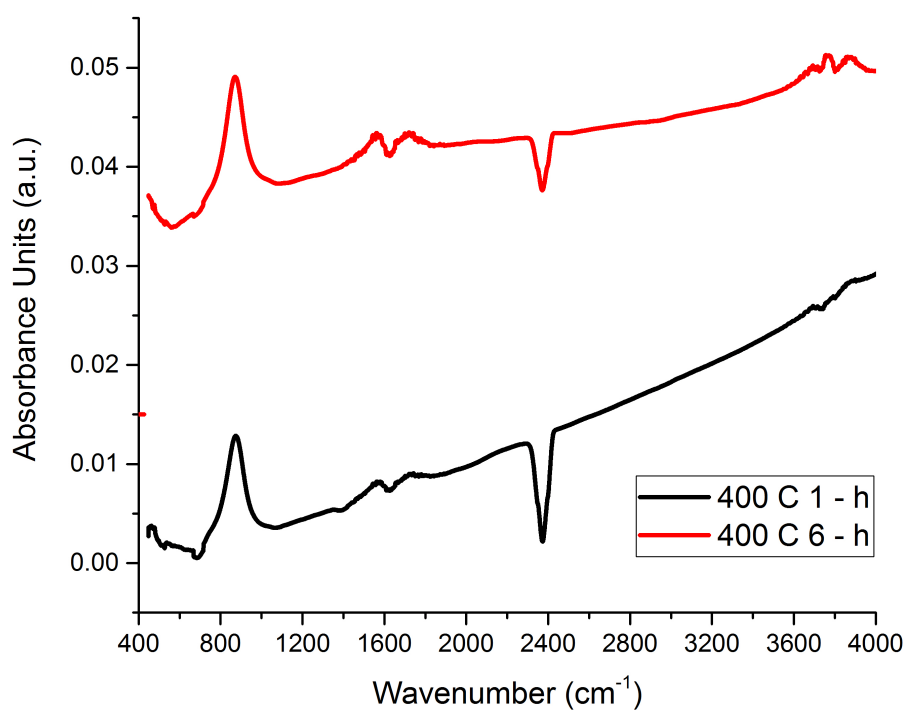


Figure 40: Absorbance Fourier transform infrared (FTIR) spectra of 400 °C TO-treated samples. Peaks are observed for changes in chemical composition in the metal-oxide region (400-1200 cm⁻¹) as a function of treatment time. Absorbance FTIR spectroscopy was conducted with a diffuse reflectance accessory, a deuterated triglycine sulfate (DTGS) KBr detector, and purging time of 1 h.

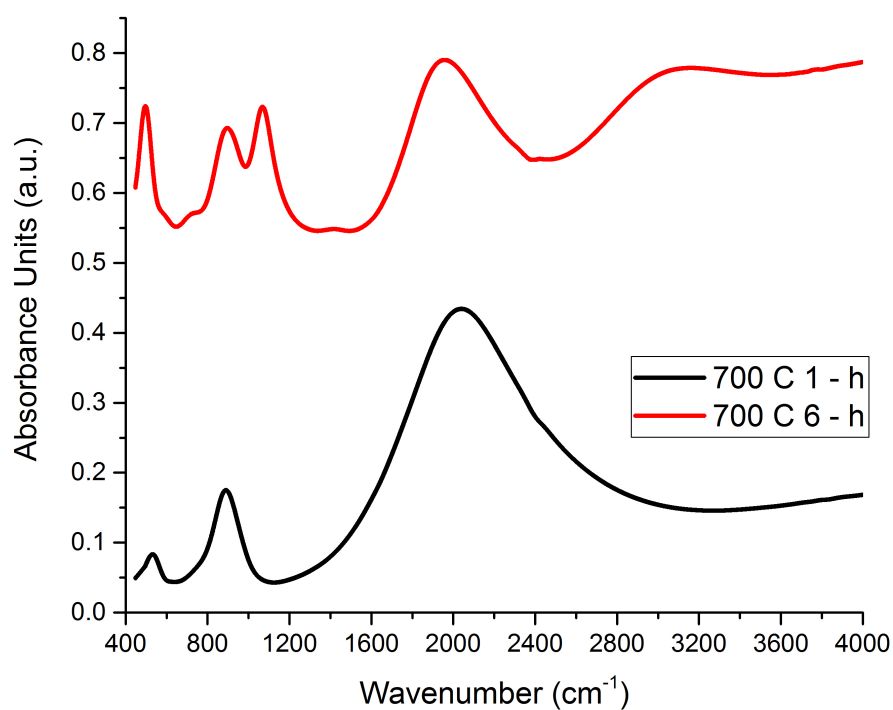


Figure 41: Absorbance Fourier transform infrared (FTIR) spectra of 700 °C TO-treated samples. Peaks are observed for changes in chemical composition in the metal-oxide region (400-1200 cm⁻¹) as a function of treatment time. Absorbance FTIR spectroscopy was conducted with a diffuse reflectance accessory, a deuterated triglycine sulfate (DTGS) KBr detector, and purging time of 1 h.

wise, increased intensity is observed in the metal-oxide region ($1200\text{--}400\text{ cm}^{-1}$) with increased temperature of treatment, with the greatest change seen in the $700\text{ }^{\circ}\text{C}$ TO-treated sample. In addition, anatase TiO_2 is observed to increase and decrease as temperature of treatment is raised from $300\text{ }^{\circ}\text{C}$ and disappear by $600\text{ }^{\circ}\text{C}$ (**Figure 42**). At the same time, rutile TiO_2 is observed to increase at treatment temperatures $\geq 400\text{ }^{\circ}\text{C}$ (**Figure 42**). It is noted that not all peaks for anatase or rutile are observed where these TiO_2 structures are present, which leads to the suggestion that certain temperature of treatments produce different facets of the same TiO_2 structure. Finally, a significant increase in alumina and byproducts of reactions between rutile and surface CO_2 , carbon contamination, and H_2O are observed in the spectra of $700\text{ }^{\circ}\text{C}$ TO-treated samples. However, the main area of interest is the surface oxide region between $400\text{--}1200\text{ cm}^{-1}$ where significant changes occur as a result of thermal oxidation.

2.5.3.2 Electrochemical Characterization

Figure 43 and **Figure 44** show the potentiodynamic scans, clearly indicating that higher temperature treated samples show nobler E_{CORR} , lower I_{CORR} , and lower I_{PASS} values as compared to control and low temperature treated samples. In particular samples TO-treated with $700\text{ }^{\circ}\text{C}$ 1 and 6 h were the two most improved sample groups in either pH. Specifically, E_{CORR} increased from -0.8 V to between -0.3 and -0.4 V (nobler), I_{CORR} decreased from μA 's to the order of nA 's and I_{PASS} decreased from 10's of μA 's to single digit μA 's. The improved values correlate with lower corrosion potential, lower corrosion rate, and lower passivation current, respectively. Interestingly, $400\text{ }^{\circ}\text{C}$ 6 h TO-treated samples in pH 3.0 behaved even

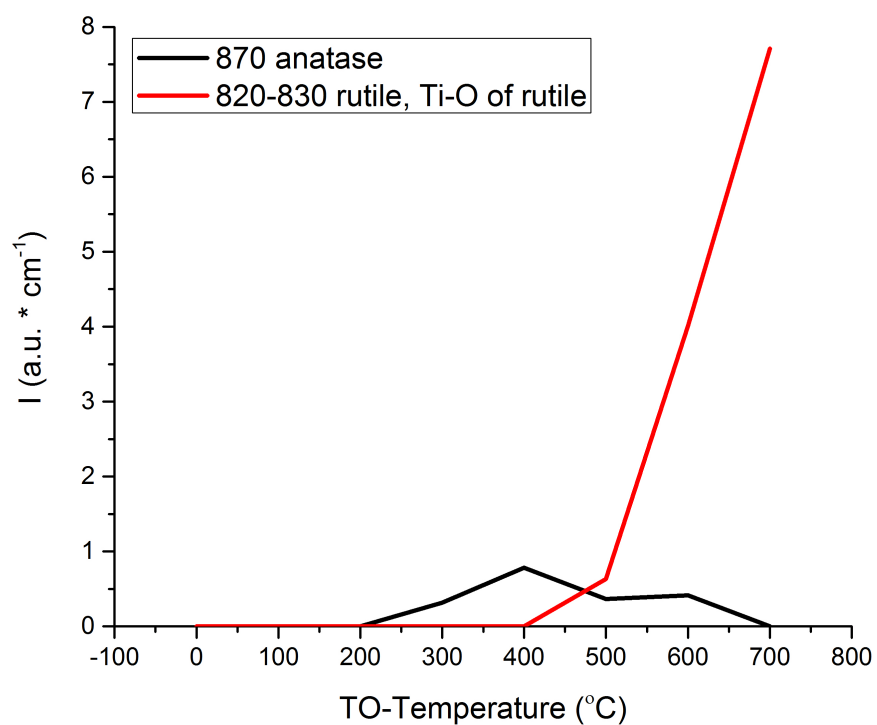


Figure 42: Anatase and rutile TiO_2 plot vs. TO-treatment temperature. Absorbance FTIR spectra have shown that anatase TiO_2 is present on samples surfaces TO-treated between 300 and 600 $^{\circ}\text{C}$, reaching their peak for samples TO-treated at 400 $^{\circ}\text{C}$. Rutile TiO_2 is present on samples TO-treated at temperatures ≥ 400 $^{\circ}\text{C}$.

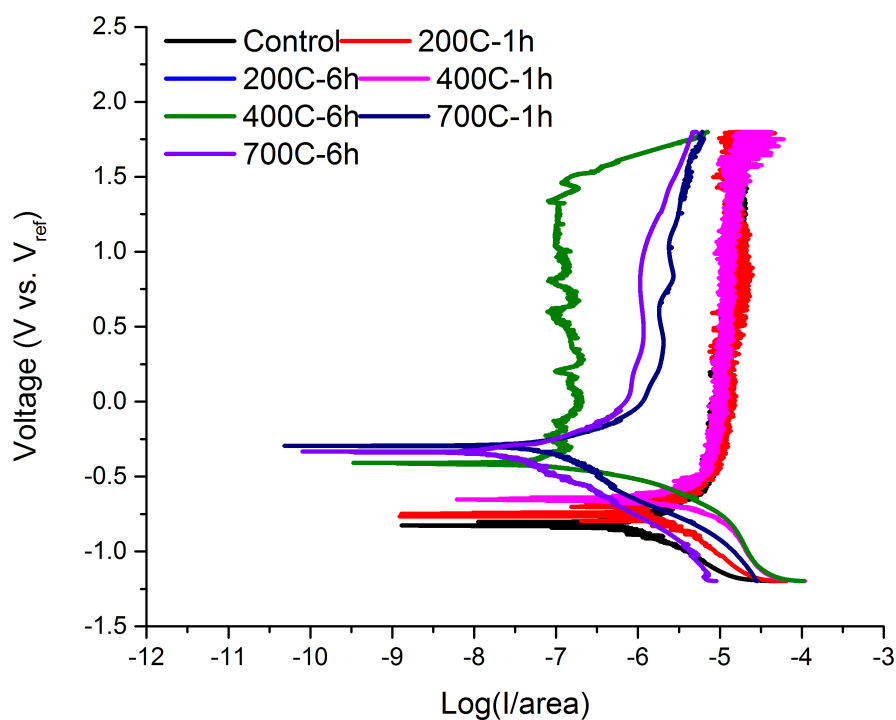


Figure 43: Potentiodynamic scans of TO-treated titanium alloy samples in pH 3.0 artificial saliva solution. High temperature treated samples have superior corrosion potential, corrosion rate, and passivation current readings. Interestingly, 400 °C 6h thermally oxidized samples are observed to have best tribocorrosion resistive properties.

better, where changes in E_{CORR} and I_{CORR} were similar to the 700 °C TO-treated samples, but I_{PASS} decreased from 10's of μA 's to the order of nA's.

Figure 45 and **Figure 46** show the free potential scans, which corroborate with PD scans indicating that that 700 °C temperature TO-treated samples resisted tribocorrosion in both pH levels, and 400 °C 6 h TO-treated sample behaved similarly, but only in pH 3.0. For

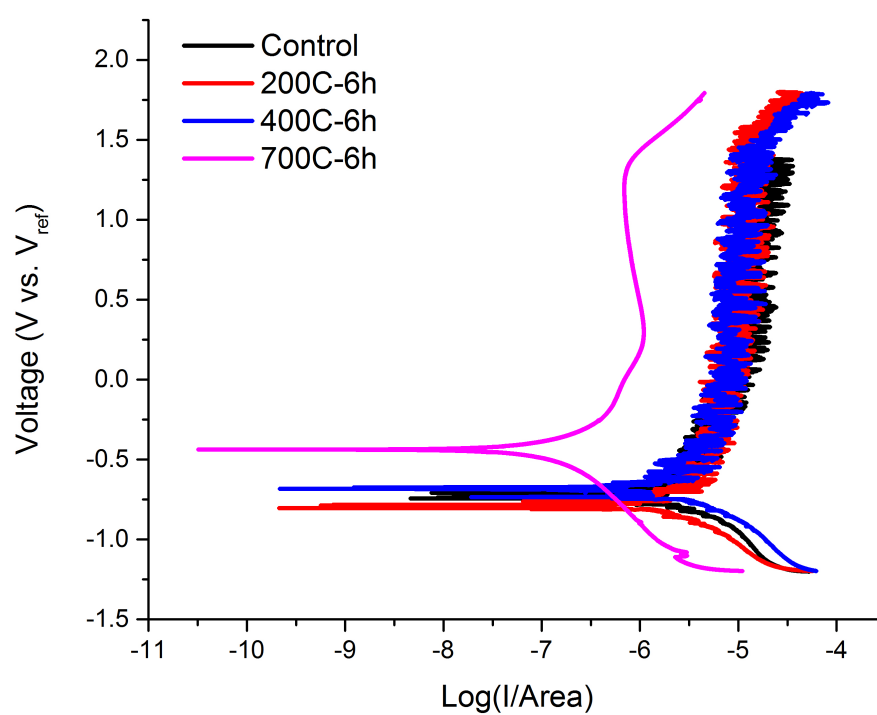


Figure 44: Potentiodynamic scans of TO-treated titanium alloy samples in pH 6.5 artificial saliva solution. High temperature treated samples have superior corrosion potential, corrosion rate, and passivation current readings.

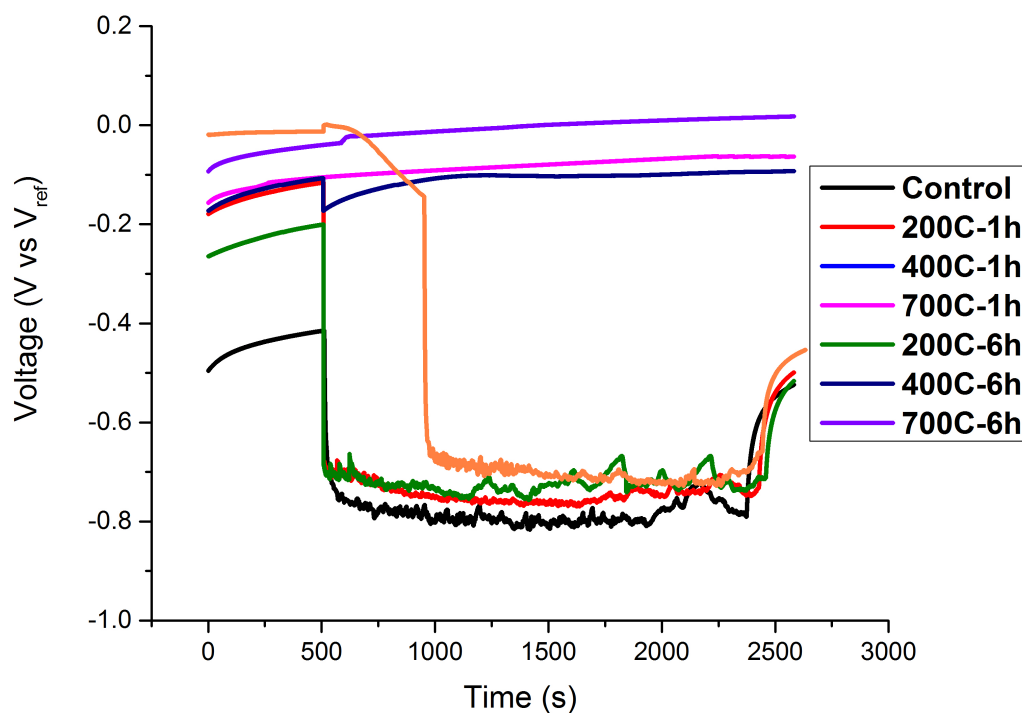


Figure 45: Evolution of potential curves of TO-treated titanium alloy samples for tribocorrosion experiment in pH 3.0 artificial saliva solution. Initiation of sliding results in an increase in cathodic voltage and cessation of sliding results in a decrease in cathodic voltage. High temperature treated samples have delayed or reduced potential drops.

all improved samples in either pH, potential drop during sliding improved from between -0.7 and -0.8 V to between 0 and -0.2 V. for In addition, 400 °C 1 h TO-treated sample resisted tribocorrosion for the early portion of the test, where potential drop was linear between 0 and -0.2 V in pH 3.0 but soon succumbed to tribocorrosion forces and potential drop increased to around -0.7 V.

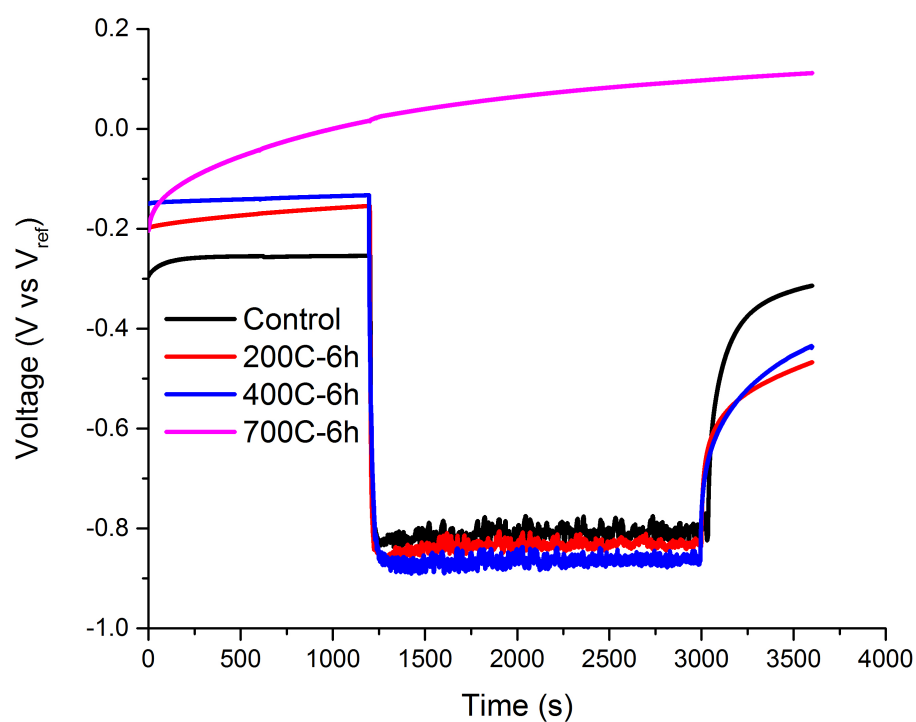


Figure 46: Evolution of potential curves of a TO-treated titanium alloy samples for tribocorrosion experiment in pH 6.5 artificial saliva solution. Initiation of sliding results in an increase in cathodic voltage and cessation of sliding results in a decrease in cathodic voltage. High temperature treated samples have reduced potential drops.

Figure 47 and **Figure 48** show the potentiostatic scans, which also substantiate observations made in PD and FP scans, indicating that 700 °C 1 and 6 h TO-treatment improve tribocorrosion resistance in AS of both pH and 400 °C 6 h TO-treatment. It is also observed that current does not initially rise for 400 °C 1 h TO-treated samples, however as tribocorrosion test progresses, the oxide film is penetrated and corrosion of the surface begins. with the exception of 700 °C 1 and 6 h TO-treated samples in both pH and 400 °C 6 h TO-treated in pH 3.0, current increased to 10's of μA 's during sliding.

2.5.3.3 Wear Scar Analysis

Total mass loss, mass loss due to corrosion, and mass loss due to wear is given in **Table XIII** and **Figure 49**.

As indicated in **Table XIII** and **Figure 49**, total mass loss is significantly reduced for samples treated at 700 °C as compared to control samples in both pH 3.0 and 6.5. Specifically, a 93 % and 95 % decrease in mass loss is observed for 700 °C 1 h TO-treated samples in pH 3.0 and 6.5, respectively and 79 % and 70 % decrease in mass loss is observed for 700 °C 6 h TO-treated samples in pH 3.0 and 6.5, respectively. No mass loss was observed for 400 °C 6 h TO-treated samples in pH 3.0. It is also observed that the synergistic weight loss ratio for these samples is calculated to be “0,” indicating a wear dominated tribocorrosion. For all other samples the ratio is calculated to $0.1 \leq K_C/K_W \leq 1.0$ where both corrosion and wear are active components of mass loss. All other samples were observed to have mass loss similar to control samples.

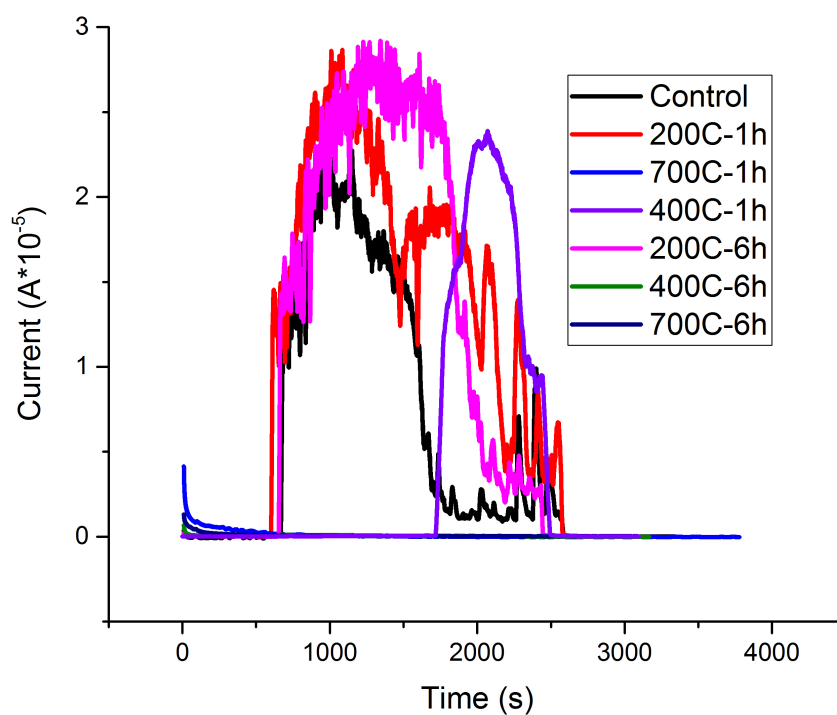


Figure 47: Potentiostatic scans of TO-treated titanium alloy samples for tribocorrosion experiment in pH 3.0 artificial saliva solution. Initiation of sliding results in an increase in current observed over a period of sliding and cessation of sliding results in a gradual decrease in current observed over a period of rest until equilibrium is reached. High temperature treated samples have reduced or no current changes..

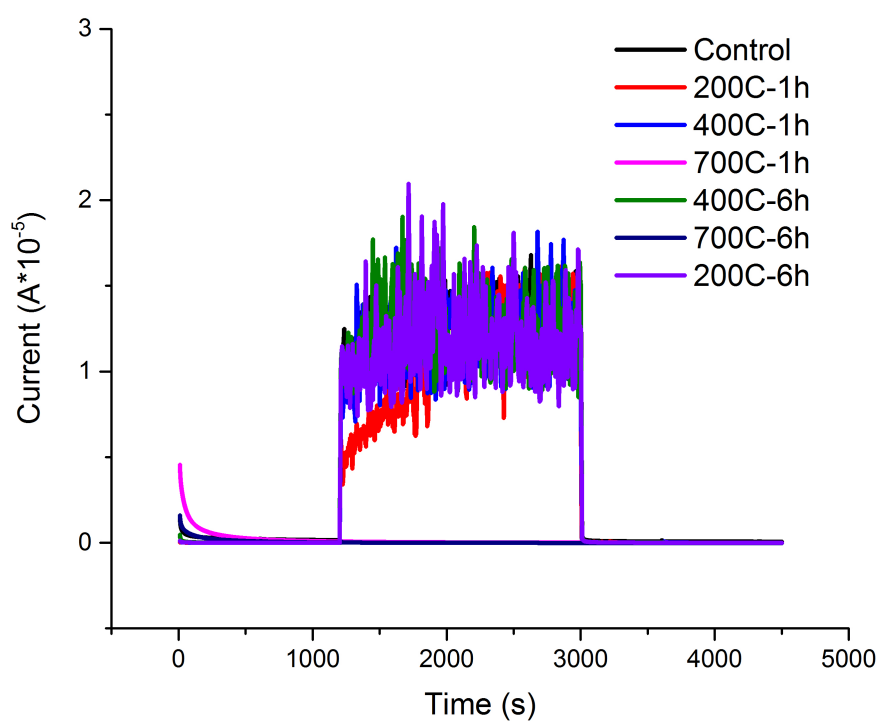


Figure 48: Potentiostatic scans of TO-treated titanium alloy samples for tribocorrosion experiment in pH 3.0 artificial saliva solution. Initiation of sliding results in an increase in current observed over a period of sliding and cessation of sliding results in a gradual decrease in current observed over a period of rest until equilibrium is reached. High temperature treated samples have reduced or no current changes.

Tribocorrosion Mass loss in Artificial Saliva pH 3.0 (in grams)							
Sample	Control	200 °C- 1h	200 °C- 6h	400 °C- 1h	400 °C- 6h	700 °C- 1h	700 °C- 6h
Total		7.89E-06	9.37E-06	1.18E-05	1.37E-05	0.00E+00	8.10E-07
		3.13E-06	3.25E-06	4.68E-06	7.13E-06	0.00E+00	7.20E-07
Corrosion		4.57E-06	6.88E-06	7.34E-06	5.78E-06	2.68E-08	0.00E+00
		1.42E-06	1.40E-06	2.39E-06	3.10E-06	1.07E-08	0.00E+00
Wear		3.32E-06	2.49E-06	4.44E-06	7.92E-06	0.00E+00	8.10E-07
		3.44E-06	3.54E-06	5.26E-06	7.77E-06	1.07E-08	7.20E-07
Kc/Kw		1.38	2.76	1.65	0.73	∞	0.00
Tribocorrosion Mass loss in Artificial Saliva pH 6.5 (in grams)							
Sample	Control	200 °C- 1h	200 °C- 6h	400 °C- 1h	400 °C- 6h	700 °C- 1h	700 °C- 6h
Total		1.20E-05	1.28E-05	1.18E-05	1.11E-05	1.16E-05	5.60E-07
		1.11E-06	3.08E-06	2.09E-06	2.68E-06	3.20E-07	4.80E-07
Corrosion		5.25E-06	5.12E-06	5.09E-06	4.69E-06	5.28E-06	0.00E+00
		8.01E-13	1.55E-07	5.36E-08	8.54E-07	1.93E-07	0.00E+00
Wear		6.75E-06	7.72E-06	6.69E-06	6.45E-06	6.33E-06	5.60E-07
		1.11E-06	3.08E-06	2.09E-06	2.81E-06	3.74E-07	4.80E-07
Kc/Kw		0.78	0.66	0.76	0.73	0.84	0.00

TABLE XIII: Total weight loss data as derived from white light interferometry. Total mass loss was calculated based on a ellipsoid volume assumption and it was observed that samples treated at 700 °C in both pH 3.0 and 6.5 environments have the least mass loss.

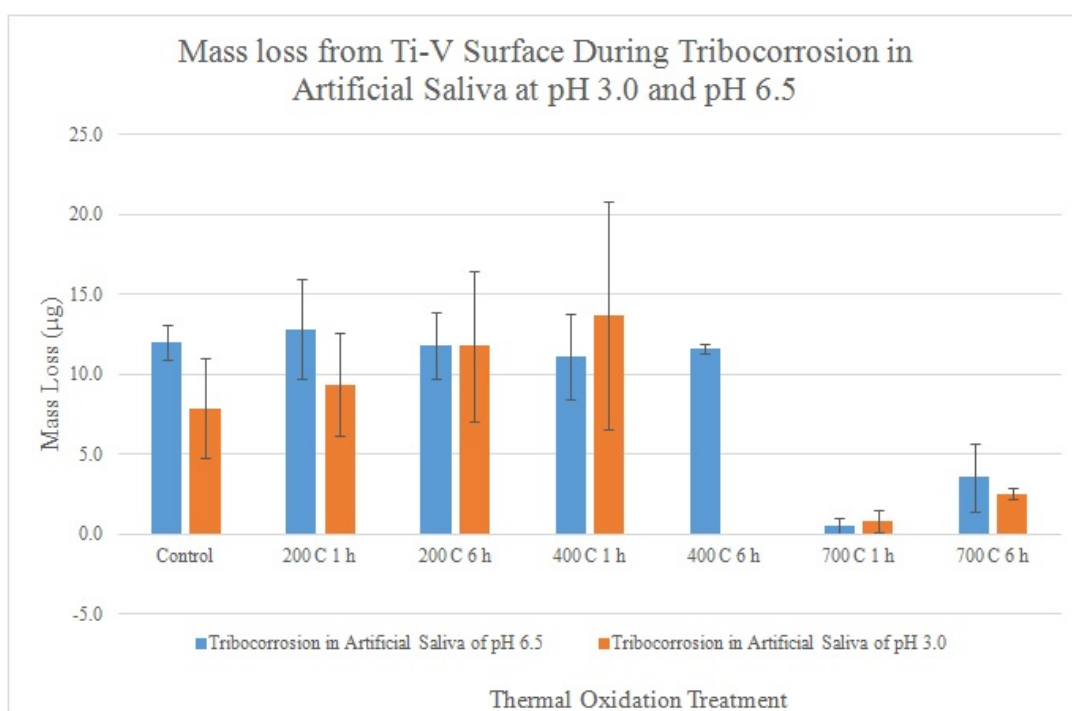


Figure 49: Potentiostatic scans of TO-treated titanium alloy samples for tribocorrosion experiment in pH 3.0 artificial saliva solution. Initiation of sliding results in an increase in current observed over a period of sliding and cessation of sliding results in a gradual decrease in current observed over a period of rest until equilibrium is reached. High temperature treated samples have reduced or no current changes.

2.5.4 Discussion

While titanium alloys are excellent for implants requiring mechanical loading and direct contact with host bone, contact which results in shear produces significant surface wear.(262; 263; 264; 265) Tribocorrosion results of control and 200 °C treated surfaces in both pH 3.0 and 6.5 are typical of this occurrence. The poor tribocorrosion property is namely due to the difference in the mechanical properties of the surface oxide and substrate bulk such as the Young's Modulus which is known to be 230 GPa versus 110 GPa for the oxide and bulk titanium, respectively. For a thin hard oxide film on a relatively ductile substrate, an external force may cause failure of the film as compared to an oxide film and substrate with similar ductility or hardness.(266) As mentioned previously, thermal oxidation produces a thick hard oxide coupled with a diffusion zone which may reduce the plastic deformation of the oxide under an external force.(63; 261) Therefore, oxide-substrate hardness may be similar which may explain the reduced mass loss observed on 700 °C TO-treated surfaces. As reported in literature, a high temperature treatment results in a multi-layered structure containing a titanium dioxide layer, titanium-oxygen diffusion zone, and a bulk titanium substrate.(63; 64) Previously, observed frictional zones correlate well with the oxide layer (lowest friction coefficients(63; 64)), the oxygen diffusion zone (higher friction coefficients), and the substrate (highest friction coefficients).(63) Similarly, deposition of elemental Ti on AISI 316L steel followed by thermally oxidation produced a layered oxide film, much like the oxide film produced from thermal oxidation of titanium alloy.(267) In addition to the surface oxide layer, the film included a diffusion zone and an interfacial layer between Ti and the steel substrate.(267) Similar to results presented in the present study, the

layered oxide improved tribocorrosion resistance. While similar/dissimilar hardness of oxide-substrate structures may explain why control and 200 °C treated samples do poorly and why 700 °C treated samples do well, the phenomena observed for 400 °C treated samples needs further investigation. Specifically, what quality of the anatase oxide produced from 400 °C TO-treatment provides excellent protection in pH 3.0 but very poor protection in pH 6.5. It is reported in literature and previously by this group, that anatase is reactive and rutile is inert.(68; 2) The Pourbaix diagram of titanium (not shown) illustrates the vulnerability of metal to corrosion in various pH and potentials.(4) In addition to areas labeled as "corrosion," "passive," and "immune," there are areas where hydrogen or oxygen are evolved (below and above 0.2 V, respectively). Namely, the diagram indicates that when hydrogen content is increased, as in an acidic environment, the "corrosion" area is reduced to an area between 0 and -1.0 V and pH of up to 5.0, whereas without the increased hydrogen content, the area is between 0 and -1.8 V and pH of up to 8.0. This may indicate that in pH 6.5, the area is under corrosion and a reactive anatase may further exasperate the behavior and weaken the thermally produced oxide. The potentiostatic scans may support this argument as current values are very high, indicating occurrence of corrosive reactions. In contrast, the potentiostatic scans of 400 °C 1 h and 6 h TO-treated surfaces during tribocorrosion in pH 3.0 show that the surface is not corroding. In this case, the surface oxide is only exposed to the counter body wear. The oxide may be too thin for 400 °C 1 h TO-treated samples, however, therefore the oxide-bulk differences in ductility results in tribocorrosion failure, while the oxide of 400 °C 6 h TO-treated samples

is thick enough to withstand the counter body. However further investigation of the 400 °C TO-treatment is needed.

2.5.5 Conclusion

A thick and crystallized TiO₂ layer possesses improved corrosion and wear resistance, biological and mechanical properties. From wear track and electrochemical data, anatase TiO₂ produced from 400 °C 6 h TO-treatment provided the most inert and hardest surface for tribocorrosion resistance in pH 3.0, however such behavior was not observed in pH 6.5. Samples of 700 °C 1 and 6 h TO-treatment provided the best surface in both pH 3.0 and 6.5. In general, lower temperature TO-treatment provided relatively weaker and thinner oxides and higher temperature treatment provided thick, multi-layered, hard oxides. While there are studies which show similar results, many of them involve precursors, low pressure environment, or other gases, while thermal oxidation was conducted in this study with air in a furnace. In addition to improved tribocorrosion properties, changes to titanium surfaces due to thermal oxidation promote chemical and biological processes which improve implant-biological integration.

CITED LITERATURE

1. Butt, A., Lucchiari, N. B., Royhman, D., Runa, M. J., Mathew, M. T., Sukotjo, C., and Takoudis, C. G.: Design, Development, and Testing of a Compact Tribocorrosion Apparatus for Biomedical Applications. Journal of Bio- and Tribo-Corrosion, 1(1):4, December 2014.
2. Butt, A., Hamlekhan, A., Patel, S. B., Royhman, D., Sukotjo, C., Mathew, M. T., Shokuhfar, T., and Takoudis, C.: A Novel Investigation of the Formation of TiO Nanotubes on Thermally Formed Oxide of Ti-6Al-4V. The Journal of oral implantology, March 2014.
3. Patel, S., Butt, A., Tao, Q., Royhman, D., Sukotjo, C., and Takoudis, C.: Novel Functionalization of Ti-V Alloy and Ti-II using Atomic Layer Deposition for Improved Surface Wettability. Colloids and Surfaces B: Biointerfaces, 2013.
4. Wood, D. J.: The Characterization of Particulate Debris Obtained from Failed Orthopedic Implants. Research report, San José State University, 1993.
5. Ogawa, T., Sukotjo, C., and Nishimura, I.: Modulated bone matrix-related gene expression is associated with differences in interfacial strength of different implant surface roughness. Journal of prosthodontics : official journal of the American College of Prosthodontists, 11(4):241–7, December 2002.
6. Adya, N., Alam, M., Ravindranath, T., Mubeen, a., and Saluja, B.: Corrosion in titanium dental implants: literature review. The Journal of Indian Prosthodontic Society, 5(3):126, 2005.
7. Dong, H. and Li, X.: Oxygen boost diffusion for the deep-case hardening of titanium alloys. Materials Science and Engineering: A, 280(2):303–310, March 2000.
8. Rinner, M., Gerlach, J., and Ensinger, W.: Formation of titanium oxide films on titanium and Ti6Al4V by O₂-plasma immersion ion implantation. Surface and Coatings Technology, 132(2-3):111–116, 2000.
9. MacDonald, D. E., Rapuano, B. E., Deo, N., Stranick, M., Somasundaran, P., and Boskey, a. L.: Thermal and chemical modification of titanium-aluminum-vanadium implant

materials: effects on surface properties, glycoprotein adsorption, and MG63 cell attachment. Biomaterials, 25(16):3135–46, July 2004.

10. Minagar, S., Berndt, C. C., Wang, J., Ivanova, E., and Wen, C.: A review of the application of anodization for the fabrication of nanotubes on metal implant surfaces. Acta biomaterialia, 8(8):2875–88, August 2012.
11. Park, J. H., Schwartz, Z., Olivares-Navarrete, R., Boyan, B. D., and Tannenbaum, R.: Enhancement of surface wettability via the modification of microtextured titanium implant surfaces with polyelectrolytes. Langmuir : the ACS journal of surfaces and colloids, 27(10):5976–85, May 2011.
12. Hwa, J., Olivares-navarrete, R., Baier, R. E., Meyer, A. E., Tannenbaum, R., Boyan, B. D., Schwartz, Z., and Park, J. H.: Effect of cleaning and sterilization on titanium implant surface properties and cellular response. Acta biomaterialia, 8(5):1966–75, May 2012.
13. Nikolopoulou, F.: Saliva and dental implants. Implant dentistry, 15(4):372–6, December 2006.
14. Correa, C. B., Pires, J. R., Fernandes-Filho, R. B., Sartori, R., and Vaz, L. G.: Fatigue and fluoride corrosion on Streptococcus mutans adherence to titanium-based implant/component surfaces. Journal of prosthodontics : official journal of the American College of Prosthodontists, 18(5):382–7, July 2009.
15. Joska, L., Fojt, J., Hradilova, M., Hnilica, F., and Cvrcek, L.: Corrosion behaviour of TiN and ZrN in the environment containing fluoride ions. Biomedical materials (Bristol, England), 5(5):054108, October 2010.
16. Huang, H.-H.: Effect of fluoride and albumin concentration on the corrosion behavior of Ti-6Al-4V alloy. Biomaterials, 24(2):275–82, January 2003.
17. Chen, J., Yan, F. Y., Chen, B. B., and Wang, J. Z.: Assessing the tribocorrosion performance of Ti-6Al-4V, 316 stainless steel and Monel K500 alloys in artificial seawater. Materials and Corrosion, 64(5):394–401, May 2013.
18. Elias, C. N., Oshida, Y., Lima, J. H. C., and Muller, C. A.: Relationship between surface properties (roughness, wettability and morphology) of titanium and dental implant removal torque. Journal of the mechanical behavior of biomedical materials, 1(3):234–42, July 2008.

19. Wall, I., Donos, N., Carlqvist, K., Jones, F., and Brett, P.: Modified titanium surfaces promote accelerated osteogenic differentiation of mesenchymal stromal cells in vitro. Bone, 45(1):17–26, July 2009.
20. Miyauchi, Y., Ninomiya, K., Miyamoto, H., Sakamoto, A., Iwasaki, R., Hoshi, H., Miyamoto, K., Hao, W., Yoshida, S., Morioka, H., Chiba, K., Kato, S., Tokuhisa, T., Saitou, M., Toyama, Y., Suda, T., and Miyamoto, T.: The Blimp1-Bcl6 axis is critical to regulate osteoclast differentiation and bone homeostasis. The Journal of experimental medicine, 207(4):751–62, April 2010.
21. Vlacic-Zischke, J., Hamlet, S. M., Friis, T., Tonetti, M. S., and Ivanovski, S.: The influence of surface microroughness and hydrophilicity of titanium on the up-regulation of TGF β /BMP signalling in osteoblasts. Biomaterials, 32(3):665–71, January 2011.
22. Keshmiri, M. and Troczynski, T.: Apatite formation on TiO₂ anatase microspheres. Journal of Non-Crystalline Solids, 324(3):289–294, September 2003.
23. Amin, M., Randeniya, L., Bendavid, a., Martin, P., and Preston, E.: Apatite formation from simulated body fluid on various phases of TiO₂ thin films prepared by filtered cathodic vacuum arc deposition. Thin Solid Films, 519(4):1300–1306, December 2010.
24. Maranda-niedbała, A.: Properties of the surface layers on titanium alloy and their biocompatibility in in vitro tests. Journal of Materials Processing Technology, 92-93:190–194, 1999.
25. Kasuga, T., Kondo, H., and Nogami, M.: Apatite formation on TiO₂ in simulated body fluid. Journal of Crystal Growth, 235(May 2001):235–240, 2002.
26. Oh, S., Brammer, K. S., Li, Y. S. J., Teng, D., Engler, A. J., Chien, S., and Jin, S.: Stem cell fate dictated solely by altered nanotube dimension. Proceedings of the National Academy of Sciences of the United States of America, 106(7):2130–5, February 2009.
27. Hanawa, T.: A comprehensive review of techniques for biofunctionalization of titanium. Journal of periodontal & implant science, 41(6):263–72, December 2011.
28. Pakhlov, E. M., Voronin, E. F., Borysenko, M. V., and Yurchenko, G. R.: Study of Water, Methanol, and Isopropanol Adsorption on the Surface of Titanosilicas of Different Structure. Journal of Thermal Analysis and Calorimetry, 62:395–399, 2000.

29. Miyauchi, M., Kieda, N., Hishita, S., and Mitsuhashi, T.: Reversible wettability control of TiO₂ surface by light irradiation. Surface Science, 511:401–407, 2002.
30. Ponsonnet, L., Reybier, K., Jaffrezic, N., Comte, V., Lagneau, C., Lissac, M., and Martelet, C.: Relationship between surface properties (roughness, wettability) of titanium and titanium alloys and cell behaviour. Materials Science and Engineering: C, 23(4):551–560, June 2003.
31. Health, C. f. D. and Radiological: Safety Communications - FDA Safety Communication: Metal-on-Metal Hip Implants, 2013.
32. REUTERS: F.D.A. Plans a New Review of Metal-on-Metal Hip Implants - NYTimes.com, 2012.
33. Meier, B.: A Scramble for Solutions as a Hip Device Fails - NYTimes.com, 2011.
34. Meier, B.: Studies Ordered for Makers of Artificial Hips - NYTimes.com, 2011.
35. Fawzi, N.: Knee Replacement Statistics, 2012.
36. Ogawa, T., Sukotjo, C., and Nishimura, I.: Modulated bone matrix-related gene expression is associated with differences in interfacial strength of different implant surface roughness. Journal of prosthodontics : official journal of the American College of Prosthodontists, 11(4):241–7, December 2002.
37. Statistics, N. C. f. H.: Health, United States, 2011: With Special Feature on Socioeconomic Status and Health., 2012.
38. Bozic, K. J., Harry E. Rubash, Berry, J., Khaled J. Saleh, M., and Durbhakula, S. M.: Modes of Failure in Revision Hip and Knee Replacement. Technical report, Center of Disease Control, 2004.
39. Haswell, M.: Clinical debate Dental implants : a different perspective Part one. Implant Practice, 2(1):44–57, 2009.
40. Meier, B.: Maker Aware of 40% Failure in Hip Implant - NYTimes.com, 2013.
41. Health, C. f. D. and Radiological: Safety Communications - Updated FDA Safety Communication: Stryker Neptune Waste Management Systems, 2013.

42. Abu-Amer, Y., Darwech, I., and Clohisy, J. C.: Aseptic loosening of total joint replacements: mechanisms underlying osteolysis and potential therapies. Arthritis research & therapy, 9 Suppl 1:S6, January 2007.
43. Sharma, S. K.: Green Corrosion Chemistry and Engineering: Opportunities and Challenges. Wiley-VCH Verlag GmbH & Co. KGaA, first edition, 2012.
44. Vieira, A., Ribeiro, A., Rocha, L., and Celis, J.: Influence of pH and corrosion inhibitors on the tribocorrosion of titanium in artificial saliva. Wear, 261(9):994–1001, November 2006.
45. Licausi, M. P., Igual Muñoz, a., and Borrás, V. A.: Tribocorrosion mechanisms of Ti 6 Al 4 V biomedical alloys in artificial saliva with different pHs. Journal of Physics D: Applied Physics, 46(40):404003, October 2013.
46. Sivakumar, B., Kumar, S., and Sankara Narayanan, T.: Fretting corrosion behaviour of Ti6Al4V alloy in artificial saliva containing varying concentrations of fluoride ions. Wear, 270(3-4):317–324, January 2011.
47. Guleryuz, H. and Cimenoglu, H.: Oxidation of Ti6Al4V alloy. Journal of Alloys and Compounds, 472(1-2):241–246, March 2009.
48. Zaveri, N., McEwen, G. D., Karpagavalli, R., and Zhou, A.: Biocorrosion studies of TiO₂ nanoparticle-coated Ti6Al4V implant in simulated biofluids. Journal of Nanoparticle Research, 12(5):1609–1623, July 2009.
49. Boyan, B. D., Lohmann, C. H., David, D., Sylvia, V. L., Cochran, D. L., and Schwartz, Z.: Mechanisms Involved in Osteoblast Response to Implant Surface Morphology. Annual Review of Materials Research, 31:357–71, 2001.
50. Turner, N., Armitage, M., Butler, R., and Ireland, G.: An in vitro model to evaluate cell adhesion to metals used in implantation shows significant differences between palladium and gold or platinum. Cell biology international, 28(7):541–7, January 2004.
51. Alves, C., Guerra Neto, C., Morais, G., da Silva, C., and Hajek, V.: Nitriding of titanium disks and industrial dental implants using hollow cathode discharge. Surface and Coatings Technology, 194(2-3):196–202, May 2005.

52. Guerra Neto, C. L. B., da Silva, M. a. M., and Alves, C.: Osseointegration evaluation of plasma nitrided titanium implants. Surface Engineering, 25(6):434–439, August 2009.
53. Clem, W. C., Konovalov, V. V., Chowdhury, S., Vohra, Y. K., Catledge, S. A., and Bellis, S. L.: Mesenchymal stem cell adhesion and spreading on microwave plasma-nitrided titanium alloy. Journal of biomedical materials research. Part A, 76(2):279–87, February 2006.
54. Kragh, K. C.: Atomic Layer Deposition of Hafnium Oxide on Silicon and Polymer Fibers at Temperatures below 100 °C. Journal of Undergraduate Research, 1:2–5, 2008.
55. George, S. M.: Atomic layer deposition: an overview. Chemical reviews, 110(1):111–31, January 2010.
56. Overhage, K., Tao, Q., Jursich, G., and Takoudis, C. G.: Selective Atomic Layer Deposition (SALD) of Titanium Dioxide on Silicon and Copper Patterned Substrates. Journal of Undergraduate Research, 4(1):5–8, 2010.
57. Ivanoff, C. J., Hallgren, C., Widmark, G., Sennerby, L., and Wennerberg, a.: Histologic evaluation of the bone integration of TiO₂ blasted and turned titanium microimplants in humans. Clinical oral implants research, 12(2):128–34, April 2001.
58. Hirakawa, Y., Jimbo, R., Shibata, Y., Watanabe, I., Wennerberg, A., and Sawase, T.: Accelerated bone formation on photo-induced hydrophilic titanium implants: an experimental study in the dog mandible. Clinical oral implants research, 24 Suppl A:139–44, August 2013.
59. Watanabe, T., Nakajima, A., Wang, R., Minabe, M., Koizumi, S., Fujishima, A., and Hashimoto, K.: Photocatalytic activity and photoinduced hydrophilicity of titanium dioxide coated glass. Thin Solid Films, 351(1-2):260–263, August 1999.
60. Hashimoto, K., Irie, H., and Fujishima, A.: TiO₂ Photocatalysis: A Historical Overview and Future Prospects. Japanese Journal of Applied Physics, 44(12):8269–8285, December 2005.
61. Irie, H., Tsuji, K.-I., and Hashimoto, K.: Hydrophobic anatase TiO₂-based thin films modified with Al, Cr derivatives to reach reversible wettability control. Physical chemistry chemical physics : PCCP, 10(21):3072–6, June 2008.

62. Iwasa, F., Tsukimura, N., Sugita, Y., Kanuru, R. K., Kubo, K., Hasnain, H., Att, W., and Ogawa, T.: TiO₂ micro-nano-hybrid surface to alleviate biological aging of UV-photofunctionalized titanium. International journal of nanomedicine, 6:1327–41, January 2011.
63. Bailey, R. and Sun, Y.: Unlubricated sliding friction and wear characteristics of thermally oxidized commercially pure titanium. Wear, 308(1-2):61–70, November 2013.
64. Dahm, K.: Fatigue-like failure of thermally oxidised titanium in reciprocating pin-on-plate wear tests. Wear, 267(1-4):409–416, June 2009.
65. Jamesh, M., Sankara Narayanan, T., and Chu, P. K.: Thermal oxidation of titanium: Evaluation of corrosion resistance as a function of cooling rate. Materials Chemistry and Physics, 138(2-3):565–572, March 2013.
66. Lee, Y.-J., Cui, D.-Z., Jeon, H.-R., Chung, H.-J., Park, Y.-J., Kim, O.-S., and Kim, Y.-J.: Surface characteristics of thermally treated titanium surfaces. Journal of periodontal & implant science, 42(3):81–7, June 2012.
67. Lim, Y. J., Oshida, Y., Andres, C. J., and Barco, M. T.: Surface characterizations of variously treated titanium materials. The International journal of oral & maxillofacial implants, 16(3):333–42, January.
68. Bloyce, A., Qi, P.-Y., Dong, H., and Bell, T.: Surface modification of titanium alloys for combined improvements in corrosion and wear resistance. Surface and Coatings Technology, 107(2-3):125–132, September 1998.
69. Oh, S., Brammer, K. S., Li, Y. S. J., Teng, D., Engler, A. J., Chien, S., and Jin, S.: Stem cell fate dictated solely by altered nanotube dimension. Proceedings of the National Academy of Sciences of the United States of America, 106(7):2130–2135, 2009.
70. Donos, N., Hamlet, S., Lang, N. P., Salvi, G. E., Huynh-Ba, G., Bosshardt, D. D., and Ivanovski, S.: Gene expression profile of osseointegration of a hydrophilic compared with a hydrophobic microrough implant surface. Clinical oral implants research, 22(4):365–72, April 2011.
71. Gong, D., Grimes, C. a., Varghese, O. K., Hu, W., Singh, R. S., Chen, Z., and Dickey, E. C.: Titanium oxide nanotube arrays prepared by anodic oxidation. Journal of Materials Research, 16(12):3331–3334, January 2011.

72. Panaitescu, E.: Titanium oxide nanotubes : synthesis, properties and applications for solar energy harvesting. Doctoral dissertation, 2009.
73. Shin, D. H., Shokuhfar, T., Choi, C. K., Lee, S.-H., and Friedrich, C.: Wettability changes of TiO₂ nanotube surfaces. Nanotechnology, 22(31):315704, August 2011.
74. Das, K., Bose, S., and Bandyopadhyay, A.: TiO₂ nanotubes on Ti: Influence of nanoscale morphology on bone cell-materials interaction. Journal of biomedical materials research. Part A, 90(1):225–37, July 2009.
75. Kowalski, D., Kim, D., and Schmuki, P.: TiO₂ nanotubes, nanochannels and mesosponge: Self-organized formation and applications. Nano Today, 8(3):235–264, June 2013.
76. Chen, B., Hou, J., and Lu, K.: Formation mechanism of TiO₂ nanotubes and their applications in photoelectrochemical water splitting and supercapacitors. Langmuir : the ACS journal of surfaces and colloids, 29(19):5911–9, May 2013.
77. Berger, S., Albu, S. P., Schmidt-Stein, F., Hildebrand, H., Schmuki, P., Hammond, J. S., Paul, D. F., and Reichlmaier, S.: The origin for tubular growth of TiO₂ nanotubes: A fluoride rich layer between tube-walls. Surface Science, 605(19-20):L57–L60, October 2011.
78. Peng, L., Mendelsohn, A. D., Latempa, T. J., Yoriya, S., Grimes, C. A., and Desai, T. A.: Long-Term Small Molecule and Protein Elution from TiO₂ Nanotubes 2009. 2009.
79. Sul, Y.-T.: Electrochemical growth behavior, surface properties, and enhanced in vivo bone response of TiO₂ nanotubes on microstructured surfaces of blasted, screw-shaped titanium implants. International journal of nanomedicine, 5:87–100, January 2010.
80. Bjursten, L. M., Rasmusson, L., Oh, S., Smith, G. C., Brammer, K. S., and Jin, S.: Titanium dioxide nanotubes enhance bone bonding in vivo. Journal of biomedical materials research. Part A, 92(3):1218–24, March 2010.
81. Patel, S. B., Hamlekhan, A., Royhman, D., Butt, A., Yuan, J., Shokuhfar, T., Sukotjo, C., Mathew, M. T., Jursich, G., and Takoudis, C. G.: Enhancing surface characteristics of Ti6Al4V for bio-implants using integrated anodization and thermal oxidation. Journal of Materials Chemistry B, 2(23):3597, 2014.

82. Manivasagam, G., Dhinasekaran, D., and Rajamanickam, A.: Biomedical Implants : Corrosion and its Prevention - A Review. (i):40–54, 2010.
83. Abdolldhi, Z., Ziaee, A. A. M., and Afshar, A.: Investigation of Titanium Oxide Layer in Thermal-Electrochemical Anodizing of Ti6Al4V Alloy. pages 44–47, 2009.
84. Ashrafizadeh, A. and Ashrafizadeh, F.: Structural features and corrosion analysis of thermally oxidized titanium. Journal of Alloys and Compounds, 480(2):849–852, July 2009.
85. McCafferty, E. and Wightman, J.: An X-ray photoelectron spectroscopy sputter profile study of the native air-formed oxide film on titanium. Applied Surface Science, 143(1-4):92–100, April 1999.
86. Brunette, D. M., Tengvall, P., Textor, M., and Thomsen, P.: Titanium in Medicine. Engineering Materials. Berlin, Heidelberg, Springer Berlin Heidelberg, 2001.
87. Kamachimudali, U., Sridhar, T. M., and Raj, B.: Corrosion of bio implants. Sadhana, 28(3-4):601–637, June 2003.
88. Clem, W. C., Konovalov, V. V., Chowdhury, S., Vohra, Y. K., Shane, A., and Bellis, S. L.: NIH Public Access. 76(2):279–287, 2008.
89. Grigal, I., a.M. Markeev, Gudkova, S., a.G. Chernikova, a.S. Mityaev, and a.P. Alekhin: Correlation between bioactivity and structural properties of titanium dioxide coatings grown by atomic layer deposition. Applied Surface Science, 258(8):3415–3419, February 2012.
90. Li, Z., Rahtu, A., and Gordon, R. G.: Atomic Layer Deposition of Ultrathin Copper Metal Films from a Liquid Copper(I) Amidinate Precursor. Journal of The Electrochemical Society, 153(11):C787, November 2006.
91. Ritala, M. and Leskela, M.: Handbook of Thin Films, Five-Volume Set, 1st Edition. Finland, Academic Press, 1 edition, 2001.
92. Sammelselg, E., Uustare, T., Ritala, M., and Leskela, M.: Characterization of titanium dioxide atomic layer growth from titanium ethoxide and water. 370:163–172, 2000.

93. Yanguas-Gil, A. and Elam, J. W.: Simple model for atomic layer deposition precursor reaction and transport in a viscous-flow tubular reactor. Journal of Vacuum Science & Technology A: Vacuum, Surfaces, and Films, 30(1):01A159, December 2012.
94. Ding, J., Wang, X., Yuan, N., Li, C., Zhu, Y., and Kan, B.: The influence of substrate on the adhesion behaviors of atomic layer deposited aluminum oxide films. Surface and Coatings Technology, 205(8-9):2846–2851, January 2011.
95. Oh, S., Daraio, C., Chen, L.-H., Pisanic, T. R., Fiñones, R. R., and Jin, S.: Significantly accelerated osteoblast cell growth on aligned TiO₂ nanotubes. Journal of biomedical materials research. Part A, 78(1):97–103, July 2006.
96. Uchida, M., Kim, H.-M., Kokubo, T., Fujibayashi, S., and Nakamura, T.: Structural dependence of apatite formation on titania gels in a simulated body fluid. Journal of Biomedical Materials Research, 64A(1):164–170, January 2003.
97. Yamamoto, O., Alvarez, K., Kikuchi, T., and Fukuda, M.: Fabrication and characterization of oxygen-diffused titanium for biomedical applications. Acta biomaterialia, 5(9):3605–15, November 2009.
98. Qu, J., Blau, P. J., Howe, J. Y., and Meyer III, H. M.: Oxygen diffusion enables anti-wear boundary film formation on titanium surfaces in zinc-dialkyl-dithiophosphate (ZDDP)-containing lubricants. Scripta Materialia, 60(10):886–889, May 2009.
99. Guleryuz, H. and Cimenoglu, H.: Surface modification of a Ti6Al4V alloy by thermal oxidation. Surface and Coatings Technology, 192(2-3):164–170, March 2005.
100. Bruni, S., MARTINESI, M., Stio, M., TREVES, C., Bacci, T., and BORGIOLI, F.: Effects of surface treatment of Ti-6Al-4V titanium alloy on biocompatibility in cultured human umbilical vein endothelial cells. Acta biomaterialia, 1(2):223–34, March 2005.
101. Han, J.-B., Wang, X., Wang, N., Wei, Z.-H., Yu, G.-P., Zhou, Z.-G., and Wang, Q.-Q.: Effect of plasma treatment on hydrophilic properties of TiO₂ thin films. Surface and Coatings Technology, 200(16-17):4876–4878, April 2006.
102. Song, X., Gopireddy, D., and Takoudis, C. G.: Characterization of titanium oxynitride films deposited by low pressure chemical vapor deposition using amide Ti precursor. Thin Solid Films, 516(18):6330–6335, July 2008.

103. Qu, J., Blau, P. J., and Jolly, B. C.: Oxygen-diffused titanium as a candidate brake rotor material. Wear, 267(5-8):818–822, June 2009.
104. Dong, H. and Bell, T.: Enhanced wear resistance of titanium surfaces by a new thermal oxidation treatment. Wear, 238(2):131–137, March 2000.
105. Aarik, J., Aidla, A., Uustare, T., and Sammelselg, V.: Morphology and structure of TiO₂ thin films grown by atomic layer deposition. Journal of Crystal Growth, 148(3):268–275, March 1995.
106. Aarik, J., Aidla, A., Sammelselg, V., Siimon, H., and Uustare, T.: Control of thin film structure by reactant pressure in atomic layer deposition of TiO₂. Journal of Crystal Growth, 169(3):496–502, December 1996.
107. Aarik, J., Aidla, A., Kiisler, A.-A., Uustare, T., and Sammelselg, V.: Effect of crystal structure on optical properties of TiO₂ films grown by atomic layer deposition. Thin Solid Films, 305(1-2):270–273, August 1997.
108. Ritala, M.: Atomic Layer Deposition of Oxide Thin Films with Metal Alkoxides as Oxygen Sources. Science, 288(5464):319–321, April 2000.
109. Pore, V., Rahtu, A., Leskelä, M., Ritala, M., Sajavaara, T., and Keinonen, J.: Atomic Layer Deposition of Photocatalytic TiO₂ Thin Films from Titanium Tetramethoxide and Water. Chemical Vapor Deposition, 10(3):143–148, June 2004.
110. Tao, Q., Overhage, K., Jursich, G., and Takoudis, C.: On the initial growth of atomic layer deposited TiO₂ films on silicon and copper surfaces. Thin Solid Films, 520(22):6752–6756, September 2012.
111. Katamreddy, R., Omarjee, V., Feist, B., and Dussarrat, C.: Ti Source Precursors for Atomic Layer Deposition of TiO₂, STO and BST. In ECS Transactions, volume 16, pages 113–122. ECS, October 2008.
112. Huang, Y., Pandraud, G., and Sarro, P. M.: Characterization of low temperature deposited atomic layer deposition TiO₂ for MEMS applications. Journal of Vacuum Science & Technology A: Vacuum, Surfaces, and Films, 31(1):01A148, 2013.
113. Le Guehennec, L., Lopez-Heredia, M.-A., Enkel, B., Weiss, P., Amouriq, Y., and Layrolle, P.: Osteoblastic cell behaviour on different titanium implant surfaces. Acta biomaterialia, 4(3):535–43, May 2008.

114. Kawakami, H., Ilola, R., Straka, L., Papula, S., Romu, J., Hanninen, H., Mahlberg, R., and Heikkila, M.: Photocatalytic Activity of Atomic Layer Deposited TiO₂ Coatings on Austenitic Stainless Steels and Copper Alloys. Journal of The Electrochemical Society, 155(2):C62, February 2008.
115. Tao, Q. T. Q., Jursich, G., and Takoudis, C.: Structural and dielectric characterization of atomic layer deposited HfO₂ and TiO₂ as promising gate oxides. Advanced Semiconductor Manufacturing Conference ASMC 2010 IEEESEMI, pages 17–22, 2010.
116. Tao, Q., Jursich, G., and Takoudis, C.: Structural and dielectric characterization of atomic layer deposited HfO₂ and TiO₂ as promising gate oxides. 2010 IEEE/SEMI Advanced Semiconductor Manufacturing Conference (ASMC), pages 17–22, July 2010.
117. Martínez-Martínez, D., Sánchez-López, J., Rojas, T., Fernández, A., Eaton, P., and Belin, M.: Structural and microtribological studies of TiCN based nanocomposite coatings prepared by reactive sputtering. Thin Solid Films, 472(1-2):64–70, January 2005.
118. Fujishima, A., Rao, T. N., and Tryk, D. A.: Titanium dioxide photocatalysis. 1(March):1–21, 2000.
119. Nakata, K. and Fujishima, A.: TiO₂ photocatalysis: Design and applications. Journal of Photochemistry and Photobiology C: Photochemistry Reviews, 13(3):169–189, September 2012.
120. Linsebigler, A. L., Lu, G., and Yates, J. T.: Photocatalysis on TiO₂ Surfaces: Principles, Mechanisms, and Selected Results. Chemical reviews, 95:735–758, 1995.
121. Ketteler, G., Yamamoto, S., Bluhm, H., Andersson, K., Starr, D. E., Ogletree, D. F., Ogasawara, H., Nilsson, A., Salmeron, M., Berkeley, L., Sciences, M., Di, V., Road, S. H., and Park, M.: The Nature of Water Nucleation Sites on TiO₂ (110) Surfaces Revealed by Ambient Pressure X-ray Photoelectron Spectroscopy. Journal of Physical Chemistry C, 2(110):8278–8282, 2007.
122. Gemelli, E. and Camargo, N.: Oxidation kinetics of commercially pure titanium. Matéria (Rio de Janeiro), 12(3):525–531, 2007.

123. Zhu, K., Neale, N. R., Halverson, A. F., Kim, J. Y., and Frank, A. J.: Effects of Annealing Temperature on the Charge-Collection and Light-Harvesting Properties of TiO₂ Nanotube-Based Dye-Sensitized Solar Cells. pages 13433–13441, 2010.
124. Lee, C.-C., Chen, H.-C., and Jaing, C.-C.: Effect of thermal annealing on the optical properties and residual stress of TiO₂ films produced by ion-assisted deposition. Applied optics, 44(15):2996–3000, May 2005.
125. Fang, W. Q., Gong, X.-q., and Yang, H. G.: On the Unusual Properties of Anatase TiO₂ Exposed by Highly Reactive Facets. pages 725–734, 2011.
126. Yang, H. G., Sun, C. H., Qiao, S. Z., Zou, J., Liu, G., Smith, S. C., Cheng, H. M., and Lu, G. Q.: Anatase TiO₂ single crystals with a large percentage of reactive facets. Nature, 453(7195):638–41, May 2008.
127. Cho, C. H., Han, M. H., Kim, D. H., and Kim, D. K.: Morphology evolution of anatase TiO₂ nanocrystals under a hydrothermal condition (pH=9.5) and their ultra-high photo-catalytic activity. Materials Chemistry and Physics, 92(1):104–111, July 2005.
128. Lu, J., Dai, Y., Jin, H., and Huang, B.: Effective increasing of optical absorption and energy conversion efficiency of anatase TiO₂ nanocrystals by hydrogenation. Physical chemistry chemical physics : PCCP, 13(40):18063–8, October 2011.
129. Young, T.: An Essay on the Cohesion of Fluids. Philosophical Transactions of the Royal Society of London, 95:65–87, January 1805.
130. Fox, H. W. and Zisman, W. A.: I31. 1, 1960.
131. Kloubek, J.: Development of methods for surface free energy determination using contact angles of liquids on solids. Advances in Colloid and Interface Science, 38:99–142, March 1992.
132. Adam, N.: The physics and chemistry of surfaces,. London, Oxford University Press ;H. Milford, 1941.
133. a.W Neumann, Good, R., Hope, C., and Sejpal, M.: An equation-of-state approach to determine surface tensions of low-energy solids from contact angles. Journal of Colloid and Interface Science, 49(2):291–304, November 1974.

134. enkiewicz, M.: Methods for the calculation of surface free energy of solids. 24(1):137–145, 2007.
135. Oliveira, P. T. D., Zalzal, S. F., Beloti, M. M., Rosa, A. L., Nanci, A., Box, P. O., Centre-ville, S., and de Oliveira, P. T.: Enhancement of in vitro osteogenesis on titanium by chemically produced nanotopography. Journal of biomedical materials research. Part A, 80(3):554–64, March 2007.
136. Bruzzone, A., Costa, H., Lonardo, P., and Lucca, D.: Advances in engineered surfaces for functional performance. CIRP Annals - Manufacturing Technology, 57(2):750–769, January 2008.
137. Jayaraman, M., Meyer, U., Bühner, M., Joos, U., and Wiesmann, H.-P.: Influence of titanium surfaces on attachment of osteoblast-like cells in vitro. Biomaterials, 25(4):625–31, February 2004.
138. Bezrodna, T., Puchkovska, G., Shymanovska, V., Baran, J., and Ratajczak, H.: IR-analysis of H-bonded H₂O on the pure TiO₂ surface. Journal of Molecular Structure, 700(1-3):175–181, August 2004.
139. Balachandaran, K., Venckatesh, R., and Sivara, R.: Synthesis Of Nano TiO₂-SiO₂ Composite Using Sol-Gel Method: Effect On Size, Surface Morphology And Thermal Stability. International Journal of Engineering Science and Technology, 2(8):3695–3700, 2010.
140. Thibault, S.: Infrared reflection-absorption spectra of oxide films on titanium. Thin Solid Films, 35:L33–L35, 1976.
141. Velten, D., Biehl, V., Aubertin, F., Valeske, B., Possart, W., and Breme, J.: Preparation of TiO₂ layers on cp-Ti and Ti6Al4V by thermal and anodic oxidation and by sol-gel coating techniques and their characterization. Journal of biomedical materials research, 59(1):18–28, January 2002.
142. Arun Kumar, D., Alex Xavier, J., Merline Shyla, J., and Xavier, F. P.: Synthesis and structural, optical and electrical properties of TiO₂/SiO₂ nanocomposites. Journal of Materials Science, 48(10):3700–3707, January 2013.
143. Perkins, B. G., Häber, T., and Nesbitt, D. J.: Quantum state-resolved energy transfer dynamics at gas-liquid interfaces: IR laser studies of CO₂ scattering from

- perfluorinated liquids. The journal of physical chemistry. B, 109(34):16396–405, September 2005.
144. Magni, D., Deschenauz, C., Hollenstein, C., Creatore, A., and Fayet, P.: Oxygen diluted hexamethyldisiloxane plasmas investigated by means of in situ infrared absorption spectroscopy and mass spectrometry. Journal of Physics D: Applied Physics, 34:87–94, 2001.
 145. Zeitler, V. A., Brown, C. A., and Brown, A.: The Infrared Spectra of Some Ti-O-Si, Ti-O-Ti and Si-O-Si Compounds. The Journal of Physical Chemistry, 61(9):1174–1177, September 1957.
 146. Eisenbarth, E., Velten, D., Schenk-Meuser, K., Linez, P., Biehl, V., Duschner, H., Breme, J., and Hildebrand, H.: Interactions between cells and titanium surfaces. Biomolecular engineering, 19(2-6):243–9, August 2002.
 147. Fujino, T. and Matzuda, T.: Synthetic Process of Titanium Dioxide Coating on Aluminum by Chemical Conversion Method. Materials Transactions, 47(3):849–853, 2006.
 148. Hadjiivanov, K., Lamotte, J., and Lavalley, J.-c.: FTIR Study of Low-Temperature CO Adsorption on Pure and Ammonia-Precovered TiO₂ (Anatase). 2(7):3374–3381, 1997.
 149. Mali, S. S., Shinde, P. S., Betty, C., Bhosale, P. N., Lee, W. J., and Patil, P. S.: Nanocoral architecture of TiO₂ by hydrothermal process: Synthesis and characterization. Applied Surface Science, 257(23):9737–9746, September 2011.
 150. Vieira, F. T. G., Melo, D. S., de Lima, S. J. G., Longo, E., Paskocimas, C. A., Júnior, W. S., de Souza, A. G., and dos Santos, I. M. G.: The influence of temperature on the color of TiO₂:Cr pigments. Materials Research Bulletin, 44(5):1086–1092, May 2009.
 151. Nakamura, R. and Nakato, Y.: Primary intermediates of oxygen photoevolution reaction on TiO₂ (Rutile) particles, revealed by in situ FTIR absorption and photoluminescence measurements. Journal of the American Chemical Society, 126(4):1290–8, February 2004.
 152. Nakamura, R., Imanishi, A., Murakoshi, K., and Nakato, Y.: In situ FTIR studies of primary intermediates of photocatalytic reactions on nanocrystalline TiO₂ films

- in contact with aqueous solutions. Journal of the American Chemical Society, 125(24):7443–50, June 2003.
153. Fujishima, a., Zhang, X., and Tryk, D.: TiO₂ photocatalysis and related surface phenomena. Surface Science Reports, 63(12):515–582, December 2008.
 154. Nolan, N. T., Seery, M. K., and Pillai, S. C.: Spectroscopic Investigation of the Anatase-to-Rutile Transformation of SolGel-Synthesized TiO₂ Photocatalysts. The Journal of Physical Chemistry C, 113(36):16151–16157, September 2009.
 155. Dam Le, D., Dung Dang, T. M., Thang Chau, V., and Chien Dang, M.: The fabrication of visible light responsive Ag-SiO₂ co-doped TiO₂ thin films by the solgel method. Advances in Natural Sciences: Nanoscience and Nanotechnology, 1(1):015007, March 2010.
 156. Narayanan, R. and Seshadri, S.: Phosphoric acid anodization of Ti6Al4V Structural and corrosion aspects. Corrosion Science, 49(2):542–558, February 2007.
 157. Lee, H. U., Lee, S. C., Choi, S., Son, B., Lee, S. M., Kim, H. J., and Lee, J.: Efficient visible-light induced photocatalysis on nanoporous nitrogen-doped titanium dioxide catalysts. Chemical Engineering Journal, 228:756–764, July 2013.
 158. Freund, J. H. and Roberts, M. W.: Surface chemistry of carbon dioxide. Surface Science Reports, 25:225–273, 1996.
 159. Haoyong, Y., Zhensheng, J., Shunli, Z., Shoubin, W., and Zhijun, Z.: Reason for the loss of hydrophilicity of TiO₂ film and its photocatalytic regeneration. Science in China Series B: Chemistry, 45(6):625–632, December 2002.
 160. Massaro, C., Rotolo, P., Riccardis, F. D., Milella, E., Napoli, A., Wieland, M., Textor, M., Spencer, N. D., and Brunette, D. M.: Comparative investigation of the surface properties of commercial titanium dental implants. Part I: chemical composition. Journal of Materials Science: Materials in Medicine, 13(6):535–548, June 2002.
 161. Rupp, F., Scheideler, L., Rehbein, D., Axmann, D., and Geis-Gerstorfer, J.: Roughness induced dynamic changes of wettability of acid etched titanium implant modifications. Biomaterials, 25(7-8):1429–1438, March 2004.
 162. Rupp, F., Scheideler, L., Olshanska, N., de Wild, M., Wieland, M., and Geis-Gerstorfer, J.: Enhancing surface free energy and hydrophilicity through chemical modifica-

- tion of microstructured titanium implant surfaces. Journal of biomedical materials research. Part A, 76(2):323–34, February 2006.
163. Butt, H.-J., Graf, K., and Kappl, M.: Physics and Chemistry of Interfaces. Weinheim, 2nd edition, 2003.
 164. Hashimoto, K., Irie, H., and Fujishima, A.: A Historical Overview and Future Prospects. 17(6), 2007.
 165. Park, K.-H., Koak, J.-Y., Kim, S.-K., and Heo, S.-J.: Wettability and cellular response of UV light irradiated anodized titanium surface. The journal of advanced prosthodontics, 3(2):63–8, June 2011.
 166. Zhao, G., Schwartz, Z., Wieland, M., Rupp, F., Geis-Gerstorfer, J., Cochran, D. L., and Boyan, B. D.: High surface energy enhances cell response to titanium substrate microstructure. Journal of biomedical materials research. Part A, 74(1):49–58, July 2005.
 167. Zanjanchi, M. and Jabariyan, S.: Application of ultrasound and methanol for rapid removal of surfactant from MCM-41. Journal of the Serbian Chemical Society, 79(1):25–38, 2014.
 168. Yamakata, A., Ishibashi, T.-a., and Onishi, H.: Kinetics of the photocatalytic water-splitting reaction on TiO₂ and Pt/TiO₂ studied by time-resolved infrared absorption spectroscopy. Journal of Molecular Catalysis A: Chemical, 199(1-2):85–94, May 2003.
 169. Mills, A., Hodgen, S., and Lee, S. K.: Self-cleaning titania films: an overview of direct, lateral and remote photo-oxidation processes. Research on Chemical Intermediates, 31(4-6):295–308, June 2005.
 170. Auvinen, J. and Wirtanen, L.: The influence of photocatalytic interior paints on indoor air quality. Atmospheric Environment, 42(18):4101–4112, June 2008.
 171. Nakajima, A., Koizumi, S.-i., Watanabe, T., and Hashimoto, K.: Photoinduced Amphiphilic Surface on Polycrystalline Anatase TiO₂ Thin Films. (11):7048–7050, 2000.

172. Selvaraj, S. K., Jursich, G., and Takoudis, C. G.: Design and implementation of a novel portable atomic layer deposition/chemical vapor deposition hybrid reactor. The Review of scientific instruments, 84(9):095109, September 2013.
173. Peixoto, C., Butt, A., and Takoudis, C. G.: Effect of Storage Conditions on Ti-6Al-4V Surface Wettability. Journal of Undergraduate Research, (7):18–22, 2014.
174. Averill, B. and Eldredge, P.: General Chemistry: Principles, Patterns, and Applications. 1.0 edition, 2011.
175. Lu, H., Zhou, L., Wan, L., Li, S., Rong, M., and Guo, Z.: Effects of storage methods on time-related changes of titanium surface properties and cellular response. 055002, 2012.
176. Ulrich, S. D., Seyler, T. M., Bennett, D., Delanois, R. E., Saleh, K. J., Thongtrangan, I., Kuskowski, M., Cheng, E. Y., Sharkey, P. F., Parvizi, J., Stiehl, J. B., and Mont, M. a.: Total hip arthroplasties: what are the reasons for revision? International orthopaedics, 32(5):597–604, October 2008.
177. Gallo, J.: Aseptic Loosening of Total Hip Arthroplasty as a Result of Local Failure of Tissue Homeostasis. 2007.
178. Joos, U. and Meyer, U.: New paradigm in implant osseointegration. Head & face medicine, 2:19, January 2006.
179. Feng, B., Weng, J., Yang, B., Qu, S., and Zhang, X.: Characterization of surface oxide films on titanium and adhesion of osteoblast. Biomaterials, 24(25):4663–4670, November 2003.
180. Khan, M. R., Donos, N., Salih, V., and Brett, P. M.: The enhanced modulation of key bone matrix components by modified Titanium implant surfaces. Bone, 50(1):1–8, January 2012.
181. Montes, C. C., Pereira, F. A., Thomé, G., Alves, E. D. M., Acedo, R. V., de Souza, J. R., Melo, A. C. M., and Trevilatto, P. C.: Failing factors associated with osseointegrated dental implant loss. Implant dentistry, 16(4):404–12, December 2007.
182. García-Alonso, M. C., Saldaña, L., Vallés, G., González-Carrasco, J. L., González-Cabrero, J., Martínez, M. E., Gil-Garay, E., and Munuera, L.: In vitro corrosion be-

- haviour and osteoblast response of thermally oxidised Ti6Al4V alloy. Biomaterials, 24(1):19–26, January 2003.
183. Onoda, K. and Yoshikawa, S.: Effect of pre-nitridation treatment on the formation of anatase TiO₂ films by anodization. Ceramics International, 34(6):1453–1457, August 2008.
 184. Range, T. and Garcia, E. A.: A Study of the Diffusion of Oxygen in a -Titanium Oxidized in the Temperature Range 460-700 C. Journal of Electrochemical Society, 130(6):1423–1426, 1983.
 185. Rogers, J., Erickson, K., Belton, D., Springer, R., Taylor, T., Beery, J., and J.W. Rogers, Jr., K. L. Erickson, D. N. Belton, R. W. Springer, T. N. Taylor, J. G. B.: Low temperature diffusion of oxygen in titanium and titanium oxide films. Applied Surface Science, 35(1):137–152, October 1988.
 186. R. Padma, K. Ramkumar, M. S.: Growth of titanium oxide overlayers by thermal oxidation of titanium. Journal of Materials Science, 23(5):591–597, 1988.
 187. Wouters, O., Vellinga, W., Vantijum, R., and Dehossion, J.: Effects of crystal structure and grain orientation on the roughness of deformed polycrystalline metals. Acta Materialia, 54(10):2813–2821, June 2006.
 188. Ottermann, C. and Bange, K.: Correlation between the density of TiO₂ films and their properties. Thin Solid Films, 286(1-2):32–34, September 1996.
 189. Martin, N., Rousselot, C., Rondot, D., Palmino, F., and Mercier, R.: Microstructure modification of amorphous titanium oxide thin films during annealing treatment. Thin Solid Films, 300(1-2):113–121, May 1997.
 190. Aarik, J., Aidla, A., Kiisler, A.-a., and Uustare, T.: Effect of crystal structure on optical properties of TiO₂ films grown by atomic layer deposition. 305:270–273, 1997.
 191. Shin, H., Jeong, D.-K., Lee, J., Sung, M., and Kim, J.: Formation of TiO₂ and ZrO₂ Nanotubes Using Atomic Layer Deposition with Ultraprecise Control of the Wall Thickness. Advanced Materials, 16(14):1197–1200, July 2004.
 192. Roy, P., Berger, S., and Schmuki, P.: TiO₂ nanotubes: synthesis and applications. Angewandte Chemie (International ed. in English), 50(13):2904–39, March 2011.

193. Park, N., Lagemaat, J. V. D., and Frank, A. J.: Comparison of Dye-Sensitized Rutile- and Anatase-Based TiO₂ Solar Cells. Journal of Physical Chemistry B, 104:8989–8994, 2000.
194. Wagemaker, M., van de Krol, R., Kentgens, a. P., van Well, a. a., and Mulder, F. M.: Two phase morphology limits lithium diffusion in TiO₂(anatase): a ⁷Li MAS NMR study. Journal of the American Chemical Society, 123(46):11454–61, November 2001.
195. Hu, Y.-S., Kienle, L., Guo, Y.-G., and Maier, J.: High Lithium Electroactivity of Nanometer-Sized Rutile TiO₂. Advanced Materials, 18(11):1421–1426, June 2006.
196. Mishra, S., Gupta, S. K., Jha, P. K., and Pratap, A.: Study of dimension dependent diffusion coefficient of titanium dioxide nanoparticles. Materials Chemistry and Physics, 123(2-3):791–794, October 2010.
197. Dozzi, M. and Selli, E.: Specific Facets-Dominated Anatase TiO₂: Fluorine-Mediated Synthesis and Photoactivity. Catalysts, 3(2):455–485, May 2013.
198. Wu, Y., Xing, M., Tian, B., Zhang, J., and Chen, F.: Preparation of nitrogen and fluorine co-doped mesoporous TiO₂ microsphere and photodegradation of acid orange 7 under visible light. Chemical Engineering Journal, 162(2):710–717, August 2010.
199. Susilo, S.: Anodization Growth and Integration of Titanium Dioxide. Doctoral dissertation, 2011.
200. Wei, W., Berger, S., Hauser, C., Meyer, K., Yang, M., and Schmuki, P.: Transition of TiO₂ nanotubes to nanopores for electrolytes with very low water contents. Electrochemistry Communications, 12(9):1184–1186, September 2010.
201. Macak, J., Hildebrand, H., Marten-Jahns, U., and Schmuki, P.: Mechanistic aspects and growth of large diameter self-organized TiO₂ nanotubes. Journal of Electroanalytical Chemistry, 621(2):254–266, September 2008.
202. Suwanchawalit, C. and Wongnawa, S.: Triblock copolymer-templated synthesis of porous TiO₂ and its photocatalytic activity. Journal of Nanoparticle Research, 12(8):2895–2906, February 2010.

203. Poliah, R. and Sreekantan, S.: Characterization and Photocatalytic Activity of Enhanced Copper-Silica-Loaded Titania Prepared via Hydrothermal Method. Journal of Nanomaterials, 2011:1–8, 2011.
204. Fahim, N. F., Morks, M. F., and Sekino, T.: Electrochemical synthesis of silica-doped high aspect-ratio titania nanotubes as nanobioceramics for implant applications. Electrochimica Acta, 54(12):3255–3269, April 2009.
205. Krasowska, M., Zawala, J., and Malysa, K.: Air at hydrophobic surfaces and kinetics of three phase contact formation. Advances in colloid and interface science, 147-148:155–69, 2009.
206. Asmatulu, R.: Improving the dewetability characteristics of hydrophobic fine particles by air bubble entrapments. Powder Technology, 186(2):184–188, August 2008.
207. Hafner, B.: Energy Dispersive Spectroscopy on the SEM : A Primer. Technical report, 2013.
208. Sandborg, A.: Energy Dispersive X-Ray Spectrometry – EDS Instrumentation & Signal Detection.
209. Landolt, D., Mischler, S., Stemp, M., and Barril, S.: Third body effects and material fluxes in tribocorrosion systems involving a sliding contact. Wear, 256(5):517–524, March 2004.
210. Mathew, M. T., Srinivasa Pai, P., Pourzal, R., Fischer, a., and Wimmer, M. a.: Significance of Tribocorrosion in Biomedical Applications: Overview and Current Status. Advances in Tribology, 2009:1–12, 2009.
211. Jemmely, P., Mischler, S., and Landolt, D.: Electrochemical modeling of passivation phenomena in tribocorrosion. Wear, 237(1):63–76, January 2000.
212. FDA’s MedWatch Safety Alerts: January 2013, 2013.
213. Kux, L.: June 27-28, 2012: Orthopaedic and Rehabilitation Devices Panel of the Medical Devices Advisory Committee Meeting Announcement, 2012.
214. Bozic, K. J., Lau, E., Ong, K., Chan, V., Kurtz, S., Vail, T. P., Rubash, H. E., and Berry, D. J.: Risk factors for early revision after primary total hip arthroplasty

- in Medicare patients. Clinical orthopaedics and related research, 472(2):449–54, February 2014.
215. Class 2 Recall DePuy ASR Resurfacing Femoral Heads, 2011.
 216. Narkbunnam, R. and Chareancholvanich, K.: Causes of failure in total knee arthroplasty. Journal of the Medical Association of Thailand = Chotmai het thangphaet, 95(5):667–73, May 2012.
 217. Kurtz, S. M., Ong, K. L., Lau, E., and Bozic, K. J.: Impact of the economic downturn on total joint replacement demand in the United States: updated projections to 2021. The Journal of bone and joint surgery. American volume, 96(8):624–30, April 2014.
 218. Barril, S., Mischler, S., and Landolt, D.: Triboelectrochemical investigation of the friction and wear behaviour of TiN coatings in a neutral solution. Tribology International, 34(9):599–608, September 2001.
 219. Jemmely, P., Mischler, S., and Landolt, D.: Tribocorrosion behaviour of Fe 17Cr stainless steel in acid and alkaline solutions. Tribology International, 32(1999):295–303, 1999.
 220. Mischler, S., Spiegel, a., and Landolt, D.: The role of passive oxide films on the degradation of steel in tribocorrosion systems. Wear, 225-229:1078–1087, April 1999.
 221. Takadoum, J.: The influence of potential on the tribocorrosion of nickel and iron in sulfuric acid solution. Corrosion Science, 38(4):643–654, April 1996.
 222. Hassani, S., Raeissi, K., Azzi, M., Li, D., Golozar, M., and Szpunar, J.: Improving the corrosion and tribocorrosion resistance of NiCo nanocrystalline coatings in NaOH solution. Corrosion Science, 51(10):2371–2379, October 2009.
 223. Berradja, a., Déforge, D., Nogueira, R. P., Ponthiaux, P., Wenger, F., and Celis, J.-P.: An electrochemical noise study of tribocorrosion processes of AISI 304 L in Cl⁻ and media. Journal of Physics D: Applied Physics, 39(15):3184–3192, August 2006.
 224. Mischler, S., Rosset, E., Stachowiak, G., and Landolt, D.: Effect of sulphuric acid concentration on the rate of tribocorrosion of iron. Wear, 167(2):101–108, August 1993.

225. Berradja, a., Bratu, F., Benea, L., Willems, G., and Celis, J.-P.: Effect of sliding wear on tribocorrosion behaviour of stainless steels in a Ringer's solution. Wear, 261(9):987–993, November 2006.
226. Sun, D., Wharton, J., and Wood, R.: Abrasive size and concentration effects on the tribocorrosion of cast CoCrMo alloy in simulated body fluids. Tribology International, 42(11-12):1595–1604, December 2009.
227. Jellesen, M. S. and Hilbert, L. R.: A block-on-ring tribocorrosion setup for combined electrochemical and friction testing. (March):115–127, 2007.
228. Mischler, S., Debaud, S., and Landolt, D.: Wear-Accelerated Corrosion of Passive Metals in Tribocorrosion Systems. Journal of Electroanalytical Society, 145(3):750–8, 1998.
229. Azzi, M. and Szpunar, J. a.: Tribo-electrochemical technique for studying tribocorrosion behavior of biomaterials. Biomolecular engineering, 24(5):443–6, November 2007.
230. Yan, Y., Neville, A., Dowson, D., and Williams, S.: Tribocorrosion in implants assessing high carbon and low carbon CoCrMo alloys by in situ electrochemical measurements. Tribology International, 39(12):1509–1517, December 2006.
231. Ferreira, S., Ariza, E., Rocha, L., Gomes, J., Carvalho, P., Vaz, F., a.C. Fernandes, Rebouta, L., Cunha, L., Alves, E., Goudeau, P., and Rivière, J.: Tribocorrosion behaviour of ZrOxNy thin films for decorative applications. Surface and Coatings Technology, 200(22-23):6634–6639, June 2006.
232. Benea, L., Wenger, F., Ponthiaux, P., and Celis, J.: Tribocorrosion behaviour of NiSiC nano-structured composite coatings obtained by electrodeposition. Wear, 266(3-4):398–405, February 2009.
233. Bratu, F., Benea, L., and Celis, J.-P.: Tribocorrosion behaviour of NiSiC composite coatings under lubricated conditions. Surface and Coatings Technology, 201(16-17):6940–6946, May 2007.
234. Relation of the Equilibrium Contact Angle to Liquid and Solid Constitution. 1964.
235. Liu, C., Chu, P. K., Lin, G., and Yang, D.: Effects of Ti/TiN multilayer on corrosion resistance of nickel-titanium orthodontic brackets in artificial saliva. Corrosion Science, 49(10):3783–3796, 2007.

236. Hidaka, O., Iwasaki, M., Saito, M., and Morimoto, T.: Influence of Clenching Intensity on Bite Force Balance, Occlusal Contact Area, and Average Bite Pressure. Journal of Dental Research, 78(7):1336–1344, July 1999.
237. Harada, K. and Ohkura, K.: Measure of Bite Force and Occlusal Contact Area Before and After Bilateral Sagittal Split Ramus Osteotomy of the Mandible Using a New Pressure-Sensitive Device: A Preliminary Report. Journal of Oral and Maxillofacial Surgery, 58(4):370–373, 2000.
238. Kumagai, H., Suzuki, T., Hamada, T., Sondang, P., Fujitani, M., and Nikawa, H.: Occlusal force distribution on the dental arch during various levels of clenching. Journal of oral rehabilitation, 26(12):932–5, December 1999.
239. Mathew, M., Uth, T., Hallab, N., Pourzal, R., Fischer, a., and Wimmer, M.: Construction of a tribocorrosion test apparatus for the hip joint: Validation, test methodology and analysis. Wear, 271(9-10):2651–2659, July 2011.
240. Roy, M., Sundararajan, G., Stack, M., Mathew, M., Ariza, E., Rocha, L., a.C. Fernandes, and Vaz, F.: TiCxOy thin films for decorative applications: Tribocorrosion mechanisms and synergism. Tribology International, 41(7):603–615, July 2008.
241. Mathew, M. T., Abbey, S., Hallab, N. J., Hall, D. J., Sukotjo, C., and Wimmer, M. A.: Influence of pH on the tribocorrosion behavior of CpTi in the oral environment: synergistic interactions of wear and corrosion. Journal of biomedical materials research. Part B, Applied biomaterials, 100(6):1662–71, August 2012.
242. Barão, V. A. R., Mathew, M. T., Assunção, W. G., Yuan, J. C.-C., Wimmer, M. A., and Sukotjo, C.: Stability of cp-Ti and Ti-6Al-4V alloy for dental implants as a function of saliva pH - an electrochemical study. Clinical oral implants research, 23(9):1055–62, September 2012.
243. Jiang, J., Stack, M., and Neville, a.: Modelling the tribo-corrosion interaction in aqueous sliding conditions. Tribology International, 35(10):669–679, October 2002.
244. Landolt, D., Mischler, S., and Stemp, M.: Electrochemical methods in tribocorrosion: a critical appraisal. Electrochimica Acta, 46(24-25):3913–3929, August 2001.
245. Stack, M., Jawan, H., and Mathew, M.: On the construction of micro-abrasion maps for a steel/polymer couple in corrosive environments. Tribology International, 38(9):848–856, September 2005.

246. Wood, R. J. K.: Tribo-corrosion of coatings: a review. Journal of Physics D: Applied Physics, 40(18):5502–5521, September 2007.
247. Shahba, R. M. A., Ghannem, W. A., and El-shenawy, A. E.-s.: Corrosion and Inhibition of Ti-6Al-4V Alloy in NaCl Solution. 6:5499–5509, 2011.
248. Iwabuchi, a., Lee, J., and Uchidate, M.: Synergistic effect of fretting wear and sliding wear of Co-alloy and Ti-alloy in Hanks solution. Wear, 263(1-6):492–500, September 2007.
249. Manhabosco, T., Tamborim, S., dos Santos, C., and Müller, I.: Tribological, electrochemical and tribo-electrochemical characterization of bare and nitrided Ti6Al4V in simulated body fluid solution. Corrosion Science, 53(5):1786–1793, May 2011.
250. a.K. Shukla, Balasubramaniam, R., and Bhargava, S.: Properties of passive film formed on CP titanium, Ti6Al4V and Ti13.4Al29Nb alloys in simulated human body conditions. Intermetallics, 13(6):631–637, June 2005.
251. Barril, S., Mischler, S., and Landolt, D.: Influence of fretting regimes on the tribocorrosion behaviour of Ti6Al4V in 0.9wt.% sodium chloride solution. Wear, 256(9-10):963–972, May 2004.
252. Royhman, D., Yuan, J. C., Shokuhfar, T., Takoudis, C., Sukotjo, C., and Mathew, M. T.: Tribocorrosive behaviour of commonly used temporomandibular implants in a synovial fluid-like environment: Ti6Al4V and CoCrMo. Journal of Physics D: Applied Physics, 46(40):404002, October 2013.
253. Alves, S. A., Bayón, R., Igartua, A., Saénz de Viteri, V., and Rocha, L. A.: Tribocorrosion behaviour of anodic titanium oxide films produced by plasma electrolytic oxidation for dental implants. Lubrication Science, pages n/a–n/a, July 2013.
254. Runa, M., Mathew, M., and Rocha, L.: Tribocorrosion response of the Ti6Al4V alloys commonly used in femoral stems. Tribology International, 68:85–93, December 2013.
255. Yang, B.: Preparation of bioactive titanium metal via anodic oxidation treatment. Biomaterials, 25(6):1003–1010, March 2004.

256. Tarniowy, A., Mania, R., and Rekas, M.: The effect of thermal treatment on the structure, optical and electrical properties of amorphous titanium nitride thin films. Thin Solid Films, 311(1-2):93–100, December 1997.
257. Wang, S., Liao, Z., Liu, Y., and Liu, W.: Different tribological behaviors of titanium alloys modified by thermal oxidation and spraying diamond like carbon. Surface and Coatings Technology, 252:64–73, August 2014.
258. Luo, Y., Chen, W., Tian, M., and Teng, S.: Thermal oxidation of Ti6Al4V alloy and its biotribological properties under serum lubrication. Tribology International, January 2015.
259. Utu, I., Marginean, G., Hulka, I., Serban, V., and Cristea, D.: Properties of the thermally sprayed Al₂O₃TiO₂ coatings deposited on titanium substrate. International Journal of Refractory Metals and Hard Materials, 51:118–123, July 2015.
260. Wang, S., Liu, Y., Zhang, C., Liao, Z., and Liu, W.: The improvement of wettability, biotribological behavior and corrosion resistance of titanium alloy pretreated by thermal oxidation. Tribology International, 79:174–182, November 2014.
261. Dalili, N., Edrisy, A., Farokhzadeh, K., Li, J., Lo, J., and Riahi, A.: Improving the wear resistance of Ti6Al4V/TiC composites through thermal oxidation (TO). Wear, 269(7-8):590–601, August 2010.
262. Materials Properties Handbook: Titanium Alloys. ASM International, 1993.
263. for Metals, A. S.: Metals Handbook. 9th Ed. Vol.3. Properties and Selection Stainless Steels, Tool Materials & Special-purpose Metal. ASM, 1980.
264. Committee, A. I. H.: Properties and Selection: Nonferrous Alloys and Special- Purpose Materials. ASM International, 1990.
265. Holt, J. M.: Structural Alloys Handbook, Volume 3. CINDAS/Purdue University, 1999.
266. Lee, D. H.: Characterization Of A Thin Hard Layer On A Soft Substrate Theory And Its Application On A Surface-Modified PDMS. Doctor of philosophy, The University of Michigan, 2008.

267. Siva Rama Krishna, D. and Sun, Y.: Effect of thermal oxidation conditions on tribological behaviour of titanium films on 316L stainless steel. Surface and Coatings Technology, 198(1-3):447–453, August 2005.
268. Rosu, M.-C., Suci, R.-C., Mihet, M., and Bratu, I.: Physicalchemical characterization of titanium dioxide layers sensitized with the natural dyes carmine and morin. Materials Science in Semiconductor Processing, 16(6):1551–1557, December 2013.
269. Song, X., Gopireddy, D., and Takoudis, C. G.: Characterization of titanium oxynitride films deposited by low pressure chemical vapor deposition using amide Ti precursor. Thin Solid Films, 516(18):6330–6335, July 2008.
270. Phillippi, C. M. and Lyon, S. B.: Longitudinal-Optical Phonons in TiO₂ (Rutile) Thin-Film Spectra. Physical Review B, 3(6):2086–2087, 1971.
271. Brazdova, V., Veronica, M. G.-P., and Sauer, J.: Vanadium Oxides on Aluminum Oxide Supports . 2 . Structure , Vibrational Properties , and Reducibility of V₂O₅ Clusters on alpha-Al₂O₃(0001). Journal of Physical Chemistry B, 109:23532–23542, 2005.
272. Basset, J. M., Baudouin, A., and Candy, J. P.: Preparation of Single Site Catalysts on Oxides and Metals Prepared via Surface Organometallic Chemistry. 2009.
273. Dhonge, B. P., Mathews, T., Sundari, S. T., Thinaharan, C., Kamruddin, M., Dash, S., and Tyagi, A.: Spray pyrolytic deposition of transparent aluminum oxide (Al₂O₃) films. Applied Surface Science, 258(3):1091–1096, November 2011.
274. Zhang, Y., Liu, Y., Ge, C., Yin, H., Ren, M., Wang, A., Jiang, T., and Yu, L.: Evolution mechanism of alumina nanofilms on rutile TiO₂ starting from sodium metaaluminate and the pigmentary properties. Powder Technology, 192(2):171–177, June 2009.
275. Tilocca, A. and Selloni, A.: Methanol Adsorption and Reactivity on Clean and Hydroxylated Anatase(101) Surfaces. The Journal of Physical Chemistry B, 108(50):19314–19319, December 2004.
276. Sorescu, D. C., Lee, J., Al-Saidi, W. A., and Jordan, K. D.: Coadsorption properties of CO₂ and H₂O on TiO₂ rutile (110): a dispersion-corrected DFT study. The Journal of chemical physics, 137(7):074704, August 2012.

277. Szekeres, M., Fodor, G., Fazekas, A., Radnai, M., Turzo', K., and De'ka'ny, I.: Formation of octacalcium phosphate by heterogeneous nucleation on a titania surface. Colloid and Polymer Science, 283(6):587–592, December 2004.
278. Popa, M. V., Demetrescu, I., Vasilescu, E., Drob, P., Lopez, A. S., Mirza-Rosca, J., Vasilescu, C., and Ionita, D.: Corrosion susceptibility of implant materials Ti5Al4V and Ti6Al4Fe in artificial extra-cellular fluids. Electrochimica Acta, 49(13):2113–2121, May 2004.
279. Pankewitz, T., Lagutschenkov, A., Niedner-Schatteburg, G., Xantheas, S. S., and Lee, Y.-T.: Infrared spectrum of $\text{NH}_4^+(\text{H}_2\text{O})$: evidence for mode specific fragmentation. The Journal of chemical physics, 126(7):074307, February 2007.
280. Lambert, J. B.: Introduction to organic spectroscopy. New York, Macmillan, 1987.
281. Galhotra, P.: Carbon dioxide adsorption on nanomaterials, 2010.
282. Rubasinghege, G.: Chemical and photochemical reactions on mineral oxide surfaces in gaseous and liquid phases: environmental implications of fate, transport and climatic impacts of mineral dust aerosol, 2011.
283. Maeland, A. J., Rittenhouse, R., Lahar, W., and Romano, P. V.: Infrared reflection-absorption spectra of anodic oxide films on aluminum. Thin Solid Films, 21(1):67–72, March 1974.
284. Khafagy, A. H., Ewaida, M. A., Higazy, A. A., Ghoneim, M. M. S., Hager, I. Z., and El-Bahnasawy, R.: Infrared spectra and composition dependence investigations of the vitreous V205 / P205 system. Journal of Materials Science, 27:1435–1439, 1992.

APPENDICES

Appendix A

PERMISSION TO USE PREVIOUSLY PUBLISHED MATERIALS

Chapter 2.1 was previously published as "Novel functionalization of Ti-V alloy and Ti-II using atomic layer deposition for improved surface wettability" in Colloids and Surfaces B: Biointerfaces. This journal permits authors to use their paper in thesis. The following statement is given on their webpage,

http://www.elsevier.com/about/policies/lightbox_scholarly-purposes

"Lightbox Personal Use Personal use Authors can use their articles, in full or in part, for a wide range of scholarly, non-commercial personal purposes as outlined below:

1. Use by an author in the authors classroom teaching (including distribution of copies, paper or electronic)
2. Distribution of copies (including through e-mail) to known research colleagues for their personal use (but not for Commercial Use)
3. Inclusion in a thesis or dissertation (provided that this is not to be published commercially)
4. Use in a subsequent compilation of the authors works
5. Extending the Article to book-length form
6. Preparation of other derivative works (but not for Commercial Use)
7. Otherwise using or re-using portions or excerpts in other works

Appendix A (Continued)

8. In addition to this, authors can also use their article for scholarly purposes.

Please note these rights apply for all Elsevier authors who publish their article as either a subscription article or an open access article. In all cases we require that all Elsevier authors always include a full acknowledgement and, if appropriate, a link to the final published version hosted on Science Direct.”

Parts of chapter 2.2 were previously published in Journal of Oral Implantology (JOI) as “Investigation of the Formation of TiO₂ Nanotubes on Thermally Formed Oxide of Ti-6Al-4V”. JOI is published by Allen Press Publishing Services. Written permission from Allen Press Publishing Services is given in the next page.

Chapter 2.4 was previously published as ”Design, Development, and Testing of a Compact Tribocorrosion Apparatus for Biomedical Applications” in Journal of Bio- and Tribo-Corrosion. Written permission for the use of tables and figures & text from Springer Science+Business Media, which controls the copyright, is given in the next pages.

Appendix A (Continued)



Date: February 16, 2015

Dear Arman Butt,

On behalf of Allen Press Publishing Services, I am pleased to grant permission to you for the reprinting of the following:

"A Novel Investigation of the Formation of TiO₂ Nanotubes on Thermally Formed Oxide of Ti-6Al-4V" by Butt, et al. anticipated in the *Journal of Oral Implantology*.

For use in thesis.

This permission is a one-time, non-exclusive, electronic worldwide grant for English language use as described in this letter, and is subject to the following conditions:

1. No payment required.
2. Each copy containing our material that you reproduce or distribute must bear the appropriate copyright information, crediting the author, journal, and publisher (*Journal of Oral Implantology* Allen Press Publishing Services).

If these terms are acceptable, please sign and date, and fax back to my attention at 785-843-1853. This permission will be effective upon our receipt of the signed contract. If applicable, when sending payment, please make clear reference to our title and author. Materials should be addressed to the *Journal of Oral Implantology*, c/o Lindsey Givens, P.O. Box 1897, Lawrence, KS 66044.

Sincerely,

Lindsey Givens
Associate Publisher
Allen Press Publishing Services

AGREED: Arman Butt DATE: 3/27/15
We have elected not to use this material

Figure 50: Permission for use of the material in Chapter 2.2 previously published in *Journal of Oral Implantology* (JOI).

Appendix A (Continued)



01_02

PERMISSION LETTER

May 13, 2015

Springer reference

Journal of Bio- and Tribo-Corrosion

December 2014, 1:4

Date: 12 Dec 2014

Design, Development, and Testing of a Compact Tribocorrosion Apparatus for Biomedical Applications

Authors: Arman Butt, Newton B. Lucchiari Jr., Dmitry Royhman, Maria J. Runa, Mathew T. Mathew, Cortino Sukotjo, Christos G. Takoudis

© Springer International Publishing AG 2014

Materials to be used: All tables and figures

DOI 10.1007/s40735-014-0004-6

Print ISSN 2198-4220

Online ISSN 2198-4239

Journal no. 40735

Your project

Requestor: Arman Butt
jamilarman@gmail.com

University: University of Illinois

Purpose: Dissertation/Thesis

With reference to your request to reuse material in which **Springer Science+Business Media** controls the copyright, our permission is granted free of charge under the following conditions:

Springer material

- represents original material which does not carry references to other sources (if material in question refers with a credit to another source, authorization from that source is required as well);
- requires full credit (Springer and the original publisher, book/journal title, chapter/article title, volume, year of publication, page, name(s) of author(s), original copyright notice) to the publication in which the material was originally published by adding: "With permission of Springer Science+Business Media";
- figures, illustrations, and tables may be altered minimally to serve your work. Any other abbreviations, additions, deletions and/or any other alterations shall be made only with prior written authorization of the author and/or Springer Science+Business Media;
- **Springer does not supply original artwork or content.**

This permission

- is non-exclusive;
- is valid for one-time use only for the purpose of defending your thesis limited to university-use only and with a maximum of 100 extra copies in paper. If the thesis is going to be published, permission needs to be reobtained.
- includes use in an electronic form, provided it is an author-created version of the thesis on his/her own website and his/her university's repository, including UMI (according to the definition on the Sherpa website: <http://www.sherpa.ac.uk/romeo/>);
- is subject to courtesy information to the author (address is given in the publication);
- is personal to you and may not be sublicensed, assigned, or transferred by you to any other person without Springer's written permission;
- is only valid if no personal rights, trademarks, or competitive products are infringed.

Figure 51: Permission for use of tables and figures in Chapter 2.4 previously published in Journal of Bio- and Tribo-Corrosion.

Appendix A (Continued)



01_03

PERMISSION LETTER

May 13, 2015

Springer reference

Journal of Bio- and Tribo-Corrosion

December 2014, 1:4

Date: 12 Dec 2014

Design, Development, and Testing of a Compact Tribocorrosion Apparatus for Biomedical Applications

Authors: Arman Butt, Newton B. Lucchiarri Jr., Dmitry Royhman, Maria J. Runa, Mathew T. Mathew, Cortino Sukotjo, Christos G. Takoudis

@ Springer International Publishing AG 2014

DOI 10.1007/s40735-014-0004-6

Print ISSN 2198-4220

Online ISSN 2198-4239

Journal no. 40735

Your project

Requestor: Arman Butt
jamilarman@gmail.com

University: University of Illinois

Purpose: Dissertation/Thesis

With reference to your request to reuse material in which Springer Science+Business Media controls the copyright, our permission is granted free of charge under the following conditions:

Springer material

- represents original material which does not carry references to other sources (if material in question refers with a credit to another source, authorization from that source is required as well);
- requires full credit (Springer and the original publisher, book/journal title, chapter/article title, volume, year of publication, page, name(s) of author(s), original copyright notice) to the publication in which the material was originally published by adding: "With permission of Springer Science+Business Media";
- may not be altered in any manner. Abbreviations, additions, deletions and/or any other alterations shall be made only with prior written authorization of the author and/or Springer Science+Business Media;
- Springer does not supply original artwork or content.

This permission

- is non-exclusive;
- is valid for one-time use only for the purpose of defending your thesis and with a maximum of 100 extra copies in paper. If the thesis is going to be published, permission needs to be reobtained.
- includes use in an electronic form, provided it is an author-created version of the thesis on his/her own website and his/her university's repository, including UMI (according to the definition on the Sherpa website: <http://www.sherpa.ac.uk/romeo/>);
- is subject to courtesy information to the co-author or corresponding author;
- is personal to you and may not be sublicensed, assigned, or transferred by you to any other person without Springer's written permission;
- is only valid if no personal rights, trademarks, or competitive products are infringed.

This license is valid only when the conditions noted above are met.

Permission free of charge does not prejudice any rights we might have to charge for reproduction of our copyrighted material in the future.

Branch of Springer-Verlag GmbH, Heidelberger Platz 3, 14197 Berlin, Germany | Amtsgericht Berlin-Charlottenburg, HRB 91881 B
Managing Directors: Derk Haank, Martin Mos, Peter Hendriks | Springer is part of Springer Science+Business Media

Figure 52: Permission for use of the text in Chapter 2.4 previously published in Journal of Bio- and Tribo-Corrosion.

Appendix B

SUPPLEMENTARY MATERIAL

B.1 Fourier Transform Infrared Spectroscopy

B.1.1 Surface Composition and Crystallinity

GIXRD Analysis for Chapter 2.3

Group labels are given in Chapter 2.3. Peaks at 2θ of 35.5, 38.4, 40.3, 53.4, 63.5, 71.0, and 77.0 are observed on all of the GIXRD spectra and are assigned to titanium at 2θ of 35.094 {100}, 38.422 {002}, 40.171 {101}, 53.005 {102}, 62.950 {110}, 70.662 {103}, and 77.370 {201}. Only spectra of TO-600 and TO-700 samples did not have titanium peak at 2θ of 77.0, possibly due to the large scale oxidation of Ti to TiO_2 (corroborated by the calculated diffusion depths). Similarly, the peak at 2θ of 53.4 was not observed in the spectra of TO-700 samples. The peak at 77.0 may also be assigned to vanadium at 2θ of 77.081 {211}. A peak at 2θ of 78.0 is observed on all GIXRD spectra except for control and TO-700 samples that may be assigned to aluminum at 2θ of 78.229 {311} or to alumina at 2θ of 78.199 {311}. However, since this peak does not appear on TO-700 samples, where alumina is observed in EDS spectra (explained later), the peak is more likely to be for aluminum. Large titanium peaks such as at 2θ of 40.5 decrease dramatically in the spectra of TO-700 samples, indicating much of the surface titanium has been converted to TiO_2 . While anatase of 38.572 {112} and 53.885 {105} may exist under the peaks at 2θ of 38.4 and 53.4, it is difficult to determine whether the peaks size and location

Appendix B (Continued)

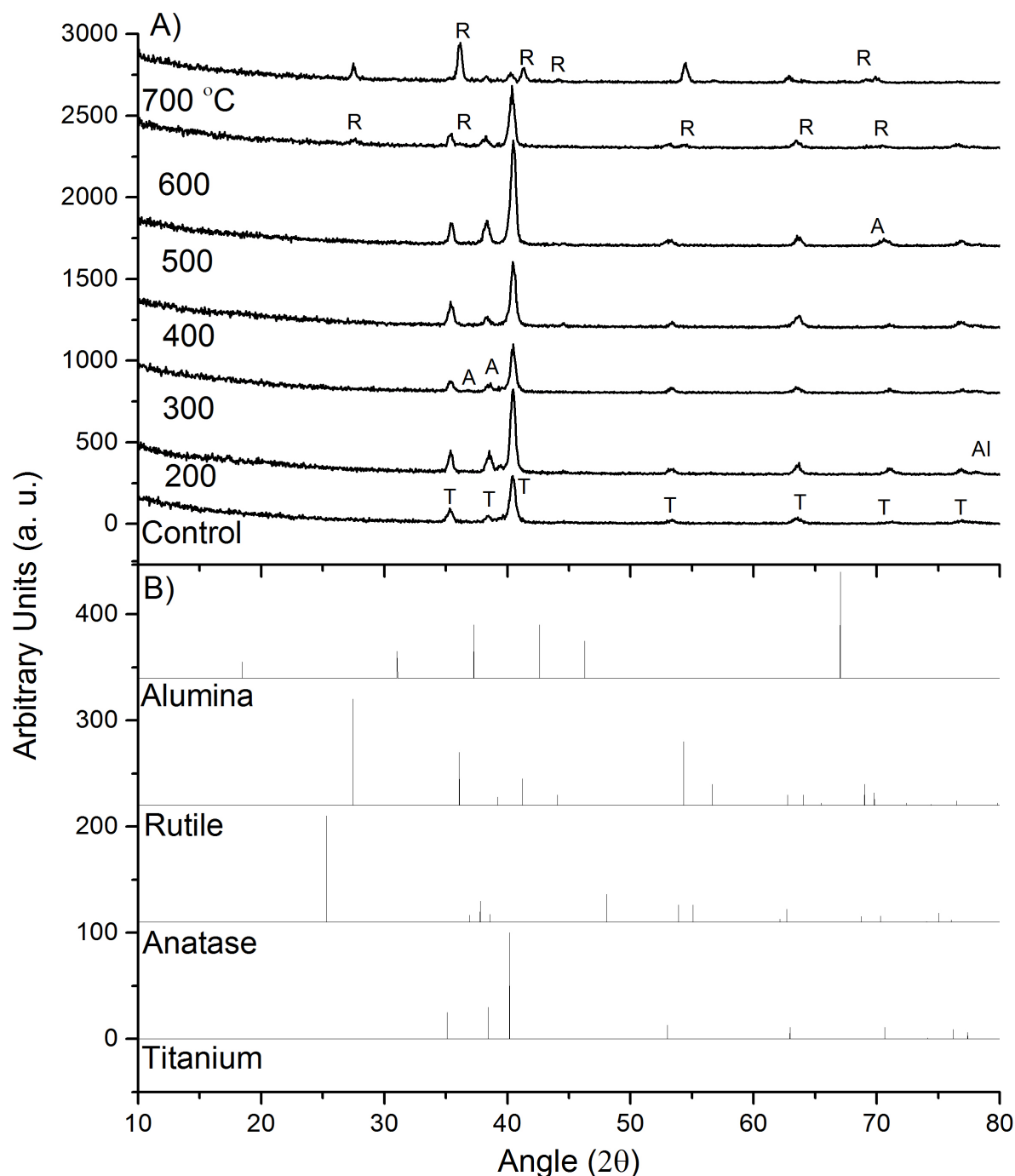


Figure 53: A) Grazing incidence x-ray diffraction (GIXRD) spectroscopy of control and TO-treated samples. Significant differences in crystalline structures are observed as a function of treatment temperature. B) PDF spectra of titanium, anatase, rutile, and alumina are provided. GIXRD spectroscopy was conducted using a point parallel plate configuration, 0.1542 nm x-ray emission line of Cu point focus x-ray source, and 2-theta-omega setting. An angle of incidence of 1 ° was used to optimize sensitivity for the thin crystalline TiO₂ films.

Appendix B (Continued)

are shifting due to the incorporation of the anatase peaks. A spectra-to-spectra comparison suggests that for the peak at 2θ of 38.4, there is a slight increase in the peak size between the spectra of TO-300 and TO-500 samples, possibly due to the incorporation of anatase, followed by a decrease in the peak size in spectra of TO-600 and further in the spectra of TO-700, possible due to the anatase converting to rutile. In the spectra of TO-300, it can be seen that the peak centered at 2θ of 38.5 has two shoulder peaks, one at 2θ of 38.6 and the other at 2θ of 38.4, corresponding to anatase and titanium, respectively. Although a likely irregularity, the spectra of TO-200 samples suggests an increase in the intensity of the peak centered at 2θ of 38.5; nearly all peaks for TO-200 are larger as compared to spectra of other samples. The changes in the peak at 2θ of 53.4 are less clear. There is a down-shift in the peak location starting with the spectra of TO-500 and a decrease in the intensity in the spectra of TO-700 samples. The two peaks for anatase and Ti near 2θ of 53.4 are in close proximity, therefore it is likely that as Ti converts to anatase, the loss and gain of peak intensities occurs close to each other and the change is not obvious, except for when both Ti and anatase convert to rutile and the peak intensity decreases in the spectra for 700TNT samples. Anatase peaks of 62.117 $\{213\}$ and 62.692 $\{204\}$ at 2θ of 62.6 are observed in the spectra of TO-400 samples, however, the intensity is low and the peaks do not appear for the other spectra. It may be that these anatase facet(s) only appear at heat treatments of 400 °C and are converted to rutile above 400 °C. An anatase peak of 70.303 $\{220\}$ is observed in the spectra of 500TNT, which declines in the spectra of 600TNT samples and more so in spectra of TO-700 samples. A peak at 2θ of 27.5 is observed in the spectra of 600TNT which becomes larger in the spectra of TO-700, and

Appendix B (Continued)

is assigned to the rutile peak at 2θ of 27.447 {110}. Large rutile peaks at 2θ of 36.086 {101}, 41.226 {111}, 54.323 {211}, a smaller rutile peak at 2θ of 62.742 {002}, and two minor peaks at 2θ of 69.010 {301} and 69.790 {112} are observed only in the spectra of TO-700 samples. The shoulders at 2θ of 64.1 and 76.5 for the larger titanium peaks at 2θ of 63.5 and 77.0 are observed starting in the spectra of TO-400 samples and both may be assigned to rutile of 64.040 {310} and 76.509 {202}. There is a clear down-shift to 2θ of 76.5 in the spectra of TO-600 samples. Based on the GIXRD data, it can be seen that some facets of anatase, such as the (1 1 2) facet, appear at temperature of treatment as low as 200 °C, however anatase is clearly observed at temperature of treatment of 300 °C. Similarly, some facets of rutile are observed at temperature of treatment as low as 400 °C. In addition, the lower quantities of anatase suggest that longer durations of TO treatment at 300 and 400 °C are needed for significant presence of anatase.

*FTIR Spectra Analysis of TO-treated Samples (**Figure 55**, **Figure 56**, **Figure 57**, **Figure 58**, **Figure 59**, **Figure 60**, and **Figure 61**)*

For FTIR analysis, the de-convolution may include peak positions blue-shifted (lower cm^{-1}) or red-shifted (higher cm^{-1}) compared to absorption bands reported in literature due to 1) the irregular surface roughness and 2) the various components of the alloy and their effect on surrounding bond stretch/vibrations. Due to the residual air in the FTIR purging chamber, the following peaks are observed for all FTIR spectra. Three minor peaks seen between 2320 - 2380 cm^{-1} are associated with gas phase CO_2 (158) and the noise seen between 3000-3800 cm^{-1} and between 1400-2000 cm^{-1} are associated with the O-H bond stretch and vibration

Appendix B (Continued)

intensities of absorbed/adsorbed and dissociated H_2O (153; 202; 150; 157; 149; 155; 156; 203), CO_2 (158), CO_3^{-2} (158; 204), or carboxyl groups (COO^-) from interaction of TiO_2 with CO_2 or any surface carbon contamination(203; 203). While a low quantity, a sharp CO_2 peak is observed at 667 cm^{-1} which increases as a function of TO-treatment temperature, suggesting that crystalline TiO_2 more readily accepts CO_2 absorption.(144; 143) As stated earlier, TO-treatment induces crystallinity and thicker oxides, which increase peaks at certain locations within the metal-oxide region of $400\text{-}1200\text{ cm}^{-1}$, therefore altering the overall peak location in the metal-oxide region. In general, crystallization downshifts the metal-oxide peaks. The common peak regions mentioned earlier are labeled in **Figure 54** in the main paper.

In **Figure 55**, with the exception of the characteristic regions for CO_2 and H_2O signatures from the chamber, there should be no peaks in the spectra of control samples since the background sample and control sample are the same.

The FTIR spectra of TO-200 sample (**Figure 56**), is also nearly flat with some minor peaks. Likewise, samples with high temperature of treatment are observed to have peaks of higher intensities.

In addition, anatase TiO_2 is observed to increase and decrease as temperature of treatment is raised from 300 to $600\text{ }^\circ\text{C}$ (**Figure 57**, **Figure 58**, **Figure 59**,and **Figure 60**) and disappear by $700\text{ }^\circ\text{C}$ (**Figure 61**). At the same time, rutile TiO_2 is observed to increase at treatment temperatures $\geq 400\text{ }^\circ\text{C}$ (**Figure 58**, **Figure 59**, **Figure 60**, and **Figure 61**).

It is noted that not all peaks for anatase or rutile are observed where these TiO_2 structures are present, which leads to the assumption that certain temperature of treatments produce

Appendix B (Continued)

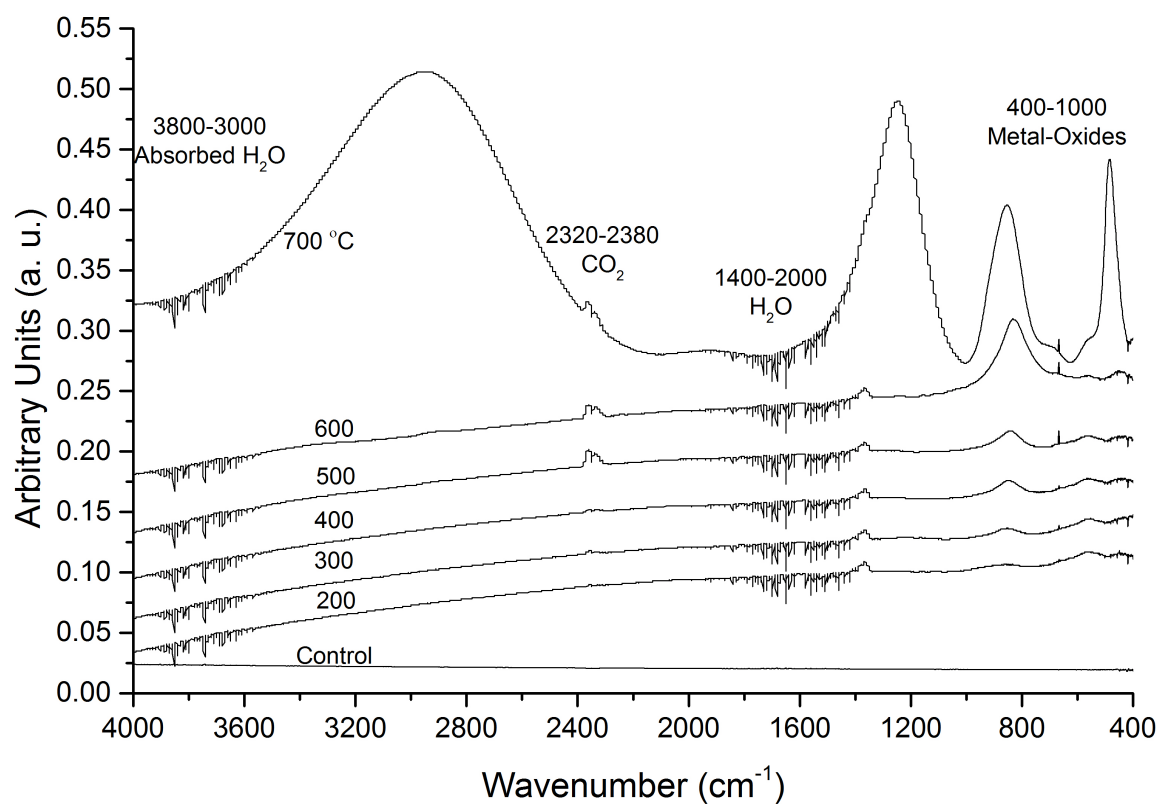


Figure 54: Compiled FTIR spectra of all TO-treated and control samples. Common peaks are labeled.

Appendix B (Continued)

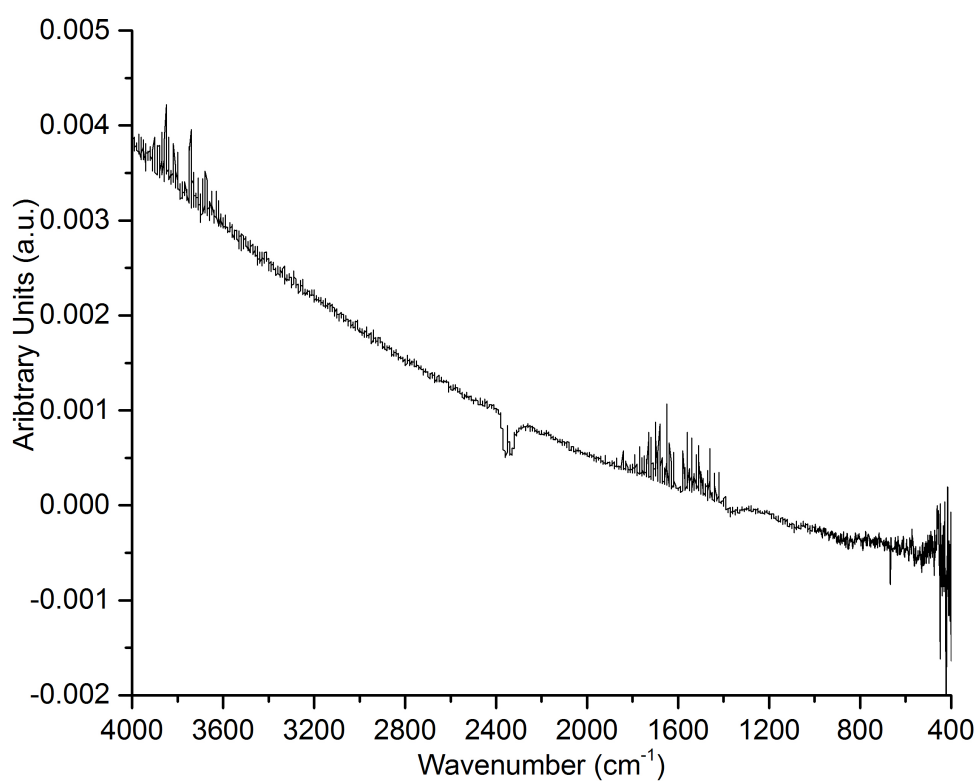


Figure 55: Absorbance Fourier transform infrared (FTIR) spectrum of a control sample. The water (3800-3000 and 2000-1400 cm^{-1}) and carbon dioxide (2380-2320 and 667 cm^{-1}) regions are from the FTIR chamber gases. No other significant signatures are observed as both the background and control have similar chemical composition. Absorbance FTIR spectroscopy was conducted with a diffuse reflectance accessory and a deuterated triglycine sulfate (DTGS) KBr detector.

Appendix B (Continued)

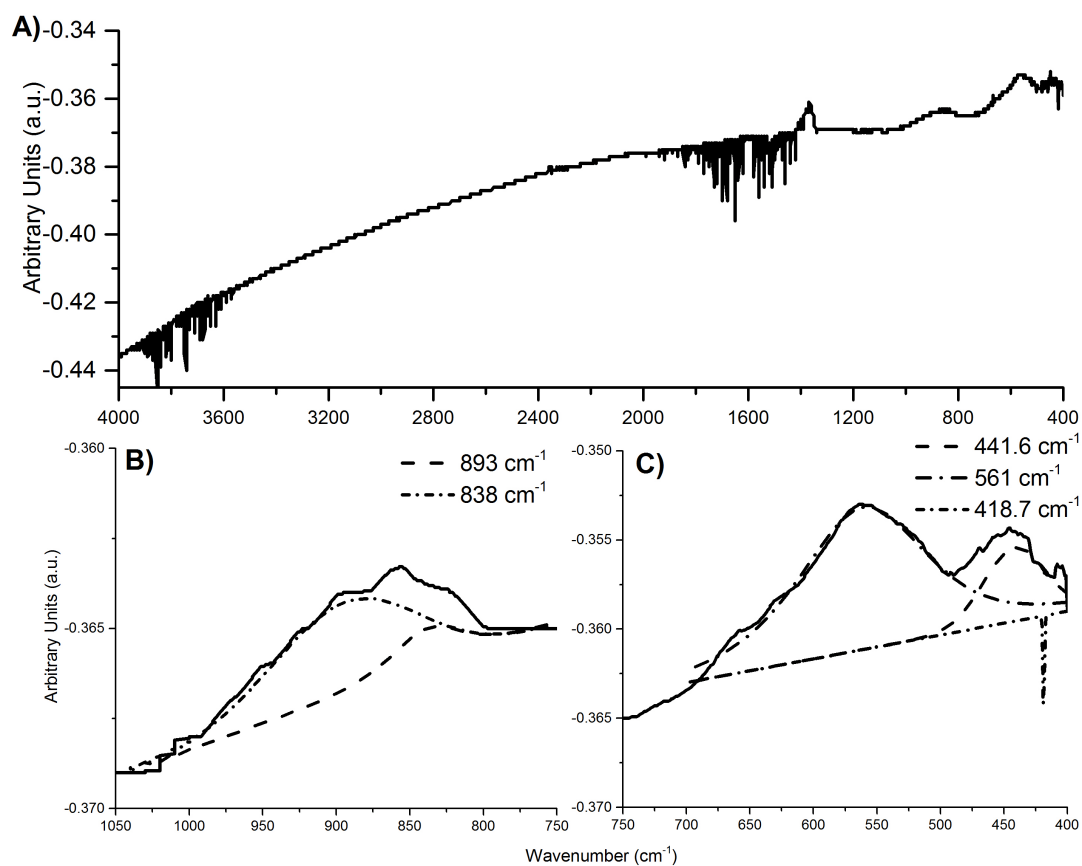


Figure 56: Absorbance FTIR spectra of a TO-200 sample. The water (3800-3000 and 2000-1400 cm^{-1}) and carbon dioxide (2380-2320 and 667 cm^{-1}) regions are from the ambient gases in the FTIR chamber. Part A contains the entire spectra and parts B-C contain sections of the spectra containing deconvoluted peaks. Characterization conditions are same as in **Figure 55**.

Appendix B (Continued)

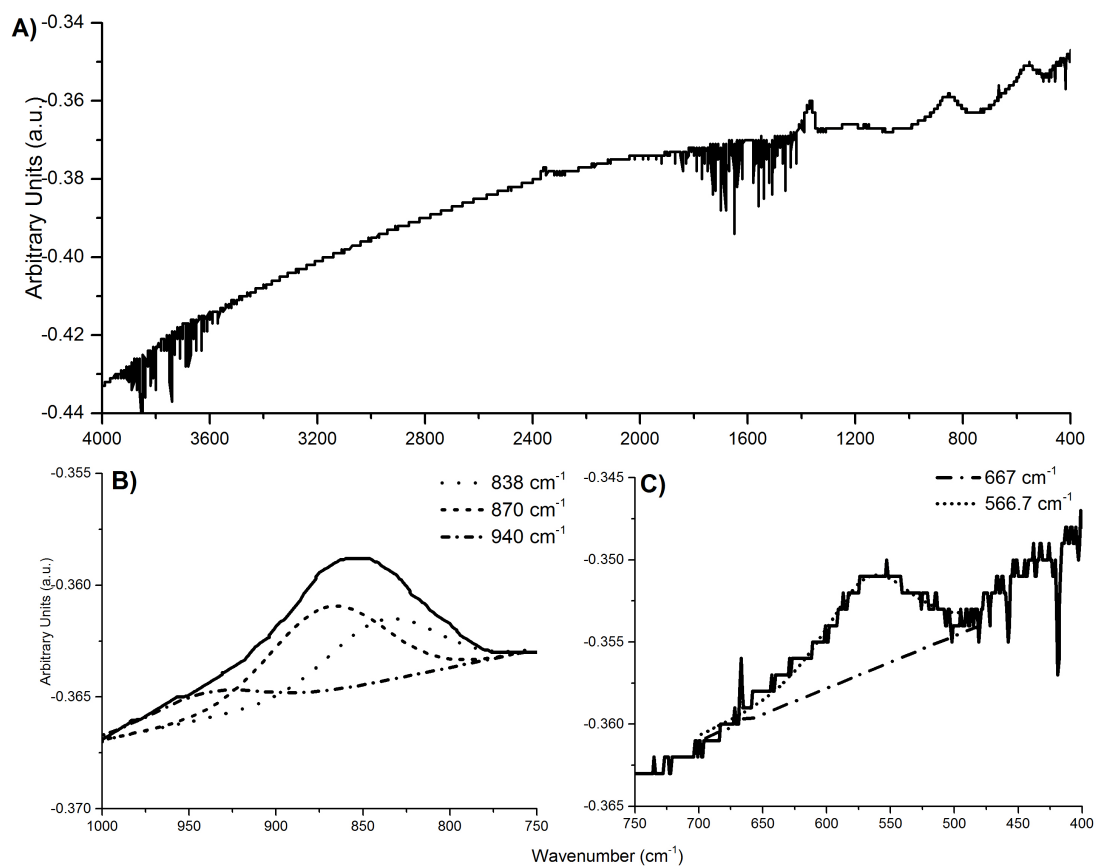


Figure 57: Absorbance FTIR spectra of a TO-300 sample. The water (3800-3000 and 2000-1400 cm^{-1}) and carbon dioxide (2380-2320 and 667 cm^{-1}) regions are from the ambient gases in the FTIR chamber. Part A contains the entire spectra and parts B-C contain sections of the spectra containing deconvoluted peaks. Characterization conditions are same as in **Figure 55**.

Appendix B (Continued)

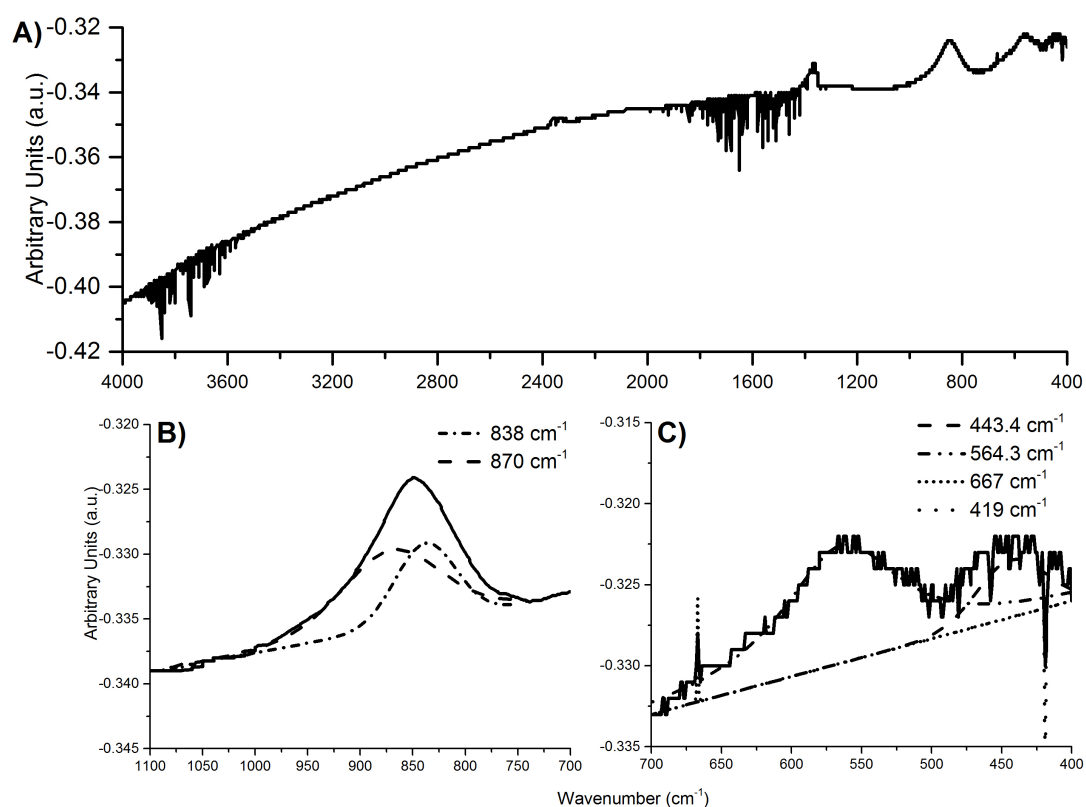


Figure 58: Absorbance FTIR spectra of a TO-400 sample. The water (3800-3000 and 2000-1400 cm⁻¹) and carbon dioxide (2380-2320 and 667 cm⁻¹) regions are from the ambient gases in the FTIR chamber. Part A contains the entire spectra and parts B-C contain sections of the spectra containing deconvoluted peaks. Characterization conditions are same as in **Figure 55**.

Appendix B (Continued)

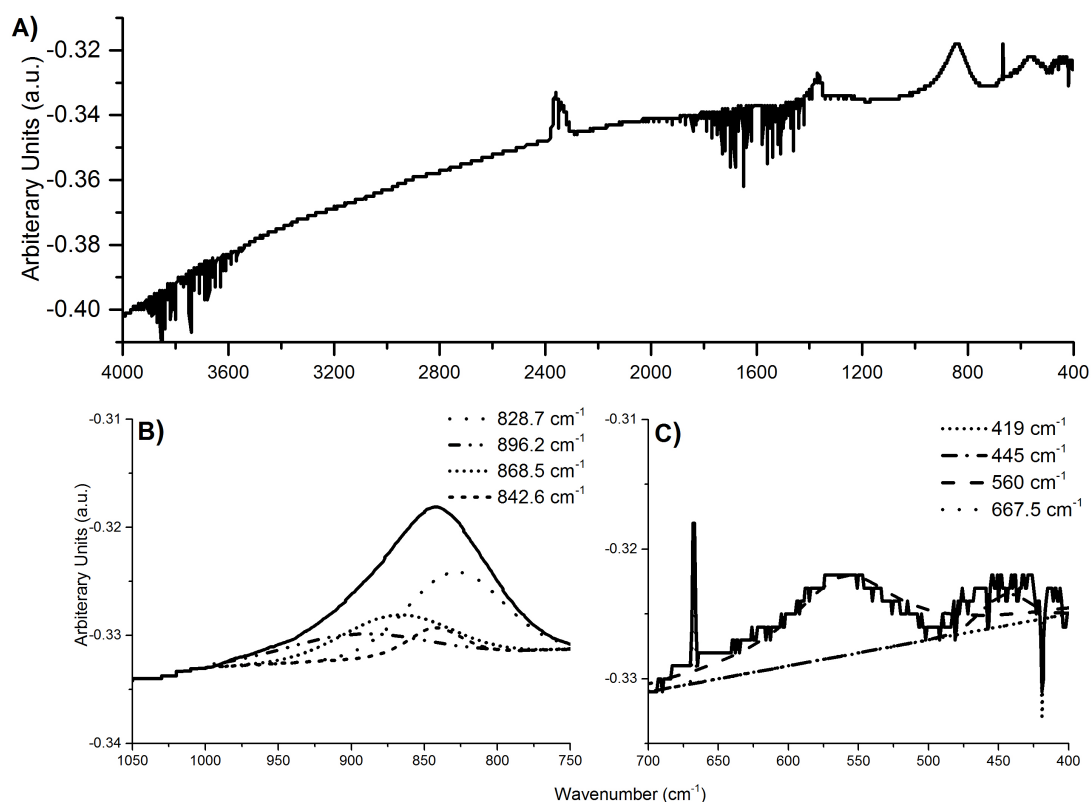


Figure 59: Absorbance FTIR spectra of a TO-500 sample. The water (3800-3000 and 2000-1400 cm^{-1}) and carbon dioxide (2380-2320 and 667 cm^{-1}) regions are from the ambient gases in the FTIR chamber. Part A contains the entire spectra and parts B-C contain sections of the spectra containing deconvoluted peaks. Characterization conditions are same as in **Figure 55**.

Appendix B (Continued)

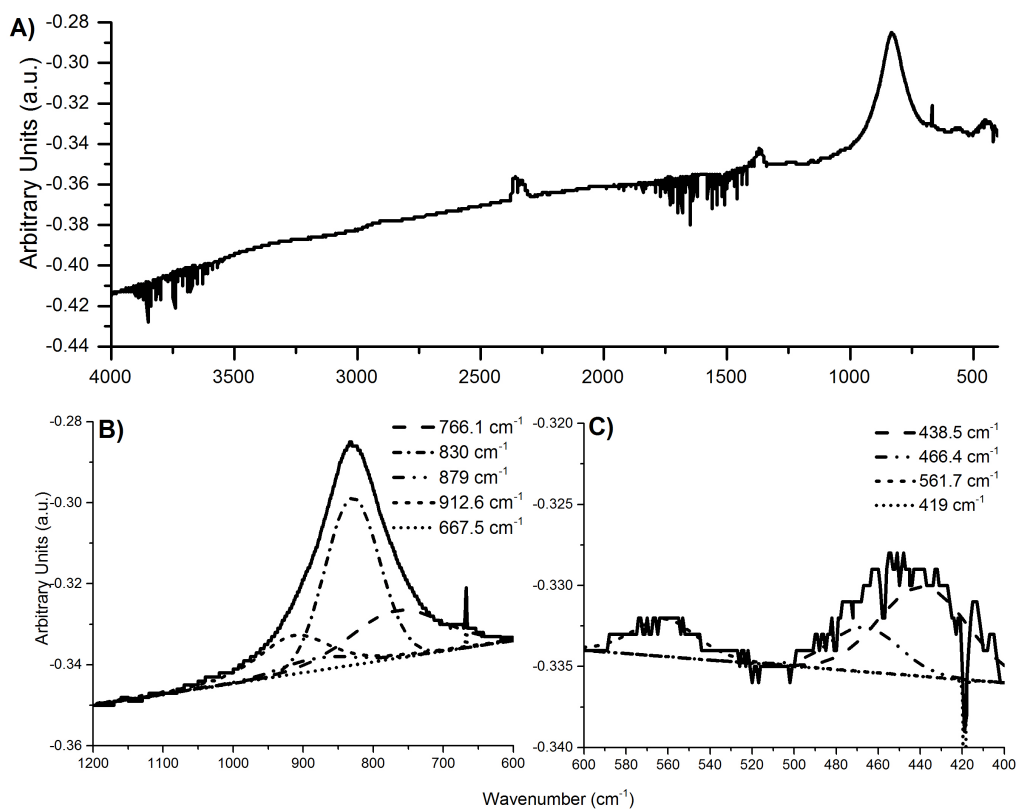


Figure 60: Absorbance FTIR spectra of a TO-600 sample. The water (3800-3000 and 2000-1400 cm^{-1}) and carbon dioxide (2380-2320 and 667 cm^{-1}) regions are from the ambient gases in the FTIR chamber. Part A contains the entire spectra and parts B-C contain sections of the spectra containing deconvoluted peaks. Characterization conditions are same as in **Figure 55**.

Appendix B (Continued)

different facets of the same TiO_2 structure. Finally, a significant increase in alumina and byproducts of reactions between rutile and surface CO_2 , carbon contamination, and H_2O are observed in the spectra of TO-700 samples (**Figure 61**). Further explanation is given next.

For the various peaks found in all the spectra, deconvolution of the peaks and a plot of the area under the peaks provides information regarding trends of amorphous, anatase, and rutile TiO_2 (not shown). Specifically, certain peaks have several assignments in literature and by comparing the areas under the peaks between the TO-treated samples, we can deduce which assignment is more likely. For example, all TO-treated samples contain a peak between 558-567 cm^{-1} that can be assigned to anatase (550 cm^{-1}) (141), Ti-O bonds (550 cm^{-1}) (139), Ti-O-Ti bonds (500-680 cm^{-1}) (268), or rutile (550-560 cm^{-1}) (150). By plotting the area under the respective peaks, it is found that the peak may belong to amorphous TiO_2 . The area under the peak is highest for TO-200 samples (**Figure 56**) and an erratic but overall decrease is observed as a function of treatment temperature and since anatase and rutile first appear in GIXRD spectra of TO-300 and TO-400 samples (figure 9 in main paper), respectively, anatase and rutile can be ruled out. Anatase would experience an increase and reduction and rutile would experience an increase between 300-700 °C TO-treatment, however this is not observed. A general Ti-O and Ti-O-Ti bond would increase continuously for higher temperature of treatment, and this is also not observed. Therefore the peak may belong to amorphous TiO_2 , which, as observed, would decrease as a function of treatment temperature. Similar assessment is made for all other deconvoluted peaks. For TO-200, 500, and 700 samples, a peak is observed between 893-896 cm^{-1} and due the peak areas exponential growth, it is assigned to the O-

Appendix B (Continued)

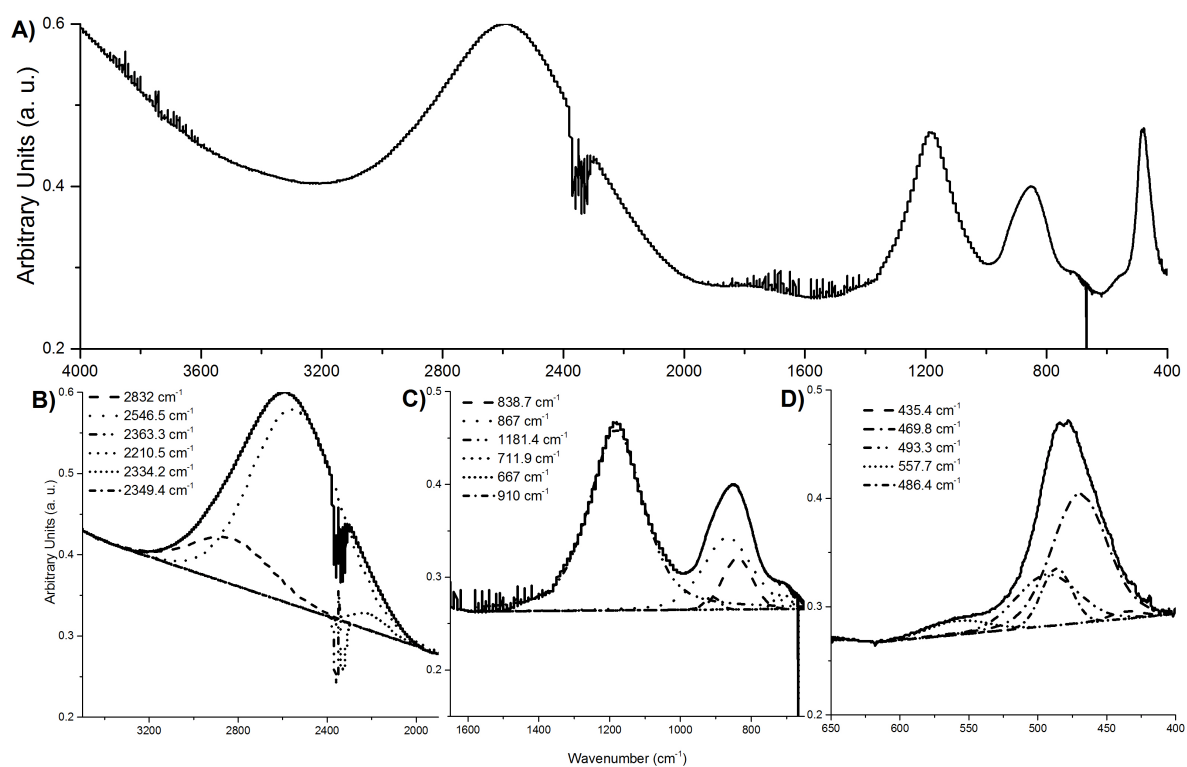


Figure 61: Absorbance FTIR spectra of a TO-700 sample. The water (3800-3000 and 2000-1400 cm^{-1}) and carbon dioxide (2380-2320 and 667 cm^{-1}) regions are from the ambient gases in the FTIR chamber. Part A contains the entire spectra and parts B-C contain sections of the spectra containing deconvoluted peaks. Characterization conditions are same as in **Figure 55**.

Appendix B (Continued)

O bonds in $\text{TiO}_2(147)$ (**Figure 56**, **Figure 59**, and **Figure 61**). Similarly, for TO-200, 300, 400 and 500 samples, a peak is observed between $838\text{-}843\text{ cm}^{-1}$ that is assigned to $\text{TiO-OH}(151)$ (**Figure 56**, **Figure 57**, **Figure 58**, **Figure 59**). These two peaks suggest an increase in TiO_2 as temperature of treatment is increased. For all samples except for TO-300, peaks centered between $442\text{-}445\text{ cm}^{-1}$ are observed that may be assigned to anatase and rutile ($435/440\text{ cm}^{-1}$)(150; 155; 203), Ti-O-Ti bonds ($436\text{-}495\text{ cm}^{-1}$) (138), or Ti-O bonds (450 cm^{-1}) (154). However, the peak area does not increase significantly for most samples, except for TO-700, therefore it may correspond to a specific facet of rutile TiO_2 which appears only for 700 °C TO-treatment (**Figure 61**). Looking at GIXRD data (**Figure 53**), large peaks appear representing rutile facets at 27.447 ° {110}, 36.086 ° {101} and 41.226 ° {111} which do not exist for the other temperature treatments. Another peak observed at 493 cm^{-1} for only TO-700 samples is assigned to rutile(269). For all samples, except for TO-200 and TO-700 samples, a peak is observed located between $868\text{-}879\text{ cm}^{-1}$ that can be assigned to the anatase peak located at 870 cm^{-1} (141; 146). The peak area plots show that the peak appears on TO-300 samples (**Figure 57**), reaches its maximum on TO-400 samples (**Figure 58**), and decreases thereon and is no longer present on TO-700 samples (**Figure 61**). This is also corroborated with GIXRD data in **Figure 53**. In addition, a peak is observed between $820\text{-}840\text{ cm}^{-1}$ for TO-500, 600, and 700 samples that can be assigned to rutile (830 cm^{-1}) (141; 146; 270; 140) and the Ti-O bond of rutile (820 cm^{-1}) (145) (**Figure 59**, **Figure 60**, and **Figure 61**). The peak at 54.323 ° {211} in GIXRD spectra was observed to be increasing steadily for TO-500, TO-600, and TO-700 samples, therefore the FTIR peak may represent the {211} facet of rutile.

Appendix B (Continued)

D. Velten *et al.* also showed with a comparison of heat-treated commercially pure Ti and Ti-alloy that 830 cm^{-1} may entirely belong to rutile TiO_2 and not due to the other elements in the alloy. The dramatic increase in rutile on TO-600 and TO-700 samples is also represented by a peak in the spectra that is observed between $755\text{--}766\text{ cm}^{-1}$ assigned to Ti-O-Ti bonds of rutile (763 cm^{-1}) (145). The peaks at 485 and 848 cm^{-1} are assigned to Al-O bonds of alumina (485 and 845 cm^{-1} , respectively) (269; 271). It should be noted that the alumina signatures are considerably greater for TO-700 samples and EDS data confirms presence of alumina at larger quantities than in other samples (**Figure 61**). This may be in part due to the melting temperature of aluminum being 650°C . TO-treatment at 700°C may have diffused the aluminum to the surface of the sample where it may then be oxidized. A minor sharp negative peak appears at 419 cm^{-1} for all samples except for TO-300 samples (**Figure 57**). This peak, due to its negative area may correspond to amorphous TiO_2 , however, due its small quantity, may simply be noise. While certain general oxide bonds appear, the specific 940 cm^{-1} of amorphous TiO_2 reported in literature(141; 146) was only detected for TO-300 samples. The CO_2 peak of 667 cm^{-1} is observed for all samples except for TO-200 samples (**Figure 56**). This may occur if the purging time for the background sample and TO-200 sample results in equal amount of CO_2 being present in the chamber. Interestingly, the area under the sharp peaks of CO_2 steadily as a function of treatment temperature. As mentioned earlier, crystalline TiO_2 is known to interact with CO_2 .(203; 154) There are several other peaks which are only found in the spectra of TO-700 samples (**Figure 61**). The $1600\text{--}1000\text{ cm}^{-1}$ region is fitted with peaks at 1449.3 , 1372.5 , 1248.3 , 1117.3 , 1541.8 , and 1597 cm^{-1} . The peak

Appendix B (Continued)

at 1449.3 cm^{-1} is assigned to C-O of CO_3^{-2} or CO_2 ($1420/1453$ (158; 204) and 1424 cm^{-1} (158), respectively). The peaks at 1372.5 and 1541.8 cm^{-1} are assigned to COO- bonds (1350 and 1550 cm^{-1}) (154), however, signatures at 1550 cm^{-1} (and 1617 cm^{-1}) can also represent the Ti-OH bond and surface adsorbed H_2O , respectively (149; 204; 154; 139; 268; 138; 272). In addition, peaks at 1370 and 1500 cm^{-1} have been shown to represent the C-O bonds of CO_2 , CO, and CO_3^{-2} . (158; 204; 138; 273) The peak at 1248.3 cm^{-1} is assigned to the bonds between H_2O and -OH groups on TiO_2 and Ti-O-O-H complexes (1222 (138) and 1250 (152) cm^{-1} , respectively) which arise from the dissociation of H_2O when in contact with TiO_2 ; the peak at 1117.3 cm^{-1} is assigned to Ti-OH and hydrated Al-O bonds (1000 - 1300 and $1135/1127/1129\text{ cm}^{-1}$ (274), respectively); the peak at 1597 cm^{-1} is assigned to H-O-H bonds (1600 - 1650 cm^{-1}). In this region are signatures for liquid H_2O (153; 138), H-O-H bending (202; 150), -OH vibration (157; 204; 139), -OH radicals (203), and adsorbed H_2O (155; 156; 138). An additional peak at 1927.1 cm^{-1} is observed. This peak is assigned to the C-O bonds of CO_2 on TiO_2 (1975 cm^{-1}) (272). The 4000 - 2200 cm^{-1} is fitted with peaks at 2335 , 3398.1 , 3164.8 , 2908.1 , and 2365 cm^{-1} . The peaks at 2335 and 2365 cm^{-1} are assigned to CO_2 (2320 - 2380 cm^{-1}); the minor peaks at 2320 , 2350 , and 2380 cm^{-1} represent C-O bonds of CO_2 , CO, and CO_3^{-2} that may arise from the presence and reaction of CO_2 with the surface rutile TiO_2 . (158; 204; 138; 273) The peaks at 3164.8 and 3398.1 cm^{-1} is assigned to OH absorbed on TiO_2 and H_2O on the surface (3400 and 2700 - 3667 cm^{-1}) (153; 150; 151; 138; 148); the peak at 2908.1 cm^{-1} is assigned to C-H bonds (2800 - 3000 and 2932 cm^{-1}) (157; 268). This large peak may be due to chemical signatures of C-H bonds (202; 157; 204; 268; 151; 275) of products from possible reactions between the surface

Appendix B (Continued)

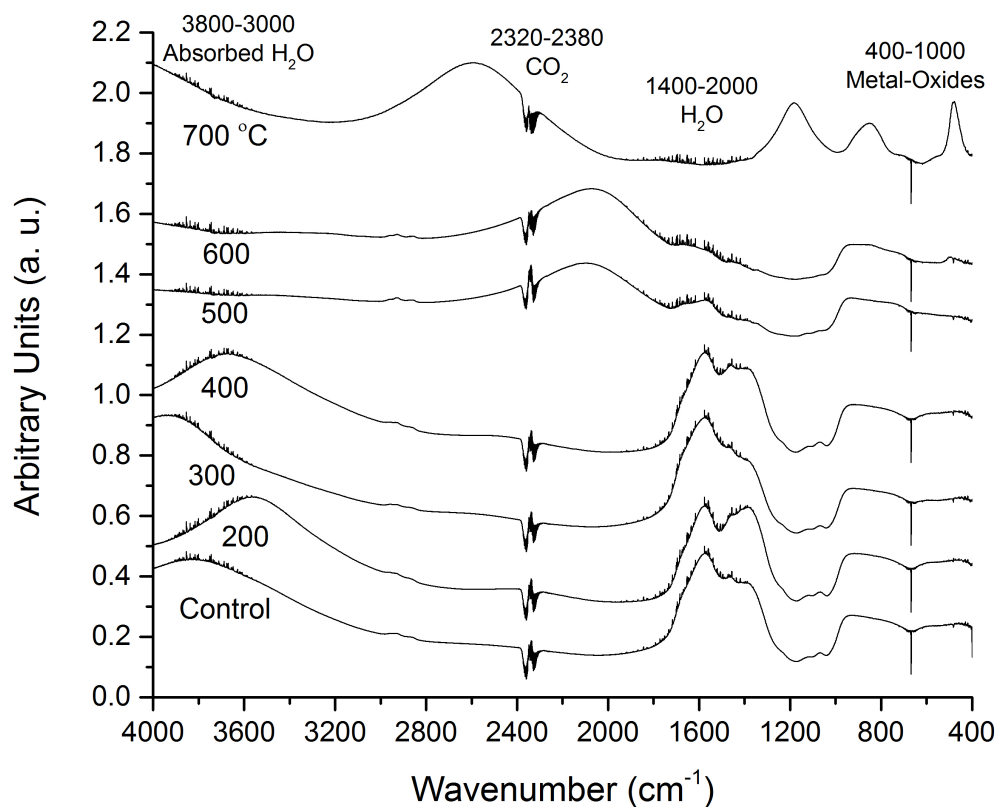


Figure 62: Absorbance FTIR spectra of all anodized samples. Common peaks are labeled. Characterization conditions are same as in **Figure 55**.

rutile TiO_2 and the CO_2 and H_2O in the chamber as discussed by Sorescu et al.³² Fahim et al. states that the C-H signatures may be from surface contamination, however, the lack of C-H signatures in the other spectra leads us to agree with Sorescu *et al.* (204; 276)

FTIR Spectra Analysis of TO/Anodized Samples (**Figure 66**, **Figure 67**, **Figure 68**, **Figure 69**, **Figure 64**, **Figure 65**, and **Figure 68**)

Appendix B (Continued)

As can be seen from **Figure 62** in main paper, the FTIR spectra of TO/anodized samples are nearly identical, with the exception of 700TNT samples. There are five main regions of interest: 2800-4000 cm^{-1} (water adsorption/absorption), 2800-1800 cm^{-1} (water adsorption/absorption and CO_2 adsorption and reaction by-productions), 1800-1200 cm^{-1} (water adsorption/absorption and anodization electrolyte residue), and 1200-400 cm^{-1} (metal-oxide). As it will be later explained, dissolution of TiO_2 is the initial step of anodization, before which nanotubes cannot form.

The oxide obtained on TO-700 samples may have been too thick to be dissolved within 15 minutes. As a result, FTIR spectra of 700TNT samples look similar to that of TO-700 samples (**Figure 61** and **Figure 63**).

In addition, FTIR spectra of 500TNT and 600TNT samples differ from the other FTIR spectra in nearly all the regions of interest, which may be correlated with the lack of surface pores observed (**Figure 64** and **Figure 65**). Lack of surface pores would alter the interaction of ambient H_2O and CO_2 with TNTs, and therefore affect the FTIR spectra. Based on area-under-the-peak plots, no consistent observations for TiO_2 crystalline structure can be made. Amorphous, anatase, and rutile signatures are seen in all samples with significantly larger intensities as compared to TO-treated samples. Significant signatures for H_2O , CO_2 , and contamination from anodization electrolyte are observed on all TO/anodized samples. All samples also have signatures for alumina, which may be present in small quantities left-over from the anodization process. Generally speaking, the analysis of FTIR spectra in this study are in agreement with those reported by D. H. Shin et al. and S. Patel, et al., however, this

Appendix B (Continued)

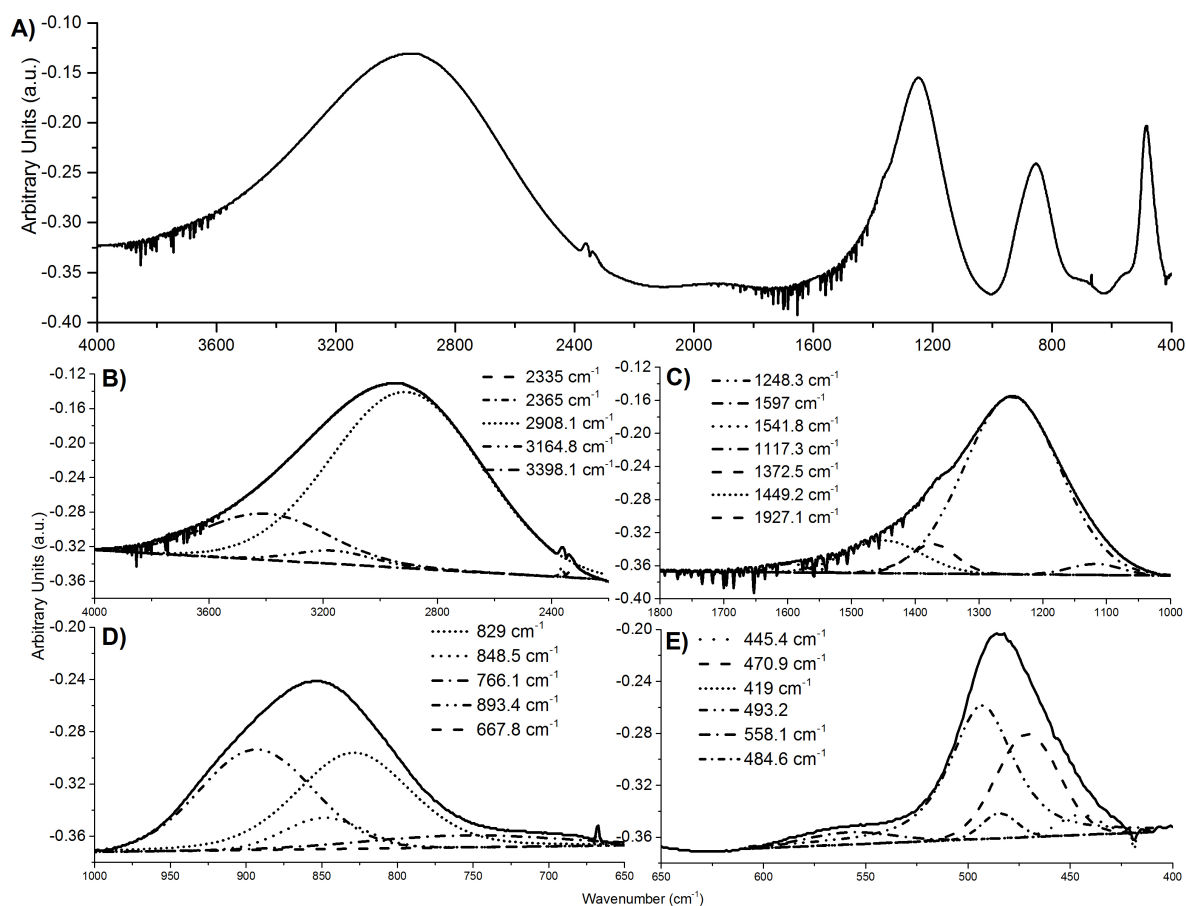


Figure 63: Absorbance FTIR spectra of a 700TNT sample. The water (3800-3000 and 2000-1400 cm⁻¹) and carbon dioxide (2380-2320 and 667 cm⁻¹) regions are from the ambient gases in the FTIR chamber. Part A contains the entire spectra and parts B-D contain sections of the spectra containing deconvoluted peaks. Characterization conditions are same as in **Figure 55**.

Appendix B (Continued)

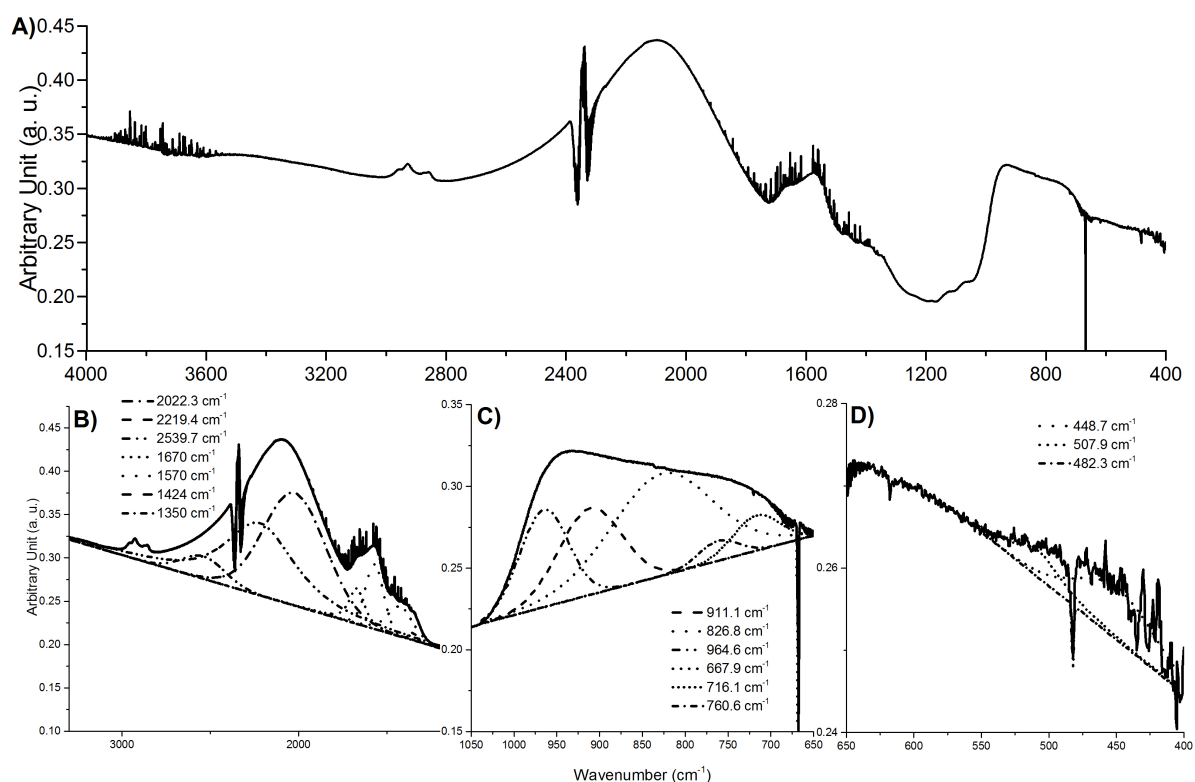


Figure 64: Absorbance FTIR spectra of a 500TNT sample. The water (3800-3000 and 2000-1400 cm^{-1}) and carbon dioxide (2380-2320 and 667 cm^{-1}) regions are from the ambient gases in the FTIR chamber. Part A contains the entire spectra and parts B-D contain sections of the spectra containing deconvoluted peaks. Characterization conditions are same as in **Figure 55**.

Appendix B (Continued)

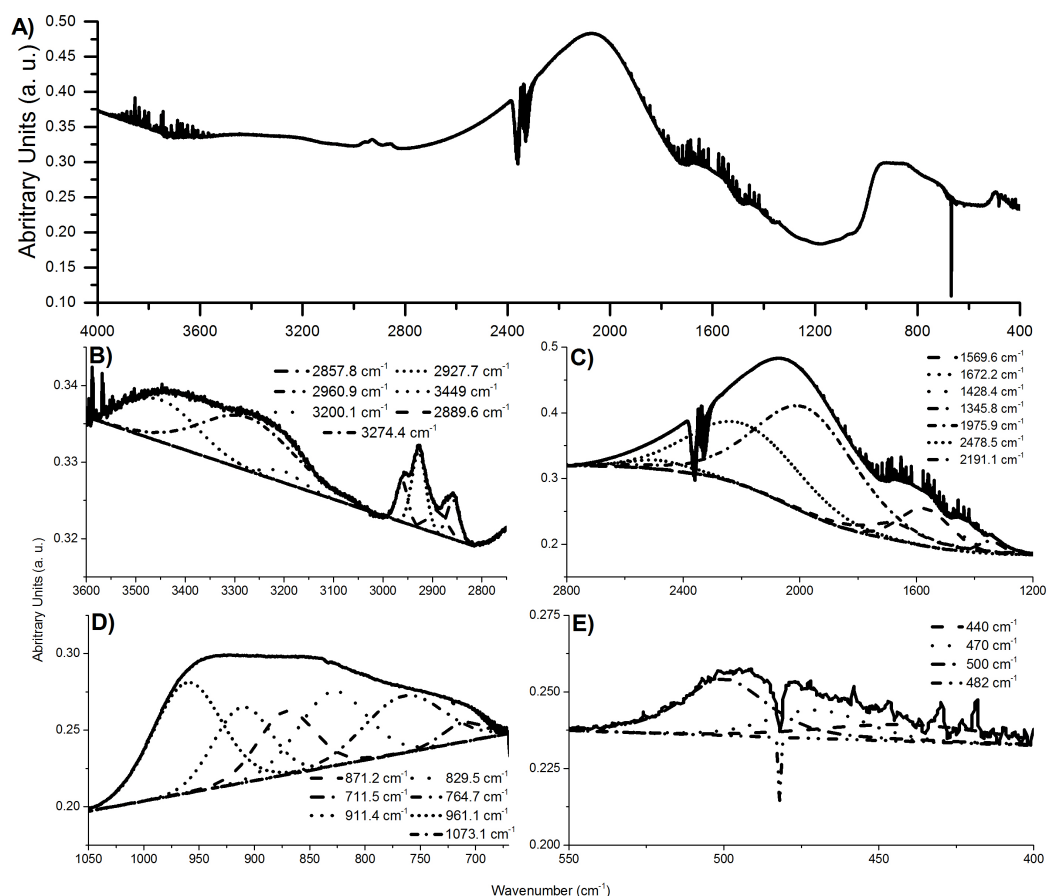


Figure 65: Absorbance FTIR spectra of a 600TNT sample. The water (3800-3000 and 2000-1400 cm⁻¹) and carbon dioxide (2380-2320 and 667 cm⁻¹) regions are from the ambient gases in the FTIR chamber. Part A contains the entire spectra and parts B-D contain sections of the spectra containing deconvoluted peaks. Characterization conditions are same as in **Figure 55**.

Appendix B (Continued)

study offers in-depth deconvolution analysis not addressed in those studies.(73) With the exception of H₂O/CO₂ regions, FTIR spectra of TNTs have distinct signatures. Finally, due to the similarities to TO-700 FTIR spectra, see previous section for discussion of the peaks for 700TNT.

In in the 4000-2800 cm⁻¹ region, CTNT, 200TNT, 300TNT, and 400TNT anodized samples contained a peak related to adsorbed/absorbed H₂O and -OH bonds within 2800-3800 cm⁻¹ (**Figure 66**, **Figure 67**, **Figure 68**, and **Figure 69**).(156; 203; 204; 154; 139; 268; 147; 138; 142; 277; 278) While several peak locations are reported in literature and the following were consistently used to fit this region of the spectra; 3915, 3834-40, 3710-70, 3591-3625, 3449-77 and 3200-05 cm⁻¹. The absorbed H₂O signature would imply the H₂O have physically incorporated into the TiO₂. However, it is more likely that H₂O adsorbed inside the TNTs would provide similar chemical signature as absorbed H₂O. Alternatively, due to the very small and few, if any, surface pores present on 500TNT and 600TNT samples, and no nanotubes present on 700TNT samples, peaks for adsorbed/absorbed H₂O and -OH bonds within the 2800-3800 cm⁻¹ region are absent (**Figure 64**, **Figure 65**, and **Figure 63**). Peaks assigned to N-H bonds (3375 cm⁻¹)(272) were observed on CTNT and 400TNT at locations of 3360-66 cm⁻¹ likely due to the ammonium residues left over from the electrolyte (**Figure 66** and **Figure 69**). In addition, the bonds of NH₄⁺ on H₂O (3250-3810 cm⁻¹) (148; 279) fall within the 2800-3800 cm⁻¹ for adsorbed/absorbed H₂O and -OH bonds. Three smaller peaks are observed in spectra of all samples located at 2857-90, 2928-30, and 2961-2 cm⁻¹ and assigned to C-H bonds at 2800-3000 cm⁻¹ (158; 202; 157; 268), 2852-55 and 2968-3038 cm⁻¹ (275), 2922/2853 cm⁻¹ (275), and

Appendix B (Continued)

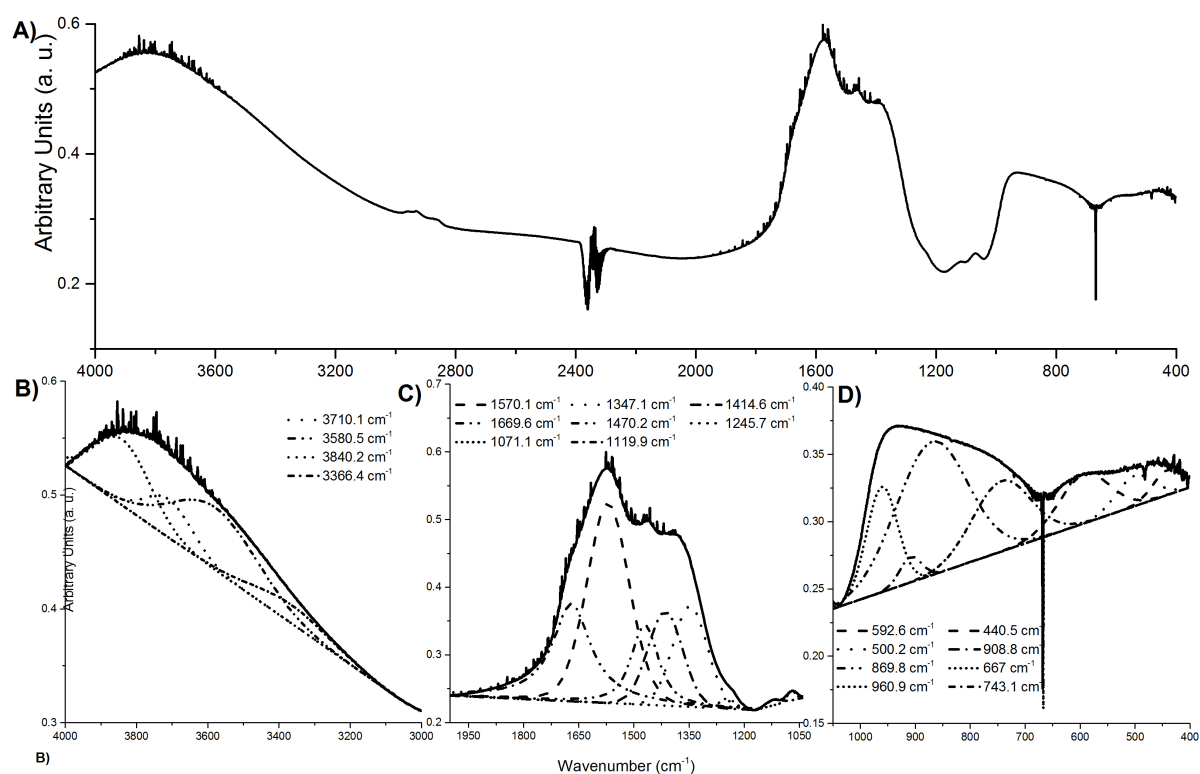


Figure 66: Absorbance FTIR spectra of a CNT sample. The water (3800-3000 and 2000-1400 cm^{-1}) and carbon dioxide (2380-2320 and 667 cm^{-1}) regions are from the ambient gases in the FTIR chamber. Part A contains the entire spectra and parts B-D contain sections of the spectra containing deconvoluted peaks. Characterization conditions are same as in **Figure 55**.

Appendix B (Continued)

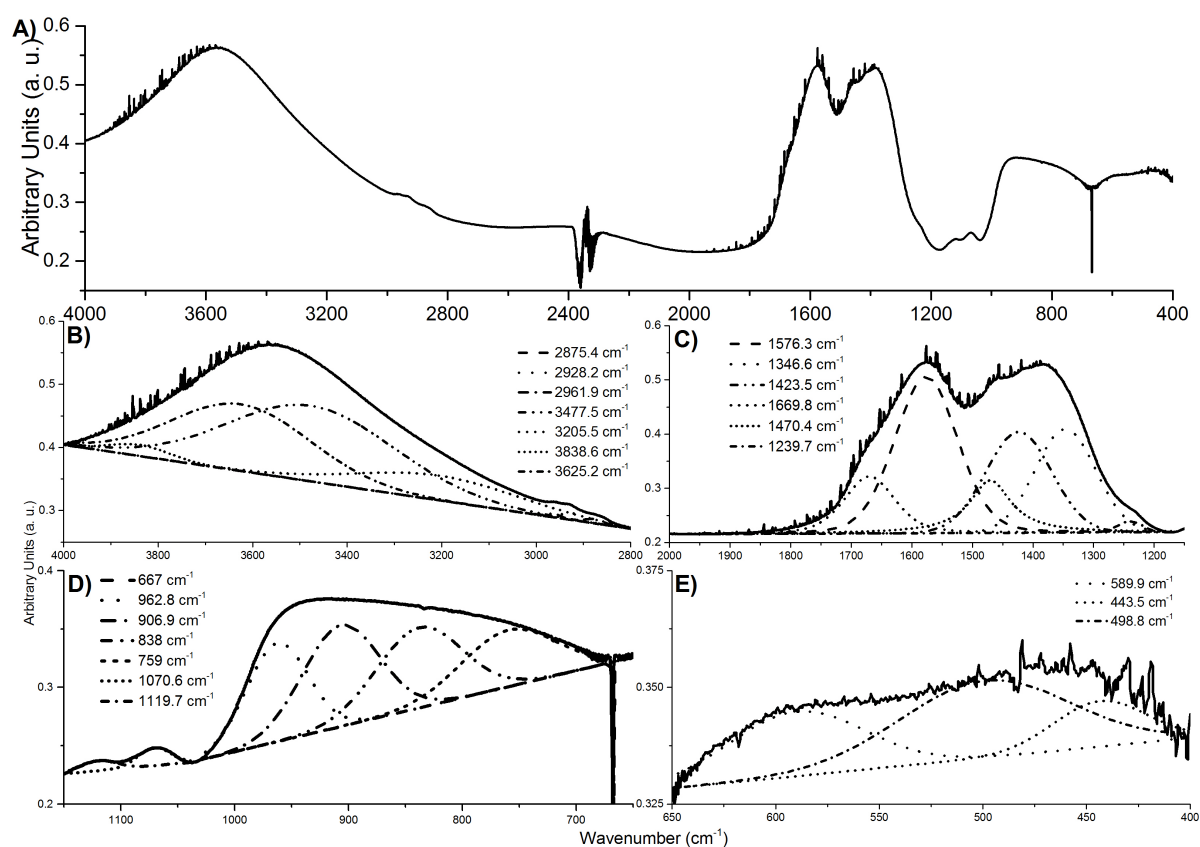


Figure 67: Absorbance FTIR spectra of a 200TNT sample. The water (3800-3000 and 2000-1400 cm⁻¹) and carbon dioxide (2380-2320 and 667 cm⁻¹) regions are from the ambient gases in the FTIR chamber. Part A contains the entire spectra and parts B-D contain sections of the spectra containing deconvoluted peaks. Characterization conditions are same as in **Figure 55**.

Appendix B (Continued)

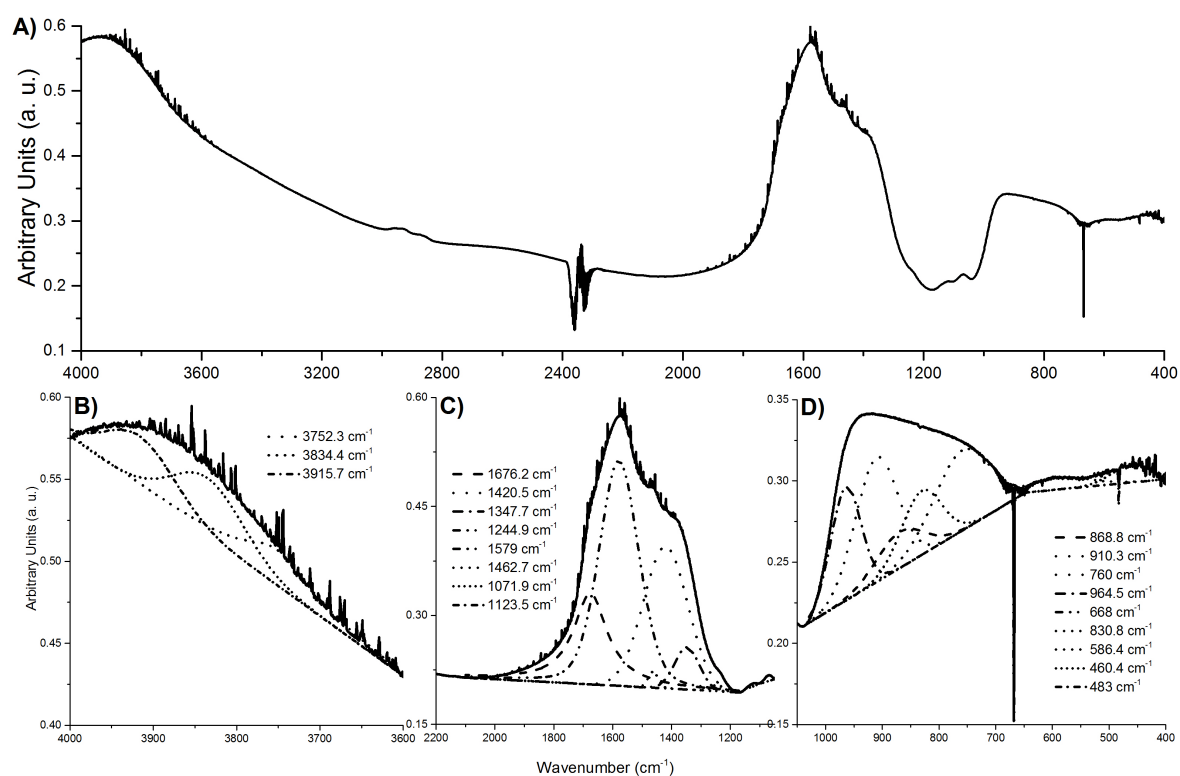


Figure 68: Absorbance FTIR spectra of a 300TNT sample. The water (3800-3000 and 2000-1400 cm^{-1}) and carbon dioxide (2380-2320 and 667 cm^{-1}) regions are from the ambient gases in the FTIR chamber. Part A contains the entire spectra and parts B-D contain sections of the spectra containing deconvoluted peaks. Characterization conditions are same as in **Figure 55**.

Appendix B (Continued)

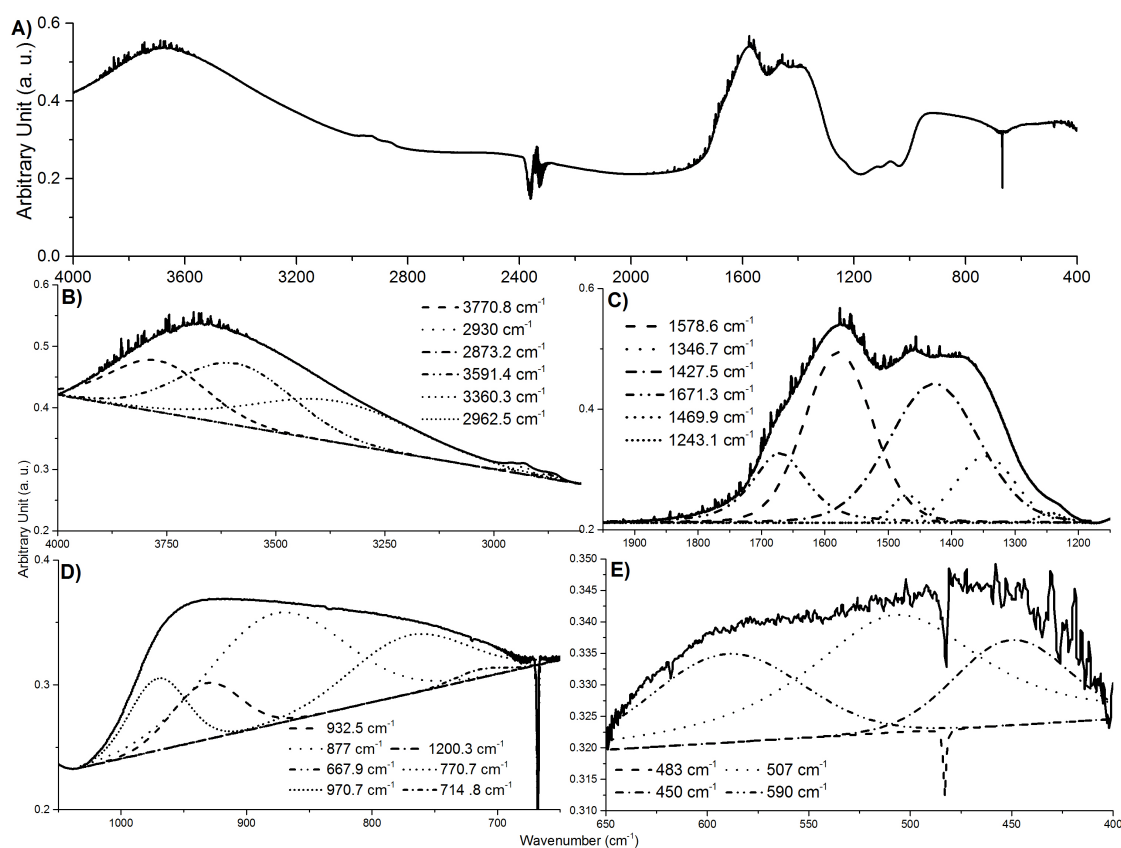


Figure 69: Absorbance FTIR spectra of a 400TNT sample. The water (3800-3000 and 2000-1400 cm^{-1}) and carbon dioxide (2380-2320 and 667 cm^{-1}) regions are from the ambient gases in the FTIR chamber. Part A contains the entire spectra and parts B-D contain sections of the spectra containing deconvoluted peaks. Characterization conditions are same as in **Figure 55**.

Appendix B (Continued)

2900 cm^{-1} (151). In the 2800-1800 cm^{-1} region, several small peaks at 2327-34, 2349, and 2361-63 cm^{-1} are observed on all samples and are assigned to gaseous CO_2 (2320-2380 and 2350 cm^{-1}) (158). Additionally, 400TNT and 600TNT spectra contain peak located between 2400-2463 for OH bonds are associated with adsorbed/absorbed H_2O (2442, 2435, and 2463 cm^{-1}) (**Figure 69** and **Figure 65**). (153) In spectra of 500TNT, 600TNT and 700TNT samples, peaks at 1975-2022, 2191-219, and 2540-46 cm^{-1} are observed and are assigned to C-O bonds of CO_2 (1975 (272) and 2206-08, 2185-91(148) cm^{-1} , respectively) (**Figure 64**, **Figure 64**, and **Figure 63**). The third peak is assigned to N-H bonds (2750-2350 cm^{-1}) (280). In the large 1800-1200 cm^{-1} region, several bond signatures are present in all spectra, with the exception of spectra for 700TNT samples (**Figure 66**, **Figure 67**, **Figure 68**, **Figure 69**, **Figure 64**, and **Figure 65**). Peaks at 1670-76, 1570-79, 1346-50, and 1414-28 cm^{-1} are assigned to CO_2 (1671 cm^{-1}) (158), N-H bonds (1500-1700 cm^{-1}) (157), and COO^- bonds (1350 and 1550 cm^{-1})(154) which may arise as a by-product of hydrothermal oxidation of carbon during anodization(154), and TiO_2 (149) or N-H bonds of NH_4^+ (147), respectively. The peak at 1240-46 cm^{-1} is observed on spectra of CTNT, 200TNT, 300TNT, and 400TNT and are assigned to the H_2O interaction with the hydrogen of -OH groups (1222 cm^{-1}) (138) and Ti-O-O-H bonds (1250 cm^{-1}) (152) (**Figure 66**, **Figure 67**, **Figure 68**, and **Figure 69**). All spectra also contain two peaks at 1030-1080 and 1127-1135 cm^{-1} for byproduct of CO_2 reaction with TiO_2 and its hydroxides (1063 cm^{-1}) (281; 282) and for hydrated alumina which be part of the TNT structure (1135/1127/1129 cm^{-1}) (274). The peak at 1463-1470 cm^{-1} is observed for all spectra except for 500TNT and 600TNT samples and is assigned to N-H bonds

Appendix B (Continued)

of NH_4^+ ($1462\text{-}1465\text{ cm}^{-1}$) 30, C-H bonds (1463 cm^{-1}) (268), or Ti-O-Ti bonds (1450 cm^{-1}) (139), which are all possibilities due to the formation of TNTs and residue from the electrolyte (**Figure 65** and **Figure 63**).

In the region between $1200\text{-}400\text{ cm}^{-1}$, the following peaks are observed. For all spectra of anodized samples (**Figure 66**, **Figure 67**, **Figure 68**, **Figure 69**, **Figure 64**, **Figure 65**, and **Figure 63**) the peak between $435\text{-}60\text{ cm}^{-1}$ is assigned to rutile ($435/440\text{ cm}^{-1}$) (150; 155; 203), Ti-O-Ti bonds ($436\text{-}95\text{ cm}^{-1}$) (138), and Ti-O bonds (450 cm^{-1}) (154); the peak between $667\text{-}68$ is assigned to CO_2 (667 cm^{-1}) (144; 143); the peak between $961\text{-}71\text{ cm}^{-1}$ is assigned to Al-O bonds of alumina ($900\text{-}1000\text{ cm}^{-1}$) (283), or Al-OH bonds and alumina (960 cm^{-1}) (141; 283); the peak at $743\text{-}770\text{ cm}^{-1}$ is observed for all spectra and is assigned to alumina ($700\text{-}800\text{ cm}^{-1}$) (271) or rutile (763 cm^{-1}) (145). The peak at $498\text{-}508\text{ cm}^{-1}$ is observed for all anodized samples except for 300TNT samples, that can be assigned to Ti-O-Ti bonds ($450\text{-}550\text{ cm}^{-1}$) (139), rutile (493 cm^{-1}), and Ti-O bonds in TNTs ($400\text{-}613\text{ cm}^{-1}$) (204) (**Figure 66**, **Figure 67**, and **Figure 69**, **Figure 64**, **Figure 65**, and **Figure 63**). The peak between $482\text{-}83\text{ cm}^{-1}$ is observed for all anodized samples except for CTNT and 200TNT samples, that can be assigned to Al-O bonds of alumina (485 cm^{-1}) (269) (**Figure 68**, **Figure 69**, **Figure 64**, **Figure 65**, and **Figure 63**). The peak between $586\text{-}93\text{ cm}^{-1}$ is observed for all anodized samples except for 500TNT and 600TNT samples, that can be assigned to anatase (590 cm^{-1}) (141) (**Figure 64** and **Figure 65**). The peak between 470 cm^{-1} is only observed for 600TNT samples that can be assigned to Ti-O-Ti ($436\text{-}95\text{ cm}^{-1}$) or V_2O_5 bonds (470 cm^{-1}) (284). It may be that for the 600TNT sample, some of the dissolved vanadium

Appendix B (Continued)

deposited onto the anodized sample. The peak at 933 cm^{-1} is observed only in spectra of 400TNT samples and is assigned to amorphous TiO_2 (**Figure 69**).^(141; 146) The peak at 838 cm^{-1} is observed on only spectra of 200TNT and is may be assigned to the O-O bonds of TiO-OH (**Figure 67**).⁽¹⁵¹⁾ The peak at $712\text{-}716\text{ cm}^{-1}$ is observed for spectra of 400TNT, 500TNT and 600TNT and is assigned to anatase (690 cm^{-1}) (**Figure 69**, **Figure 64**, and **Figure 65**).¹⁴ The peak at $827\text{-}831\text{ cm}^{-1}$ is observed for 300TNT and 600TNT samples and is assigned to rutile (830 cm^{-1}) (**Figure 68** and **Figure 65**). ^(141; 146; 270; 140) The peak at $907\text{-}11\text{ cm}^{-1}$ is observed for all spectra except for spectra of 400TNT samples and is assigned to Al-O bonds of alumina (914 cm^{-1})⁽²⁷¹⁾ (**Figure 66**, **Figure 67**, **Figure 68**, **Figure 64**, **Figure 65**, and **Figure 63**). The peak at $869\text{-}77\text{ cm}^{-1}$ is observed for all spectra except for 200TNT and 500TNT samples and is assigned to anatase (870 cm^{-1}) (**Figure 66**, **Figure 68- Figure 69**, **Figure 65- Figure 63**).^(141; 146)

VITA

Arman Butt

Education

Ph.D., Bioengineering
University of Illinois at Chicago, USA
August 2015

B.S., Bioengineering
University of Illinois at Chicago, USA
May 2010

B.S., Physics
Loyola University Chicago, USA
May 2010

B.S., Biophysics
Loyola University Chicago, USA
May 2010

Publications

Butt, Arman, et al.: Thermal-Oxidation Treatment of Ti-V Alloy for Improved Tribocorrosion Resistance, Submitted.

Butt, Arman, et al.: Investigation of Long-term Wettability and Storage of TiO₂ ALD Deposited CP-Ti and Ti6Al4V Surfaces, Submitted.

Butt, Arman, et al.: Investigation of Anodization on Crystalline Chemical Vapor Deposited Titanium Oxide Films, Submitted.

Butt, Arman, et al.: Design, Development and Testing of a Compact Tribocorrosion Apparatus for Biomedical Applications, Journal of Bio- and Tribo-Corrosion, 1:4, 2 (2014).

Butt, Arman, et al.: A Novel Investigation of the Formation of TiO₂ Nanotubes on Thermally Formed Oxide of Ti-6Al-4V, Journal of Bio- and Tribo-Corrosion, In Press (2014).

Publications

Patel, Sweetu, Butt, Arman, et al.: Novel Functionalization of Ti-V Alloy and Ti-II using Atomic Layer Deposition for Improved Surface Wettability, Colloids and Surfaces B: Biointerfaces Journal, 115, 280 (2014).

Hamlekhan, Azhang, Butt, Arman, et al.: Anti-Aging Heat Treatment of Hydrophilic TiO₂ Nanotubes for Bone/Dental Implants, PLoS One, 9:5, e96213 (2014).

Patel, Sweetu, Hamlekhan, Azhang, Royman, Dmitry, Butt, Arman, et al.: Enhancing Surface Characteristics of Ti-6Al-4V for Bio-implants Using Integrated Anodization and Thermal Oxidation, Journal of Materials Chemistry B, 2, 3597 (2014).